SP-1233 (3)

REPORTS FOR MISSION SELECTION

THE FOUR CANDIDATE EARTH EXPLORER CORE MISSIONS

Gravity Field and Steady-State Ocean Circulation Mission
Land-Surface Processes and Interactions Mission
Earth Radiation Mission
Atmospheric Dynamics Mission

European Space Agency
Agence spatiale européenne

ESA SP-1233 (3)
July 1999

Reports for Mission Selection

THE FOUR CANDIDATE EARTH EXPLORER CORE MISSIONS

Earth Radiation Mission

European Space Agency
Agence spatiale européenne

ESA SP-1233 (3) – The Four Candidate Earth Explorer Core Missions -
EARTH RADIATION

Report prepared by: Earth Sciences Division
Scientific Co-ordinators: Paul Ingmann &
J. Pedro Poiares Baptista

Earth Observation Preparatory Programme
Technical Co-ordinator: Wolfgang Leibrandt

Cover: Richard Francis & Carel Haakman

Published by: ESA Publications Division
c/o ESTEC, Noordwijk, The Netherlands
Editor: Bruce Battrick

ISBN 92-9092-528-0

Price: 70 DFl

CONTENTS

1 Introduction

The 'ESA Living Planet Programme' (ESA SP-1227, 1998) describes the plans for the Agency's new strategy for Earth Observation in the post-2000 time frame. It marks a new era for European Earth Observation based on smaller more focused missions and a programme that is user driven, covering the whole spectrum of interests ranging from scientific research-driven Earth Explorer missions through to application-driven Earth Watch missions. The user community is therefore now able to look forward to a programme of more frequent but very specific missions directed at the fundamental problems of Earth system sciences.

Of the nine Earth Explorer core missions identified in ESA SP-1196 (1-9), four core missions were selected for Phase-A studies, which began in June 1998, namely: the Land Surface Processes and Interaction Mission; the Earth Radiation Mission; the Gravity Field and Steady-State Ocean Circulation Mission; and the Atmospheric Dynamics Mission. The Phase-A studies were all completed in June 1999.

This 'Report for Mission Selection' for the Earth Radiation Mission (ERM) was prepared by a Core Mission Drafting Team consisting of four members of the ERM Advisory Group (ERMAG); C. Flesia, A. Illingworth, E. Raschke and A. van Lammeren. The other MAG members, namely F. Berger, J.-P. Blanchet, J. Bösenberg, R. Kandel and J. Testud, supported them. Complementary contributions were provided by the Japanese ATMOS-B1 Team (team leader: T. Takamura). The technical content of the report (notably Chapter 6) has been compiled by the Executive based on inputs provided by the industrial Phase-A contractor. Others who, in various ways, have contributed to the report are listed in the Acknowledgements.

The primary aim of the ERM is to determine world-wide the vertical profiles of aerosol and cloud field characteristics to provide basic input data for numerical modelling and atmospheric studies. The mission supports the goals of the World Climate Research Programme (WCRP) and, in particular, of its sub-programme Global Energy and Water Experiment (GEWEX), which is intended to develop an improved understanding of energy and water fluxes within the climate system, to secure reliable forecasts of weather and climate. The primary aims of the mission are schematically illustrated in Figure 1.1.

New insights into the divergence of radiative energy, the interaction of clouds, aerosols and radiation, the vertical distribution of water and ice and their transport by clouds, the vertical cloud field overlap and cloud-precipitation interactions are expected. The ERM is therefore addressing one of the main areas discussed under Theme 2 of the 'ESA Living Planet Programme' (ESA SP-1227, 1998). To realise the measurement goals and meet the scientific objectives, a payload consisting of two active sounders (lidar and radar) and two complementary passive instruments (multi-spectral imager and broad-band radiometer), embarked on a single platform, is proposed. The two active instruments will provide vertical profiles of clouds and aerosol. The multi-spectral imager will enable the different cloud types and aerosols to be distinguished, while the radiometer will provide values of broad-band radiances at the top of the atmosphere.

This Report for Mission Selection for the ERM, together with those for the other three Earth Explorer Core Missions, is being circulated amongst the Earth Observation research community in preparation for The Four Candidate Earth Explorer Core Missions Consultative Workshop in Granada (Spain) in October 1999.

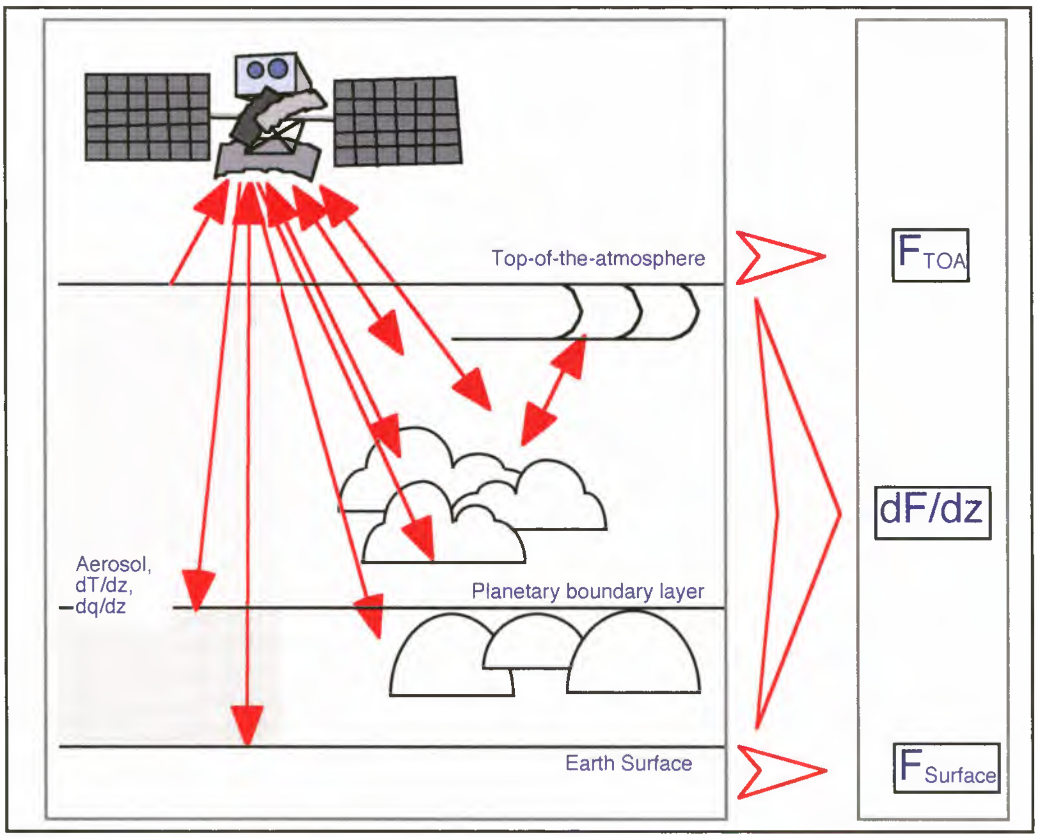

Figure 1.1. *The mission objectives of the ERM (schematically) – the objective of the ERM is to determine the radiative flux gradients (dF/dz) within the atmosphere as well as the fluxes (F_{TOA}) at the top-of-the-atmosphere and the fluxes at the surface ($F_{Surface}$) as derived quantities.*

Following this Introduction, the report is divided into eight chapters:

– Chapter 2 addresses the background and provides the scientific justification for the mission set in the context of issues of concern and the associated need to advance current scientific understanding. These objectives are not only those of the European scientific community, but also those of the Japanese scientific community with whom extensive scientific discussions have taken place with the goal of implementing a joint Japanese-European mission. The chapter identifies the problems and gives the relevant background. It provides a review of the current status and the clear identification of the 'gaps' in knowledge. In so doing, it provides a clear identification of the potential 'delta' this mission would provide.

- Drawing on these arguments, Chapter 3 discusses the importance of the scientific objectives. It then identifies the need for such observations by comparing the data that will be provided by this mission with that available from existing and planned data sources, highlighting the unique contribution of the mission.
- Chapter 4 focuses on mission requirements, comparing 'current practice' with the novelty of the mission and derives, in the context of the scientific objectives, the mission-specific observational requirements. It confirms that the ERM, with its well-balanced measurement capabilities, would be unique in obtaining a new and quantitative understanding of the Earth's radiation field.
- Chapter 5 provides an overview of the various mission elements such as the space and ground segments and external sources laying the foundations for mission implementation. It is demonstrated that the scientific objectives and observational requirements can only be met by co-located observations provided by the two active instruments on a single spacecraft.
- Drawing on Chapter 5, Chapter 6 provides a complete summary description of the proposed technical concept (space and ground segments). The technical maturity of the concept is illustrated by the way it meets the observational requirements addressed in Chapter 4.
- Chapter 7 outlines the envisaged data-processing scheme. It includes a description of the algorithms proposed, in particular, for the synergetic processing. The processing chain is described, clearly demonstrating the feasibility of transforming the raw data via calibration and validation into the requisite geophysical products.
- Drawing on Chapters 5 to 7, a comparison of expected mission performance versus performance requirements (Chapter 4) is provided in Chapter 8. This draws on the main findings of the previous chapters, complemented by results of an end-to-end simulation tool, to demonstrate that the expected mission performance is indeed capable of meeting (a) the observational requirements (Chapter 4) and (b) the ERM scientific objectives as outlined in Chapter 2.
- Programme implementation, including risks, development schedule and international collaboration, is discussed in Chapter 9. In particular, drawing on the previous chapters, Chapter 9 discusses the ERM in the context of other related missions. Here, in particular, reference is made to ATMOS-B1. A possible co-operation of ERM with ATMOS-B1 would offer a unique opportunity to enhance the mission return. It is concluded finally that the

proposed launch in the 2005/6 time frame would be very timely for the scientific community.

2 Background and Scientific Issues

2.1 The Problem

Governments urgently need to make major political and economic decisions based upon predictions of future global warming. At present, all such predictions rely on global numerical models that, while very powerful, have limitations arising from the modelling or parameterisation of the geophysical variables considered. As stated by the IPCC (1995), "the most urgent scientific problems requiring attention to determine the rate and magnitude of climate change and sea-level rise are the factors controlling the distribution of clouds and their radiative characteristics…". Furthermore, aerosols impact directly (through scattering and absorption) and indirectly (by altering the structure and radiative properties of clouds) on climate. Clouds are very important for our weather and play a crucial role in the hydrological cycle and the energy balance of the climate. Despite their importance there are still large deficiencies in the representation of clouds and aerosols in present-day atmospheric models. The advances in model representation are hampered by the lack of data sets on the vertical distribution and characteristics of clouds and aerosols. Vertical profiles of cloud and aerosols cannot be derived with the required accuracy from present space observations. This is a serious deficiency when attempting to validate the representation of the present climate in models to establish confidence in the latter's ability to predict future climate change.

Clouds also play a crucial role in atmospheric circulation processes, due to their ability to redistribute large amounts of energy and water, and also in atmospheric-chemistry processes and precipitation. In addition, they are important in atmospheric dynamics as they transport water vapour and trace gases to higher altitudes. Early predictions based on the doubling of carbon dioxide alone (assuming cloud cover remains constant) suggest global warming of about 2.5 K in the next hundred years. More recent models, which include cloud-cover feedbacks, predict atmospheric temperature rises ranging from 1.2 to 5 K. This level of uncertainty does not lend confidence to predictions of future climate.

Moreover, it must be emphasised that any global warming above a fraction of a degree corresponds to some positive water-vapour feedback, i.e. to a perturbation of the hydrological cycle entailing modification of the spatial distributions of evaporation, precipitation, water resources, soil moisture and in a general way a new bio-climatological map. These changes will have serious ecological and economical impacts, and they are not reliably predicted by the existing climate-change simulations.

The vertical structure and distribution of clouds have an important effect on heating profiles in the atmosphere (Fig. 2.1). Low-level clouds tend to cool the atmosphere by reflecting visible radiation, whilst an increase in cold high-level clouds leads to less infrared radiation escaping to space and so tends to warm the atmosphere. Global observations are needed to validate that present numerical models have correctly represented the vertical distribution of clouds and their impact on the Earth's radiation.

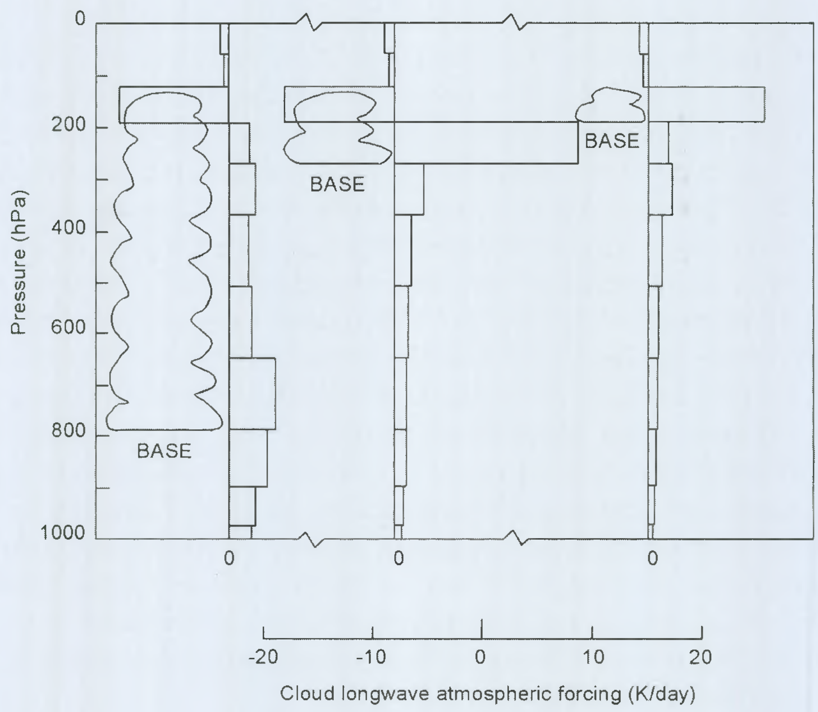

Figure 2.1. *Infrared radiative heating/cooling profiles, calculated for three different cloud base levels (after Slingo and Slingo, 1988). These profiles demonstrate the need for an accurate knowledge of upper and in particular the lower cloud boundaries.*

Currently, it is estimated (e.g. Harrison et al., 1990) that the reflection of short-wave radiation (by mainly low-level clouds) results in a mean global cooling of 50 Wm^{-2}, while the greenhouse warming (mainly from high clouds) results in a long-wave warming of 30 Wm^{-2}. Thus, the net global effect of clouds is a cooling of about -20 Wm^{-2}. This should be compared with a doubling of atmospheric carbon dioxide, which would produce an increase of about 4 Wm^{-2} by direct radiative forcing. Clearly, changes in cloud cover and its height distribution, as a response to increased carbon dioxide in a future climate, could lead to much larger changes in net radiative flux than that caused by the original change in carbon dioxide. These could give either a positive or a negative feedback. A similar assessment of the impact of cloud height on down-welling long-wave flux with slightly different premises was carried out by Chahine (1992), leading to the same conclusions.

Since its establishment in 1989 by the World Climate Research Programme (WCRP), the Atmospheric Model Intercomparison Project (AMIP) has become the focus for international efforts devoted to the diagnosis, validation, and intercomparison of global atmospheric models' ability to simulate the climate. AMIP has become a de facto standard climate performance test of atmospheric General Circulation Models (GCMs). Numerous analyses of the AMIP I results (e.g. Gates et al., 1999; Weare et al., 1996) have shown large discrepancies between the results of different models. Even a parameter such as fractional cloud cover is not well-represented in current models.

Figure 2.2 (from Gates et al., 1999) shows a comparison of zonally averaged outgoing long-wave radiation (OLR) at the top of the atmosphere (upper panel) and total cloudiness (lower panel) calculated from about 30 different atmospheric models. In both cases observations from the National Centre for Environmental Prediction (NCEP, for OLR) and the International Satellite Cloud Climatology Project (ISCCP, for total cloudiness) have been added, and a general tendency for most models to underestimate cloud cover is apparent. It should be noted that, while the agreement between models for OLR is reasonably good, the disagreement among modelled cloud coverages is very high

Aerosols efficiently reflect and scatter short-wave solar radiation and so act to reduce any greenhouse warming. They interact with clouds since they can act as the source of cloud condensation nuclei and alter their microphysical and radiative-transfer properties. They also impact on precipitation.

Circulation models generally use an estimated level of background aerosol (e.g. D'Almeida et al., 1991) to account for the reflection of solar radiation. However, there is still incomplete knowledge about their characteristics, i.e. amount and size distribution, altitude and thickness of layers. The addition of aerosols in simulations of climate change reduces the computed increase in near-surface temperature considerably, as shown in Figure 2.3.

To address these issues, the ERM has specifically been defined with the scientific objective of determining world-wide the vertical profiles of cloud and aerosol field characteristics to provide basic input data for numerical modelling and studies (on a global scale) of:

- the divergence of radiative energy
- aerosol-cloud-radiation interactions
- the vertical distribution of water and ice and their transport by clouds
- the vertical cloud field overlap and cloud-precipitation interactions.

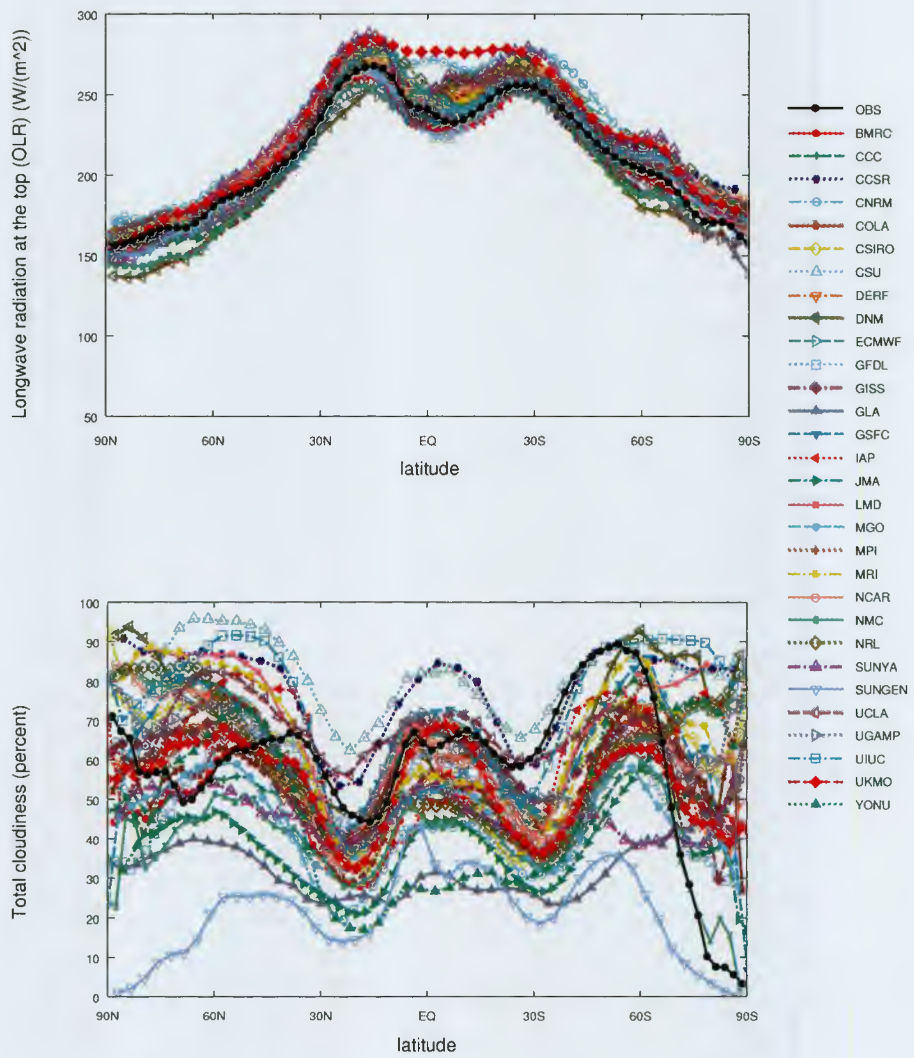

Figure 2.2. *AMIP I model intercomparison of 30 atmospheric models for outgoing long-wave radiation and total cloudiness for DJF (December, January, February) of the period 1979-1988 (Gates et al., 1999). The upper panel shows comparisons of the outgoing long-wave radiation with observations (black line) from the NCEP database (Gruber and Krueger, 1984); the lower panel shows total cloudiness with observations (black line) from ISCCP for 1983–90 (Rossow et al., 1991).*

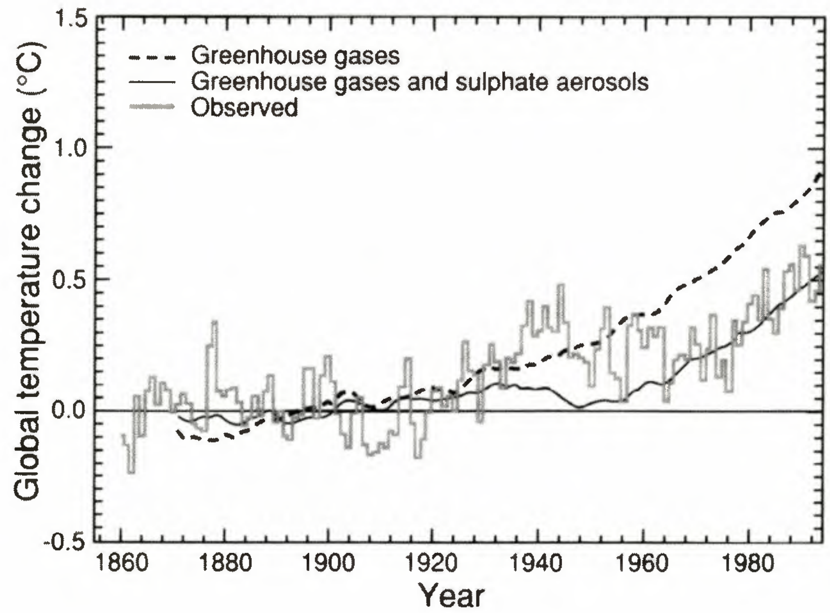

Figure 2.3. *Comparison of observations of global mean temperature from 1860 to 1990 with simulated warming from models that have greenhouse gases only and those that have greenhouse gases and aerosols (direct effect). The inclusion of aerosols has slowed the predicted warming since 1920 so that there is better agreement of the models with observed warming (from IPCC, 1995).*

In order to meet above objectives, the mission should provide the following observations on a global scale:

- Cloud boundaries (top and base) even of multilayer clouds and consequently height-resolved fractional cloud cover
- Vertical profiles of ice water content and ice particle size
- Vertical profiles of liquid water content
- Detection of precipitation and estimation of light precipitation
- Detection of aerosol layers and estimates of their optical depth
- Short- and long-wave radiances at the top-of-the-atmosphere.

The mission objectives of the ERM are also summarised schematically in Figure 1.1. These requirements of the ERM will now be addressed in more detail.

2.2 Background

2.2.1 Need for Climate System Research

The climate system consists of the atmosphere, the oceans, the cryosphere, the continental surfaces and their various constituents. These components are coupled and there are complex, non-linear interactions between them. To model these requires a thorough knowledge and understanding of all the physical and chemical processes involved. This requires modelling of the whole Earth System, as discussed in 'ESA's Living Planet Programme' (ESA, 1998), to predict future weather and climate on time scales ranging from days to decades so that reliable advice can be provided to policy makers. A new generation of computing systems will provide the potential for including much more detail in Earth-system simulations of present and future climate, but this increased capability will be wasted without a parallel advance in knowledge and data.

Clouds and aerosols play a crucial role in the Earth's radiation. They reflect and absorb radiation and affect the distribution of heat which drives the fundamental dynamical processes moving air and moisture around the planet.

2.2.2 Role of Clouds

Clouds mainly consist of particles of ice or liquid water. On a global scale they reflect about twice as much solar radiation back to space than the combination of a cloudless atmosphere and the ground. Locally, this reflected solar radiation can reach much higher magnitudes. In addition, high-level cold clouds contribute very effectively to the long-wave greenhouse effect of the atmosphere by absorbing the upward heat radiation and re-emitting less energy to space because of their lower temperatures. This is illustrated quantitatively in Figure 2.4, taken from Wang et al. (1995). The reduction of the emissions from the surface (as given by the surface temperature) by cloud-free and cloudy atmospheres are plotted. These diagrams show that clouds can add 20 to 60 Wm^{-2} to the absorption of thermal long-wave radiation in the atmosphere. These values have been determined from measurements of the Earth Radiation Budget Experiment (ERBE) and are being used to validate numerical models.

Many radiative-transfer studies have shown that, in general, cloud fields are cooled by radiation at their tops, and heated from below at their lower boundaries. This forces an additional destabilisation and its vertical extent depends on the cloud thickness and can affect the life cycle of clouds. Furthermore, cloud formation releases latent heat of condensation in certain altitude ranges, depending on the dominating cloud types (see e.g. Webster and Stephens, 1984). Figure 2.5a illustrates the differential vertical heating of the troposphere by radiation and by the release of latent heat for different latitudes. Figure 2.5b compares the regions of the mostly cloud-free Arabian Sea and the Bay of Bengal during monsoon (which is often covered with deep convective cloud systems reaching altitudes of about 20 km) and shows the very different profiles of vertical heating that result from varying amounts of cloud.

Clouds transport energy and water in the atmosphere. For example, convective cloud towers provide an efficient transport mechanism from the lower troposphere into the stratosphere. Thus, they are responsible for the movement of anthropogenic substances, such as the CFCs and some aerosol species, to those altitudes. Finally, clouds also alter the magnitudes and spectral characteristics of the radiation fields at the ground, which in turn determine many dynamical and biological processes.

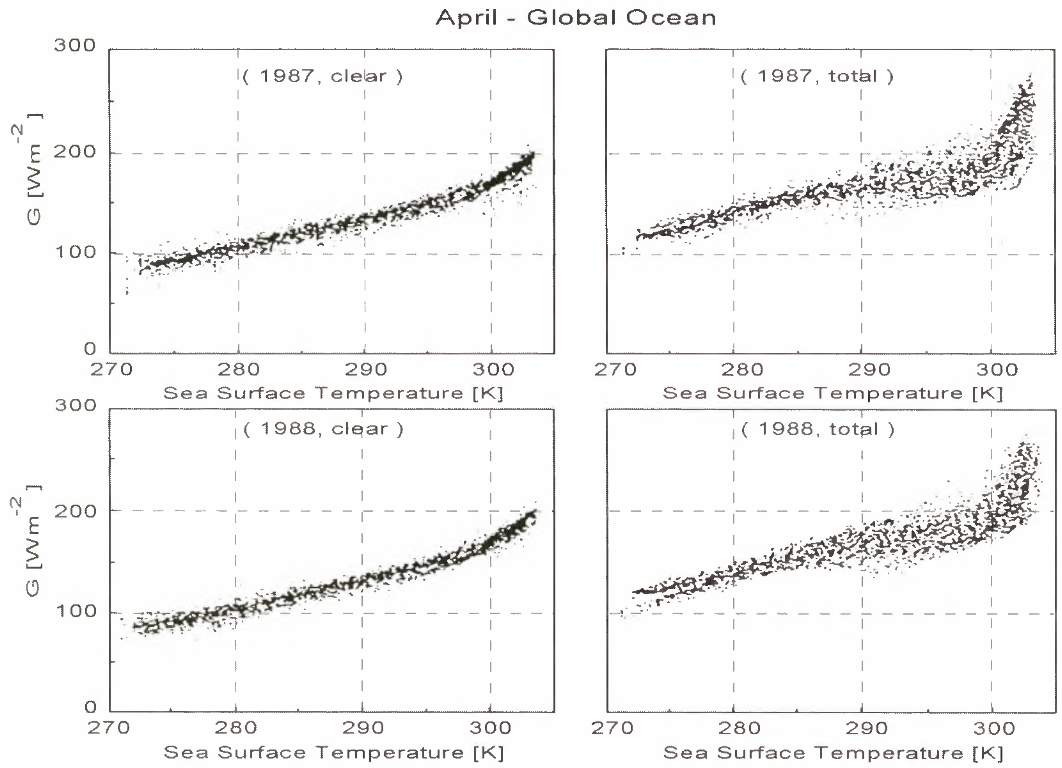

Figure 2.4. Atmospheric greenhouse effect in April 1987 and 1988 over oceans, determined from differences between the emission of long-wave radiation from the sea surface and the emission leaving to space, plotted versus the sea surface temperature (after Wang, Dudek and Liang, 1995). Clouds absorb a further 20 to 60 Wm^{-2}. Doubling of the present concentration of carbon dioxide and the expected increase of other greenhouse gases in a cloud-free atmosphere may add a steady 'force' of 4 to 6 Wm^{-2}.

As shown in Figures 2.1 and 2.5, the heating by radiation and condensation is dependent on the altitude of cloud layers. This means that both the vertical cloud profiles and the corresponding cloud water contents must be known. In addition, the horizontal structure of cloud fields needs to be considered.

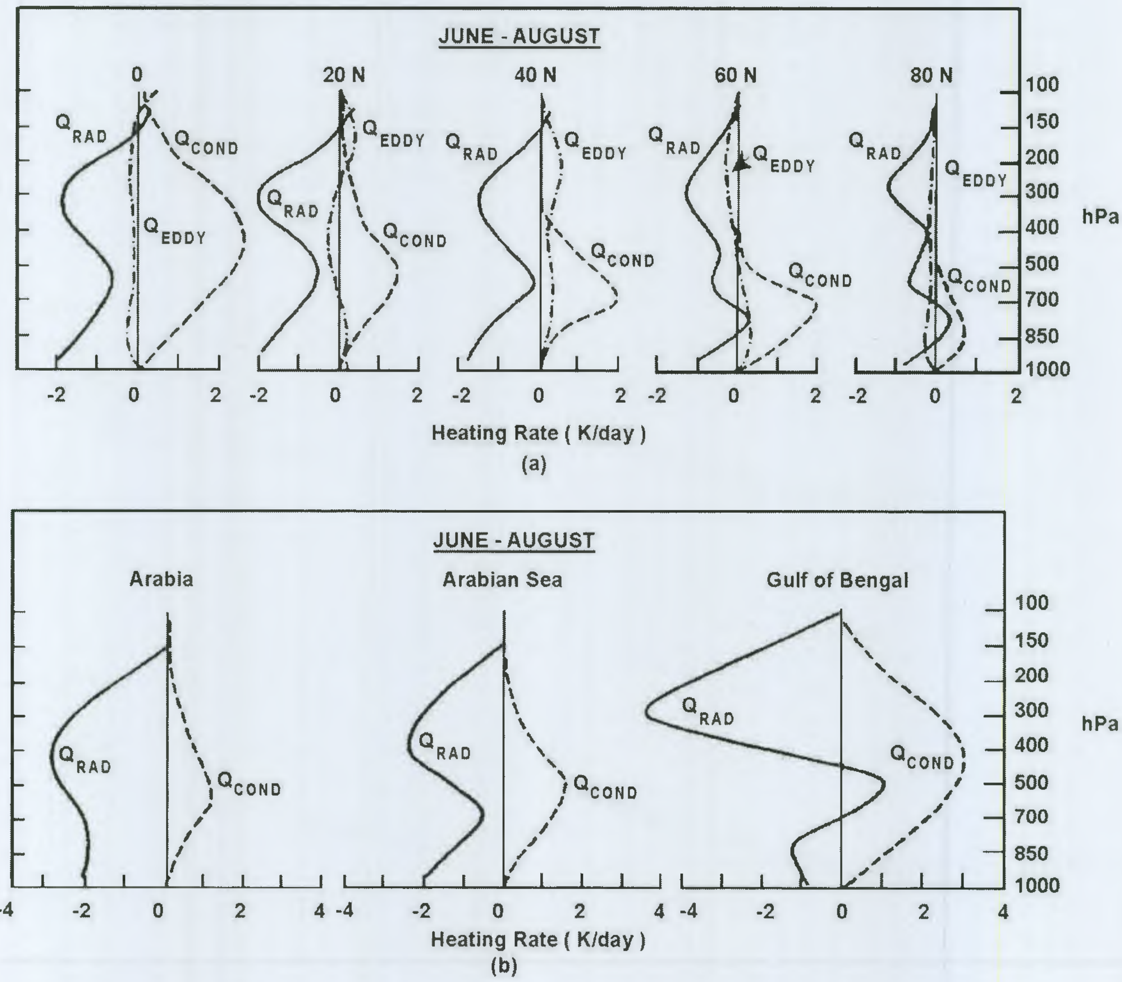

Figure 2.5. *Heating rates due to radiation (RAD), latent heat release (COND), macro-scale transport (EDDY) and other horizontal transports (from Webster and Stephens, 1984) for (a) zonal means and (b) region specific (for about 20 N). These diagrams demonstrate the height dependence of radiative and latent heating, which in turn interacts with atmospheric dynamics.*

Cloud fields, measured through passive remote sensing from space, are now the subject of continuous monitoring within international (e.g. ISCCP; Rossow and Schiffer, 1999) and various national projects. However, although they are used as essential inputs for the validation of cloud parameterisation and modelling for climate research, such data provide little information on the vertical distribution of clouds.

Recent sensitivity studies performed at ECMWF have shown that cloud overlap assumptions used in atmospheric models have a large impact on predictions of surface precipitation through the rain evaporation process. Jakob and Klein (1999) found differences in large-scale precipitation of up to 2 mm day^{-1} in zonal means in tropical regions. The distribution of clouds on the vertical (see Fig. 4.3) can also significantly modify the energy balance at the top of the atmosphere. Between two extreme overlap assumptions, Morcrette and Jakob (1999) showed differences of 10 W m^{-2} in monthly mean values of the OLR. The amount of cloud ice water in atmospheric models is strongly influenced by the ice fall speeds used to describe the ice settling process. Parameterisation sensitivity experiments by Jakob (personal communication) have demonstrated that increasing the ice fall speed in the ECMWF model from 0.4 m s^{-1} to 1 m s^{-1} reduces the ice water path from 75 g m^{-2} to 50 g m^{-2} in global mean.

These results show that there are still important issues involving the description of clouds in atmospheric models that need to be resolved. Progress in these areas depends on improving the representation of both the vertical structure of clouds and the cloud ice microphysics in climate and Numerical Weather Prediction (NWP) models.

The description of clouds in GCMs remains difficult because they encompass a broad spectrum of scales from the very small which describe microphysical processes, to planetary scales describing cloud organisation in large systems (frontal bands, ITCZ, easterly waves, ...). GCMs can only explicitly describe atmospheric motions having horizontal scales larger than 100 km or more. This means that important physical processes describing the formation and dissipation of clouds cannot be explicitly resolved by global numerical models. These processes are implicitly accounted for through parameterisation schemes, which represent the effects of sub-grid-scale processes on resolved model scales. The parameterisation of sub-grid-scale processes is a key issue of both climate and NWP models. The reason is that they describe phenomena that are not properly sampled by conventional observations and, as a consequence, there is no firm observational database on which to base parameterisations of sub-grid processes.

To study the role of clouds in the climate system, the following cloud characteristics must be known:

- the *macro-physical properties of cloud fields* – fractional cover, height ranges, vertical thicknesses and geometrical inhomogeneities;
- the *micro-physical properties of cloud fields* – liquid and ice water concentrations in each layer (including particle sizes);
- the *radiative-transfer properties* – reflectance and transmittance, absorptance and emittance;
- mutual overlap of cloud elements in multi-layer systems;
- light precipitation between and below cloud layers.

2.2.3 Role of Aerosols

Aerosols can be of natural or anthropogenic origin. The latter component shows increasing concentration not only in the planetary boundary layer (primarily the result of urban life and biomass burning), but also near the tropopause due to the increase of air traffic. Increases in aerosol levels reduce, at least regionally, the solar radiation reaching the ground (aerosol direct radiative effect; see Fig. 2.3). They absorb solar radiation in their respective altitude ranges and also influence the chemical composition of the atmosphere. Furthermore, there are strong interactions between aerosols and cloud particles.

The effects of aerosol in changing the radiative properties of clouds (aerosol indirect effect) were discussed in IPCC (1995). Two effects were identified, namely the effect on cloud albedo due to decreases in the droplet effective radius, and the consequent effect of this decrease on cloud lifetime and possibly cloud cover. Although 'mean aerosol statistics' or 'background aerosol' have been derived from a large variety of different sources (e.g. D'Almeida et al., 1991), the actual aerosol distribution within the atmosphere must be known for climate simulations and analyses. The recent creation of a special International Aerosol Climatology Project within the frame of GEWEX confirms the importance of this issue.

> To study the role of aerosols in the climate system, the following aerosol characteristics must be known:
>
> – altitude and geometrical thickness of aerosol layers
> – the optical properties (optical thickness, particle size distributions)
> – the distribution, characteristics and amount of the 'background' aerosol.

2.2.4 Radiative Forcing

Radiative forcing is known to drive the entire circulation in the terrestrial climate system. The Sun, with a radiative power of about 1372 Wm^{-2} (Fröhlich and Lean, 1998) reaching the outer boundary of the Earth, provides the power for a cascade of processes. These in turn are linked to all the circulation processes in the atmosphere and in the oceans. Due to the Earth's curvature, only 25% of this power (i.e. 343 Wm^{-2}) is on average available, where the molecular atmosphere, clouds, aerosols and the ground reflect about 30% back to space.

Figure 2.6 (from Peixoto and Oort, 1992) describes schematically the redistribution of the solar short-wave radiation (spectral range between about 0.3 and 4.0 μm) and of the terrestrial long-wave radiation (spectral range between about 3.5 and 50 μm) in the global climate system. Also indicated in this figure are the amounts of sensible and latent heat generated at ground. It illustrates the dominating influence of clouds on the redistribution of radiative energy within the climate system, as well as radiation exchange with space.

This radiative forcing is responsible for the variation of temperature with height in the Earth's atmosphere. Changes in the concentration of greenhouse gases can modify this temperature variation. The most important 'greenhouse gases' are water vapour, carbon dioxide, methane, nitrous oxides, ozone and chloro-fluorocarbons. Considerable increases of the latter five species have been observed since the beginning of the industrial era about 150 years ago. This 'additional greenhouse effect' may force our climate system into possibly a more unstable state, which in turn would compromise the habitability of many regions of our planet. As shown in Figure 2.4, observations over the ocean show that clouds can add about 20 to 60 Wm^{-2} to the greenhouse effect of the cloudless atmosphere.

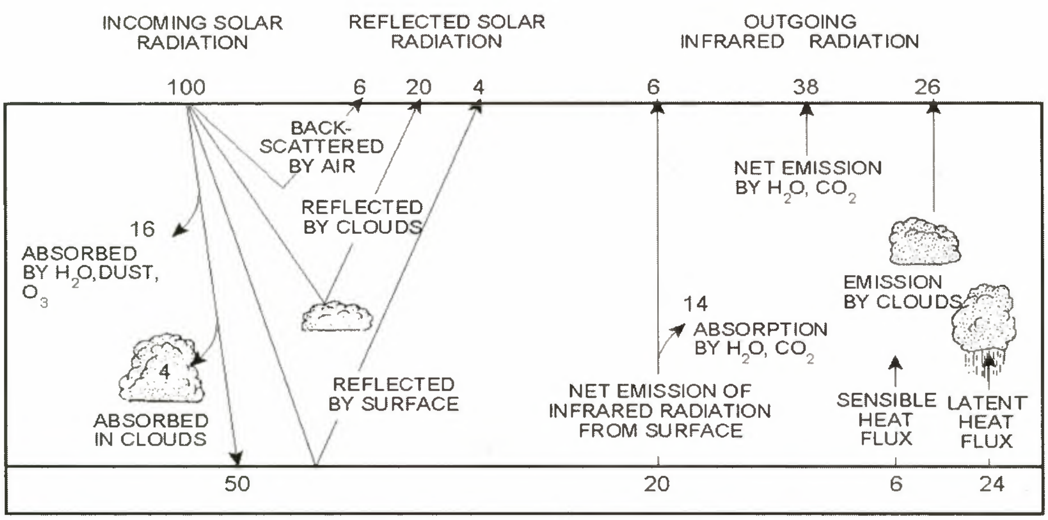

Figure 2.6. *Global annual means of the redistribution of incident solar radiation (100% corresponds to an incoming radiative flux density of 343 Wm^{-2}) by infrared heat radiation and sensible and latent heat in the climate system (from Peixoto and Oort, 1992).*

A comparison between the radiative fluxes derived from the ERBE measurements and those from the AMIP simulations is shown in Figure 2.7. Cloud radiative forcing (CRF) is the difference between the cloud-free radiation and that observed when the clouds are present. Short-wave forcing is usually negative (cooling) because the clouds reflect more sunlight, whereas long-wave forcing is usually positive (warming) because cold clouds loose less infrared radiation to space. Net forcing (in the upper panel of Fig. 2.7) observed for the month of January is the difference between the two and is much smaller than either component (short- and long-wave). In the tropics, the net forcing is close to zero because the two large short- and long-wave components almost cancel out. The net forcing is negative over the southern oceans because of the sunlight reflected from the clouds in local summer, whereas at northern latitudes the forcing is positive in winter because clouds lessen the long-wave loss to space. The rather large differences between the ERBE observations of net cloud radiative forcing and those simulated by the AMIP models are displayed in the lower panel. Note that the models underestimate the cloud forcing which should cool the southern oceans in summer by more than 100 Wm^{-2}, and the net heating by clouds expected in the northern winter is underestimated by about 20 Wm^{-2}.

The products generated by the ERM will provide the essential data to address these issues.

2.2.5 International Programmes

There are at present two major international research programmes which need detailed information on the radiative-transfer properties of the atmosphere and of the ground to reach their goals. These are the World Climate Research Programme (WCRP) dealing with all physical aspects of the climate system, and the International Geosphere Biosphere Programme (IGBP) concentrating on the interactions between climate and the biosphere.

Special projects in both Programmes, namely GEWEX (Global Energy and Water Cycle Experiment) and BAHC (Biospheric Aspects in the Hydrological Cycle) and others in the IGBP, have initiated research efforts to tackle relevant questions. They involve very many research groups. GEWEX in particular has formulated the request for more accurate measurements of cloud bases to determine the long-wave radiation budget in particular over the oceans with uncertainties of better than 10 Wm^{-2}.

The Joint Scientific Committee for the WCRP re-emphasised in its recent annual review of climate research activities the need for 'vertical profiles of atmospheric radiative fluxes and for quantitative details of cloud micro-physical properties and dynamics' as a prerequisite for the further refinement of parameterisations in large-scale atmospheric models (JSC, 1998).

Within GEWEX, various subprojects are concerned with the problems related to accurate measurements and modelling of cloud fields and their radiative-transfer properties. In a comparative study (AMIP; e.g. Gates, 1992; Gates, 1995; Gates et al., 1999) all global climate models showed large deviations in simulated cloud cover for

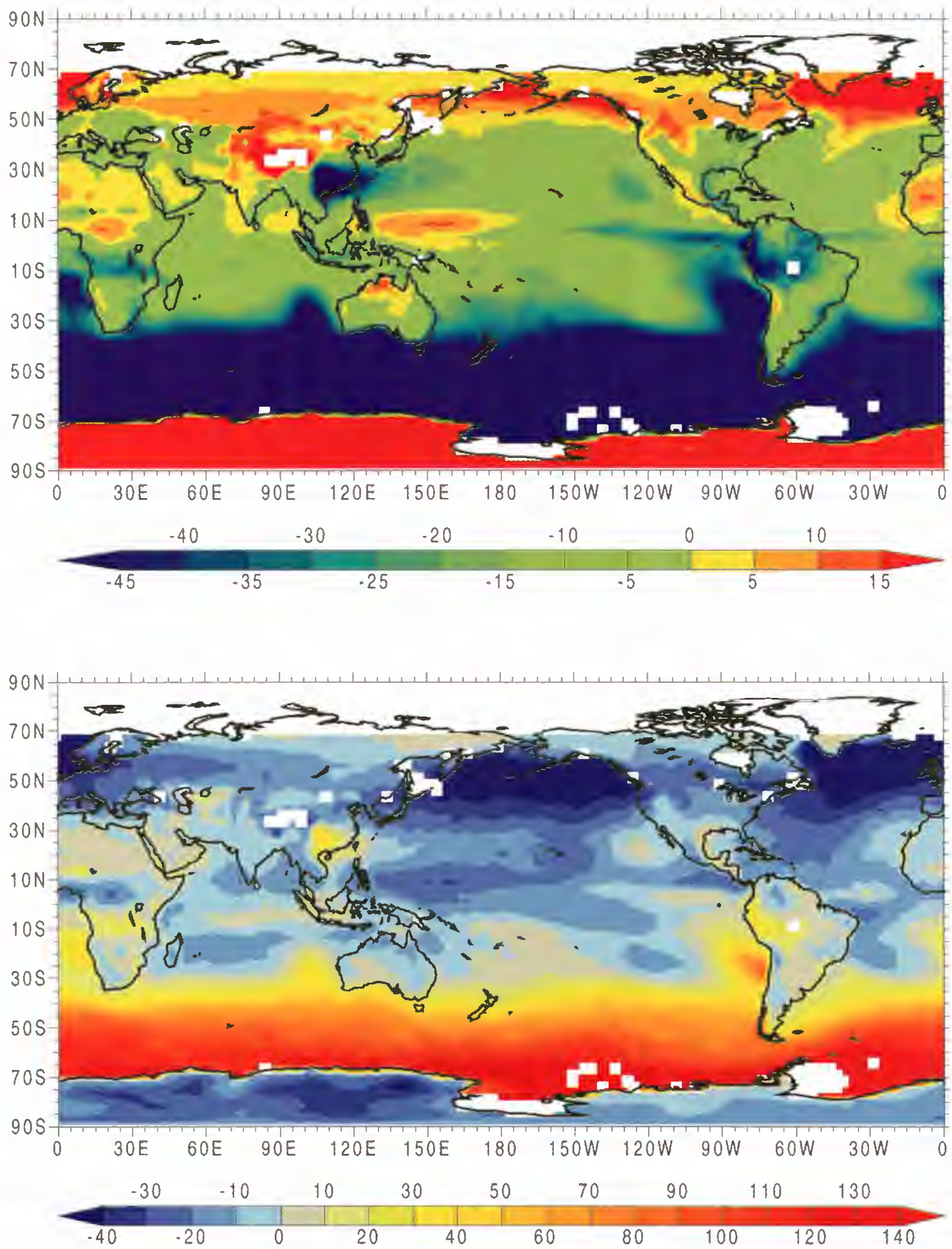

Figure 2.7. *Upper panel – ERBE observations of the net cloud radiative forcing during the month of January (upper panel). Lower panel – net AMIP model simulations of forcing minus the ERBE observations, showing that the models underestimate both the cooling due to reflection of sunlight over the southern oceans during their summer and the warming due to clouds in the northern winter (Potter, 1998).*

the same OLR (cf. Fig. 2.2) due to their different physical and numerical background. None of them agrees with the set of available observations.

Several new global networks are evolving as a consequence of our need to observe and monitor 'Global and Regional Climate Changes', which will be investigated within the frame of CLIVAR (Climate Variability). Other environmental changes will also be monitored as a result of the Kyoto agreements.

In spite of all of these activities, none of these international projects will provide the vertical profile data required to meet the objectives of the proposed ERM.

2.3 Current Status

This section describes the current status of cloud- and aerosol-related modelling and provides an overview of the observational capabilities using ground-based and spaceborne systems.

2.3.1 Observations

The best current attempt at describing cloud properties from existing spaceborne instruments (fractional coverage in at least three layers of the troposphere, optical thickness and also cloud water amounts and thermodynamic phases) is being carried out within the GEWEX-project ISCCP (see e.g. Rossow and Schiffer, 1999). This activity is now run almost operationally based on the operational multi-spectral imagery of geostationary and polar-orbiting satellites. The ISCCP data set now covers about 15 years. However, the spatial resolution (while original data are at much higher resolution) is about 250 km. However, all of these efforts fall short in providing observations of vertical cloud structure and the location of cloud boundaries.

Several attempts have been made to derive information on effective droplet or particle sizes in the upper layers of a cloud from multi-spectral data such as that used in ISCCP. Airborne in-situ measurements have already been performed within the frame of large field experiments (e.g. FIRE in the US, EUCREX in Europe, etc.) to validate such information. However, there is no way to attribute such retrieved quantities to a particular height range within the cloud from passive signals.

World-wide distributions (primarily concentrated over the regions between about 60°N and 60°S) of tropospheric aerosol properties (mostly optical thickness) have been derived from both in-situ and ground-based, remote-sensing data and combined into a 'standardised aerosol climatology' (e.g. D'Almeida et al., 1991). Operational multi-spectral satellite imagery can identify aerosol optical thickness over cloud-free areas. However, sub-visible (i.e. undetected) thin clouds (e.g. cirrus) bias such statistics (Stowe et al., 1992 and 1997). It is now the purpose of the GEWEX Aerosol

Climatology Project to channel all related activities into a concerted worldwide effort and to combine all existing global and regional data sets into a unique one. The ECLIPS (Platt et al., 1994) experiment that ran until 1994 aimed to measure, with all available means, cloud- and aerosol-layer boundaries. However, this data set did not provide instantaneous vertical profiles on a global basis – there are no global observations other than climatologies.

So far, from space, only LITE (laser in orbit technology experiment, e.g. McCormick et al., 1993) has provided observations of cloud and aerosol layers over different climate zones. This spaceborne data set has been complemented by correlative airborne observations. However, data were only taken during a very short period of time.

Other data have also been collected by ground-based measurements in special experiments or experiments of regional extent. In a few locations, such as the ARM stations of the US or the Arctic Station at Ny-Ålesund, there are now almost continuous measurements of cloud and aerosol fields with lidar and/or radar. However, these observations only provide regional or local data sets.

2.3.2 Modelling

During the last decade, the parameterisation of clouds in climate GCMs has greatly improved (Heise and Roeckner, 1990; Ricard and Royer, 1993; Fowler et al., 1995). Such effort was stimulated by the fact that the response of GCMs to climate changes is extremely sensitive to cloud description. This has been demonstrated in various inter-comparison studies (Cess et al., 1990; Cess et al., 1996) and recognised by IPCC (1995). Cloud type, fractional coverage and optical properties play a role in determining feedback mechanisms that will amplify or reduce an initial external radiative forcing (Senior and Mitchell, 1993). Early descriptions of clouds using empirical dependencies with relative humidity and other quantities (Slingo, 1987) are now progressively being replaced by prognostic cloud schemes. This empirical approach was initially chosen because of its simplicity, but also due to the lack of proper understanding on cloud formation and dissipation.

Typically the horizontal resolution of climate models is of the order of about 100 km, while the vertical resolution is 500 m to 1 km (or even less).

The modelling of cloud-radiation interactions in atmospheric models is described differently according to the scales of interest. At small-scale (few kilometres), 'cloud-resolving models' represent explicitly the bulk microphysical processes for cloud and rain formation. At large-scale (few hundreds of kilometres), GCMs include cloud and rain processes in a highly parameterised way. All of these dynamical models need to use simplified 'radiative-transfer models' (plan-parallel approximation, small number of spectral intervals) in order to keep computational costs reasonable.

- *Radiative-transfer models* – are now available with different spectral assumptions or computational approximations. They are tested in intercomparisons for cloud-free model atmospheres; a new test series for cloudy atmospheres is underway, organised by the GEWEX Radiation Panel (GRP). There are quite detailed models available to study the radiative transfer in three-dimensional models taking account of cloud-field inhomogeneities. Such models are used to study static situations. In all numerical simulations of cloud-field dynamics in global circulation models, quite simple radiative-transfer codes are used to meet required computational economy. These models have usually been tested against more complex ones, but they can barely represent the radiative transfer through three-dimensional cloud fields.
- *Cloud-resolving models* – are simulations of cloud microphysics and of formation/dissipation processes including their feedbacks to the dynamics of the ambient air. One GEWEX project, the GCSS (GEWEX Cloud Systems studies; Browning, 1993) uses cloud-resolving models to study such processes in great detail.

  In global and regional circulation models, the parameterisation schemes currently use a water-budget equation (e.g. Sundqvist, 1995) and have to simplify most microphysical processes. The mean liquid water and ice contents, the fractional cover or some measure of sub-grid-scale fluctuations are given by prognostic variables. In the near future, probably several different types of ice will be held as explicit variables and the prescribed effective size will become a prognostic variable. Aerosol is mostly prescribed according to origin and type.

  Such schemes are mostly 'calibrated' against observations and/or simulations with more sophisticated models. Spatial details in cloud fields can only be computed according to the spatial resolution of the dynamical 'mother' model. The validation of clouds in such models is at present only possible by intercomparison with the worldwide ISCCP data set, though this only distinguishes between three cloud levels and the fractional cloud cover at each level. Other data on ice or water contents or such quantities as effective radius appear to be purely speculative, since they are obtained using retrieval techniques that still require full validation.

- *General Circulation Models (GCMs)* – while the positions of cloud fields simulated in atmospheric models often show good agreement with observed cloud fields, there is no data to validate other parameters such as their vertical profile characteristics. In GCMs, used for atmospheric analyses and forecasts as well as climate simulations, considerable disagreement is also found in simulated macro-physical and radiative-transfer properties. This was shown in the AMIP project (see e.g. Fig. 2.2 and in various other publications by e.g. Weare et al., 1996 and Gates et al., 1999). This concerns also the computation of the actinic flux, which is required to understand photochemical reactions inside cloud fields. Since these simulations are expected to provide the basis for weather- and climate-impact studies and predictions of immediate or longer-term socio-economic value, they definitely need further improvements. Wild et al. (1998) summarised their analyses of global surface radiation budget on the basis of measurements and ECMWF re-analyses (ERA).

Currently, operational data-assimilation systems only use ground-based and satellite observations of pressure, temperature, wind and water vapour. They do not explicitly include any quantity related to the condensed phase of water (cloud water, cloud ice, rain...). Operational analysis is currently the only technique able to supply a global three-dimensional coherent description of cloud properties as a byproduct. Comparisons of ECMWF model products with radar and lidar observations (Mace et al., 1998b; Miller et al., 1999) have demonstrated an improved skill due to the strong coupling of clouds with dynamical processes (explicitly described in data-assimilation systems) and recent improvements in the description of cloud processes.

Data from the ERM will provide a unique set of observations that could be used for improving the quality of operational forecast products in various ways. As model resolution increases and description of parameterised processes improves, some of the forecast products will become more reliable for a wide range of potential applications. A better understanding of cloud-radiation interactions will lead to improved forecasts of weather parameters in the medium-range (two-metre temperature, cloudiness, precipitation...) and also to a more reliable seasonal forecasting system since the ocean-atmosphere coupling in the tropics is strongly driven by the energy and water fluxes between the two systems.

At ECMWF, a prognostic cloud scheme has been introduced into the operational forecast model in April 1995, with a strong positive impact on objective scores and also in reducing systematic biases in cloud cover (Miller et al., 1995). This scheme attempts to describe in a physical way the major processes leading to the production and dissipation of clouds (Tiedtke, 1993). It implies an explicit coupling with dynamics, radiation, turbulence, and cumulus convection. However, not all these processes are properly described in the ECMWF model and extensive comparisons with observations reveal weaknesses of the cloud scheme and also of other physical parameterisations.

Recent studies comparing ground-based radar data with simulations for the same site showed an encouraging degree of skill in the models. One example is given in Figure 2.8 where the fractional cloud cover inferred from ground-based radar signals is compared with the fractional cloud cover computed by ECMWF.

The ERM data sets will contribute considerably to the validation of cloud and moisture fields simulated in operational weather-forecast models. However, this would require their availability in a 'near-real-time' mode. To study the impact on models, these observations could be included in an offline mode.

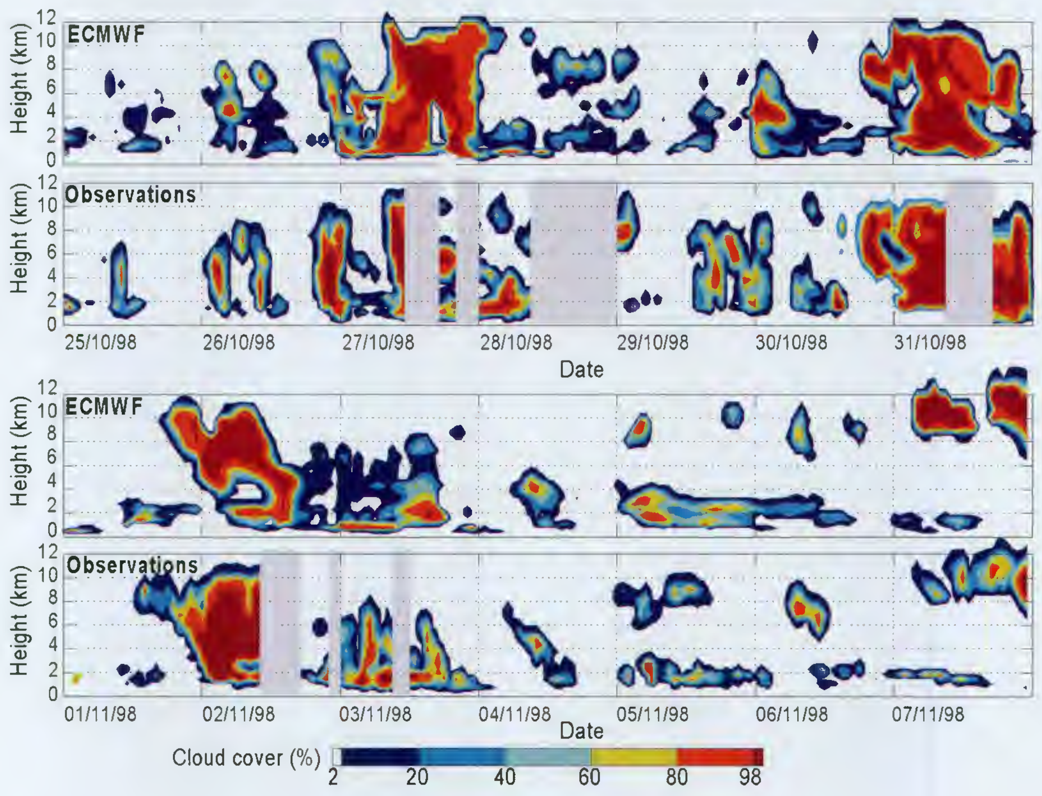

Figure 2.8. Observations of fractional cloud cover from ground-based radar at Chilbolton in the UK compared with predictions of fractional cloud cover (from ECMWF) over the same site.

2.4 The Contribution of the ERM

This section identifies where ERM will make major contributions by providing additional geophysical properties.

2.4.1 Cloud boundaries

Cloud tops of the uppermost cloud field in each area can be estimated using existing methods either from measurements of the cloud-top temperature, by using carbon-dioxide methods (e.g. 'slicing') or during the daylight period with data measured in the oxygen A bands (e.g. GOME). The 'split-window methods' applied to operational sounder and imager data have also proven useful.

Cloud-base altitudes must be known to within a few hundred metres to minimise errors in the computations of downward atmospheric heat radiation. At present, no satellite or ground-based system measures this property on a global scale.

Contribution from Active Sensors

Radar and lidar can both detect cloud-top altitudes with the required accuracy. Radar can penetrate clouds and thus measure the cloud-base altitude and identify any multiple-level clouds. Lidar can penetrate moderately thick ice clouds, but not liquid water clouds.

An example of radar and lidar observation of a cloud structure is shown in Figure 2.9. These measurements were obtained with a ground-based cloud radar at 95 GHz (MIRACLE-GKSS) and an airborne lidar (ALEX-DLR) during the CLARE'98 campaign.

2.4.2 Cloud Structures/Multiple Layer Cloud

Horizontal structures in the uppermost cloud decks can be identified from imager data in great detail from presently available multi-spectral imagery. The best examples occur in outbreaks of cold air over both Polar Regions. The skilled observer, when using composite techniques, may also be able to distinguish between three to four different cloud decks, but only when gaps or transparent regions in the upper deck allow views onto lower decks.

Contribution from Active Sensors

A cloud radar can penetrate clouds, providing detailed information on cloud overlap. However, sub-visible thin cloud layers can only be detected and located with sufficient detail with lidar measurements. The LITE observations (e.g. McCormick et al., 1993) demonstrated that the detailed structure of boundary-layer clouds and of aerosol layers can often be seen below cirrus and middle-level cloud decks with the aid of a backscatter lidar.

2.4.3 Ice Clouds

The upper boundary layer of cirrus can be identified in a relatively easy fashion in multi-spectral imagery, where the optical thickness can also be estimated once the spectral albedo of lower clouds or the ground is known precisely enough. Airborne measurements have confirmed the strong spatial inhomogeneities and variable particle sizes and their distributions (Raschke et al., 1998). Methods have been developed to monitor the occurrence and areal extent of contrails. However, ice water content and effective radius cannot be derived from multi-spectral imagery.

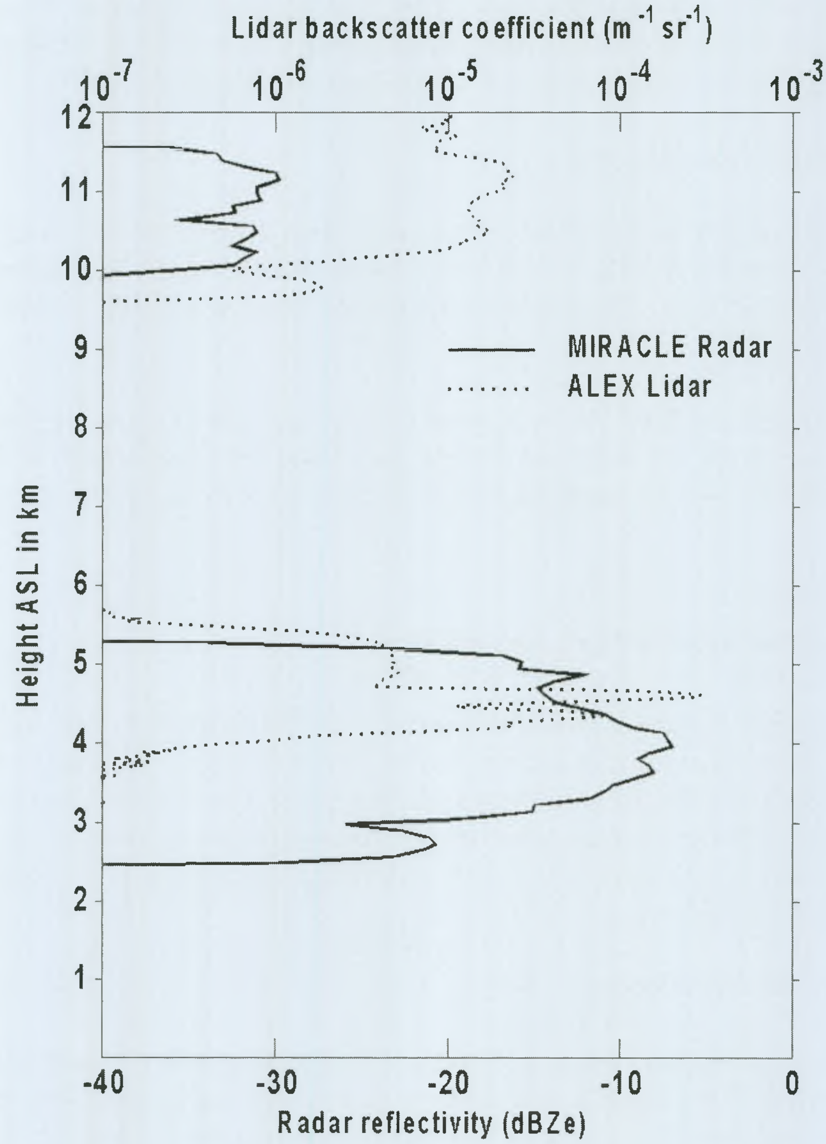

Figure 2.9. *Example of cloud-structure observation during CLARE'98 (20 October 1998, 14.32 UTC) using a ground-based 95 GHz radar (MIRACLE-GKSS) and over-flying airborne 1064 nm lidar (ALEX-DLR). Two cloud layers can easily be recognised. The upper layer is a cirrus cloud, while the lower layer is an altostratus. The lidar signal has been extinction-corrected. In the lower layer, the lidar signal shows a strong peak followed by complete extinction. This peak and the subsequent extinction are due to supercooled layers. For more details see Figures 4.2 (same date) and 5.8.*

Estimates of effective particle sizes from passive multi-spectral imagery have often been suggested and reported in the literature. However, such estimates require many assumptions regarding cloud properties and are only available at cloud top.

Contribution from Active Sensors

The radar penetrates thicker cirrus and can locate lower cloud decks and their vertical structure. It also can identify fall-streaks. Radar and lidar used together allow estimates of the vertical distribution of ice water content and particle size to be derived. A profile of the effective particle size can be derived much more accurately from the lidar/radar ratio when both signals are present. To ensure this retrieval operates reliably, it is essential that the measurements from both active instruments are collocated in both space and time. The method for retrieving the effective particle size is described in more detail in Section 5.4.

Ice water content is highly variable. An estimate to within a factor of two can be made from the radar reflectivity. Once a measure of the particle sizes is known from, for example, the radar/lidar backscatter ratio, then a more accurate ice content to 40% can be estimated on the basis of the strength of back-scattered signals.

2.4.4 Water Clouds

Low-altitude water clouds can easily be identified during the day from passive sensors where no high-altitude clouds are present. Again, some methods have been developed which exploit imager data to estimate an effective radius for prescribed size distribution functions, though this quantity may only be representative for the uppermost layers. 'Typical' vertical profiles of the water clouds and cloud amounts cannot be derived from these data.

Column-integrated liquid water content has been obtained from microwave radiance temperatures from SSM/I data. However, the accuracy and detection sensitivity of this data is limited.

Contribution from Active Sensors

A radar can identify low-level stratus and strato-cumulus fields. Discrimination of internal structures appears feasible once such layers are thicker than 500 m. Unless the upper ice clouds are strongly attenuating, the simultaneous lidar signals would help to locate the cloud top with an accuracy of 100 m. For thin stratus, even the base can be detected by a lidar, but larger uncertainties are expected due to multiple forward scattering. A radar can also identify the possible precipitation (e.g. drizzle) underneath. From these data, an estimate of the cloud-liquid-water-content profile can be made.

2.4.5 Mixed Phase Clouds

From passive data it is very difficult to identify the presence of cloud water in both the ice and liquid phases. Automated methods – even those based on logic or neural networks – have great difficulties with these scenes. No information is available on the vertical structure, nor for water content, phase, or effective radius. Often such fields are very inhomogeneous in the vertical.

Contribution from Active Sensors

Mixed-phase middle-level clouds in frontal systems can be identified by radar and lidar. Unless the ice clouds are very highly attenuating, lidar can detect the cloud tops. For these situations, the radar/lidar combination can also identify layers of super-cooled water inside ice clouds (as recently demonstrated in CLARE'98).

Ground-based cloud radar has demonstrated that it can also penetrate deep convective clouds in regions away from the most intense precipitation and can locate the thickness and position of upper-level anvils and of internal structures.

2.4.6 Light Precipitation

Light precipitation may alter the cloud dynamics, and consequently also its radiative-transfer properties. So far there are no systematic global observations of light precipitation.

Contribution from Active Sensors

Precipitation as snow should be identifiable in the radar signals. This would be extremely valuable for estimates of solid precipitation. A radar will also see precipitation beneath low-level clouds. Radar detects precipitating ice from higher clouds, which is part of the vertical exchange of water in the atmosphere and which may even trigger precipitation from low clouds.

2.4.7 Aerosols

Present-day passive sounders are not able to locate the vertical structures of major aerosol layers. Estimates of the optical thickness from ground signals are also still quite uncertain. In particular, over land aerosol layers cannot be identified due to the dominating signal of the surface. There are, however, possibilities for identifying desert storms and the smoke of biomass burning. In the presence of clouds, aerosol layers cannot be identified at all. Furthermore, at present only vague estimates of effective sizes (radii) seem to be possible when the size distribution function is prescribed and vertical homogeneity is assumed.

Contribution from Active Sensors

A lidar in space can be used to measure tropospheric aerosol characteristics on a horizontal scale of 100 km with 100 m vertical resolution, so that anthropogenic aerosol plumes can be resolved. The next step then would be to investigate any changes in cloud properties associated with such plumes.

Such a lidar would also provide estimates of the vertical structure of optical depth over land and ocean, day and night.

2.5 Conclusions

Present measurement capabilities do not provide the information such as the vertical structure of clouds and aerosols which is needed to close the global and regional energy budgets. An uncertainty limit of about ± 10 Wm^{-2} is used as a guideline for the mission. This accuracy is required to validate present atmospheric models.

The use of a combination of a co-located space-based lidar/radar will provide a unique set of observations of the vertical and horizontal structure of clouds and aerosols and their physical properties in the atmosphere for all levels, even when multiple cloud layers are present.

This will represent a major step forward in climate research, leading to a better understanding of atmospheric processes which are driven by radiative forcing and to an improvement of atmospheric models.

3 Research Objectives of the ERM

The ERM has been defined specifically with the scientific objective of determining worldwide the vertical profiles of cloud and aerosol field characteristics to provide basic input data for numerical modelling and studies (on a global scale) of:

- the divergence of radiative energy
- aerosol-cloud-radiation interactions
- the vertical distribution of water and ice and their transport by clouds
- the vertical cloud field overlap and cloud-precipitation interactions

as discussed in Section 2.1.

3.1 Data Requirements to Evaluate the Role of Clouds and Aerosols

3.1.1 Clouds

To establish the quality of the description of clouds by models, a thorough intercomparison with observations taken at different altitude levels is needed. The most straightforward method of validating atmospheric models is comparing predicted spatial and/or temporal mean values of cloud parameters (e.g. cloud cover, cloud base/top height) with observations. But, just as it is possible to get the correct outgoing long-wave radiation from a variety of cloud structures, the same temporal mean cloud property can originate from very different temporal behaviour. So, different validations are necessary:

- Firstly, it is necessary to derive *area-averaged properties* of cloud parameters such as cloud cover, liquid water path and ice water path.
- Secondly, the *height resolved values* of fractional cloud cover (Charlock et al., 1992), degree of cloud overlap, and ice and liquid water content (IWC/LWC) are needed. Information on the particle size would also be very valuable, since it influences the radiative properties of the cloud directly.
- Thirdly, information on the *spatial variability* of these properties is needed. The geometrical and physical properties of clouds that influence atmospheric radiative transfer span many orders of magnitude and are inherently difficult to measure.

The final evolution of this sequence is to consider case studies in which the observed cloud properties are used to validate a numerical model simulating that particular case. A group of similar such cases can then be gathered together for particular process studies: examples would be subtropical strato-cumulus, tropical cirrus, mid-latitude cirrus, mid-latitude frontal cloud and so forth.

Aerosols

The role of aerosols in present-day climate is the subject of intensive studies. The quantitative estimates of the direct and indirect aerosol effect contain large uncertainties (IPCC, 1995). There is a great need for reliable global data sets of aerosol concentrations and the vertical structure of aerosol layers.

3.2 Existing and Planned Data Sources

Chapter 2 provides a fairly comprehensive overview of existing data sources. At present, most of the cloud and aerosol parameters are derived from passive instruments and very crude assumptions are made to derive these properties. Almost no direct information on the vertical structure of clouds and aerosol fields is available.

The space agencies in the US (NASA), Japan (NASDA) and Europe (ESA) have all developed plans for satellites carrying radar and lidar. Similar plans have also been developed by national space agencies (e.g. CNES). The Japanese Space Agency (NASDA) is preparing for a lidar demonstration mission (MDS-2) around the year 2002, while a larger satellite with both lidar and radar (ATMOS-B1) is still in the planning stage.

At present, a lidar satellite (PICASSO-CENA, a joint French-US mission) is planned to be launched in the year 2003 into a nearly polar orbit flying in formation with EOS-PM. With the lidar it should be possible to derive cloud-top heights from this data, but the limited penetration capability of the lidar restricts the use of the data. It will be very difficult to retrieve reliable cloud-base information and to derive information on LWC/IWC as a lidar signal alone is subject to strong attenuation. Also, it will not be possible to derive reliable information on particle size.

CLOUDSAT (joint US-Canadian mission), a cloud-profiling radar mission, is planned to join the formation of PICASSSO-CENA and EOS-PM. These measurements are planned to be carried out until the year 2006. However, these combined missions have several limitations:

- While the planned CLOUDSAT mission will provide cloud-top and cloud-base observations, the sensitivity of the CLOUDSAT radar is lower in comparison with the ERM-radar. This limits the performance, especially for low water clouds and thin cirrus clouds. CLOUDSAT can achieve a sensitivity similar to ERM at the expense of not measuring the lowest 5000 m of the atmosphere. This has fundamental implications for cloud observation at mid- and high latitudes.

- The planned formation flight of CLOUDSAT, PICASSO-CENA and EOS-PM will not make particle-size retrievals possible to the accuracy required to meet the objectives of the ERM. The combined missions cannot provide observations of microscopic geophysical parameters from synergetic observations as the two active instruments will be embarked on two separate satellites. Because of the high spatial and temporal variability of the microphysical parameters in clouds, it is crucial that lidar and radar observe the same cloud volume.

At present the data needed for the detailed model validation (as described in Section 3.1) is neither available nor addressed in the present plans of other agencies. From several studies (described later in this report), it is concluded that spatial/temporal separations between the lidar and radar of below 2 km and 30 s are needed to enable the retrieval of cloud micro-physical properties (see Chapters 5 and 7). The observations meeting these objectives are only possible with collocated instruments providing synergetic observations: only ERM can provide these.

3.3 The Unique Contribution of ERM

The ERM is intended to bridge the existing gap between required observations for model validation and existing and planned observation systems. ERM is intended, for the first time, to provide a multi-year set of cloud-profiling and aerosol observations essential to progress in understanding the transport of energy and water between the Earth's surface and the top of the atmosphere.

The vertical structure and horizontal distribution of radiation-budget components, cloud water and cloud ice content, aerosol optical thickness, and other geophysical parameters as outlined in sections 2.1 and 2.4 will be derived, using the ERM measurements in synergy with other simultaneous data. Such observations will provide constraints not achievable by other means, helping in the improvement of atmospheric models, e.g. for climate and NWP.

ERM will make an important contribution to many research areas, of which the following are specifically mentioned:

- The information on the vertical profiles of cloud parameters like cloud base/top, LWC/IWC, particle-size information etc. will make it possible to reproduce the fields of the divergence of radiative energy. The accuracy of these profiles is expected to be in the order of 10 Wm^{-2}.
- With the lidar, the structure of the aerosol fields will be observed over land and ocean (in the case of clear sky or gaps in the cloud deck). This is important information in order to estimate the direct aerosol effect. Together with the observed cloud parameters, this enables detailed studies of aerosol-cloud-radiation interactions.

- The information on the vertical profiles of water and ice can be coupled to the wind fields from, for example, NWPs. This will enable detailed studies of horizontal transport by clouds.
- The observations of the vertical cloud structures will give insights into the actual vertical cloud-field overlap functions. The possibility to detect light precipitation underneath cloud decks will provide valuable input for studies on cloud-precipitation interactions.

The observations made by the ERM will provide constraints essential to further improve atmospheric numerical models, both for climate simulation and prediction and for weather forecasting, by providing multi-spectral, and active and passive observations from a single spacecraft.

3.4 Expected Deliverables

Since the ERM is planned to be an Explorer mission, it cannot be expected that all of the above-mentioned quantities will be derived from its signals straight after launch. Rather, the participating research and operational teams will first have to gain experience of using these new data. This concerns both the ways in which they might be used, namely the assimilation of radiance or other appropriate quantities into regional or global circulation models, and the retrieval and further interpretation of quantities on aerosol and cloud characteristics, including the three-dimensional radiation fields.

The first-level geophysical products expected from ERM are:

- Cloud boundaries (top and base) even of multi-layer clouds and consequently height-resolved fractional cloud cover
- Vertical profiles of ice water content and ice particle size
- Vertical profiles of liquid water content
- (Detection of) precipitation and estimation of light precipitation
- (Detection of) aerosol layers and estimates of their optical depth
- Short- and long-wave radiances at the top-of-the-atmosphere.

More sophisticated deliverables will include time and space statistics of instantaneous radiances at top-of-the-atmosphere, first estimates of vertical profiles of water substance and of radiative flux divergence. Finally, the merging or synergy of such data with other satellite data (e.g. geosynchronous) will be necessary. These latter steps will include the computation of three-dimensional fields of characteristics of the cloud, aerosol and radiation fields (e.g. assimilation in NWP models).

4 Observational Requirements

In this Chapter, the observational requirements of the Earth Radiation Mission are presented by defining the geophysical parameters that must be measured and specifying the required sensitivity, accuracy and sampling.

4.1 Introduction

As previously discussed, the cloud and aerosol data presently available are of only limited value to validate atmospheric numerical models. Total cloud cover can be inferred from passive satellite observations, but knowledge of the vertical distribution of both cloud amount and the mass of condensed water is scanty. Passive satellite measurements can also be used to infer total optical depth of the aerosols, but again no information on vertical structure is available.

4.1.1 Current Practice

The traditional approach used to validate weather and climate models is to show that monthly mean values of the radiative fluxes at the top of the atmosphere (TOA) produced by the model agree with those estimated by satellites in programmes such as ERBE. Such comparisons are difficult, because instruments tend to measure radiance over a particular solid angle rather than the flux obtained by integration over the full hemisphere. Although such agreement is encouraging, it does not prove that the model representation of the atmosphere is the correct one. As demonstrated by the AMIP study (Fig. 2.2), a whole variety of models with different values of net fractional cloud covers can produce reasonably consistent TOA fluxes especially for long-wave radiation. A more rigorous validation of the model is needed.

If, for a given TOA flux, there is no unique solution for the average fractional cloud cover, then the variety of possible vertical profiles of cloud cover at different heights for the same TOA will be even larger. The next step for a more robust validation of model representations could be to compare vertical profiles of flux or radiance held in the model with those observed. However, remote sensing of flux and flux divergences is not possible; all that can be measured is the radiance at the top of the atmosphere. In fact, the numerical model does not hold flux as a prognostic variable, but diagnoses fluxes and radiances from the vertical properties of clouds, aerosols and other atmospheric variables, which are represented in the model. Accordingly, a philosophy is proposed in Section 4.1.2 in which the vertical profiles of clouds and aerosols held in the model will be validated by comparing them with observations of these profiles provided by satellite, rather than comparing them with diagnosed fluxes.

The variables presently used to represent clouds and aerosols are held as a mean value over a model grid box, with a parameter such as fractional cloud cover representing sub-grid variability of these parameters. The major prognostic variable representing clouds is the average cloud water content over the grid box. In some models, the phase of the cloud is diagnosed from the temperatures, but increasingly separate prognostic variables are used to represent liquid water clouds and the various types of ice in the cloud. At present, the mean size of the cloud particles is not held as an independent variable, but is either prescribed as a constant, or can take different values for maritime and continental clouds, or alternatively is allowed to be a simple function of water content. In a similar way, aerosols are not yet held as explicit prognostic variables, but prescribed climatological values are used which can be different for urban, rural, marine and continental air masses.

There is a complete absence of observational data of vertical profiles of cloud water content on a global scale for validating models. From passive instruments, estimates have been made of the total water path. Greenwald et al. (1995) have published a climatology of liquid water path over the oceans obtained from microwave radiance temperatures measured by the SSM/I satellite at 37 and 85.5 GHz, suggesting that the mean LWP is about 113 g m^{-2}. Estimates of LWP over land are much more difficult because of the high and variable brightness temperatures of the ground. The LWP estimates of strato-cumulus over the ocean with clear sky above are probably reliable, but the status of such inferences when upper level ice cloud is present, as would be the case in the ITCZ or mid-latitude depressions, is questionable. The use of passive techniques to derive ice water content is fraught with difficulty, as it is difficult to distinguish between emission and scattering. The best estimates are probably those from Lin and Rossow (1996) using ISCCP and SSM/I data, who quote an average IWP for cold non-precipitating clouds of about 70 g m^{-2}, and for tropical and cold clouds, give a value of around 100 g m^{-2}. Such estimates should be treated with great suspicion as the retrievals assume idealised clouds of spherical ice particles, and also assume that the LWP component can be derived from SSM/I data and then subtracted from the total cloud water path from ISCCP to leave the IWP. Such estimates could be in error by an order of magnitude. Even with these caveats, it should be borne in mind that the passive techniques yield only path-integrated quantities with no profile information.

4.1.2 'Snapshot' Validation of Models

An alternative to the traditional approach is to consider individual snapshots of vertical profiles of cloud and aerosol characteristics and to consider if they are correctly represented in the NWP model at the same time. Such an approach is not suitable for a climate model, which is run for many years to produce a statistical representation of the ensemble of weather situations that make up climate, but in which no attempt is made to represent the precise state of the atmosphere at a particular time. However, this approach is eminently suitable for validation of an operational model. An example is that provided by Mace et al. (1998a) who compared cloud boundaries observed with ground-based cloud radar over a three-month period with those held in the operational weather forecasting model of ECMWF.

Figure 2.8 (Chapter 2) displays a two-week time series comparing the ECMWF model representation of cloud cover with radar observations. The agreement is encouraging at least for fractional cloud cover. The satellite would provide such profiles sampled globally; an insight is provided by Figures 4.1 and 4.2. Figure 4.1 shows a NOAA-AVHRR over Chilbolton (marker). Figure 4.2 shows nadir lidar profiles from an aircraft flying at 13 km (DLR-Falcon 20) together with the KESTREL downward-looking 95 GHz radar on the ARAT aircraft (INSU-Fokker 27) flying just below 5 km height and the water content sampled by another aircraft (UKMO-C-130) flying at 4 km height. The changing vertical structure is clearly evident from the lidar image, whereas the NOAA-AVHRR image in Figure 4.1 (taken at the same time) reveals a quite uniform upper cloud layer at 12 km height. The nadir-looking lidar is able to penetrate the cloud until it encounters the highly reflecting layers at 6 and 5 km height, which also attenuate completely the lidar signal. The aircraft performing *in-situ* measurements at 4 km confirms that these highly reflecting layers do contain super-cooled liquid water. The airborne KESTREL radar identifies the ice component of the cloud, but the radar reflectivity of the super-cooled component is lower than the radar sensitivity because these droplets are of much smaller size. At a height below 2 km, the radar identifies liquid water clouds, where the temperature is above freezing, although the lidar signal has been completely attenuated.

The advantage of this new 'snapshot' approach of comparing specific vertical slices through the atmosphere is that it avoids sampling issues, which bedevil studies with low-Earth-orbit satellites. As an example, the TRMM satellite aims to provide monthly means of rainfall over a 250 km square box even though it only flies over such a box about twice a day. The TRMM satellite does this by having a swath width of 880 km. Clouds present much more tenuous targets for active sensors, and so to achieve the required sensitivity a satellite with active cloud sensors would have a narrower swath or even point only at nadir. The provision of reliable monthly cloud statistics over a large grid box would rely on the occasional narrow swath providing a representative sample of the clouds. It is interesting to note that TRMM is a climatological mission but that, now that it is in operation, experiments are being carried out comparing 'snapshot' profiles with NWP representation and even attempting assimilation.

This new approach, then, would be to perform a large number of snapshot comparisons of the vertical profiles of clouds and aerosols observed from a satellite at particular locations with the representation at the appropriate grid point in operational models. Analysis would be carried out to see if the representation of the clouds and aerosols in the model had any particular biases when compared to observations and, ideally, the model parameterisations could be modified to remove such biases. Modern four-dimensional variational (4D-Var) techniques of data assimilation are well suited to this approach. One can envisage the snapshots being categorised into various climatological and weather patterns so as to categorise and quantify the situations in which the model was performing badly. Examples of such climatological regions could be: deep tropical convection, mid-latitude depressions, outbreaks of showers in mid-latitude regions, polar air outbreaks, orographic and jet stream cirrus and so forth.

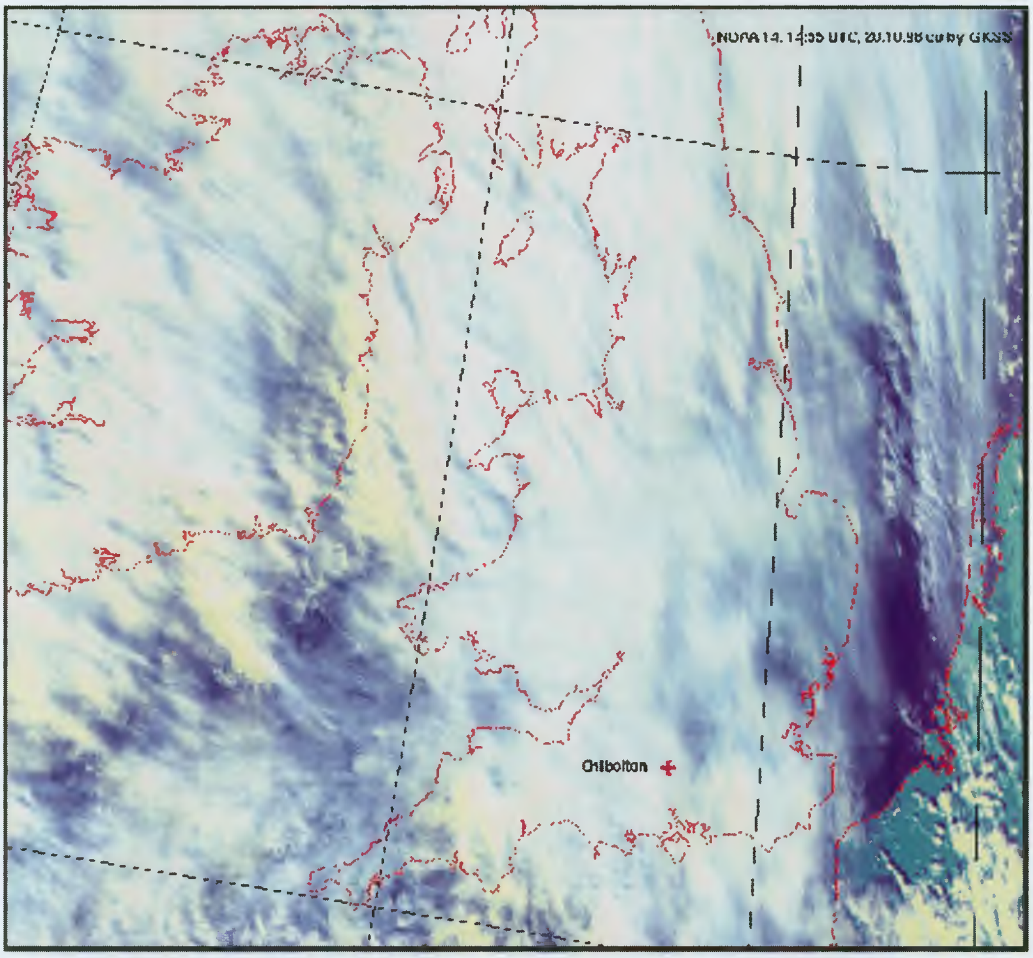

Figure 4.1. *NOAA-AVHRR image for 20 October 1998 over the UK and Ireland. The cross marks Chilbolton where CLARE'98 took place.*

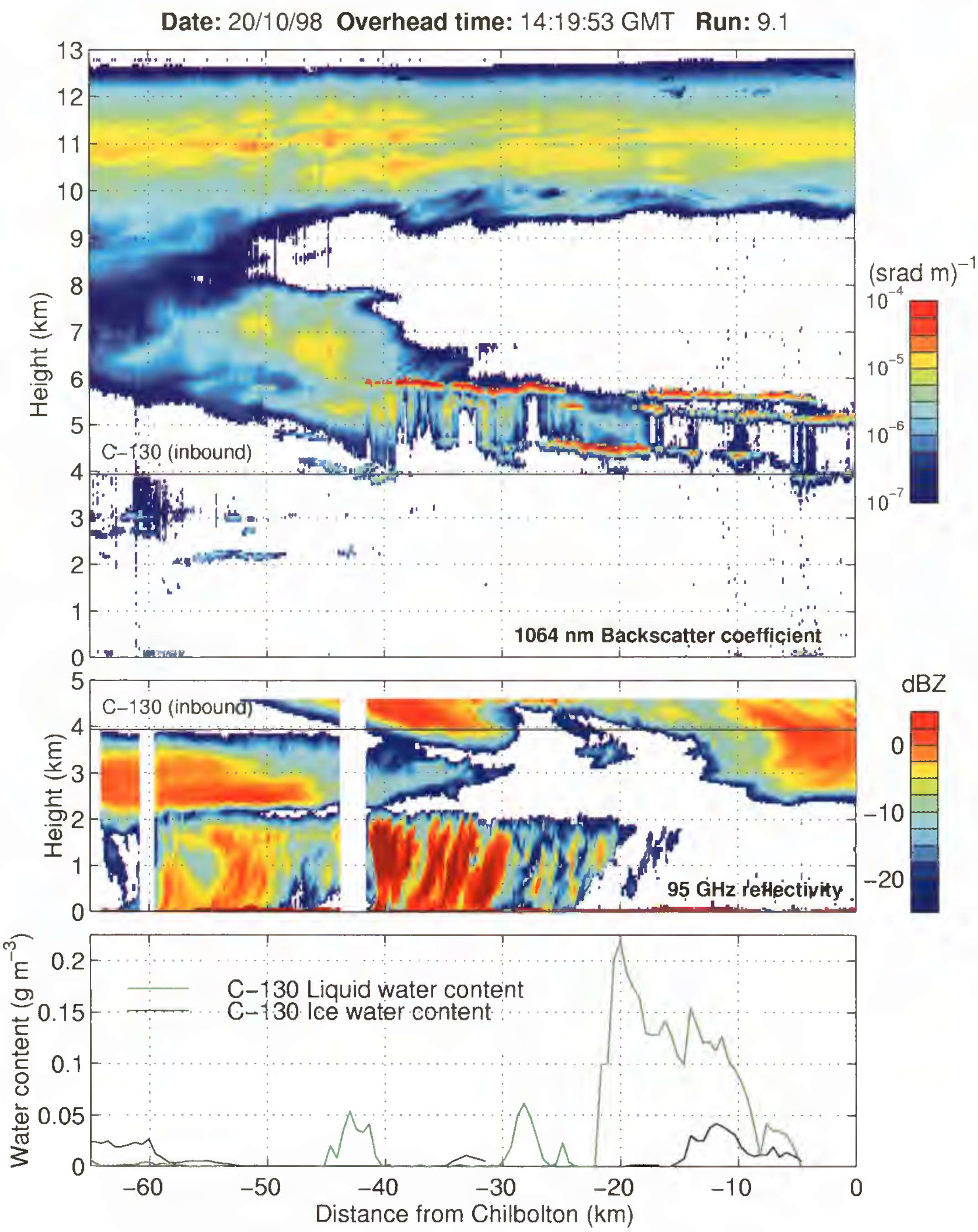

Figure 4.2. Airborne measurements carried out during CLARE'98 (see text for details).

Current models used for climate and numerical weather prediction have grid boxes that range in size from 100 km or more for climate to 50 km or less for global operational forecasting. The vertical resolution varies with height, with many more levels in the boundary layer, but at the altitude of most clouds is of the order of a few hundred metres.

For each grid box and at each height, the current prognostic variables that are typically held for clouds, are:

a) fractional cloud cover

b) ice water content

c) liquid water content

d) effective radius of the cloud particles (currently prescribed as a constant).

The values of the variables are updated for every time-step in the model. Fractional cloud cover can be carried as a prognostic variable (e.g. ECMWF), but in other models it is diagnosed from water content and an assumed sub-grid humidity probability function about the grid box mean. In some models water content is the prognostic variable, and the liquid/ice ratio is diagnosed from the temperature. The use of separate prognostic variables for ice and liquid should soon become universal, to be followed in a very few years by separate variables for different categories of ice. An important parameter is the terminal velocity of the water and ice clouds (usually expressed as a function of the water content) as this effectively governs their lifetime. Water clouds are usually persistent, but once they glaciate the higher terminal velocity of the ice particles means that they tend to disperse. In most models, the time-step is longer than the time necessary for the precipitation to fall to the ground. However, with increasing computer power, the situation is fast approaching where separate variables can be used to represent the rain and ice precipitation and their variation with height, and for each time-step the precipitation moves from one vertical level to another.

The effective radius of the cloud particles is presently prescribed or held as a function of water content. In more advanced schemes, different values are used for water drops in continental and maritime water clouds, and for ice clouds the effective radius is made a simple function of temperature to reflect the observed average decrease of ice particle size with temperature. One can envisage that, in a few years, effective radius will be held as a prognostic variable too. For water droplets, the definition is quite straightforward and effective radius is defined as the ratio of the third to the second moment of the drop size distribution. Ice particles have various shapes, sizes and densities and so the definition is less clear. The concentration of cloud particles can be derived from the size and water content.

The aerosol properties are currently prescribed, although different aerosol characteristics may be used for urban, rural, marine and continental air masses. In a few years aerosol itself will be a prognostic variable, with terms accounting for aerosol sources and removal by condensation and subsequent precipitation from clouds. At present in most operational weather-forecasting models, the most important property of the aerosols is their effect on radiation (direct effect) rather than how they might control the properties of clouds which condense upon them (indirect effect). This 'indirect effect' occurs when variations in aerosol properties lead to changes in the number of cloud concentration nuclei (CCN), resulting in changes in cloud droplet size spectra. It leads to changes in cloud albedo, cloud persistence and in the development of precipitation. The indirect effect may have considerable climate impact (IPCC, 1995).

The radiative effects of aerosol and clouds are currently computed in terms of three properties: optical depth, single scattering albedo and asymmetry function and the variability of these parameters with wavelength. A vertical profile of the aerosol properties is also usually prescribed. For ice particles, semi-empirical relationships between the ice water content and the asymmetry factor are used. The radiative code is expensive to run, so these calculations are generally only carried out infrequently and with lower spatial resolution. For aerosols this may be justified, because the bulk aerosol properties can be assumed not to vary too rapidly in time and space.

4.2 Scientific Requirements

The following requirements, especially those for clouds and TOA radiances, are derived from a vertical flux density at TOA of 10 W m^{-2} that is specified in the scientific plan of the World Climate Research Programme (WCRP) (WMO, 1984). This value for TOA flux was, however, specified for monthly means on a small spatial scale. In this proposed mission, the same value is used to derive the 'instantaneous' requirements for all instruments so that estimates equal to or better than 10 W m^{-2} can be obtained on larger spatial scales (e.g. synoptic).

4.2.1 Clouds

The ability to detect the existence of clouds and aerosols at various vertical heights, which have a significant effect on radiative fluxes, needs to be specified. Brown et al. (1995) adopted the criterion that a radiatively significant cloud should produce a change in outgoing broad-band long-wave (LW) radiation or flux divergence within a cloud layer greater than 10 W m^{-2} and in surface downward LW radiation a change in flux greater than 5 W m^{-2}. They carried out calculations with ice clouds at various heights in mid-latitude and tropical atmospheres, and deduced that it was necessary to detect cirrus ice clouds with an optical depth greater than 0.05 in the tropics and about 0.07 in the mid-latitudes. Assuming an effective radius of 20 µm for the ice crystals, this implies that the threshold of detectability should be an ice water path of about 1 gm^{-2}, or over a 1 km depth of cloud with an ice water content of 0.001 g m^{-3}.

The situation with liquid water clouds is rather different. Thin layers of water clouds such as strato-cumulus can have a large radiative effect. When compared to ice clouds, liquid water clouds consist of larger concentrations of smaller cloud droplets and also have higher water contents, so that the optical depths are generally much greater. For example, an adiabatic vertical profile of liquid water content increases typically by about 0.1 g m^{-3} per 100 m of cloud ascent, that in which case an LWP of 20 gm^{-2} would correspond to an adiabatic cloud 200 m deep with a mean LWC of 0.1 g m^{-3}. These are very low values. However, to retain a sense of perspective, it should be noted that the SSM/I retrievals of LWP (which have been used so widely for deriving LWP cloud climatology) have a standard deviation of about 20 gm^{-2}.

The optical depth of a liquid water cloud at visible wavelengths is given by Slingo and Schrecker (1982) as:

$$\tau = 3\mathrm{LWP} / 2r_e \qquad (4.1)$$

So, if the droplets in the cloud discussed above had an effective radius of 10 μm, the optical depth of the cloud would be 3. Water clouds with an optical depth of less than 1 can produce flux changes much larger than 10 W m^{-2}. This would be produced by an adiabatic cloud with an LWP of about 7 g m^{-2}; that is a cloud 120 m deep with an average liquid water content of 0.06 g m^{-3}. However, strato-cumulus (Sc) clouds with optical depths smaller than 1 are usually not persistent. These optical depths are most often reached during the formation or dispersion of thicker clouds.

Height

The studies of Brown et al. (1995) showed that a change in ice cloud top and bottom of 500 m resulted in a flux change of up to 10 W m^{-2}. For water clouds at 300 K, the specification is slightly tighter: a change of 300 m, or about 2 K, leads to a change in IR blackbody radiation of 12 W m^{-2}. These distances are comparable with the vertical resolution of current numerical models.

Fractional Cloud Cover

Models carry fractional cloud cover as a prognostic or diagnostic variable. Validation of such cloud cover is needed at each vertical model level. An accuracy of 5% is required (personal communication, J-J Morcrette). This accuracy should be available at each 500 m level. Assumptions of the degree of cloud overlap within a model grid box have a major effect on the total cloud cover, the radiative exchange and precipitation development. Three examples are shown in Figure 4.3, where the same fractional cloud cover at each height level leads to 90% total cloud cover if random-overlap is assumed, but 60% for maximum overlap. Current NWP models assume maximum random-overlap.

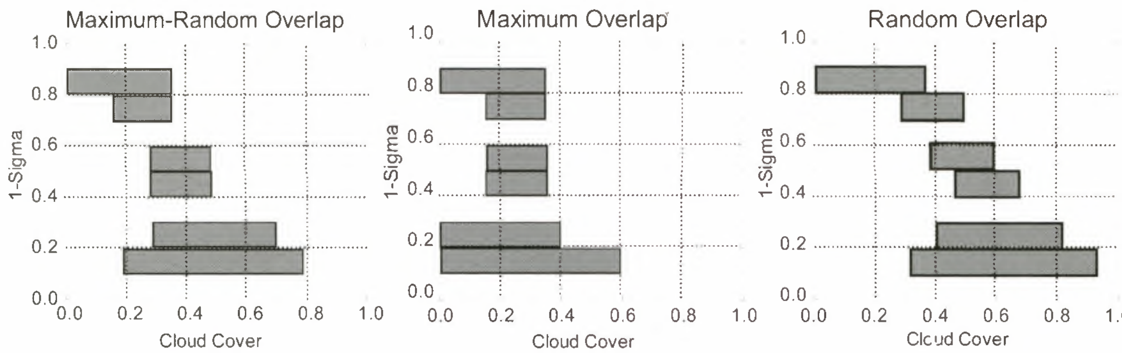

Figure 4.3. Cloud overlap assumptions. Maximum random-overlap is usually assumed in NWP (Tian and Curry, 1989).

Ice Water Content

From the previous discussion, it is concluded that the threshold sensitivity to detect ice clouds with an optical depth of about 0.05 to 0.07 is about 0.001 gm^{-3} IWC for a kilometre deep layer of ice cloud. Brown et al. (1995) extended their calculations and showed that to detect a change in flux of 10 W m^{-2} it is necessary to estimate the optical depth of mid-latitude ice clouds at 9.5 km height to an accuracy of a factor of two, but for cold tropical ice clouds at 16 km altitude an accuracy of +40/-30% is required.

Ice Water Particle Effective Radius

The relationship between optical depth, IWP, density ρ and effective radius (r_e) is given by Stephens et al. (1990) at visible wavelengths as:

$$\tau = 3 \text{ IWP} /(4 \rho r_e) \tag{4.2}$$

provided the ice particle is large compared with the wavelength of the radiation. Accordingly, the fractional accuracy in required optical depth derived above would translate, for a given ice water path, into the same fractional accuracy for effective radius.

Liquid Water Content and Effective Radius

Current SSM/I climatologies of liquid water path are based on a threshold detectability of a cloud with an optical depth of 3. The more rigorous requirement proposed here will be able to sense a water cloud with an optical depth of 1. Once the optical depth exceeds 1, the flux changes become less. For example, if the optical depth is 3, then typically the flux changes 10 W m^{-2} if it is reduced to 1 or increased to 6. Such calculations depend on solar zenith angle and the surface albedo, but considering mid-latitude and arctic conditions, this implies that knowledge of optical depth to a factor of 2 is necessary, and Equation (4.1) implies that LWP and effective radius must be provided to the same factor of 2 accuracy. For the tropics, especially due to the solar angle, the requirement would be more stringent.

Precipitation

One of the mission objectives is to evaluate the interactions of clouds and precipitation. To achieve this objective, it is necessary to detect if a given cloud structure is precipitating and to estimate the precipitation rate. It should also be possible to provide reliable estimates of light precipitation of less than 0.1 mm hr^{-1} that are important in the dispersion of clouds.

4.2.2 Aerosols

The direct radiative forcing by aerosols is comparatively small; only in a few very polluted areas during summer does it reach 10 W m^{-2}. When considering individual vertical columns, this is much less than the effect of clouds. However, aerosol concentrations tend to be more horizontally uniform, so that the spatially integrated effect is significant (IPCC, 1995). Figure 2.3 demonstrates the climatological changes in global temperatures when the direct effect of aerosols is introduced.

The requirement, therefore, is to measure tropospheric aerosol characteristics on the scale of 100 km, so that anthropogenic aerosol plumes can be resolved. The next step then would be to investigate any changes in cloud properties associated with such plumes. The indirect effect of aerosols by changing CCN has been recognised by IPCC (1995) as one of the major uncertainties in climate models.

To evaluate such effects, estimates of the vertical structure of optical depth are required. The current retrievals of optical depth are derived from solar-reflectance measured at 0.63 μm over the ocean using the AVHRR instrument on the NOAA series of satellites. The technique, as described by Stowe et al. (1997), assumes a refractive index of 1.5, a single scattering albedo of unity and a particle size distribution. Then a series of look-up tables for solar zenith angle and satellite zenith and azimuth angle are calculated to convert normalised observed radiances into aerosol optical thickness. Five parameters are needed to describe aerosol characteristics but, based on some ground-truth campaigns, the authors claim that the derived values of optical depth show a systematic error of less than 10% and a random error of about 0.04. Mean annual values can be as high as 0.3 in polluted areas.

The requirement is to measure the vertical structure of optical depth over land and ocean, day and night, with an accuracy of 10% and a random error of 0.04 km^{-1} with an integration length of 100 km.

4.2.3 Top-of-the-Atmosphere Radiance

Based on the requirements defined for vertical flux densities at the top-of–the-atmosphere in the scientific plan of the WCRP (10 W m^{-2}), an accuracy of 1.5 W m^{-2} sr^{-1} is required (WMO, 1984).

4.3 Sampling/Orbit

In traditional Earth-radiation-budget experiments, sampling is a crucial issue. One requirement is to obtain meaningful climatological averages (sometimes from different platforms) and the second is to convert each narrow beamwidth measurement of intensity into a top-of-the-atmosphere flux by integrating over the hemisphere.

The approach adopted for this mission is different. The aim is to provide a large number of samples of vertical profiles of clouds and aerosol properties constrained by a single TOA narrow-beamwidth radiance intensity measurement, and to compare these 'snapshots' of the vertical profile with the representation in a numerical model.

Accordingly, the requirement is for global coverage to sample the variety of cloud formations associated with the different characteristic weather systems and to compare the observations with the model representation, but without the requirement for the high temporal frequency needed to obtain accurate monthly mean statistics.

Clouds are very variable in space and time, so when characterising a particular profile it is important that the various sensors observe the same cloud. A typical multi-spectral imager in current use has a resolution of 1 km and, in an ideal system, the active instruments would provide a vertical profile with the same 1 km resolution. If the sensitivity specification of the active instruments requires a narrow nadir swath, then profile data would be available with an along-track resolution of 1 km for isotropically distributed clouds. This would satisfy the requirement for fractional cloud cover to be observed to within 5% for a 50 km grid box.

A broad-band radiometer embarked on the same platform could measure the nadir radiance intensity in the short-wave and long-wave, which are to be compared with computations from the observed vertical profiles of clouds and aerosols, and the values held in operational models. However, technological constraints will lead to this broad-band radiometer having a footprint of about 50 km. If the active instruments provide a profile with a swath width of only 1 km then it will be necessary for the imager to scan the 50 km field-of-view of the broad-band radiometer to gauge the representativeness of the narrow central swath sampled by the active instruments. To retrieve the vertical profiles of the geophysical parameters that will enable the computation of the TOA fluxes and flux densities, the sampling of the instruments in ERM must be coincident.

Clouds undergo a diurnal cycle and convective clouds are at their most active in the early afternoon. Accordingly, a Sun-synchronous orbit in the early afternoon is required. In order to ensure that all regions of the World are appropriately sampled during all seasons, a multi-year period of observation is required.

4.4 Data Delivery

The philosophy of the mission is to provide vertical profiles of clouds and aerosols, which can then be compared with the representation used in GCM. Such comparisons will be carried out off-line, requiring archiving facilities for the ERM data. However, as already discussed in Chapter 2, it is of high interest to assimilate some of the data into an operational forecasting model. For this purpose, a near-real-time (3-6 hours) data delivery would be required.

4.5 Summary

In order to meet the objectives of the ERM, the following observations are required on a global scale for a multi-year period:

- Cloud boundaries (top and base) even of multi-layer clouds, and consequently height-resolved fractional cloud cover
- Vertical profiles of ice water content and ice particle size
- Vertical profiles of liquid water content
- Detection of precipitation and estimation of light precipitation
- Detection of aerosol layers and estimates of their optical depth
- Short- and long-wave radiances at the top-of-the-atmosphere.

The requirements are summarised in Table 4.1.

	Detectability*	**Accuracy**
Fractional cloud cover	5%	5%
Cloud top/base ice liquid	n/a n/a	500 m 300 m
Ice water content (IWC)	0.001 g m^{-3}	+40/-30%
Ice effective radius	n/a	+40/-30%
Liquid water content (and effective radius) +	Optical depth 1	+100%/-50%
Aerosol optical depth	0.04	10%
Short-/ long-wave radiances at TOA	n/a	1.5 W m^{-2} sr^{-1}

* minimum threshold
\+ the detectability is for all liquid clouds with optical depth specified

Table 4.1. *Observation requirements for ERM geophysical products.*

5 Mission Elements

In this chapter, the various elements of the Earth Radiation Mission are introduced, and the way that these elements are intended to fulfil the requirements derived in the previous chapter is explained. Further details of the retrieval algorithms are provided in Chapter 7.

5.1 Overview

The space segment will comprise a spacecraft on which four instruments are deployed, two active and two passive, namely a lidar, radar, a multi-spectral imager and a broad-band radiometer.

- The lidar would operate in the near-IR at a wavelength of 1.064 μm with a short pulse length so that backscatter profiles can be provided with a resolution of 100 m and a footprint of about 100 m. The instrument would have a sensitivity so that it could detect a volume backscatter of $8.0\ 10^{-7}\ m^{-1}\ sr^{-1}$ for an integration length of 10 km and a signal-to-noise ratio of 2 during the day. At night, the sensitivity is twice as good.
- The radar would operate at 94 GHz with a pulse length of 3.3 μs in the nominal mode and 2.3 μs in the secondary mode, so that a range resolution of 500 m is achieved in the former, and 350 m in the latter. The radar footprint would be about 700 m, and with an along-track integration distance of 10 km, the sensitivity would be -34.4 dBZ for clouds at 1 km altitude in the tropics and -36.8 dBZ for ice clouds (at 8 km) for a radiometric accuracy of 1.7 dB. For 1 km integration length, the sensitivity is degraded by 5 dB.
- The multi-spectral imager would have a pixel size of 1 km and provide images over a swath of at least 250 km centred around nadir in the spectral bands, 0.65, 0.87, 1.6, 8.7, 10.8 and 11.8 μm. These data will provide a context in which to gauge the representativeness of the 1 km swath of the profiling data provided by the active instruments, together with the ability to derive cloud products in the same manner as used for a conventional passive imager.
- The broad-band radiometer will provide measurements of the short-wave 0.2 to 4.0 μm and long-wave 4.0 to 50 μm radiance at the top of the atmosphere. The swath will be at least 100 km with an instantaneous field-of-view of $50 \times 50\ km^2$ and a sampling distance of 30 km.

The data from the Earth Radiation Mission is to be used mainly in an offline mode. This can be achieved with a single ground-station (baseline) with adequate archiving facilities. Due to their relative simplicity, some of the Level 1 products may even be generated in a completely automatic mode.

However, due to the interest in ERM data from operational weather-forecast organisations, it is highly desirable anyway to have a near-real-time (3 to 6 hours) delivery of the Level 0 products as well as Level 1 products that can be produced on a completely automatic basis. These data would not be provided in near-real-time for the whole globe due to the baseline of one ground station, but the approximately 1/3 of the Earth covered in near-real-time would be nevertheless of high interest.

The requirement for additional information to enable geophysical parameters to be derived from ERM instruments is not critical. No specific instruments are proposed for the mission which would sense atmospheric temperature or humidity profiles. Such information is needed for the radar retrievals to correct for attenuation, but the attenuation at 94 GHz is sufficiently low that humidity profiles supplied by operational NWP products will be of sufficient quality. In addition, for more accurate retrievals of ice water content from radar reflectivity, temperature profiles are required with an accuracy of 6 K that is easily achievable by NWP products.

5.2 Backscatter Lidar

The LITE mission has demonstrated that laser remote sensing from space can provide measurements of the global distribution of the extinction and backscattering coefficients of atmospheric aerosols and clouds (Winker et al., 1996). The vertical resolution of lidar measurements makes possible accurate measurements of clouds and aerosols height, complementing the data obtained from the passive imager, which generally have poor height resolution. In addition, lidars can operate both in the night side of a satellite's orbit as well as in the sunlit portion, thus increasing observational coverage.

During the LITE experiment, the aerosol and cloud height were measured with a vertical resolution of 45 m. Cloud depth, optical depth and attenuation were observed along the LITE orbits. Multiple scattering effects caused an appreciable enhancement to the penetration of laser pulses into cirrus and dense water clouds and strong pulse stretching effects preventing observations of the base of thick clouds. Complex cloud structures were observed in storm systems. Figure 5.1 shows an example of LITE data at 1064 nm (same wavelength proposed for ERM). Aerosols can be observed in the lower right part of the figure.

While LITE demonstrated the utility of spaceborne lidars to provide crucial data for improving cloud parameterisation in atmospheric models, it also demonstrated the limitations of a single instrument mission. The knowledge regarding aerosol and cloud properties is difficult to retrieve from data measured by one single instrument, while the retrieval of their physical and microphysical characteristics can be improved by the simultaneous use of active and passive sensors and by a synergetic processing of the data.

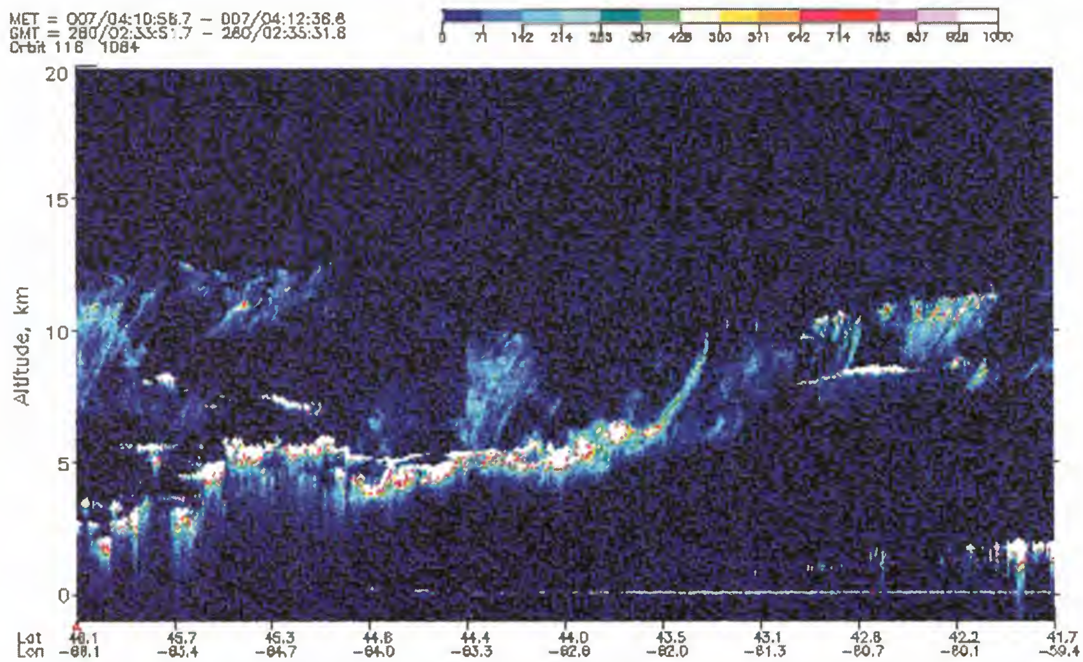

Figure 5.1. *Example of LITE data* (Winker et al., 1996) *at 1064 nm. Cloud structures and tropospheric aerosols can be observed. The data was not corrected for extinction.*

In a lidar system, the returning echo from a non-absorbing, elastic scattering atmosphere is described by the lidar equation:

$$P(R) = C\frac{\beta(R)}{R^2}(1+Q(R))\exp(-2\tau(R)) \tag{5.1}$$

where $P(R)$ is the return signal from the range R, C is the lidar system calibration constant, and $\beta(R)$ is the backscatter coefficient of the atmosphere at the distance R. Here $\tau(R)$ is the optical thickness of the distance between the range R_0 corresponding to the top of the atmosphere and the range R:

$$\tau(R) = \int_{R_0}^{R} \alpha(x)dx \tag{5.2}$$

where $\alpha(R)$ is the extinction coefficient profile of the atmosphere. The ratio of the multiple to single scattering contributions is described by a factor $Q(R)$.

If C, $\beta(R)$ and $\alpha(R)$, and $Q(R)$ are unknown, the lidar equation is undetermined, and the backscatter and the extinction profiles cannot be derived without additional assumptions on the physical properties of the probed atmosphere.

The first assumption concerns the application of the lidar equation in the presence of multiple scattering. The analytical description of the multiple-scattering signals in the narrow angle scattering regime allows the processing of the total signal including the contributions from all orders of multiple scattering.

The second assumption concerns the relationship between $\beta(R)$ and $\alpha(R)$, the lidar ratio. As the exact form of this relationship is generally not known, the simple assumption of constant β/α is used. In this case, the remaining problem is to choose a boundary value to determine the extinction and the backscatter profiles. A number of different methods for the boundary value determination have been proposed (Klett, 1981).

One approach is to use Rayleigh scattering from the air molecules on the far side of the target. Far end and middle range boundary values are generally unknown for a spaceborne lidar operating near 1 μm. Accordingly, one must resort to a gate-by-gate correction for extinction starting from the first gate where the target is detected. Such correction schemes are notoriously unstable. However in combination with the radar supplying a constraint for the lidar extinction a stable correction scheme can be implemented.

When combined with other errors, such as calibration error, statistical noise in the signal, multiple scattering, it is deduced that:

- Multiple scattering limits data interpretation to $\tau < 4$.
- Using the lidar alone, for $\tau = 0.1$, the error in retrieved extinction coefficient and optical depth is 10 to 40% and for $\tau = 0.5$ the error rises to 15 to 80%.

5.2.1 Backscatter/Extinction

One of the main physical factors limiting the performance of the lidar inversion is the variability of the backscatter-to-extinction ratio β/α. This ratio has been verified experimentally and numerically at near-infrared wavelengths. β/α is typically in the order of 0.07 sr^{-1} for cirrus and from 0.05 to 0.06 sr^{-1} for water clouds, but typical ranges are ±20% (Eloranta et al, 1998).

5.2.2 Multiple Scattering/Attenuation

In the case of a spaceborne lidar, the instrument is positioned at a great distance away from the atmospheric targets. This leads to a target linear dimension, seen by the receiver field of view, which is orders of magnitude larger than is the case for ground-based and airborne lidar systems with a comparable angular fields of view. As a result, the multiple scattering effects contribute significantly to the lidar return and give rise to adverse or, in some cases, potentially useful signals. It alters the amplitude of the lidar return as well as the shape of the signal profile compared to the single scattering.

With multiple scattering, the signal-to-noise ratio (SNR) for clouds and aerosols exceeds the corresponding SNR values for the single scattering models. The increase of the penetration depth of the laser in cirrus and in dense clouds, due to the multiple scattering, improves the capability to obtain information on the vertical stratification of cloud systems from a spaceborne lidar.

For water clouds, the multiple scattering causes a stretching of the return echo and an apparent increase in cloud depth. However, it also leads to an increase in return signal and penetration depth into the cloud, although such effects can be difficult to quantify. The effects in ice clouds are much less and any layered structure is maintained (Flesia and Starkov, 1998).

5.2.3 Detectability of Clouds and Aerosols

The lidar will have a daytime sensitivity of 8.10^{-7} m^{-1} sr^{-1} for a 10 km integration length and a signal-to-noise-ratio of 2. Using a conservative assumption that the backscatter extinction ratio, β/α is 1/14, this is equivalent to an extinction of 0.011 km^{-1} or 0.0011 per 100 m vertical resolution gate.

Such a sensitivity is more than adequate for the specifications drawn up in Chapter 4, of $\tau = 1$ for liquid clouds, $\tau = 0.05$ to 0.07 for ice clouds (assuming a cloud depth of 1 km) and α =0.04 km^{-1} for aerosol. Indeed such targets can be detected for 1 km (2.4 10^{-6} m^{-1} sr^{-1}) integration lengths with a signal-to-noise-ratio of 2.

If such ice clouds are 1 km deep, there is a margin of one order of magnitude, showing that signals can still be detected from tenuous ice clouds even in the presence of severe attenuation. It should be noted that the lidar, with its 100 m resolution and 100 m blind layer above ground, should detect fog both during day and night.

The quantitative derivation of precise values of optical depth once the value of τ exceeds 0.1 is error prone because of the problems of inverting the lidar equation. Synergy with the radar (Section 5.4) overcomes this difficulty.

5.3 Cloud Profiling Radar

5.3.1 Interpretation of Radar Reflectivity Factor, Z

The radar reflectivity factor, Z, of clouds is related to the concentration (N) and size (D) of the cloud particles by the equation $Z = \Sigma ND^6$ with a weighting which depends on the dielectric constant of the target. Z is expressed in units of $mm^6\ m^{-3}$ or in dBZ ($=10 \log_{10}Z$) where a Z of 1 (0 dBZ) corresponds to the Rayleigh scattering return from a mm raindrop per cubic metre recorded with a centimetre wavelength radar.

The cross-section per-unit-volume η is related to Z by:

$$\eta = 10^{-18} \frac{\pi^5}{\lambda^4} |K|^2 Z \tag{5.3}$$

where λ is the wavelength (in metres) and K is the dielectric factor of the cloud particles, and η is expressed in m^{-1}. An increase in the frequency (= decrease in λ) would enhance the radar backscatter, but would also increase the attenuation through cloud layers and atmosphere. The atmospheric window around 94-95 GHz is most suitable for detecting a majority of clouds. Furthermore, the use of such a millimetre-wave frequency results in a compact, yet highly sensitive radar instrument, which is amenable to a satellite-borne design.

This led to the request and approval for a primary frequency allocation for Earth Exploration satellites at WRC '97 (94.0-94.1 GHz). Therefore, the CPR frequency has been fixed at 94.05 GHz.

Ideally, there should be a unique relationship which links the observed value of Z with the water content, but water content = $(\pi/6)\ \Sigma\rho ND^3$ where ρ is the density of the material composing the particles with a diameter D. Variability in the particle size spectra (and, for ice, any changes in particle density) leads to a spread of values of water content for a given observed value of Z.

The use of precipitation radars to estimate rainfall, R, is universally established, but in fact, the same problem that arises from the variability in the raindrop size spectra in the context of rainfall estimation also affects the retrievals from a cloud radar. An empirical relationship is used to convert Z to R, but individual estimates of R made from Z may be in error by up to a factor of two. This assumes the radar beam is dwelling wholly in the rain – if ice is present then the errors are compounded. However, just as is the case for estimating rainfall rate from a rain radar, it will be shown that ice water content can be derived from radar reflectivity with a well-defined error.

Interpreting Z for liquid water clouds is simple, because the dielectric weighting is, by definition, unity. For ice clouds, the situation is rather more complicated. Several factors need to be considered:

- Ice particles have a different dielectric constant to that of liquid water. The backscattered return is weighted by $|K|^2$ where K is given by:

  $$K = \frac{m^2 - 1}{m^2 + 2} \tag{5.4}$$

  and m is the complex refractive index of the particles. The value of $|K|^2$ is a function of ice density, but for solid ice it has a value about one fifth that of liquid water, and for air-ice mixtures the factor is even lower.

- If the particle is a reasonable fraction of the wavelength, Mie scattering occurs and the return is lower than that expected for Rayleigh scattering. Typically, this becomes significant at 94 GHz when the particles reach 300 μm in size. Liquid cloud droplets are always smaller than this size, unless rain is falling, but ice particles in cirrus can be large enough for Mie scattering.

The radar reflectivity (in $mm^6\,m^{-3}$) from a cloud of ice particles can be calculated from:

$$Z = \sum_i |K(\rho)|^2 N(D) D^6 f(D,\rho) / 0.93 \tag{5.5}$$

where $f(D,\rho)$ is the ratio of the Mie scattering to the Rayleigh scattering for the sensing frequency, and the factor 0.93 is chosen so that, for water droplets in the Rayleigh region at centimetre wavelengths, the expression reduces to ΣND^6. The value of $|K|^2$ at 94 GHz and 0°C is 0.6856, but varies with temperature. So to avoid ambiguous definitions that change with temperature and to enable comparison with other instruments, we use the normalising value of 0.93.

Validation of radar estimates of rainfall is achieved by having the radar beam dwell just above a ground-based rain gauge. However, such a simple validation is not possible for cloud liquid and ice water content, because, at best, only occasional penetrations by an instrumented aircraft, which are coincident with cloud radar measurements, are available.

The approach adopted to develop empirical relationship between Z and IWC and LWC is to appeal to long series of cloud-particle-size spectra measurements made from aircraft penetrating clouds. Values of Z, IWC and LWC are calculated from these observed spectra and the statistics of the relationships examined. The approach is illustrated by the analysis of 4000 km of aircraft penetrations made through liquid water strato-cumulus cloud and 9200 km (14 701 spectra) for the EUCREX mid-latitude cirrus and 24 000 km (12 506 spectra) from the tropical CEPEX cirrus data set.

5.3.2 Cloud Detectability

Cirrus clouds generally have larger particle sizes than liquid water clouds, so for a given water content the radar reflectivity of ice clouds is much higher than that for water clouds, making ice clouds easier to detect. In addition, the larger particle sizes lead to a small optical depth for a given water content, which means that it is much easier to detect radiatively significant ice clouds than liquid water clouds. The properties of mixed-phase clouds are more uncertain.

Ice Clouds – Cirrus

If a radiatively significant cirrus cloud is defined as one that changes the OLR by 10 W m^{-2}, then Brown et al. (1995) showed that this was equivalent to an optical depth of 0.07 and 0.05 for mid-latitude and tropical cirrus, respectively. The ice water content of such clouds is around 0.001 g m^{-3}. Because the proposed spaceborne radar looks down through cold dry air at cirrus clouds, there is little attenuation at 94 GHz, so the sensitivity for cirrus is -36.8 dBZ. At this level, from the tropical CEPEX data set (see Fig. 5.2) the detectability for an extinction greater than 0.05 km^{-1} is 99%. For a 1 km along-track integration, the threshold is -31.8 dBZ (5 dB reduction) and the percentage is over 93.3%. For comparison, sensitivities of -29 and -24 dBZ (estimated sensitivity of CLOUDSAT in short-pulse mode with a radiometric accuracy as in ERM and for 10 and 1 km integration length respectively) give a detectability for cirrus of 89% and 80%, respectively. The detection efficiency for tropical cirrus at extremely low temperatures of around -80° C may be lower than these figures: this is because they may contain many extremely small particles, which may not be sensed by current aircraft instruments.

Water Clouds – Strato-cumulus

Thin water clouds contain many small droplets and so, even though they have a low radar reflectivity, they can still be radiatively significant. Calculations would initially suggest that an adiabatic cloud only 120 m deep would have a liquid water path of 7 g m^{-2}, an average liquid water content of 0.06 g m^{-3}, but would have an optical depth of 1. If one of the well-known theoretical relationships between Z and LWC (based on observed liquid droplet size distributions) is used, this would suggest a radar reflectivity of about -40 dBZ. The proposed radar would not be able to detect such a cloud.

However, once a marine strato-cumulus cloud has a thickness greater than 200 m, it invariably contains occasional 100 μm droplets (Fox and Illingworth, 1997). Such droplets make a negligible contribution to the liquid water content or precipitation rate, but because of the D^6 weighting, they dominate the radar reflectivity and increase it by 20 or 30 dB, making marine strato-cumulus clouds visible to the radar. The aircraft studies show that 90% of cloud with an LWC of 0.1 g m^{-3} should be detected with a threshold of -30 dBZ. Continental clouds probably contain many fewer 100 μm droplets and would need a sensitivity threshold of -40 dBZ to be detected. However, such clouds are detectable by lidar.

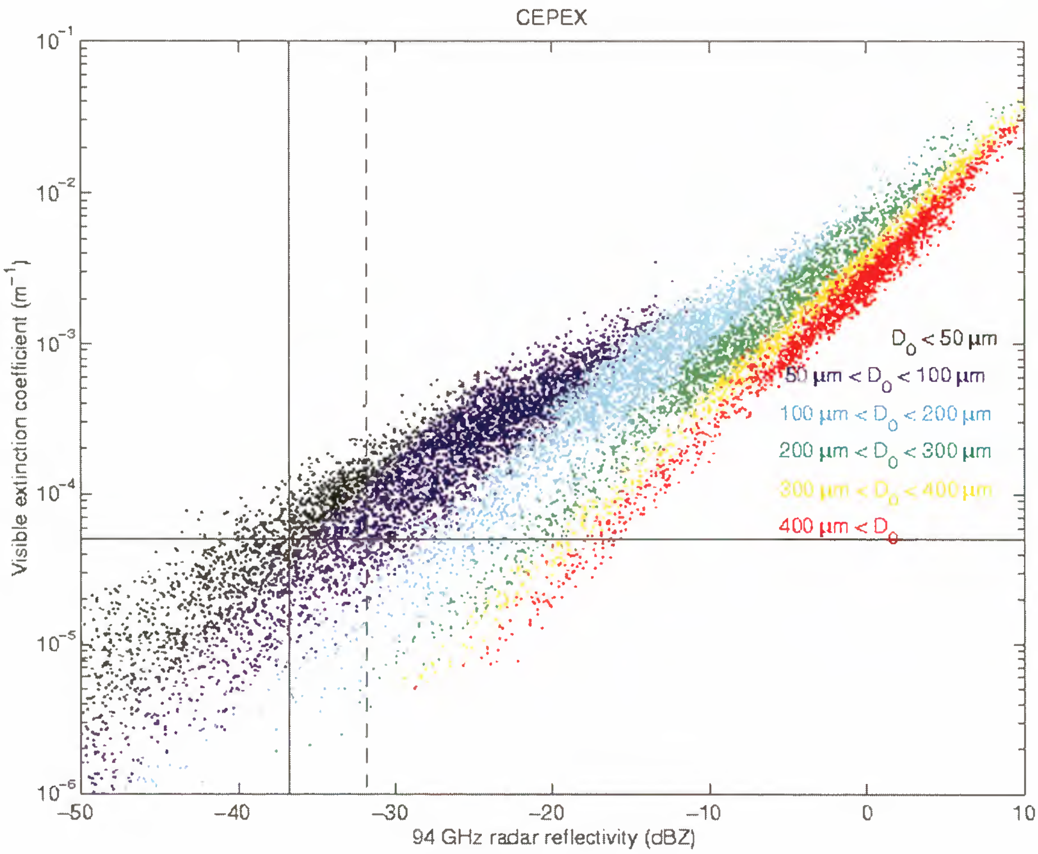

Figure 5.2. *Values of Z and extinction coefficient computed from the 12 506 ice-path spectra from the CEPEX tropical cirrus data set. D_0 is the diameter that divides the size spectra into two equal volumes of ice. The requirement is to sense all clouds with $\alpha > 0.05\ km^{-1}$ (horizontal line in the figure). The two vertical lines show that a radar sensitivity of -36.8 dBZ (10 km integration length) detects 99.0% of all cirrus samples, while -31.8 dBZ (1 km integration length) detects 93.3%..*

It might be thought that the high attenuation at 94 GHz by cloud water would have an important effect on cloud detectability. However, once the LWC, and hence the attenuation, becomes appreciable, the occasional 100 μm droplets appear and raise the radar reflectivity way above the detectability threshold. Accordingly, attenuation of the radar signal by liquid water clouds does not constitute a problem.

5.3.3 Ice Water Content

Figure 5.3 shows an example of the calculations of Z and IWC from the 12 506 ice particle spectra observed by an aircraft penetrating 24000 km of tropical cirrus clouds. The observations from mid-latitude cirrus are similar (Brown et al., 1995). This figure confirms that a radar sensitivity of -36.8 dBZ (10 km integration) and -31.8 dBZ (1 km integration) will detect the overwhelming majority of cirrus clouds (99.4 and 94.0%, respectively) with an IWC over 0.001 g m^{-3}. Because Z is proportional to D^6, but IWC to D^3, the relationship between Z and IWC varies with the median volume diameter of the ice particles, D_0, where the diameter D_0 divides the IWC into two equal halves. Analysis of the tropical and mid-latitude aircraft data shows:

- At 94 GHz, the IWC derived from individual observations of Z would be typically in error by a factor of 2. At longer wavelengths, the error is larger, but at 94 GHz Mie scattering reduces the contribution to the reflectivity by the larger particles, so lessening the dependence of the Z-IWC relationship on particle size.
- Calculations of mean values of IWC from Z reveal that the bias between tropical and mid-latitude mean retrievals of IWC is less than 20%.

These calculations are based on an ice density (ρ) which is assumed to fall with particle size according to $\rho = 0.07\, D^{-1.1}$ (where ρ is in g cm^{-3} and D in mm). Comparisons of the IWC calculated from spectra with those from total water probe, which evaporates the ice particles completely, confirm the universality of this function. However, uncertainties as to its precise form may introduce errors of 30% in IWC, particularly for the higher values of IWC (>0.01 g cm^{-3}) where the larger ice particles with their lower density are more important.

If some measure of the mean ice particle size, D_0, is available, analysis of observed spectra (e.g. Fig. 5.3) shows that the errors in derived ice water content are reduced considerably, typically to values of +40%/-30%. Most spectra are observed to be quasi-exponential, but the remaining errors are due to deviations from this spectrum in natural clouds. Accordingly, for a D_0 of 70 μm, an accuracy of $\pm$ 10 μm is needed to achieve this, but for larger values of D_0 a size accuracy of 30% is sufficient.

It is well known that there is a correlation between mean particle size and temperature. Indeed, such a correlation is incorporated in NWP cloud parameterisation schemes. If the Z values are sorted in terms of temperature, more accurate values of IWC can be derived than from Z alone. The performance of this algorithm is almost as good as that achievable from Z and size information, and approaches the +40%/-30% error level. An accuracy in T of 6 K is adequate, and this can be achieved if the cloud height is known to 1 km in the tropics, or outside the tropics if an NWP temperature product is available.

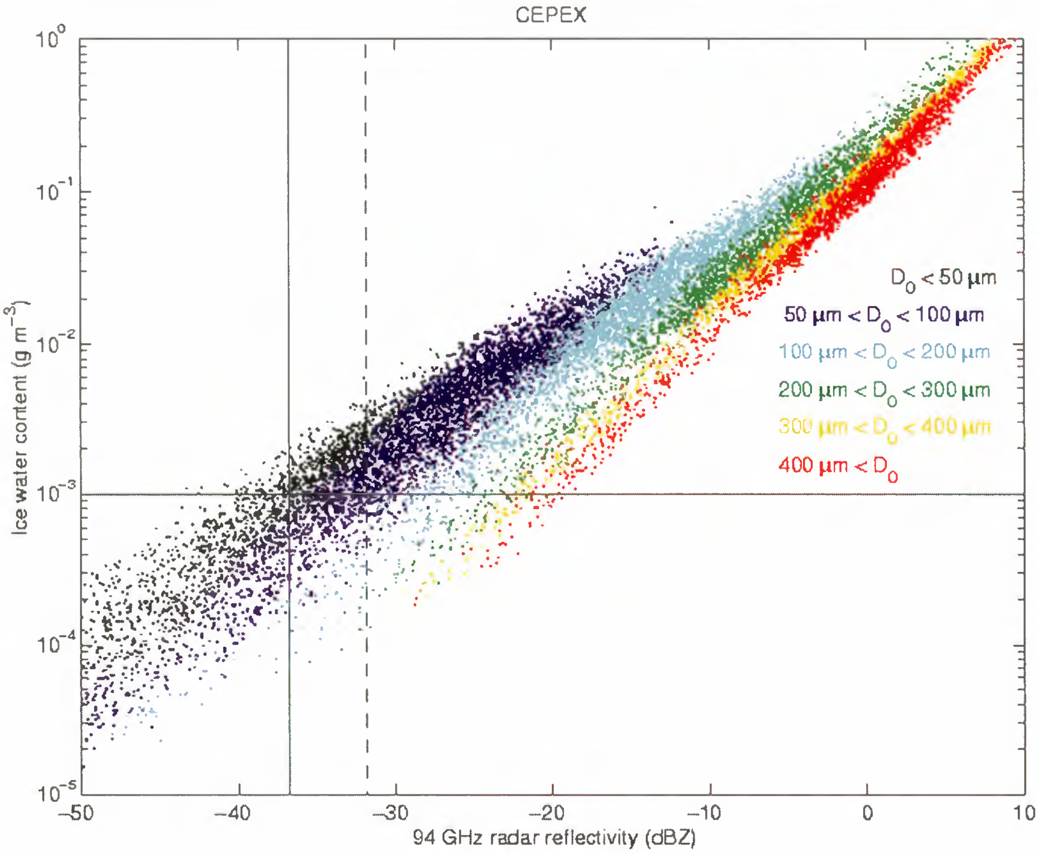

Figure 5.3. *As for Figure 5.2 but for calculated values of Z and Ice Water Content (IWC) for the CEPEX data set. The horizontal line in the figure shows the IWC threshold of 0.001 g m*$^{-3}$*. The two vertical lines show that a radar sensitivity of -36.8 dBZ (10 km integration length) detects 99.4% of all cirrus samples while -31.8 dBZ (*1 km *integration length) detects 94.0%..*

Because the relationship between *Z* and IWC is non-linear, integrating over a 10 km path to obtain more sensitivity can lead to a bias in the retrieved IWC if the radar reflectivity is very variable. Analysis shows that this bias should be less than 10%.

The presence of solid ice particles in the Mie region can lead to appreciable attenuation at 94 GHz. However, the larger particles encountered in cirrus clouds which undergo Mie scattering have all a low density (ρ), so attenuation of the radar beam by the ice particles is negligible. This is confirmed by results from vertically pointing ground-based cloud radar. Attenuation by low-level liquid water clouds is evident in the structure of upper ice clouds, with sudden drops in apparent reflectivity coinciding with the more opaque low-level water clouds, but this phenomenon is never observed for ice clouds.

5.3.4 Liquid Water Content

Droplets larger than 100 μm exist in practically all strato-cumulus. These droplets dominate the cloud reflectivity, but contribute negligibly to the liquid water content. This feature makes liquid water clouds much easier to detect by radar, but also means that there will be no relationship between cloud liquid water content and radar reflectivity. However, estimates of liquid water content to within a factor of 2 (+100%/-50%) can be made from a knowledge of cloud top and cloud base together with the multi-spectral imager data.

5.3.5 Precipitation

The radar will be able to detect light precipitation. For rainfall rates of 0.1 mm h^{-1} and assuming a Marshall-Palmer raindrop size distribution, the attenuation is less than 0.3 dB km^{-1} and Z is about 8 dBZ with negligible Mie scattering. Thus, quantitative measurements of precipitation should be possible with the radar. Difficulties in quantitative interpretation arise for precipitation rates higher than around 1 mm h^{-1}, because the attenuation exceeds 1 dB km^{-1} and a Rayleigh value of about 20 dBZ is reduced by 5 to 6 dB due to Mie scattering by the larger raindrops (Lhermitte, 1987).

5.4 Combined Radar/Lidar Backscatter Synergy

Radar and lidar, sampling a common volume of clouds, have the potential to provide estimates of cloud particle size, but to do so the footprints of the two instruments must be coincident. Such information is extremely valuable:

- as a direct validation of effective radius used when representing clouds in models
- when combined with radar reflectivity, it will enable the IWC to be estimated to an accuracy of about 30-40%.

This IWC accuracy fulfils the requirement specified in Chapter 4. Radar reflectivity alone provides an accuracy of a factor of 2, although a knowledge of temperature improves this considerably.

The combined use of the radar and lidar backscatter is a powerful technique for the all important ice clouds. Essentially, the radar return for solid ice particles is proportional to D^6, whereas the lidar backscatter varies approximately as D^2, so the ratio of the radar to the lidar backscatter should vary as D^4. The fourth-power dependence leads to a robust retrieval, a 100% error in the estimate of the radar-lidar backscatter ratio leading to a 25% error in retrieved size. A 25% error in size, when combined with the absolute value of Z, is sufficient for deriving IWC to 30-40%. Intrieri et al. (1993) demonstrated the principle of the technique, but assumed that all cloud particles were solid ice spheres and limited the lidar retrievals to an optical depth of 1. More recently, Mace et al. (1998a) have repeated this exercise but assumed a more realistic variation of ice particle density with size; they do not provide details of how they corrected for attenuation.

However, neither of these two papers has tackled the lidar attenuation aspect at all rigorously. The ice clouds, which are of most relevance from a radiative point of view, have an optical depth in the range 0.1 up to about 3. Once the optical depth becomes larger than 0.2 or 0.3, then a simple gate by gate correction becomes chronically unstable. Three factors have to be considered:

- Firstly, an initial error in the backscatter calibration of 10% leads to an error of 70% in the corrected backscatter coefficient by the time the lidar has penetrated into a cloud with a true optical depth of 1.
- Secondly, the extinction to backscatter ratio for ice particles has an uncertainty of at least 20%, which further contributes to the error.
- Thirdly, the amount of multiple scattering (especially from a spacecraft with a relatively large footprint) is uncertain to at least 20%.

The traditional solution is to constrain the retrieval by use of a reference target (such as the Rayleigh scattering of the molecules on the far side of the cloud) to provide a reliable total-path integrated attenuation. Even if this technique were possible, it would not be of much help for clouds with the above-mentioned optical depths because:

- for deep and thick clouds, there may not be any clear air from which to detect molecular backscatter
- for thick attenuating cloud, there may be insufficient sensitivity to detect molecular backscatter
- one can never be sure that the 'molecular' backscatter is not being affected by spurious returns from omnipresent aerosols.

5.4.1 New Technique

A new technique is proposed here, which overcomes these difficulties and leads to a more accurate and stable retrieval that relies on the coincident radar return to provide the constraint for the lidar attenuation retrieval. Essentially, the value of Z for the radar provides a first guess for the total lidar attenuation as well as the attenuation at each gate. Figure 5.2 displays the computed values of Z and optical extinction calculated for the CEPEX tropical cirrus data and demonstrates the potential of Z as a constraint for the attenuation affecting lidar retrievals. The mid-latitude cirrus data show a similar trend. In addition, Figure 5.2 confirms that a radar sensitivity detectability threshold of -36.8 dBZ will detect virtually all clouds with an extinction coefficient greater than 0.05 km^{-1}, as will the reduced sensitivity of -31.8 dBZ for 1 km along-track resolution.

If it is assumed for the lidar that the ice particles have an extinction-to-backscatter ratio of 14 ($\beta/\alpha = 0.07\ sr^{-1}$), the lidar sensitivity of $2.4.10^{-6}\ m^{-1}\ sr^{-1}$ is equivalent to an extinction coefficient of 0.033 km^{-1}. Accordingly, the lidar and radar sensitivities are well-matched for simultaneously detecting radiatively significant cirrus clouds. The sensitivity margin available for the lidar ensures that the cirrus clouds will still be detected even when there is attenuation on the lidar signal.

The first guess for the lidar attenuation based on Z is then used in an iterative manner with the lidar retrieval to provide a consistent retrieval for both the lidar and radar. The technique is demonstrated and shown to be stable using ground-based lidar and radar in Figure 5.4, where the radar and lidar backscatter from an ice cloud at a height of 2 to 5 km observed from the ground over a four-hour period are displayed. Typical vertical profiles before and after correction are depicted in Figure 5.5 and confirm the stable operation of the algorithm even when at an altitude above 4 km there is a lidar attenuation approaching two orders of magnitude. The example has been chosen to demonstrate the stability of the technique for this optically dense cloud. Once this consistent profile has been derived, it is possible to provide an estimate of the extinction at each gate, the effective particle size, and also the lidar extinction-to-backscatter ratio. Figure 5.6 shows the values of ice particle size and ice water content derived over this four-hour period.

This combined radar-lidar retrieval is extremely powerful. For it to operate, it is extremely important that the radar and lidar view the same cloud. Clouds are very inhomogeneous and variable, and if the radar and lidar are sensing clouds with a separation of only 4 km, the radar/lidar backscatter ratio loses all its significance.

The data over a four-hour period from two vertically pointing lidars separated by only 4 km shown in Figure 5.7 demonstrate this quantitatively. The mean backscatter profiles of the two lidars (displayed on the right-hand side) are very similar, but the standard deviation of these mean values differs by almost an order of magnitude. As a *a)*

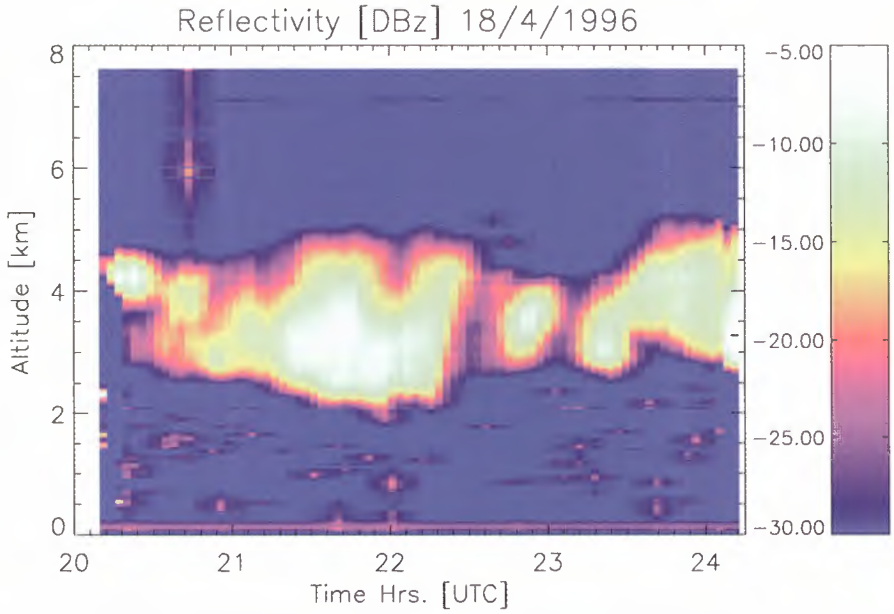

b)

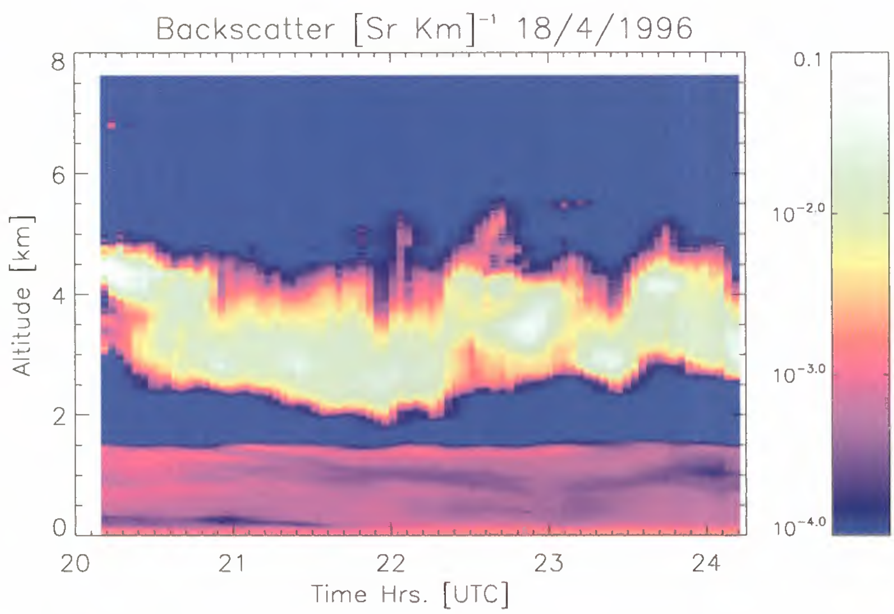

Figure 5.4. *Simultaneous vertical profiles of radar (a) and lidar (b) taken over a four-hour period during the CLARA campaign in the Netherlands. The 'pink' lidar return below 2 km altitude is the backscatter from the aerosols (van Lammeren, 1999).*

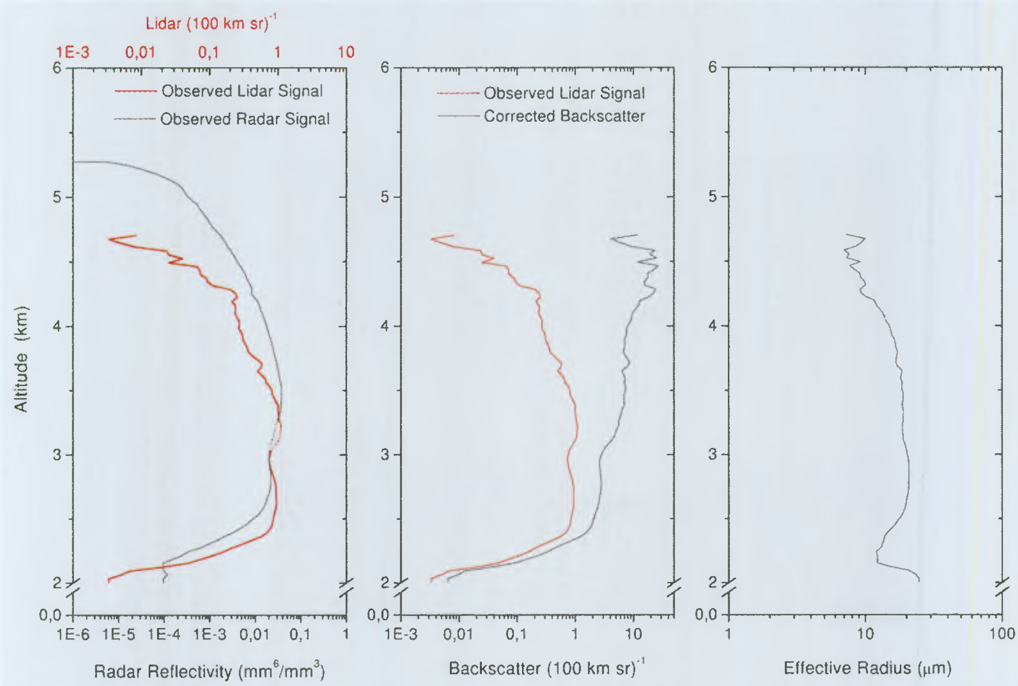

Figure 5.5. *A typical vertical profile of the radar and lidar backscatter for the data in Figure 5.4. The left-hand panel shows the raw radar and lidar signal, but the right-hand side compares the lidar return before and after correction; the correction reaches two orders of magnitude.*

result, the correlation of each individual value of the two profiles in the time series at each 100 m gate (left-hand side of the figure) varies from 1 to 0.1, with a mean value of 0.7. Further analysis shows that the retrieved size from instruments separated by only 2 km is no better than a climatological mean (see Chapter 7). For temporal separation, the loss of correlation is very small for time differences below 30 seconds.

This has profound implications for the design of the mission. It means that a separation of only 2 km between the radar and lidar footprint leads to an enormous loss of information. Accordingly, the synergy will not be possible for a lidar and radar deployed on separate satellites flown in tandem, as is being proposed with PICASSO-CENA and CLOUDSAT.

The situation for liquid water clouds is somewhat different. The lidar fails to penetrate more than a few gates before there is complete loss of signal. The radar return will often be affected by the presence of the occasional larger droplets (>100 μm), which dominate the reflectivity. In this case, it seems that the power of the lidar/radar combined is to derive cloud top and cloud bottom. Then, provided there is no upper cloud, in conjunction with the cloud optical depth and particle size estimated from the visible imager channel, estimates of LWP and the degree to which the cloud is adiabatic can be made.

a)

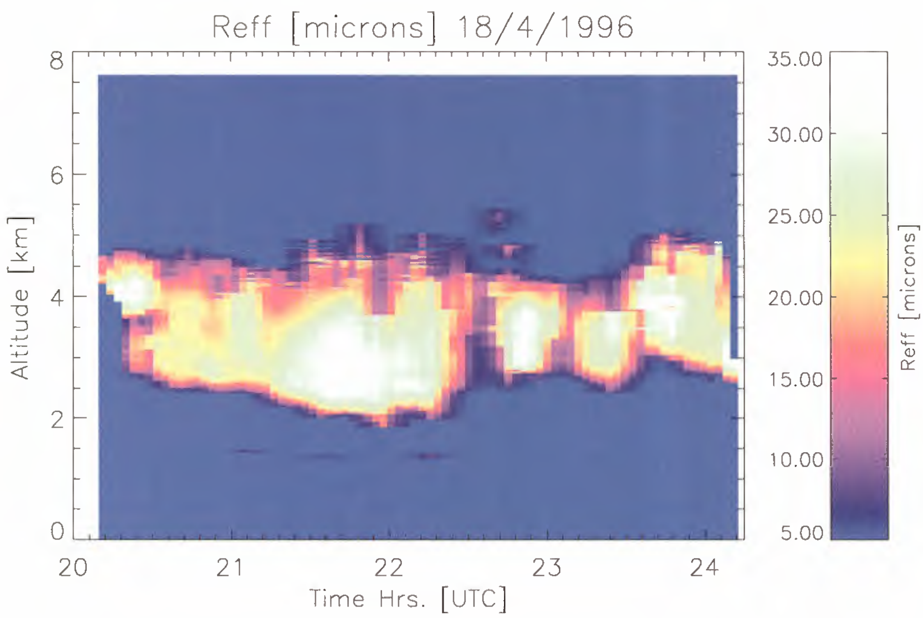

b)

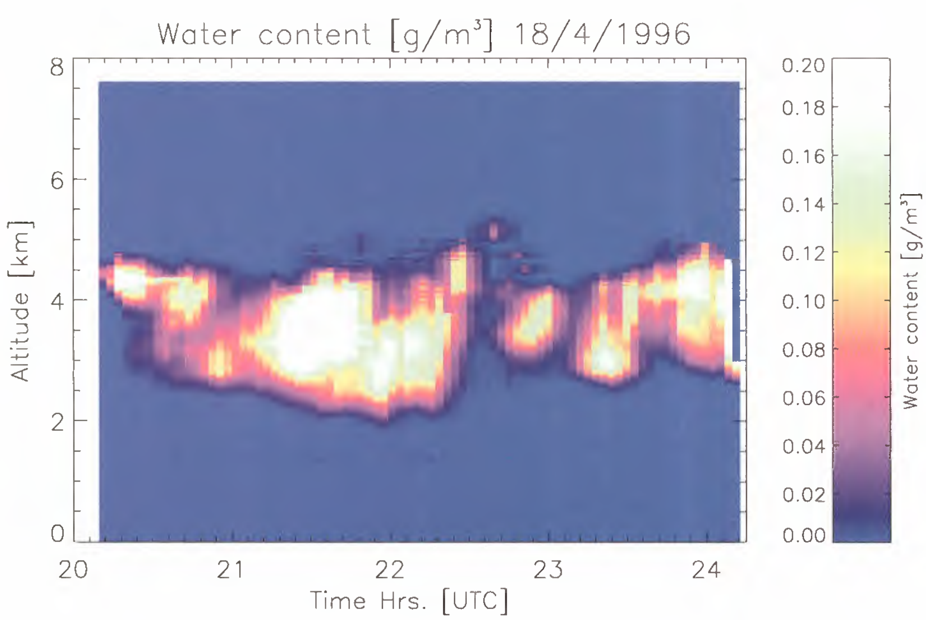

Figure 5.6. *The effective radius (a) ice water content and (b) retrieved from the radar and lidar data in Figure 5.4 after correcting the lidar for attenuation.*

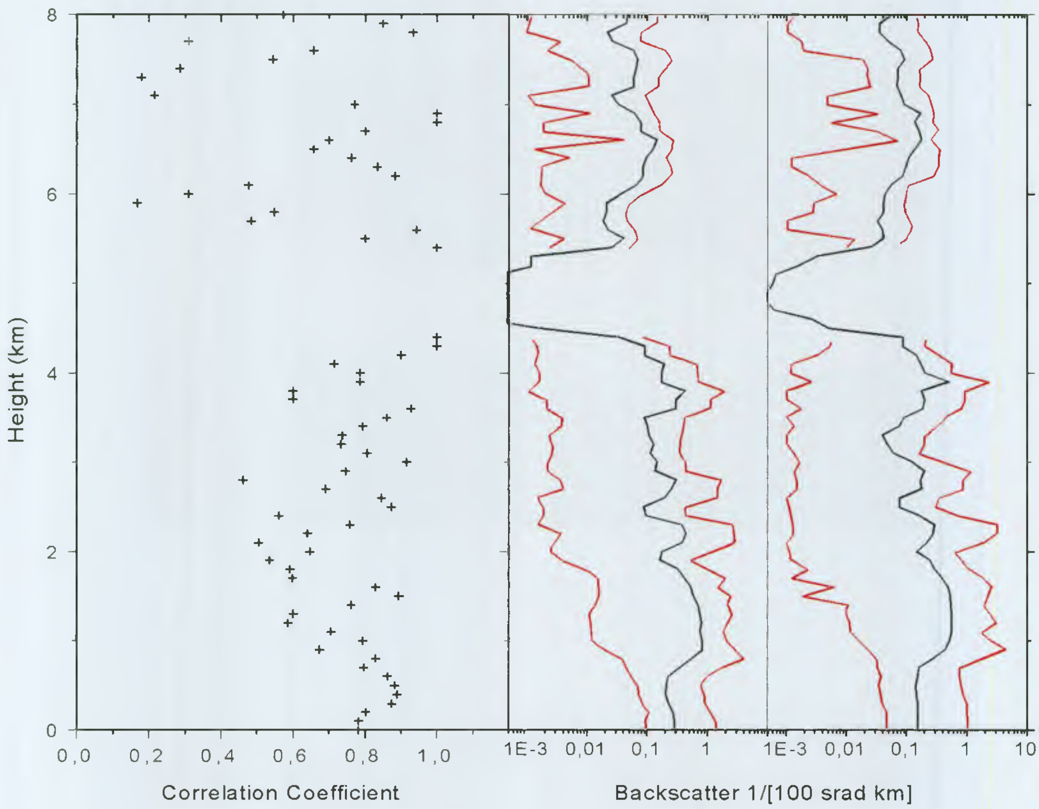

Figure 5.7. *The correlation of the lidar returns for two lidars separated by 4 km. The two right-hand panels compare the mean vertical lidar backscatter profile at the two sites over a four-hour period. The mean profiles (black line) are quite similar, but the standard deviations of the individual values (red lines) differ by typically an order of magnitude. The left-hand panel shows that the correlation between the individual points on the profiles is very low even if the mean values are similar.*

The 12-hour observations made with a co-located vertically pointing radar and lidar displayed in Figure 5.8 reveal another synergy, which should indicate the presence of layers of super-cooled water. The upper plot from the ground-based radar reveals a cloud layer, the base of which gradually descends over a twelve hour period until, for the last two hours, rain is falling at the ground, with the transition from ice to rain clearly visible at 1 km altitude. Current passive technology would only detect the cloud top, which is fairly constant at a height of 10 km during the four-hour period. No attenuation problems are evident in these radar observations. The lidar observations show a different picture. Until the rain starts at 1030h, the aerosol returns from the lowest km are visible. For the first four hours until 0400h, the returns from the ice cloud above 5 km can be combined with the radar to derive particle size and accurate IWC. After 0400h, the lidar reveals a series of highly reflective attenuating horizontal layers (the outline of these layers is shown in black in the upper panel of Fig. 5.8). The high level of backscatter combined with the evident high attenuation are strongly suggestive of super-cooled liquid water clouds – an inference which has been confirmed on other days when instrumented aircraft penetrated such regions. Note that one would expect that the small cloud droplets in the super-cooled layers to be associated with a negligible radar reflectivity compared to the radar return from the ice: the radar plot confirms that no change in reflectivity is associated with the highly reflecting lidar layers. A reflectivity smaller than 0 dBZ and a threshold level of 10^{-3} m^{-1} sr^{-1} appear to be an indicator of the presence of such super-cooled layers; this is much larger than values encountered in ice clouds – for example, the dense cloud in Figure 5.4 peaks at 5.10^{-5} m^{-1} sr^{-1}. When the rain starts at 1030h, the attenuation for the lidar is virtually total. Of course, the attenuation problem of the lidar, looking up through attenuating water clouds so visible in Figure 5.8, will be virtually absent for a spaceborne instrument looking down through ice clouds until it reaches a layer of liquid water cloud.

Table 5.1 summarises the major instrumental requirements for the radar and lidar.

	Lidar	Radar
Footprint	$\cong$ 100 m	< 1 km
Sensitivity	$\leq 8.10^{-7}$m^{-1}sr^{-1}@10km integration $\leq 2.4\ 10^{-6}$m^{-1}sr^{-1}@1km integration	≤-36dBZ@10km integration ≤-31dBZ@ 1km integration at 8 km height
Signal-to-noise-ratio	≥ 2	
Radiometric accuracy		≤ 1.7 dB
Vertical resolution	≤ 100 m	≤ 500 m
Swath	Nadir only, collocated footprints	

Table 5.1. *Summary of requirements for lidar and radar.*

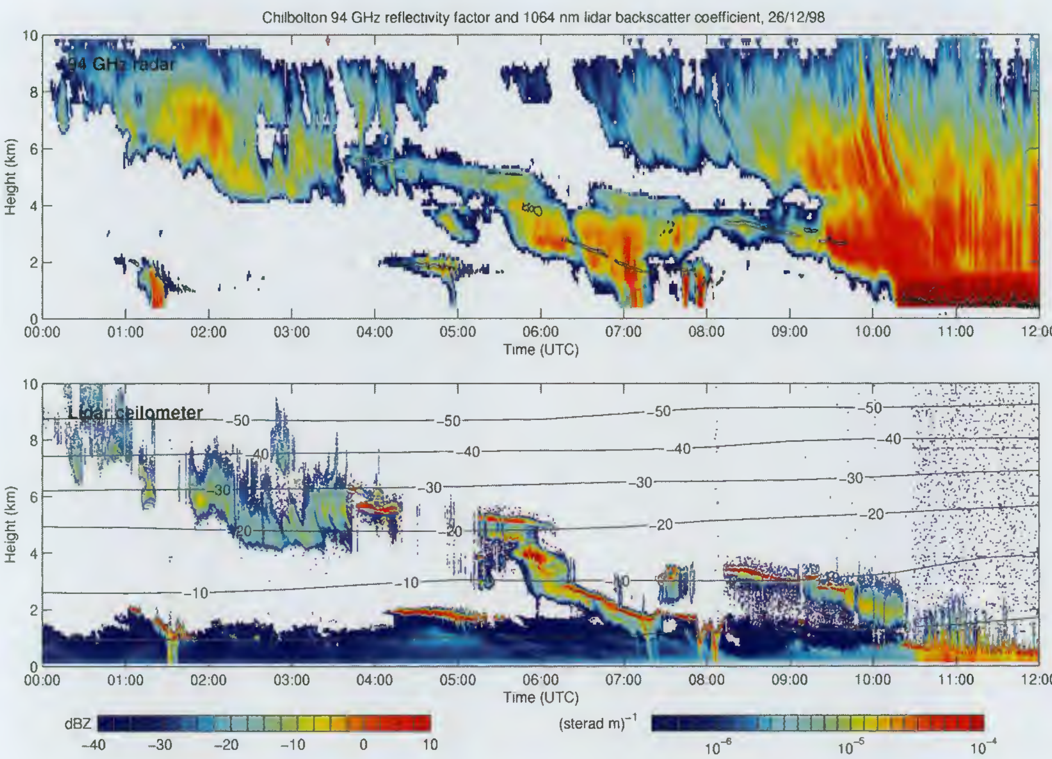

Figure 5.8. Synergy of a ground-based radar and lidar which reveals layers of super-cooled droplets within an ice cloud. The upper radar plot shows a constant cloud top, but a gradually descending cloud base culminating in rain after 1030h. The lidar return in the lower panel shows the aerosol returns in the lowest kilometre, and after 0400h some highly reflecting and attenuating layers with a $\beta > 5\ 10^{-5}\ m^{-1}sr^{-1}$ from super-cooled liquid cloud droplets. The small super-cooled droplets give a negligible radar return, but the outline of the high-β regions embedded within the ice cloud return has been superposed in black on the radar picture. From space, the lidar would penetrate through the ice cloud until being attenuated by the liquid clouds.

5.5 Multi-Spectral Imager

To understand and interpret the measurements by the BBR and the active instruments, the 'context' of the measurements should be identified. The multi-spectral imager (MSI) is intended to provide information on the horizontal variability of the atmospheric conditions and to identify atmospheric components. Quantitative analysis of the measured reflected sunlight yields information on the optical properties of the clouds and aerosols under study, while thermal-infrared measurements yield information on temperature and infrared emissivity.

The use of MSI data in the characterisation of cloud and aerosol properties is well established. There are many algorithms developed for the retrieval of cloud properties from similar instruments: AVHRR (Kriebel et al., 1989; Derrien et al., 1993), ATSR (Watts, 1996), GOES and Meteosat (Minnis and Harrison, 1984; Rossow and Garder, 1993).

The cloud reflectance at the wavelength of 650 nm is a measure of the cloud optical depth. After assuming some cloud microphysical properties, this is then related to other cloud properties like LWP. This channel is also used to determine cloud cover fraction in daytime.

The reflectance in the 1.6 μm channel shows dependence on the variation of the effective cloud droplet radius. This reflectance in this band gives an indication of the particle size. It can be shown that the reflectance increases with decreasing cloud droplet size. Results similar to 1.6 μm can be obtained using the 3.7 μm channel (Nakajima and Nakajima, 1995), but this channel is more difficult to handle due to the overlapping solar and terrestrial spectra and their corresponding low radiances.

Due to an increase in absorption for ice at 1.6 μm, the reflectance decreases. So, for optically thick ice clouds the reflectance in the 1.6 μm channel will be smaller than at 650 nm. This makes it possible to distinguish between ice and water clouds.

For semi-transparent clouds, the temperature difference between the 10.8 and 11.8 μm channels is used to distinguish between ice and water clouds ('split-window technique'). The amplitude of the temperature difference is related to the cloud optical depth in the infrared. The absolute value of the temperatures is used to derive the cloud top temperature (in the case of optically thick clouds). Ackerman et al. (1998) suggests using the combination of 8.7 and 11.8 μm for the detection of ice-clouds. This has a larger sensitivity for ice clouds. However, there might be an ambiguity in the interpretation of the data in the case of multiple layered clouds (combinations of ice and water clouds). Furthermore, the emissivity of the land surface at 8.7 μm is very variable. These factors complicate the analysis if only the 8.7 and 11.8 μm channels are available. For this reason, it is proposed to use all three IR channels (8.7, 10.8 and 11.8 μm) for ERM.

It is anticipated that information on the following cloud parameters can be derived from the multi-spectral imager data: cloud cover fraction, optical thickness, effective emissivity, top temperature and liquid water column. Also for aerosols, there are a number of algorithms developed for multi-spectral imagers like MODIS (King et al. 1992) and AVHRR (Durkee et al., 1991; Husar et al., 1997; Veefkind et al., 1999). It should be stressed that these retrievals are based on idealised models of clouds involving several assumptions.

The multi-spectral imager will, in addition, supply qualitative information in the first phase of interpretation of ERM measurements and, due to its spatial resolution, which is comparable to the resolution of the active sensors, quantify the variability within the footprint of the BBR.

The cloud products described above can be retrieved from a multi-spectral imager with six channels as specified in Table 5.2. The anticipated spatial resolution is 1×1 km^2. The multi-spectral imager will have a swath of 125 km to both sides across track (250 km total).

	Wavelength
1	650 nm
2	865 nm
3	1.6 μm
4	8.7 μm
5	10.8 μm
6	11.8 μm

Table 5.2*: Channel specifications of the multi-spectral imager.*

In order to characterise the cloud fields, the reflected sunlight in the two visible channels has to be measured with a signal-to-noise ratio (S/N) better than 200. Due to reflections at the sides of the clouds, the dynamic range for the visible channels has to be as large as 1.3. The radiometric resolution of the IR channels has to be better than 0.25 K at temperatures of 300 K. At the minimum temperature of 180 K a resolution of 0.8 K is required. The temperature difference between the infrared channels is used for deriving cloud properties. It is therefore crucial that the absolute accuracy of the infrared channels be better than 1 K over the whole temperature range. This is also needed in order to derive absolute values for the cloud optical properties. The absolute accuracy should be better than 1 K.

5.6 Broad-Band Radiometer

The broad-band radiometer is intended to measure the reflected short-wave (SW) and emitted long-wave (LW) radiances emergent from the observed vertical atmospheric column (VAC) by means of the active instruments (lidar and radar) on board. This instrument will thus provide a firm constraint on and a basis for the calculation of vertical radiative flux divergence using the information on atmospheric, cloud and aerosol physical properties in the VAC, derived from radar, lidar, multi-spectral imager and other data.

The broad-band radiometer (BBR) in the ERM space segment is designed to separate the SW (0.2-4 μm) and LW (4-50 μm). It will have very nearly flat spectral response over these domains, so that once 'filtered' radiances are obtained in absolute physical units, they will be very close to the ideal 'unfiltered' radiances corresponding to perfect spectral response and perfect separation of solar and thermal contributions in the overlap region (roughly from 3 to 5 μm wavelengths). Estimates of these 'unfiltered' radiances will therefore require only small spectral corrections and will be largely *in*sensitive to the details of the reflected and emitted spectra. The instrument will thus provide accurate measurements of the unfiltered broad-band SW and LW radiances emergent from the VAC, i.e. at the nadir point, which must be collocated with the footprints of the radar and lidar.

The broad-band SW and LW radiances emergent to zenith from the VAC can be used in two different ways:

a) *'Traditional' determination of the TOA radiation budget components*

In this approach, the SW and LW radiance data need to be converted into values of upward instantaneous radiation fluxes. A spectral correction algorithm specific to the ERM BBR using MSI and lidar data on the nadir scene will provide excellent (ERBE or CERES-style) 'scene identification' and unfiltered radiances. For conversion of these radiance measurements into instantaneous fluxes, one can make use of one of the ERBE MLE algorithms and ERBE angular models used in processing data from the American ERBE and CERES scanners, as well as from the French-Russian-German ScaRaB. It may also become possible to use advanced CERES algorithms and angular models.

Because the ERM BBR only observes nadir, this instrument is not suited to the global monitoring of TOA radiation-budget components. Even if it is assumed that the BBR pixels represent a swath of 120 km, less than 4% of the globe is observed in 12 hours, an order of magnitude less than what is observed by a cross-track scanner at a typical altitude of 800 km. Because of this, incorporating such measurements in the data collected by such monitoring-style missions as CERES, with a view to improving the time sampling, will probably not be worth the effort.

However, it is clear that satellites will be used to monitor cloud and atmospheric properties, and will in particular include multi-spectral imagers with spatial resolution and spectral channels comparable to those of the MSI on ERM. Both NOAA and European scientific groups have produced ERB estimates using narrow-band AVHRR data as well as geostationary satellite data; similarly, estimates based on the narrow-band channels of ScaRaB have been compared with the truly simultaneous collocated broad-band measurements. On ERM, the broad-band radiances measured at nadir by the BBR can be systematically compared with simultaneous collocated estimates of broad-band radiances based on the ERM MSI narrow-band data. This will help to 'tune' the algorithms for estimating TOA

SW and LW fluxes from the narrow-band data, and the success of such algorithms at nadir will help to define the limits of confidence that can be placed on ERB monitoring based on narrow-band measurements from the operational weather satellites. In addition, analysis of the lidar-radar data on the observed VAC should improve our understanding of the cases where the BBR measurements show that the estimates of ERB components using narrow-band MSI data are wrong.

b) *Constraining the derivation of radiation-budget components*

In this approach, the purpose of the BBR is to constrain the derivations of vertical profiles of Earth-radiation-budget components within the atmosphere and the vertical radiative flux divergence profiles. At this stage, it is not clear whether methods exploiting inverse or adjoint modelling, using the BBR data together with the MSI and lidar-radar data, can be developed to extract the best possible retrieval of VAC properties, including the radiative fluxes and flux divergence. It may be that the best approach will be one of forward radiative-transfer modelling using the properties retrieved from MSI, lidar and radar, and comparison of computed versus observed TOA zenith-directed LW and SW radiances.

The important point is that, while computed energy fluxes depend not only on the physical property retrievals, but also on additional necessary but only partially validated hypotheses regarding angular and spectral properties of the VAC, the BBR provides a constraint that is independent of these hypotheses. Such an integral constraint, although not information-rich, provides a firm 'anchor' to the flux divergence calculation. To have confidence in the flux divergence calculation, it is necessary, although unfortunately not sufficient, to show that the calculated TOA radiances to zenith agree with those observed by the BBR.

The major instrumental characteristics and mission requirements for this instrument are summarised in Table 5.3.

	Parameter	Mission Requirement
Number of channels	2 (SW, LW)	SW = 0.2 to 4.0 μm LW = 4 to 50 μm
Dynamic range	SW LW	0 to 450 $Wm^{-2}sr^{-1}$ 0 to 130 $Wm^{-2}sr^{-1}$
Absolute accuracy	SW & LW	< 1.5 $Wm^{-2}sr^{-1}$
Noise equivalent radiance	SW & LW	< 0.5 $Wm^{-2}sr^{-1}$
Swath	Both channels	nadir point (SSP)
Instantaneous field of view	Both channels	50×50 km^2
Sampling distance	Both channels	30 km

Table 5.3. *Summary of requirements for the broad-band radiometer.*

5.7 Synergy Between Active and Passive Instruments

The synergy between the two active instruments discussed in Section 5.4 is very important as it will allow the retrieval of vertical profiles of ice particle size and ice water content. In this section, other synergies are considered which involve the passive multi-spectral imager. The synergy between the broad-band radiometer and the other ERM instruments has already been discussed in the previous section.

5.7.1 Aerosol

Climatologies of the optical depth of aerosols over the ocean derived from the AVHRR imager have been published. In the proposed ERM mission, the lidar backscatter from the lidar should provide additional information. The height-resolved extinction from the lidar should, when integrated, be consistent with the optical depth inferred from the imager. However, the relationship can be further exploited.

The nadir-pointing lidar would detect backscatter as if the Sun was overhead, whereas the imager will detect backscattered sunlight from a finite solar zenith angle. AVHRR retrievals have assumed an aerosol size distribution, but modelling studies show that using the two angles for the backscatter provides a constraint for the particle size. Although, with only nadir views, uncertainties regarding the anisotropy of aerosol contributions to reflectance will remain, the BBR radiance measurements will help in the evaluation of the broad-band aerosol forcing even when detailed spectral properties of the aerosols remain uncertain.

5.7.2 Liquid Water Clouds

Reflectance of sunlight at 0.8 and 1.6 μm has been used to infer a value of effective radius and optical depth of water clouds; providing the optical depth is more than 3, the retrieval is unaffected by the albedo of the underlying surface. Additional possibilities in the absence of higher multi-level clouds are:

- The IR brightness temperature of the cloud can be combined with the cloud height derived from the lidar to derive a cloud emissivity that can then be converted to a liquid water path. This method only applies to thin strato-cumulus – as soon as they become thick then they have the IR temperature expected for that height. The technique has been demonstrated from the ground, and could be important for studying the mechanisms for breakup and stability of thin sheets of strato-cumulus.
- The cloud tops and bottoms as derived from lidar and radar could be compared with the optical depth of clouds from the passive instruments; this could either be used as a constraint, or it may be possible to gauge the degree to which the profile of LWC is adiabatic.

5.7.3 Ice Clouds

The ice particle size should be derivable from the brightness temperature measured at two IR wavelengths, provided the particle size is below 20 μm. Most operational models assume particle sizes much larger than this. However, the passive inferences of particle size could be checked from the size derived from the lidar/radar backscatter ratio.

The cloud top height inferred from the radar and lidar can be compared with the height derived from the IR brightness temperature. The difference can be interpreted as a finite optical depth in the IR. This inferred optical depth can be compared with the IWP, size and optical depth inferred from the radar and lidar. Any differences in the two optical depths should be consistent with the inferred ice particle size.

A comparison of the passive signal at 1.6 and 0.87 μm should be related to the ice properties. Because the imaginary part of the refractive index is higher at 1.6 μm, the ice should appear blacker in this channel, but this effect will also depend on ice particle shape.

The ideas outlined above are suggestions that have not been rigorously tested at this stage, but should provide some additional information to complement the powerful radar/lidar technique discussed in Section 5.4. The ultimate approach will be to combine all the sensors and then check the data quality by comparing the instrument responses with the state of the cloud represented in a NWP model, and then minimise the cost function to arrive at the best representation of the current state of the atmosphere.

5.8 Complementary Data from Other Sources

For the analysis and processing of ERM data, other existing and available data sources can also be used, if applicable. First of all, data from other satellites can be used to assess additional information on the scenes. Furthermore, the output from state-of-the-art numerical weather models (NWP) can be incorporated in the analysis and the processing of the data.

In the year 2000, the series of geostationary Meteosat satellites will be replaced by its successor, the Meteosat Second Generation (MSG). This satellite consists of a package of instruments, which contains the moderate-resolution imager SEVIRI and the Earth-radiation-budget radiometer GERB.

The SEVIRI imager will have a spatial resolution of 2.5×2.5 km^2 sub-satellite and a temporal resolution of 15 minutes. The 12 wavelength channels largely overlap with the channels of the ERM imager (see Section 5.5). The high time resolution and sampling provides unique information on the temporal development of the cloud fields, which are observed by the ERM satellite only once. The information on the spatial variability and the additional spectral information may be used as an additional source of information in the analysis of the ERM data. Eumetsat has organised the development of retrieval algorithms and the data processing at so-called Satellite Application Facilities (SAF). The Climate SAF is strongly oriented towards the retrieval of cloud and radiation parameters from the SEVIRI instrument. The analysis of ERM data will profit from the experience and infrastructure which is being developed in this group, but there is also a large interest in using ERM data for the validation of the Climate SAF products.

The GERB instrument observes the TOA broad-band SW and LW radiances in the direction of Meteosat every 15 minutes, i.e. for essentially all positions of the Sun at the areas observed. The spatial resolution is 48 km (sub-satellite) and a temporal resolution is 15 min. The instrument has a short-wave channel (0.35-4.0 μm) and a long-wave channel (4.0-30.0 μm). The large FOV of the GERB instrument makes this information very useful for the analysis of the larger scale phenomena.

The data from high-resolution imagers on polar satellites (AVHRR, ATSR, EOS AM/PM…) can be used to study the characteristics of the larger scale cloud fields. It is to be expected that coincident sampling of the imager scene and the ERM will rarely occur. However, the large similarity between these instruments and the multi-spectral ERM imager makes it possible to exploit the already existing knowhow on the analysis of this data. However, it should also be noted the ERM measurements of the vertical atmospheric column will also allow the validation of retrievals from multi-spectral imagers.

In recent years, strong development has taken place in terms of water vapour retrieval from the Global Positioning System (GPS) data. Both ground-based and satellite GPS receivers have the possibility to retrieve information on the water vapour column. It is to be expected that in the coming years this development will continue. However, it is unlikely that water vapour profiles will be retrieved. The use of the GPS data in the data assimilation procedures of NWPs is expected to happen very soon. Therefore, it is reasonable to expect that good and detailed information on the water vapour fields will be available from NWPs during the lifetime of the ERM satellite.

There are numerous other satellite instruments which will provide interesting and relevant data for the analysis of ERM-data. For example, the LWP information as derived from SSMI will be very useful. However, at this moment it is impossible to predict which instruments will be in space during the ERM mission and how good the collocation will be. Although the data will be used if available, they are not crucial for fulfilling the ERM objectives.

The advanced assimilation procedures of present-day numerical weather forecast models result in high-quality analysis fields. In the state-of-the-art 3DVAR and 4D-Var assimilation procedures, data from different sources are used and combined with the first guess. All available observations like radiosondes, 2-metre temperatures, surface humidity, winds, etc., are taken into account. The assimilation procedures therefore result in analysed fields of atmospheric parameters, which give the best possible description of the actual atmosphere. It is obvious that these fields will be an excellent and important additional source of information to be used in the analysis of the ERM data. For example, information of NWP fields can be used for the following topics:

- atmospheric temperature profiles in the synergy algorithms to estimate LWP from cloud geometry information and the assumption of sub-adiabatic profiles
- water vapour data in calculations of the radar attenuation
- temperature and water vapour information to calculate the atmospheric correction of the IR channels of the multi-spectral imager needed to derive an accurate cloud top temperature
- surface temperatures to set thresholds in retrieval algorithms for multi-spectral imager data.

5.9 Summary

Lidar:

- Cloud detectability: A day-time detection threshold of 2.4 10^{-6} m^{-1} sr^{-1} for a 100 m gate length and 1 km integration length should be able to detect all radiatively significant ice cloud even when there is a factor of 10 attenuation. The lidar should also detect all radiatively significant aerosols and liquid water clouds, but attenuation will mean that its ability to penetrate such water clouds will be severely limited.

- Typical accuracy of the retrieved extinction coefficient will be between 10-40% for an optical depth of 0.1. Assuming that extinction can be empirically related to water content, similar errors would be found in retrieved water content. For greater optical depths the retrievals become unstable but, when combined with radar, much improved accuracy is possible.

Radar

- For ice clouds, a detection threshold of -36.8 dBZ for an integration length of 10 km should detect over 99% of all ice clouds of thickness above 500 m and ice water content above 0.001 g m^{-3}. It will also detect over 99% of all radiatively significant clouds, i.e. with optical depth greater than 0.05. These figures are slightly reduced for the -31.8 dBZ threshold for an integration length of 1 km (94.0 and 93.3% respectively).
- The ice water content can be derived from the observed radar reflectivity to a factor of 2; when combined with the knowledge of temperature, this figure can be improved. Attenuation by ice is negligible.
- Very thin water clouds will be difficult to detect, but as soon as such clouds become thicker than 200 m, the occurrence of occasional larger 100 μm droplets raises the reflectivity level above the detection threshold. Accordingly, the presence of such droplets, which make a negligible contribution to liquid water content, means that it will not be possible to derive liquid water content from the radar signal alone, but it does mean that attenuation by the thicker clouds will not lead to a loss of detection.

Lidar/Radar Synergy

- Providing the radar and lidar footprints are co-located to better than 2 km, the ratio of the backscatter from the two instruments should provide estimates of particle size to within 30% for ice clouds, and then using the size information with the radar reflectivity, the IWC can be derived to within 30-40%.
- Direct estimation of cloud liquid water will be more difficult. The radar detects cloud top and base and so adiabatic considerations provide an upper limit on water path, but the occasional large droplets (>100 μm) prevent accurate estimates of LWC from radar measurements alone. The severe attenuation of the lidar signal provides an estimate of the optical extinction coefficient, and finally the visible reflectance measured by the imager (when there are no upper cloud layers) is also a measure of the optical depth.
- The combined radar/lidar backscatter should provide an indication of the presence of super-cooled liquid water embedded within ice clouds.

Multi-Spectral Imager

- The multi-spectral imager data provides information on the variability of clouds. Also cloud and aerosol properties will be derived based on the long-standing experience with retrieval algorithms for imager data. Furthermore, the multi-spectral imager plays a crucial role in characterising the variability within the footprint of the broad-band radiometer. Finally, the data will also be used in synergy with lidar and radar data.

Broad-Band Radiometer

- The broad-band radiometer measures the short- and long-wave radiance towards zenith. Using the observed macro- and micro-physical cloud (from lidar, radar and multi-spectral imager) to derive the emergent short- and long-wave radiances and comparing them to those measured, a new insight will be gained into the role of clouds and aerosols. This observation provides crucial information for the parameterisation of clouds and aerosols in numerical weather prediction models (NWP).

6 The ERM System

6.1 From Mission to System Requirements

The observation requirements defined in Chapter 4 (see the summary in Table 4.1) and the mission requirements given in Chapter 5 (see the summary Tables 5.1, 5.2 and 5.3) together form the basis for the system requirements of the ERM. Those requirements nominally call for a single satellite mission, as explained below.

Both the coverage and sampling requirements do not represent any stringent constraints on the completeness and frequency of coverage. The requirement to provide snapshots at the passage of the satellite leaves a large freedom in the choice of the orbit and naturally favours a synoptic-type sampling provided by a single orbiting satellite. Also, a Sun-synchronous orbit is required with the Equator nodal crossing time in the early afternoon.

The system consists of the *Space Segment,* which includes:

- Backscatter Lidar
- Cloud Profiling Radar
- Multi-Spectral Imager
- Broad-band Radiometer
- Platform

the *Launcher*,

and the *Ground Segment,* which includes:

- Command and Data Acquisition
- Mission & Satellite Control and Planning
- Data Processing and Archiving.

The observation requirement regarding collocation between the lidar and the radar, both of which provide very narrow observation strips (width $\leq$ 1 km) below the satellite, calls for a cross-track separation of less than 2 km, together with a time separation of not more than 30 seconds. This requirement is a very strong argument for a single space segment that includes both active sensors, which are the largest payload elements of the system (both the imager and the radiometer are non-driving elements of the payload).

An overview of the ERM system as baselined at the end of the Phase-A study is shown in Figure 6.1. All four instruments are accommodated on a single satellite. A lowest possible orbit of 380 km mean altitude has been selected for maximising the sensitivities of the two active sensors, which nevertheless permits the utilisation of a conventional hydrazine-based propulsion system for a minimum mission duration of two years (with the necessary propellant supply for an additional year as a margin for contingency operations and mission extension). A 1300 hrs Equator nodal crossing time would permit a simple solar-array configuration to be used without canting of the wings.

Rockot has been selected as the baseline launch vehicle because of its low cost, with ATHENA and PSLV as back-ups. The CPR antenna diameter has been selected to just fit the fairing envelope, and thus optimum use is made of the available volume.

The ground segment is based on reuse to the maximum extent possible of the Agency's existing infrastructure; only a few upgrades will be required. No stringent requirements have been identified so far for the data delivery within a specified length of time to the end users. Should the need for near-real-time data delivery emerge, e.g. for the use of ERM data for numerical weather prediction, automatic data products can be made available in this time frame.

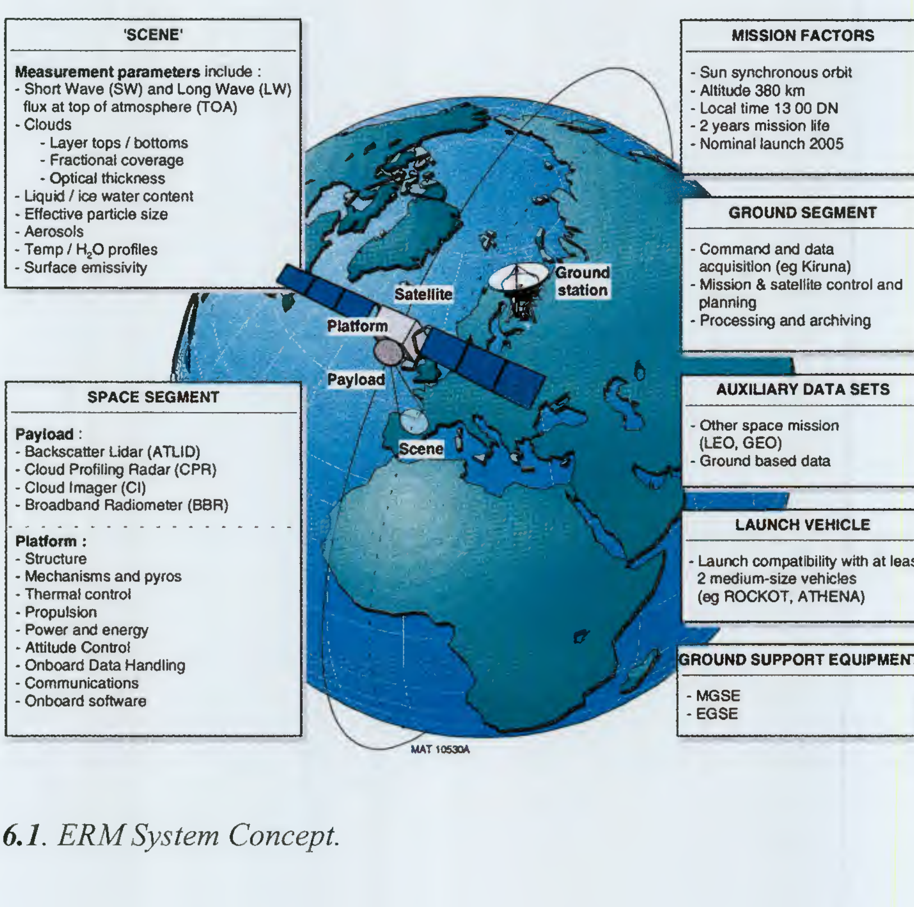

Figure 6.1. ERM System Concept.

6.2 Mission Design and Operations

6.2.1 Orbit Selection

The definition of the ERM orbit is based on the observation requirements as stipulated in Section 4, calling for a Sun-synchronous orbit with a node crossing time in the early afternoon. The other orbit parameters being to a large extent independent of the science requirements, they may be selected to best suit the performance characteristics of the instruments and to optimise the mission as a whole, mainly in terms of complexity and by inference cost. In this context it should be recalled that particularly the active instruments are very sensitive to orbit altitude in that their link budgets are strongly affected by the slant range. On the other hand, too low an altitude will increase satellite complexity, mainly in terms of orbit maintenance provision.

The selection of the orbital altitude is the result of a trade-off between the mass-to-orbit capability of the baseline launcher, the change in active instrument performance and the propellant required to achieve a three-year lifetime for consumables sizing. Orbits between 369 km and 411 km could satisfy the observation requirements. A 411 km orbit would result in a CPR performance degradation of 0.9 dB and result in a system mass about 22 kg lower than the baseline. As the system mass margin is rather healthy at about 172 kg, the lower orbit was chosen as the loss in CPR performance could not be made up by any of the system parameters other than a different launch vehicle with a larger fairing. Similar considerations apply to the performance of the lidar.

Further reductions in orbital altitude have been considered in the course of the mission design process but discarded, as increased system complexity, e.g. the use of an ion propulsion system, would outweigh the gains in instrument performance.

For comparison, a CPR flying at 705 km, which is the altitude selected for the CLOUDSAT and PICASSO-CENA missions, would have a sensitivity 5.6 dB worse than the ERM baseline, thus resulting in a significant mission degradation. Whilst the propellant mass would decrease from 109 kg to some 10 kg, the overall system mass margin would reduce to 151 kg (from the present 172 kg) because of the lower mass-to-orbit performance of the Rockot launcher. The decreased mass margin looking acceptable at this stage, there is no way to make up the CPR performance shortfall within the limits of the existing resources.

Orbital altitude also determines the repeat cycle, i.e. the interval after which the orbit intersects the same point on the equator again. The range of possible repeat patterns lies between 1 day (the minimum cycle length for a Sun-synchronous orbit) and 28 days (the minimum required for passing through all reference cells on the equator). The baseline orbit has a repeat pattern of 15 + 2/3 orbits per day, i.e. a repeat cycle of three days. Full global coverage of the Earth is not required, only a fraction thereof.

The Kepler elements of the selected orbit are shown in Table 6.1 and the derived orbit parameters in Table 6.2.

Semi-major axis (km)	6740.4
Eccentricity	0.001165
Inclination (degrees)	96.893
RAAN (degrees)	116.04
Argument of perigees (degrees)	+ 90
True anomaly (degrees)	- 90
Reference epoch	01 Jan. 2005, 00:00:00 hrs

Table 6.1. *ERM Kepler orbit elements.*

Mean orbit altitude (km):	369 km
Orbits per day:	15 + 2/3
Nodal period (mins):	91.6

Table 6.2. *ERM derived orbit parameters.*

This orbit altitude varies with respect to the reference geoid along the orbit as depicted in Figure 6.2. This variation is significant for the definition of the CPR's pulse repetition frequency (PRF), which depends on the orbit altitude profile.

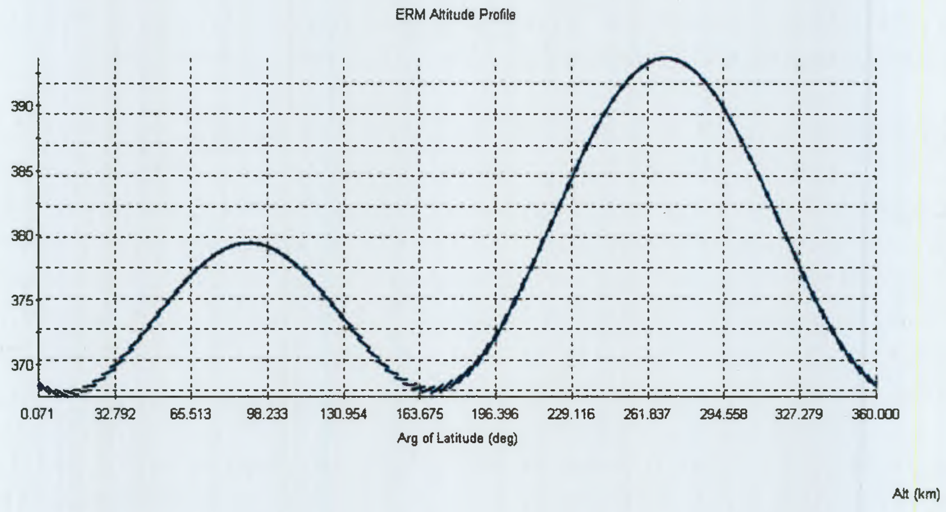

Figure 6.2. *ERM orbit altitude profile.*

6.2.2 Orbit Perturbation and Maintenance

The rather low orbital altitude is associated with significant atmospheric drag, which varies considerably throughout the solar cycle. It is therefore important that the mission life is spent as much as possible in a period of low solar activity, which would be the case for a launch in the years 2005 or 2006. Also satellite design measures have been employed, to minimise the cross-section in the direction of flight.

The frequency and magnitude of the altitude correction manoeuvres is determined by the accuracy with which the ground track has to be maintained. It has been assumed for validation purposes that the ground track has to be maintained to an accuracy ±10 km. This change in ground track is the consequence of a change in orbit altitude of about 3 km, which is the predicted orbit degradation for a ten-day period in the time frame foreseen for ERM.

This orbit control requirement transforms into a total ΔV of some 210 m/s, and 106 kg of hydrazine propellant. It is to be noted here that relaxing this control band will not change the propellant mass, but only the frequency of the manoeuvres and their duration.

Analyses have shown that, except for the correction of injection errors, only orbit altitude degradation caused by atmospheric drag will need to be compensated. Inclination changes are predicted not to exceed 0.1 degree during a three-year mission life. The right ascension of the ascending node would change by about 5 degrees, equivalent to a change of 20 minutes in node crossing time, which is considered acceptable for the mission profile.

6.2.3 Instrument Co-Registration

It has been shown that the instrument footprints should be as close together as possible in order to maintain the quality of the synergetic data retrieval. This transforms into a requirement for precise alignment of the instruments, or rather their lines-of-sight.

The lidar telescope's line-of-sight has been selected as the reference for all instruments, the laser beam being aligned such that its footprint is always within the telescope's field-of-view (FOV). Ideally, the cloud radar's footprint should encircle the telescope's FOV and likewise the imager's nadir pixel should cover the footprints of the two active instruments. The BBR's nadir pixel shall also cover these combined footprints. This arrangement is shown in Figure 6.3. The BBR's pixel is not shown as its size of 40 by 40 km^2 is much larger than the others, so its alignment does not present a technical problem.

Whilst it is technically feasible to align the instrument footprints to a high degree of accuracy approaching perfect co-registration, this would imply very precise manufacturing and alignment tolerances. It has been shown in Chapter 4 that some offset between the footprints, i.e. up to several hundred metres, is tolerable without degrading the quality of the synergetic data retrieval. For engineering purposes, offsets in the order of half the CPR's footprint have therefore been assumed. The maximum distance between the centres of the telescope's line-of-sight and the CPR has therefore been defined as 400 m, which also applies to the imager. This level of accuracy is compatible with normal mechanical design practices. The co-registration requirement for the BBR has been defined as 20% of the pixel dimension, i.e. 8 km, which is not critical.

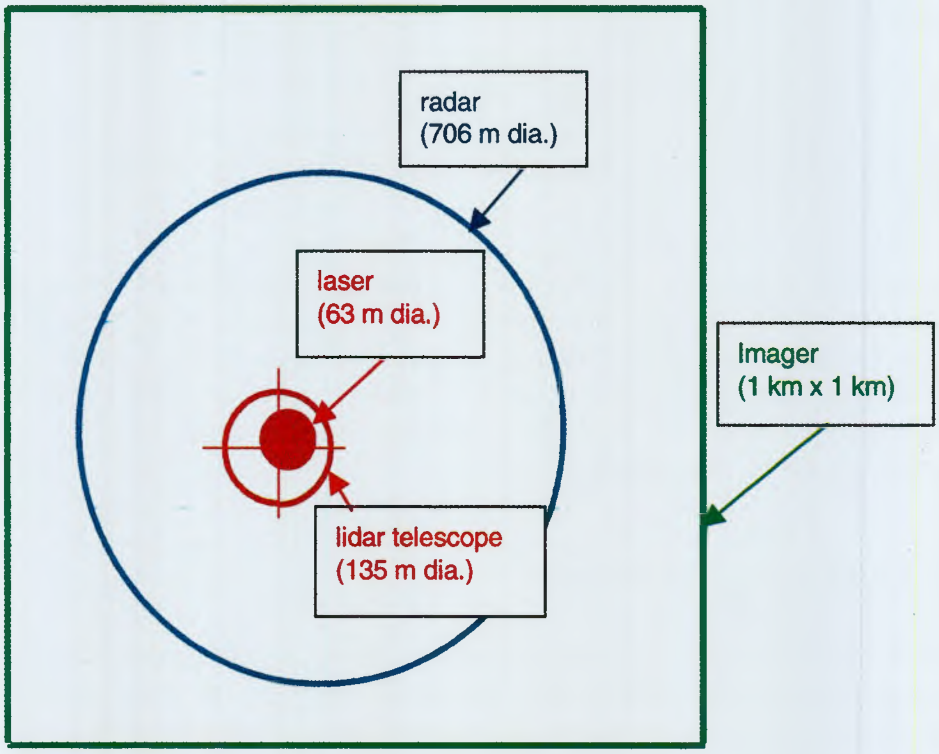

Figure 6.3. *ERM instrument co-registration; drawing not to scale and BBR omitted for clarity. The lidar telescope's line-of sight has been defined as the reference, indicated by the red cross-hairs.*

6.2.4 Ground Station Coverage

For the purpose of the Phase-A study, use of the Kiruna ground station has been assumed as baseline. The coverage parameters are listed in Table 6.3 and the communication coverage profile is shown in Figure 6.4.

Percentage of communication coverage	3.52%
Maximum coverage per day	49 min
Minimum coverage per day	41 min
Longest pass duration	7.6 min
Shortest pass duration	1.2 min
Maximum contact gap	7 orbits

Table 6.3. *ERM ground-station coverage.*

There are seven so-called blind orbits, during which no data transmission will be possible as the satellite would not be within the visibility of the ground station. This would increase to 8 orbits if the short passes of about 1.2 minutes were not used. In other words, there would be a communication gap of about 12 hours. If this gap should be considered unacceptable in the light of timeliness requirements, a second ground station with a suitable location must be used.

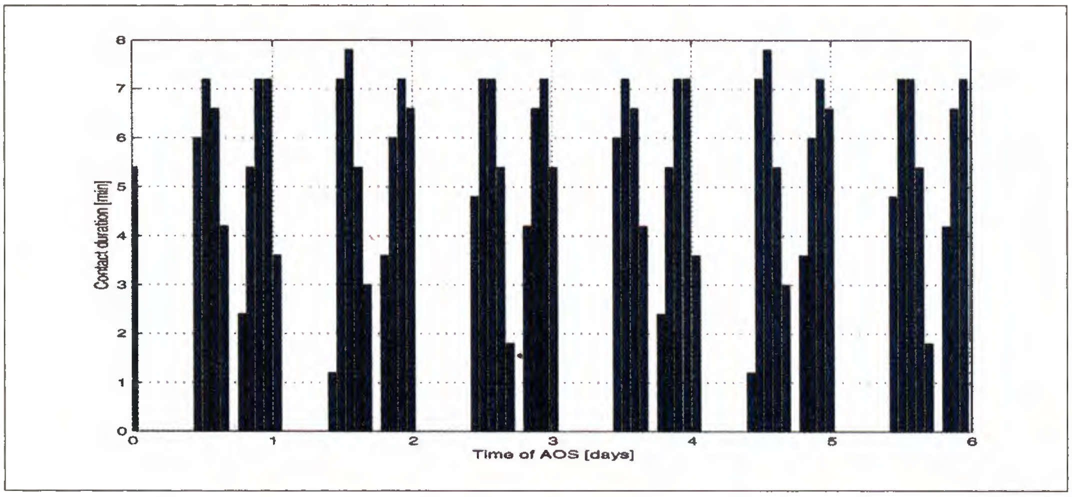

Figure 6.4. *ERM communication coverage profile.*

6.2.5 Operations

The mission life is subdivided into typical operational phases, which are listed below:

- launch and early orbit phase (LEOP), up to one week
- satellite commissioning, typically one month
- nominal operations, two years, plus one year, regarding consumables
- contingency modes
- de-commissioning.

The sequence of the LEOP events is shown in Figure 6.5. These operations will be executed automatically upon ground command. The exact timing depends on the detail design of the satellite, the subsystems involved and the number and locations of ground stations used.

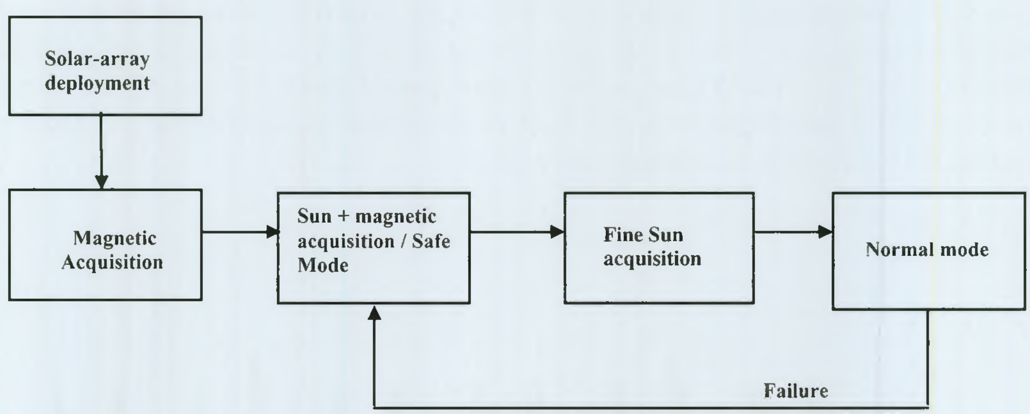

Figure 6.5. *ERM mode sequencing.*

Following separation from the launch vehicle, the solar arrays will be deployed in order to generate electrical power to supply the loads and recharge the battery. This approach is commensurate with the residual angular rate at separation from the launcher and the mechanical design of the solar-array.

Attitude acquisition and stabilisation will be performed using the Earth's magnetic field (B-dot law) with the magnetorquers and the magnetic field sensor. An angular momentum is generated by spin-up of the reaction wheels, producing a magnetic moment proportional to the derivative of the measured magnetic field. This results in a fast rate reduction and a satellite rotation at twice the orbital frequency. Simulations have shown that coarse attitude acquisition will be achieved in less than two orbits, as shown in Figure 6.6. Sun acquisition will be performed with the coarse Sun sensors, the B-dot law still being used during eclipses. Fine Sun acquisition will be performed by means of the star sensors. Normal mode with constant nadir-pointing will also be maintained with the star sensors, supported by an inertial reference unit during star-sensor outage periods. Yaw steering will be used in nominal mode to correct the mis-registration of some channels of the multi-spectral imager, caused by the VIS/NIR and TIR channel's in-field separation. The safe mode will be identical to the attitude-acquisition mode.

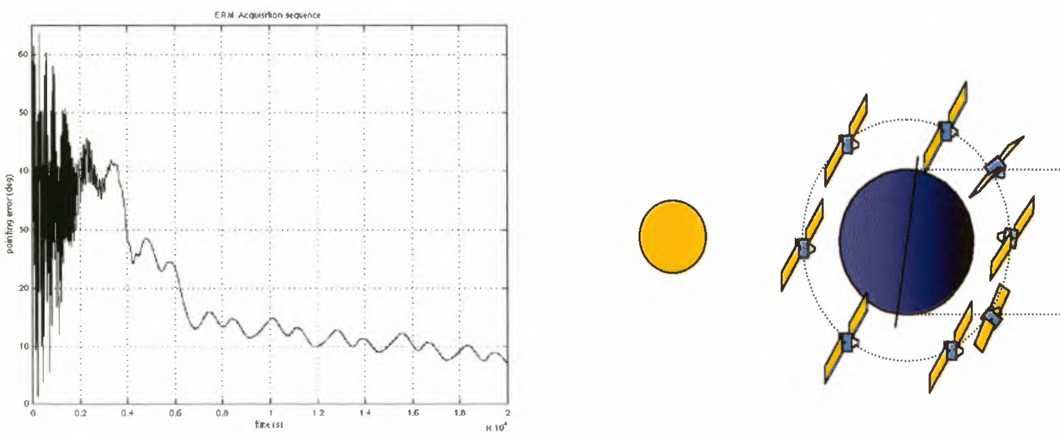

Figure 6.6. *B-dot attitude-acquisition profile.*

Satellite design will be such that autonomy of at least 72 hrs is available. Depending on the criticality of an anomaly, the support of other ground stations may be invoked.

All instruments will be operated continuously once the nominal orbit has been attained. The acquisition of scientific data may be impaired for the duration of orbit-correction manoeuvres, as the satellite attitude may lie outside the nominal range. In addition, allowance has to be made for instrument calibrations, during which only incomplete science data will be recovered. The duration of these periods will be kept as short as possible in order to maximise the mission return. Information on the calibration sessions is found in the relevant parts of Section 6.3. These instrument-specific operation modes will be run automatically by means of pre-defined sequences stored in the onboard computer. The CPR will be switched off during periods of over-flying ground-based radio astronomy sites in order to prevent damage to their receiver inputs. These periods will be short and hence the loss in observation time will be small.

6.3 The ERM Instruments

6.3.1 General

The definition of the ERM instrument suite responds to the science requirements as elaborated in Chapters 3, 4 and 5 of this report.

Whilst the active instruments are novel in the sense that relatively little flight experience is available from other missions at the time of writing this report, the passive instruments are based to a significant extent on the heritage provided by other similar instruments.

The instrument characteristics have been optimised for ERM to ensure on the one hand a maximum of synergy and on the other to arrive at a design which is as simple as possible. For the lidar, the lower orbital altitude has resulted in reduced laser pulse energy, leading to lower mass, primary-power and thermal-dissipation requirements. For the imager and the BBR, changing from the traditional horizon-to-horizon to a narrow swath has allowed simple instrument design concepts to be used. Their compact designs are also less demanding regarding accommodation on the platform.

The detailed design of the instruments, together with their performance parameters, is presented in the following sections.

6.3.2 Backscatter Lidar

Instrument Objectives and Operating Principle

ATLID (ATmospheric LIDar) is a backscatter lidar to measure vertical profiles of optically thin clouds and aerosol layers, as well as the altitude of cloud boundaries. The instrument is designed to operate continuously day and night.

The instrument will emit short laser pulses (20 ns) at a wavelength of 1.06 microns towards the atmosphere in the nadir direction. A pulse repetition frequency of 35 Hz has been selected such that a number of pulses can be averaged over an integration length of 10 km in order to improve the signal-to-noise ratio (SNR) for certain cloud scenarios. A small fraction of the emitted light is backscattered by clouds and aerosol particles, collected by a telescope and focused onto a detector. The instrument measurement principle is shown in Figure 6.7.

The observation range has been set to 0-30 km with respect to the mean geoid, thus encompassing in addition to aerosols all cloud types from those in the planetary boundary layer (PBL) to high-altitude cirrus and polar stratospheric clouds (PSC). The vertical resolution is set to 100 m with a sampling interval of 50 m. The location of the echo samples is to be known with an accuracy of 50 m, including all instrument and platform errors.

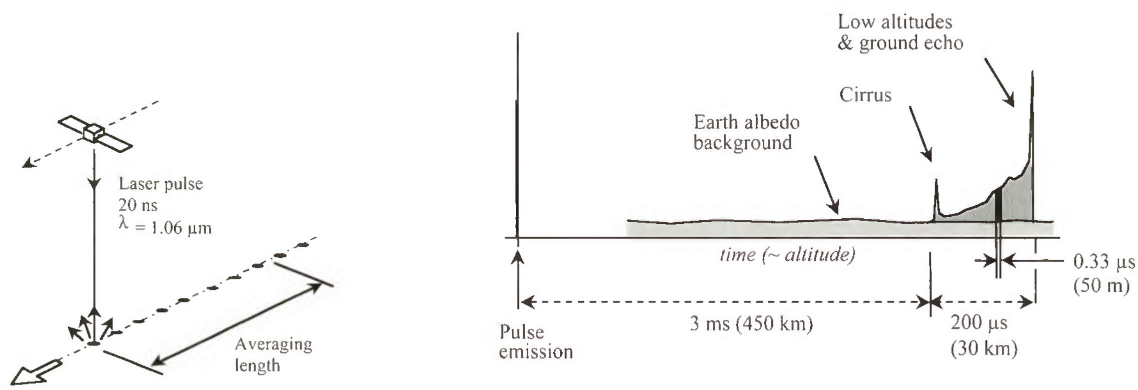

Figure 6.7. *ATLID measurement principle.*

The ATLID sensitivity has been specified to allow the detection and estimation of geo-physical parameters of a number of atmospheric targets such as thick cloud and planetary boundary layer top heights or optical thickness of thin cirrus above dense cloud with high albedo.

For calibration purposes, the instrument provides the average of the echo profile from 100 km up to 150 km altitude for dark current and solar background compensation, and echo samples between 100 km and 105 km for noise calibration of the radiometric chain. The calibration constant can be determined to an accuracy of about 10% for the lifetime of the instrument and over the full dynamic range.

Instrument Architecture and Systems

ATLID consists of a laser transmitter, a telescope and a focal-plane assembly. A coalignment mechanism ensures that the laser beam lies within the telescope's instantaneous field of view (IFOV). In addition, there is the support structure and the instrument electronics interfacing the instrument with the platform.

The ATLID functional block diagram is shown in Figure 6.8, and the main instrument parameters are given in Table 6.4. The chosen parameters have been selected to optimise laser head lifetime (PRF and pulse energy) and resource requirements (telescope mass and cost, instrument data rate and input power). It is worth noting that the instrument design is driven by the detection of the planetary boundary layer top ($\beta = 5 \times 10^{-6}$ $m^{-1}.sr^{-1}$) during daytime with a signal-to-noise ratio of 6, obtained by averaging over a 10 km along-track distance.

The laser transmitter is based on the well-established diode-pumped Nd:Yag laser technology. The transmitter features two laser units (laser head and power supply), in cold redundancy to avoid single-point failures. Switching between the two laser units is achieved by a polarisation switch. Each laser head consists of a thermally controlled pump unit, an electro-optic Q-switch device and an unstable resonator operating with a super-Gaussian mirror as output coupler. The pump unit is composed of a Nd:Yag material slab, side-pumped by close-coupled laser diode array stacks. The optical axis of the resonator is folded in a zig-zag path inside the slab in order to smooth non-uniformity distorsions. The thermal-control uses loop heat-pipe technology, which provides the required temperature stability for the pumping diodes and the slab over the lifetime of the mission. The overall efficiency of the laser units is about 5%. The beam expander unit allows the laser beam divergence to be set at a level which meets eye safety standards for a ground observer using a telescope with an aperture of 120 mm.

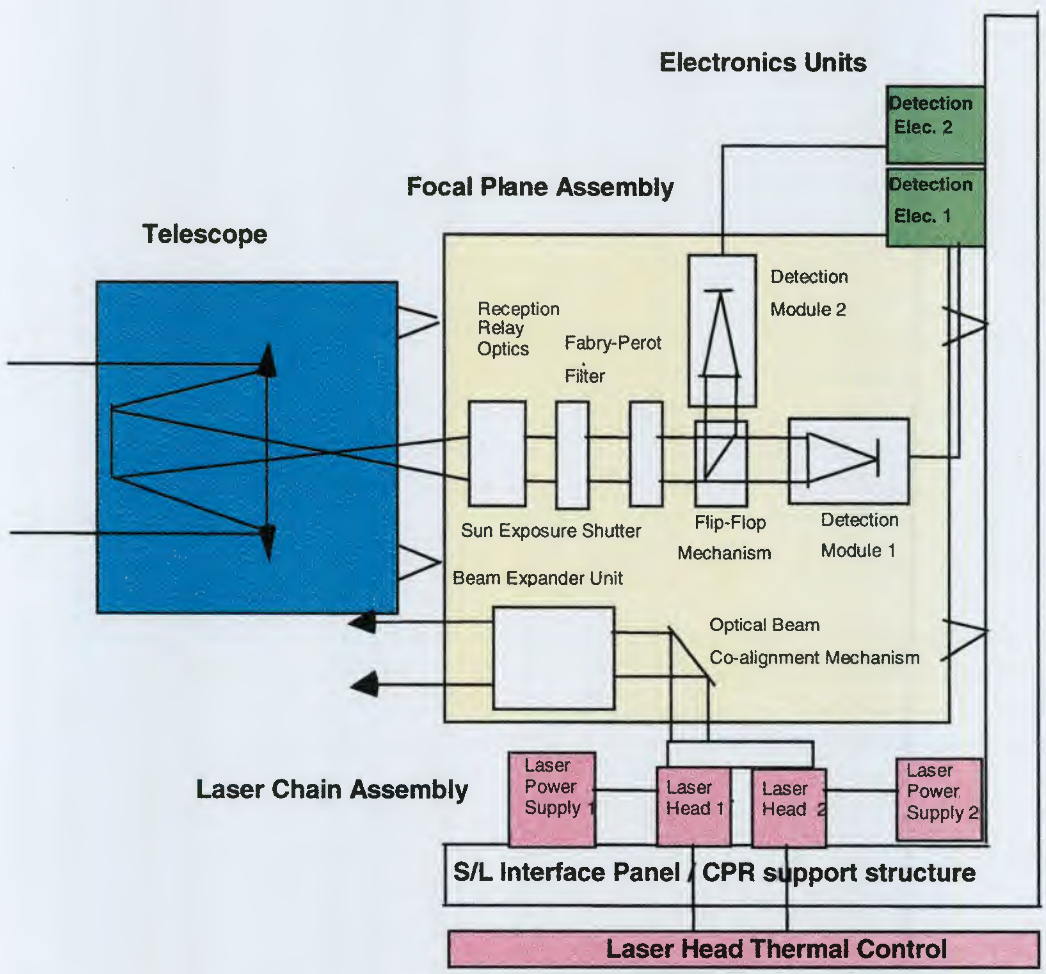

Figure. 6.8. ATLID functional block diagram.

The receiving chain consists of a Cassegrain-type telescope made of SiC because of its superior thermo-elastic performance and stiffness-to-mass ratio. The primary mirror diameter is 0.7 m. The secondary mirror directs the incoming laser light to the focal-plane assembly, where a field stop limits the telescope's field of view.

Transmitter	
Pulse energy	70 mJ
Pulse length	20 ns
Repetition rate	35 Hz
Optical transmission	0.98
Beam divergence @ $1/e^2$	170 μrad
Receiver	
Telescope collecting area	0.33 m^2
IFOV (with co-alignment device)	365 μrad
Optical transmission	0.41
Filter equivalent bandwidth	0.354 nm
Radiometric Detection	
Dark current, electronic noise	2×10^{-13} A $Hz^{-1/2}$
Electrical bandwidth	1 MHz
Sampling frequency	4 MHz
Responsivity	12 A W^{-1}
Gain	39
Noise factor	2.8

Table 6.4. *ATLID design parameters.*

The focal plane features reception relay optics to transport and collimate the beam, a shutter to avoid direct exposure of the detector to Sun illumination (in case of the instrument facing the Sun during a non-operational mode), a Fabry-Perot etalon, a blocking interference filter to reject scattered sunlight collected through the image field of view (IFOV), and a flip-flop mechanism to switch the beam between the two redundant detection chain modules. An avalanche photodiode (APD) in hybrid technology, together with a trans-impedance amplifier, is used as detector element as shown in Figure 6.9. The APD is mounted on a thermoelectric cooler (TEC) to maintain optimum performance of the detector over the mission lifetime. The APD is dc-coupled, with the front-end electronics comprising the first gain stage and an offset (dark current, drift, background) compensation circuit. Three signal-processing chains are operated in parallel:

- The peak detection chain with a sampling rate of 8 MHz, used to determine the altitude of dense cloud tops.
- The radiometric detection chain with a sampling rate of 4 MHz dedicated to the measurement of thin clouds, aerosols and Sun background.
- The calibration chain for instrument in-flight calibration, which features a circuit integrating the return signal contained in a window of pre-defined position and width. Usually, this window will be positioned to measure the energy of the ground return.

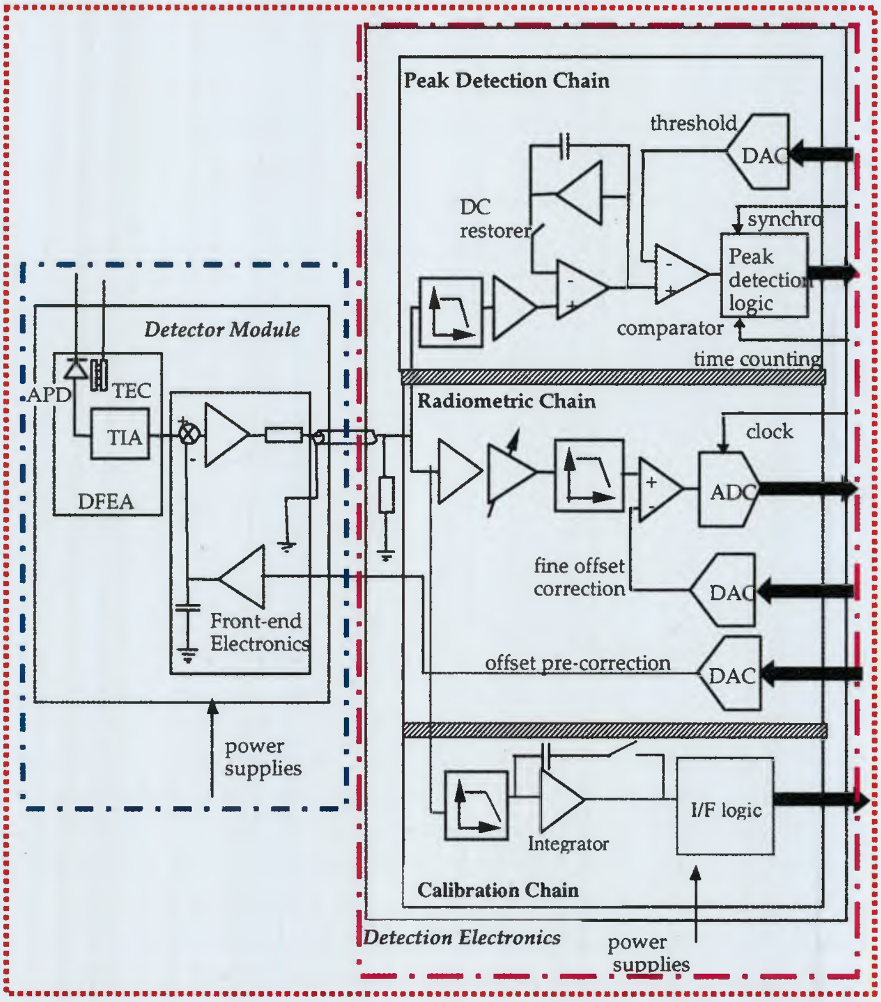

Figure 6.9. *ATLID signal processing chains.*

Instrument calibration is based on a combination of pre-launch measurements, which aim at characterising the parameters involved in the instrument radiometry (e.g. pulse energy, optics transmission, detector responsivity, electronics chain gain variations as a function of temperature) and in-flight measurements over reference scenes. The timing diagram of the calibration chain is shown in Figure 6.10.

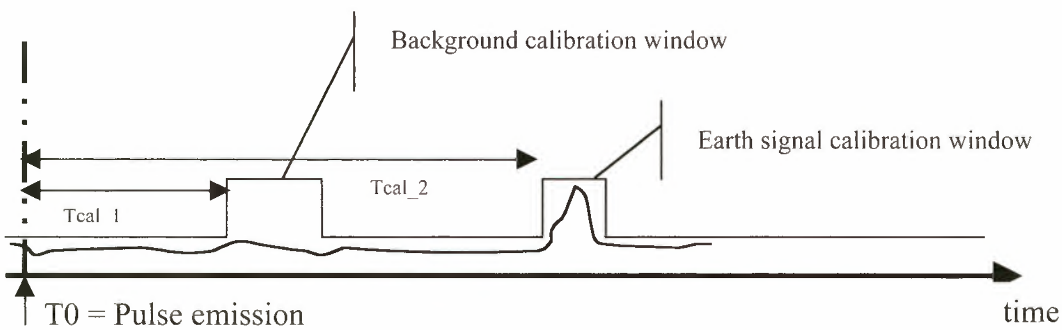

Figure 6.10. *Calibration chain timing diagram. The temporal position and the width of the calibration window can both be adjusted, and thus its altitude and height.*

The mechanical configuration is based on an optical bench supporting the telescope and the focal-plane assembly. The optical bench in turn is mounted on the ATLID interface structure, which houses the laser heads, the electronics and the power supplies. This interface structure is mounted on the satellite platform. It is sized for carrying the cloud profiling radar, thereby optimising the load paths and de-coupling the optical bench. Figure 6.11 shows the ATLID mechanical design and Figure 6.12 the ATLID overall configuration.

The active cooling system employs a loop heat-pipe system for the transfer of the laser head's heat dissipation to a dedicated radiator with an area of 1 m^2, accommodated on the anti-Sun side of the satellite. Four additional radiators are used on the Sun- and anti-Sun faces to dissipate heat generated by the optical bench and the laser electronics. All radiators are covered with OSR or white paint.

Instrument Performance

Tables 6.5 and 6.6 summarise ATLID performance as predicted at the end of the Phase-A study. Instrument performance is specified in terms of SNR and altitude restitution accuracy for the given atmospheric scenarios.

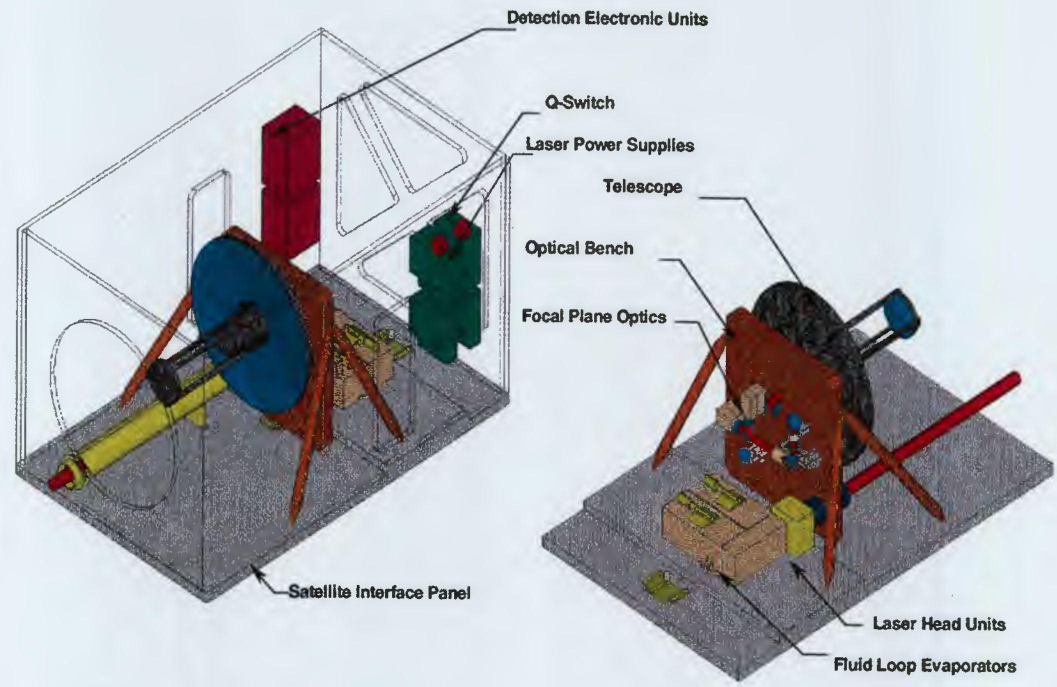

Figure 6.11. *ATLID mechanical instrument design. The optical bench is de-coupled from the interface structure to ensure stability.*

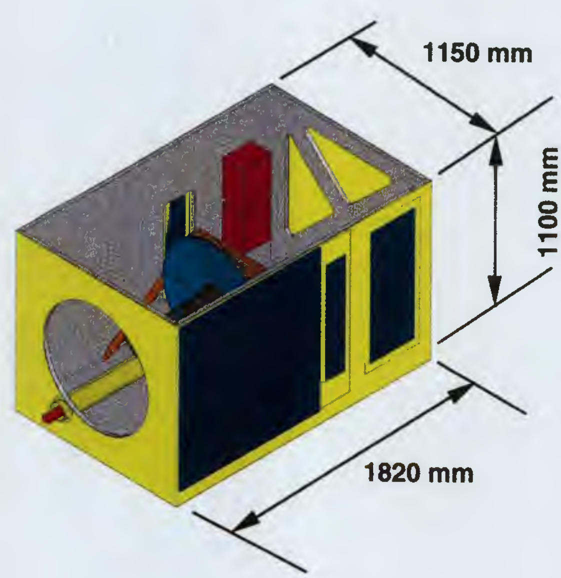

Figure 6.12*. ATLID overall configuration.*

Atmospheric scenario	**Requirement**	**EOL performance Day**	**EOL performance Night**
SNR over 10 km			
PBL, top above land, summer	6	6.2	7.7
PBL, top above land, winter	6	14.3	27.2
Cirrus bottom above stratus	8	9.1	23.9
SNR, single shot			
Fair weather cumulus	3	34.4	38
Alto-Stratus	3	46.6	50

Table 6.5. *ATLID SNR performance for specified cloud scenarios. The PBL backscatter coefficient is 2.5* $10^{-6}\ m^{-1}\ sr^{-1}$. *The cirrus backscatter coefficient is* $1.4\ 10^{-5}\ m^{-1}\ sr^{-1}$ *with an optical thickness of 0.2. An albedo of 1 has been assumed for stratus. For detection purposes, with SNR=2, the sensitivity is* $8\ 10^{-7}\ m^{-1}\ sr^{-1}$ *and* $2.4\ 10^{-6}\ m^{-1}\ sr^{-1}$ *for 10 and 1 km integration length, respectively.*

	Target	**Altitude restitution accuracy: Requirement**	**Altitude restitution accuracy: Value**
Peak Detection Chain	Dense cloud	100 m	17 m
Radiometric Chain	Cirrus top, day	100 m	69 m
	Cirrus top, night	100 m	55 m
	Cirrus bottom, day	100 m	83 m
	Cirrus bottom, night	100 m	63 m
	PBL top summer, day	100 m	100 m
	PBL top summer, night	100 m	77 m

Table 6.6. *ATLID altitude restitution accuracy, instrument only. All performance figures are at* 1σ *confidence level.*

Operations

Following instrument commissioning upon completion of LEOP, the instrument will be operated continuously. All measurements will be performed on a shot-by-shot basis, i.e. signal averaging for specific cloud scenarios will be performed on the ground. Calibration sessions are planned at intervals of at least 6 months (constrained by the long-term stability of the instrument). Calibration will interrupt the observations only for very short periods of time, when the gain of the front-end will have to be switched to a lower value for radiometric calibration over scenes with high albedo.

Contingency operations are limited to the selection of stand-by chains, which will be commanded from the ground in the event of hardware failure.

Resource Budgets

The mass and power budgets are given in Table 6.7; the margin allocations are 20% for mass and 15% for power. The data budget is shown in Table 6.8.

	Mass (kg)	**EOL Power (W)**
Telescope	16.4	-
Focal plane optics	10.4	-
Laser chain assembly	31.3	104
Electronic units	7.5	8
Beam co-alignment device	1.4	-
Optical structure	30	-
CPR support structure	51.3	-
Thermal control	23.9	77
Harness	12	-
Miscellaneous	4	-
Total	**188.2**	**189**
TOTAL with margin	**226**	**217**

Table 6.7. *ATLID mass and power budgets.*

	Data rate (kbps)
Science data, 30 km, radiometry	332
Calibration, 5 km	55
Calibration, 100 –150 km, avge.	0.4
Ancillary data	13
TOTAL	**400**

Table 6.8: *ATLID data budget.*

Development Status

ATLID has been the subject of in-depth development activities for more than one decade. These studies have been performed at instrument and subsystem level by European companies from pre-development of key technologies to breadboarding of critical elements like the laser head with its power supply and thermal control, the telescope, the optical filters and the detection chains. These activities have in many cases included extensive testing to validate the design assumptions and increase confidence in the selected concept.

Figure 6.13 presents pictures of some ATLID components manufactured in the course of the above development activities.

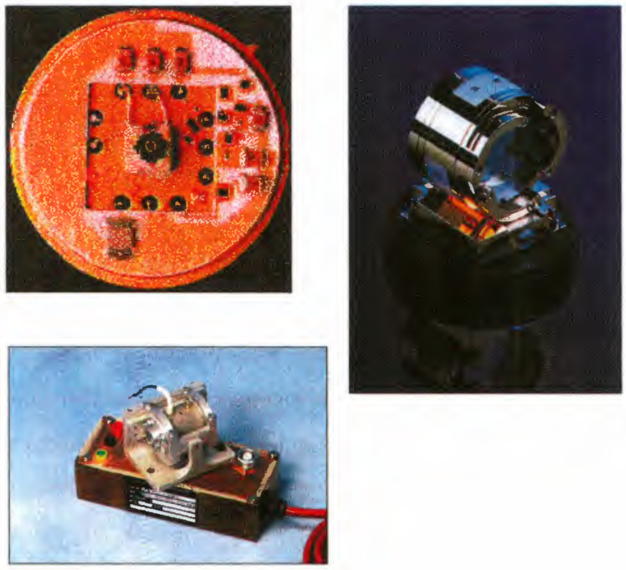

Figure 6.13. *ATLID development model breadboards. Left top: front-end hybrid, Left bottom: Q-switch, Right: Fabry-Perot filter.*

6.3.3 Cloud Profiling Radar

Instrument Objectives and Operating Principle

The Cloud Profiling Radar (CPR) will be flown on the ERM mission to determine the altitude of cloud boundaries and provide vertical profiles of cloud structure along the satellite's flight track. In particular it is the ability of the CPR to penetrate even thick clouds and to retrieve their microphysical properties which makes it an indispensable sensor for this mission. The instrument parameters have been set to offer a compromise between its sensitivity, which mainly determines the ability to penetrate clouds, and its altitude-resolving capability to provide information about their macro-physical characteristics.

The CPR is a pulsed radar operating at a frequency of 94.05 GHz, which is located within one of the atmospheric windows. The sensing polarisation is linear. The sounding altitude range has been set to 0-20 km with respect to the mean geoid. Two vertical resolution modes have been defined to optimise instrument performance in accordance with the characteristics of the cloud scenes being observed: the nominal mode with 500 m vertical resolution and a secondary mode with 350 m resolution. The higher resolution offered by the secondary mode results in a sensitivity loss of approximately 3 dB. The position of the echo samples will be known to an accuracy of 50 m rms including all instrument and platform errors.

The dynamic range of the instrument has been specified as -33 dBZ $\leq Z \leq$20 dBZ in nominal mode and -30 dBZ $\leq Z \leq$20 dBZ for the secondary mode at the bottom of the atmosphere (1 km altitude). The instrument sensitivity depends on the definition of the reference scenario for which a three-layer cloud model consisting of cirrus, alto-stratus and stratus has been used (see next).

The radar echo profiles will be incoherently averaged on-board over a distance of 1 km, producing an along-track sampling interval of this distance. Further integration over longer distances will be performed on the ground to resolve cloud scenes with the required sensitivity and horizontal resolution.

Instrument Architecture and Systems

An extremely tight range-sidelobe suppression requirement of ≥75 dB led to the selection of a short pulse and high transmitter (Tx) peak power concept. The overall instrument architecture is shown in Figure 6.14 with the current baseline of the quasi-optical design for the radar front-end. As a back-up, a waveguide-based option has also been designed. The CPR mechanical configuration is shown in Figure 6.15.

Table 6.9 summarises the instrument design parameters. The CPR configuration is dominated by the large main reflector, which together with the smaller sub-reflector forms a Cassegrain-type antenna. The aperture dimension of 1900 mm × 2150 mm has been optimised to fit into the fairing of the reference launch vehicle. The dish is made of a CFRP/Al sandwich with longitudinal and lateral stiffening ribs. It will be folded to the top panel for launch.

Instrument parameter	Value
Frequency	94.05 GHz
Polarisation	Linear
Beam pointing	Fixed nadir
Antenna type / aperture dimensions Effective area	Dual-offset Cassegrain / 1900 mm × 2150 mm ≥ 2.1 m^2
Pulse length	3.33 μs (nominal mode); 2.33 μs (secondary mode)
Pulse repetition frequency (PRF)	5310-5696 Hz (orbit position dependent)
Vertical sampling interval	100 m
Echo vs. noise meas. sequence	6 echos/noise (nominal); 7 echos/noise (secondary)
Peak RF transmit (Tx) power	≥ 1.5 kW (Extended Interaction Klystron amplifier)
Transmit / receive losses	1.13 dB / 2.63 dB (1.8 dB / 3.0 dB waveguide option)
LNA physical temperature Noise figure (NF)	≤ 240° K ≤ 3.5 dB
Processing loss	≤ 0.4 dB
On-board along-track integration	1 km

Table 6.9. *CPR instrument design parameters.*

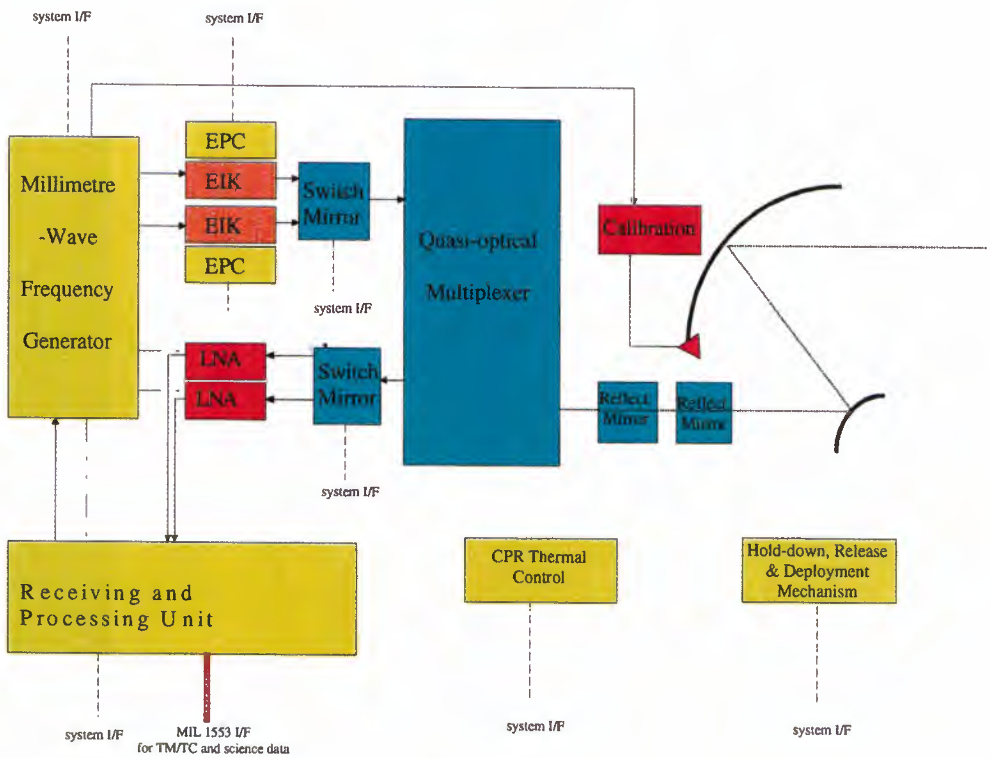

Figure 6.14. *CPR functional block diagram (redundancy at unit level is not shown).*

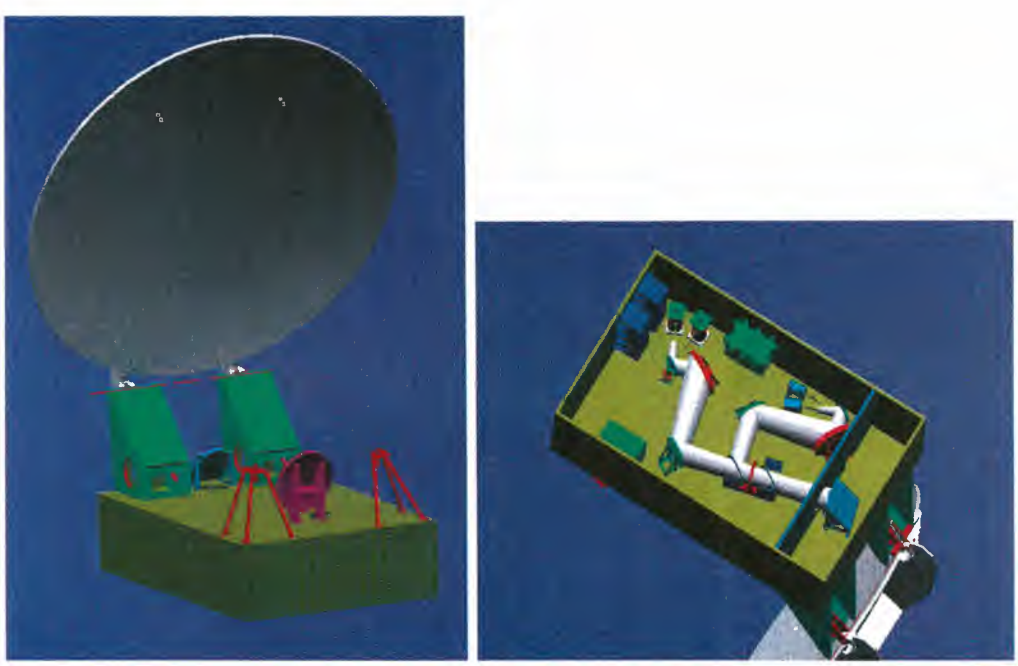

Figure 6.15. *CPR instrument configuration (left) and inside view (right) with quasi-optical beam path (-40 dB contour in white).*

With the instrument design constrained by the available peak power (technology limitation) and by the use of short, unmodulated pulses (due to the range-sidelobe requirement), the losses in the radar transmit and receive chains had to be minimised in order to achieve the required sensitivity. A quasi-optical design has been chosen as baseline as it provides the lowest losses and greatest implementation flexibility at millimetre-wave frequency (maximum avoidance of waveguides).

The layout of the quasi-optical front-end and antenna is depicted schematically in Figure 6.16. A quasi-optical diplexer (Faraday rotator) is used to separate the transmit and receive paths. As a backup, a waveguide-based design has also been investigated, which would exhibit a slightly degraded instrument sensitivity (approx. 1 dB). Although this concept is considered more mature than the baseline, its performance critically depends on a waveguide circulator, which is currently not available in a space-qualified version.

The transmit channel uses an extended interaction klystron (EIK) amplifier. This tube is derived from an existing design, which is in wide use in the commercial and military sectors. Its cooling concept will be adapted to conduction mode and also cathode life will be extended. The high-power amplifier, together with its electronic power controller will be redundant, not only because of mission life, but also because of potential failure considerations.

The receiver channel consists of a redundant set of passively cooled, low-noise amplifiers (LNA). The LNA includes the mixer for down-conversion to the first intermediate frequency at 11.5 GHz.

The back-end consists of the millimetre-wave frequency generator (MMFG), shared by the transmit and receive channels and the radio frequency and processing unit (RFPU). The MMFG consists of an ultra-stable master oscillator (USO) operating at 100 MHz and the multiplier circuits for generating the local oscillator signals for the receiver and the input signal for the transmitter. The RFPU contains the up- and the down-conversion chains as well as the mode-control and data-handling units. The final signal detection is performed by digital convolution.

The pulse repetition frequency (PRF) has to be adapted to the range between the satellite and the mean geoid, which is not constant for the chosen orbit configuration. It therefore varies between 5310 Hz and 5696 Hz. It will be controlled by a look-up table residing in the CPR back-end.

It is to be noted that the CPR has to process echo signals, which are in the worst case 15 dB below the noise floor. Thus, noise subtraction has to be applied to extract useful signals. This calls for a very accurate and continuous measurement of the background noise fluctuations, performed in an interleaved fashion between acquisitions of groups of echo profiles.

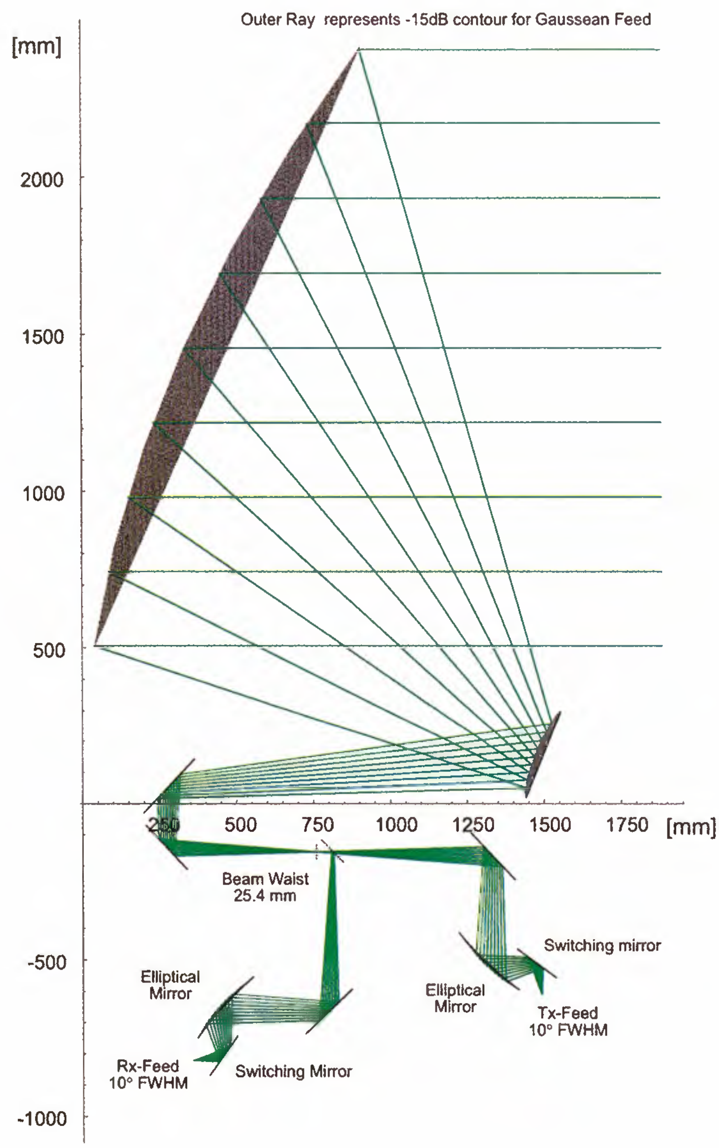

Figure 6.16. *Schematic of the quasi-optical front-end and antenna.*

A schematic layout of the internal calibration subsystem is shown in Figure 6.17. The internal calibration consists of a set of three measurements in two sequences embedded within each pulse repetition interval (PRI), except within those which are dedicated to noise measurements:

Sequence 1: The transmit pulse is measured by means of a horn antenna which is placed in the spill-over zone of the main reflector. This signal is routed through the attenuator, the T-junction (path 2-3) and the isolator and is measured by detector D1 and digitised by the ADC.

Sequence 2: A reference pulse generated at the output of the driver amplifier for the EIK is routed through the directional coupler, the PIN-switch, the isolator, the T-junction (path 1-3), the second isolator and is measured by the detector D1. At the same time, a part of this reference signal is routed to the calibration horn via the T-junction (path 1-2) and the attenuator, and is injected in the quasi-optical front-end. This injected signal is amplified by the complete receiver chain and measured by the same detector as in the case of the radar echoes.

These three measurements provide accurate estimates of the radar output power as well as of the gain of the receiver chain including the quasi-optical front-end. The remaining unknown in the radar chain is reduced to the in-orbit antenna gain pattern, which will be determined by external calibrations.

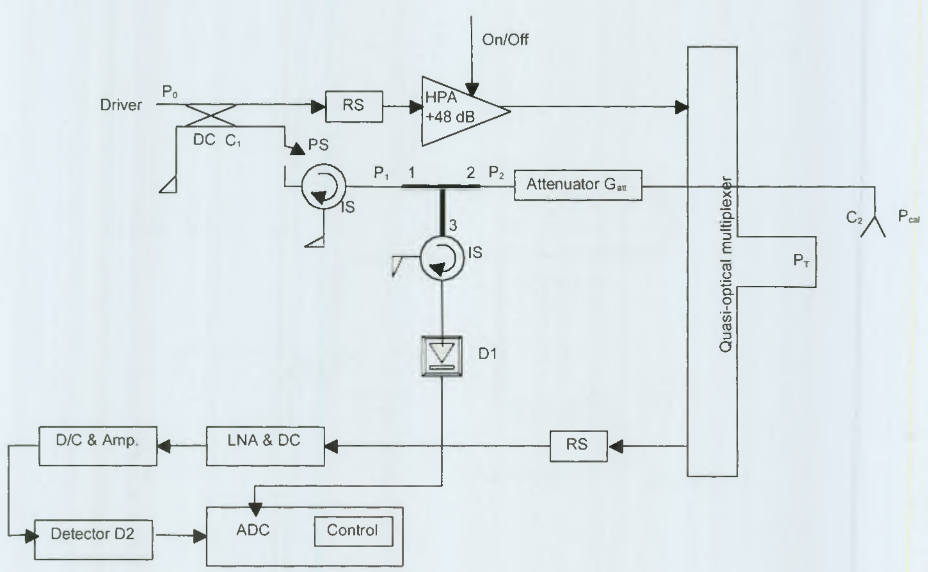

Figure 6.17. *Schematic of the internal calibration subsystem.*

The mechanical design is mainly determined by the accommodation of the antenna reflector and to a lesser extent by the accommodation requirement for the quasi-optical components. A box structure has been selected, which also houses the electronic boxes and interfaces with the ATLID support structure. The thermal dissipation of the high-power amplifier and the electric power controllers are the dominating drivers for the thermal design. These units have therefore been accommodated on the anti-Sun and zenith faces of the CPR structure to maximise the heat radiation.

Instrument Performance

Table 6.10 summarises the CPR's performance, as predicted at the end of Phase-A, measured against a rather severe cloud and atmospheric model scenario as indicated in the table and for a signal integration distance of 10 km.

The accuracy with which the altitude of cloud boundaries can be determined depends on three factors: the vertical resolution, the probability of detection for thin clouds and the altitude knowledge with which the signal samples can be positioned. In particular, the probability of detection is determined by the instrument's radiometric resolution and is worst at the bottom of the atmosphere (e.g. at 1 km). The positioning knowledge of the samples is a function of the satellite pointing and attitude-determination accuracy as well as the instrument timing accuracy. Cloud boundaries can be estimated with an accuracy of better than 197 m in the nominal and 138 m in the secondary mode.

Performance parameter	Value
Atmospheric model (clear atmosphere)	Annual Tropic: 1.21 dB total zenith attenuation (one-way) at 1 km altitude
Three-layer cloud model	0.75 km ≤ target cloud ≤ 1.25 km, $\lvert K\rvert^2$=0.6856, Im(-K)=0.1876, 4 km ≤ Alto-Stratus ≤ 4.5 km, $\lvert K\rvert^2$=0.5971, Im(-K)=0.2006 8.5 km ≤ Cirrus ≤ 9 km, $\lvert K\rvert^2$=0.1760, Im(-K)=1.46×10^{-6}
Instantaneous footprint	706 m diameter (-3 dB one-way)
Signal integration distance	10 km (for performance assessment)
Receiver noise temp.	865° K
Vertical resolution	500 m (nominal); 350 m (secondary)
Vertical positioning knowledge of samples	≤ 50 m
Noise equivalent Z	≤ -17.6 dBz (nominal); ≤ -14.5 dBz (secondary)
Minimum Z	≤ -32.3 dBz (nominal); ≤ -29.4 dBz (secondary)
Upper dynamic range	+27 dBz (nominal); +30 dBz (secondary)
Radiometric resolution	≤ 1.44 dB
Radiometric stability	≤ 0.3 dB over orbit; ≤ 0.5 dB over mission
Total radiometric accuracy	≤ 1.7 dB
Cloud-base localisation	≤ 197 m (nominal); ≤ 138 m (secondary)

Table 6.10. *CPR performance data.*

Note that the $\lvert K\rvert^2$ value of 0.6856 used for the performance estimation corresponds to the dielectric constant of water at a temperature of 0° C (the worst case for non-super-cooled water) measured at 94 GHz. A different assumption was made in Chapter 5 where a $\lvert K\rvert^2$ value of 0.93 was used to normalise the ice-cloud reflectivity factor.

The use of the latter value would increase the radar reflectivity by approximately 1.3 dB. Hence, the estimated sensitivity would improve by -1.3 dB.

For illustration, instrument sensitivity is listed in Table 6.11 for a single water-cloud layer at various altitudes: layer thickness is 500 m for the nominal and 350 m for the secondary mode. Only a 'clear' atmosphere attenuation is taken into account for this calculation. The corresponding data for atmospheric attenuation for mid-latitude summer conditions are also shown.

Altitude [km]	**Mean Annual Tropic (req.)**		**Summer Mid-Latitude**	
	Nominal (500 m) (dBz)	Secondary (350 m) (dBz)	Nominal (500 m) (dBz)	Secondary (350 m) (dBz)
0.5	-32.3	-29.5	-33.4	-30.6
1.0	-33.1	-30.3	-33.9	-31.1
2.0	-34.2	-31.4	-34.5	-31.7
4.0	-35.1	-32.3	-35.2	-32.4
6.0	-35.4	-32.6	-35.4	-32.6
8.0	-35.5	-32.7	-35.5	-32.7
12.0	-35.5	-32.7	-35.5	-32.7

Table 6.11. *Sensitivity for a single water-cloud layer of 500 m thickness (nominal mode) and 350 m thickness (secondary mode) after 10 km integration ($|K|^2$=0.6856, Im(-K)=0.1876).*

Operations

The CPR will be operated near-continuously throughout the full mission. Only short stand-by intervals will be necessary when over-flying a number of radio astronomy sites where receivers operate within the same atmospheric window. In the event of hardware malfunctions, the redundant units will be activated upon ground command to restore nominal operations. Changes between primary and secondary operation modes will be pre-programmed, the mode transition being very short.

Resource Budgets

The instrument resource budgets are given in Table 6.12. The margins are 20% for mass and 15% for power.

The instrument data rate is 30 kbps, which is based on the generation of 1 echo packet per 0.14 s, including an overhead of 10% for formatting and housekeeping.

	Mass (kg)	Power (W)
Antenna assembly	28.2	
Mechanical, thermal support	33.0	
Quasi-optical diplexer	11.5	
High power amplifier, EPC	22.5	155
LNA	0.5	0.3
Back-end electronics	17.1	81.1
Total	**112.8**	**236.4**
Total with margin	**135.4**	**271.9**

Table 6.12. *CPR mass and power budgets.*

Development Status

As far as technological or development issues are concerned, a number of areas have been identified requiring dedicated effort. These are the adaptation of the EIK to space-flight standards, detail design of the Faraday rotator for the quasi-optical diplexer, or the circulator for the waveguide option. The EIK-related activities have been started sufficiently early within ESA in order to overcome the generally long lead-time necessary for such a development. A first test EIK has been built using an improved cathode and the cathode life-test programme has been started (on-going fabrication of test diodes and automated test power supply). Regarding the quasi-optical diplexer and circulator, a first breadboard activity has just been initiated. Whilst these issues are to be considered technically challenging, their criticality is well within the limits of normal instrument development.

In other areas, technological advancements are desirable in order to increase the design margins or to improve reliability. Notable examples are the LNA based on InP technology for achieving very low noise performance, the W-band GaAs MMIC driver amplifier with sufficient output power for the EIK and the high efficiency/low mass EPC for the EIK. The relevant development activities are currently in progress.

Other units have a well-proven design maturity as they are based on designs which have a good flight record, e.g. the antenna and its deployment/hold-down mechanism. The radar up- and down-conversion chains have also been breadboarded.

6.3.4 Multi-Spectral Imager

Instrument Objectives and Operating Principle

The multi-spectral imager is designed to complement the active instruments by extending their vertical profiling data to the horizontal plane to infer three-dimensional information of the cloud and aerosol structures. There is a long history of similar instruments flying in geostationary and low Earth orbit, like the Meteosat imager, SEVIRI on MSG, (A)ATSR and the AVHRR. These instruments have been optimised for meteorological applications and thus can serve as design guidelines for the ERM imager.

In order to maintain a large degree of commonality with the fore-mentioned missions and exploit their heritage, the spectral bands have been selected to a large degree in accordance with these instruments. They are:

Band 1:	0.649-0.669 μm, visible (VIS)
Band 2:	0.855-0.875 μm, near-infrared (NIR)
Band 3:	1.58-1.64 μm, short-wave infrared (SWIR)
Band 4:	8.3-9.4 μm, thermal infrared 1 (TIR 1)
Band 5:	10.4-11.3 μm, thermal infrared 2 (TIR 2)
Band 6:	11.4-12.3 μm, thermal infrared 3 (TIR 3)

Whereas most of the previous cloud imager instruments provide a horizon-to-horizon view, the swath of the ERM multi-spectral imager has been limited, for design purposes, to a width of 100 km, which could be extended to about 300 km without major system or instrument impacts.

In the light of the constraints prevailing on the definition of the Earth Explorer Core Missions, an effort has been made to arrive at a simple instrument concept, yet one fully meeting performance requirements. Whilst existing instruments like AVHRR or (A)ATSR would have been perfectly adequate for ERM, their relatively large size would have been in conflict with a small- to medium-class mission. Moreover, these instruments were designed many years ago and thus do not incorporate new developments in instrument technology. It has therefore been found advantageous to embark on a new design concept, still making use of imager heritage where found practical.

One of the most important differences with existing instruments is the use of the push-broom principle instead of scanning. Whilst the latter may still offer better performance in the area of radiometric accuracy and pixel co-registration, the deletion of the scanning mechanism and the reduction in size of the optical aperture make a more compact design possible. In addition, the advent of new detector technologies, like bolometers for the thermal-infrared part of the spectrum, leads again to a simple design concept, as no cryogenic cooling is required.

Various concepts are possible for the implementation of the push-broom concept for a multi-spectral cloud imager. They have been studied in detail and three independent telescopes for the VIS/NIR, SWIR and TIR1/TIR2/TIR3 bands with in-field separation emerged as the baseline.

The use of the push-broom principle together with the in-field separation of some bands implies that the pixel lines, sharing the same optics, when projected onto the Earth's surface are not sampled at the same time. As a consequence, the pixels need to be co-registered by offsetting the direction of flight from the ground track to compensate the Earth's rotation (yaw steering).

The requirements on the radiometric performance imply instrument calibration at intervals commensurate with the stability of the individual channels, or rather the focal-plane detectors. The calibration frequency is expected to be very low for VNIR and SWIR, but more frequent for TIR. These calibration sequences have to take place at specific points along the orbit because of the Sun viewing geometry. The resulting data loss is small because of their short duration.

Instrument Architecture and Sub-Systems

The functional block diagram of the multi-spectral imager is shown in Figure 6.18 and the general configuration is shown in Figure 6.19.

A dioptric lens is used for the combined VIS and NIR channels (VNIR) with a focal length of 8.5 mm and an F-number of 2.5. The detector is a silicon CCD device arranged in a 384 row and two times 288 lines configuration, only one line being actually used for each channel. Band selection is performed by means of coatings on the detector windows.

The SWIR optics are very similar to the VNIR, with the same F-number, the focal length increased to 9.6 mm. An InGaAs detector array has been selected, which needs to be cooled by a thermoelectric cooler to slightly below ambient temperature.

The TIR optics are composed of four a-spherical germanium lenses with a focal length of 18.8 mm and an F-number of 1. A bolometer array with 320 by 240 pixels has been selected as detector as it can be operated at ambient temperature, though at a tightly controlled level of a few tens of mK. Although this device is commercially available, its application in a multi-spectral imager is new. The band separation will be performed by means of coatings on the window. Three groups of ten lines are used, the readings being time-delay integrated off-chip to achieve the required performance.

Calibration is performed by means of a two-point concept. One reference is used for offset, the other one for gain corrections by means of a well-defined source. The VNIR/SWIR calibration is performed by means of a solar diffuser, which is put into the light path by means of a mirror with three positions. The first one is used for the Earth view, the second for solar calibration and the third one for offset correction, for which the back of the mirror is used. TIR channel calibration is performed by means of a view to cold space and a blackbody. A three-position mirror is employed also in this concept.

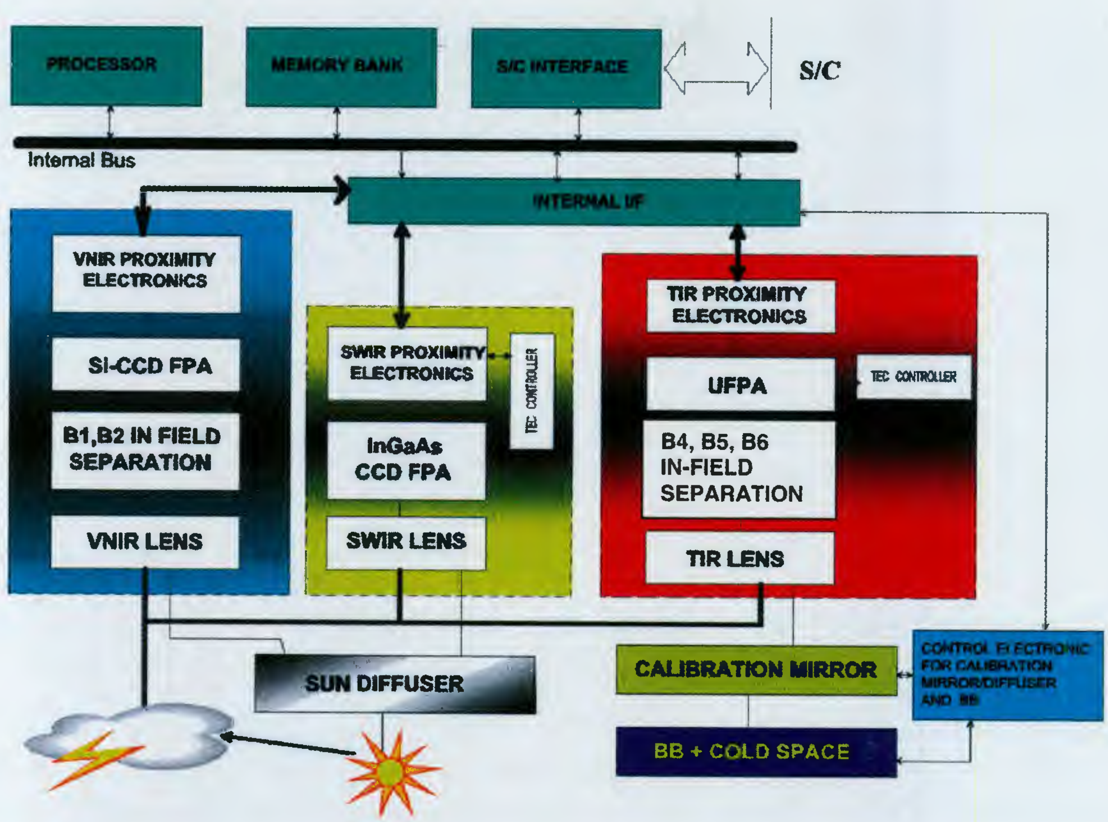

Figure 6.18. *Multi-spectral imager functional block diagram.*

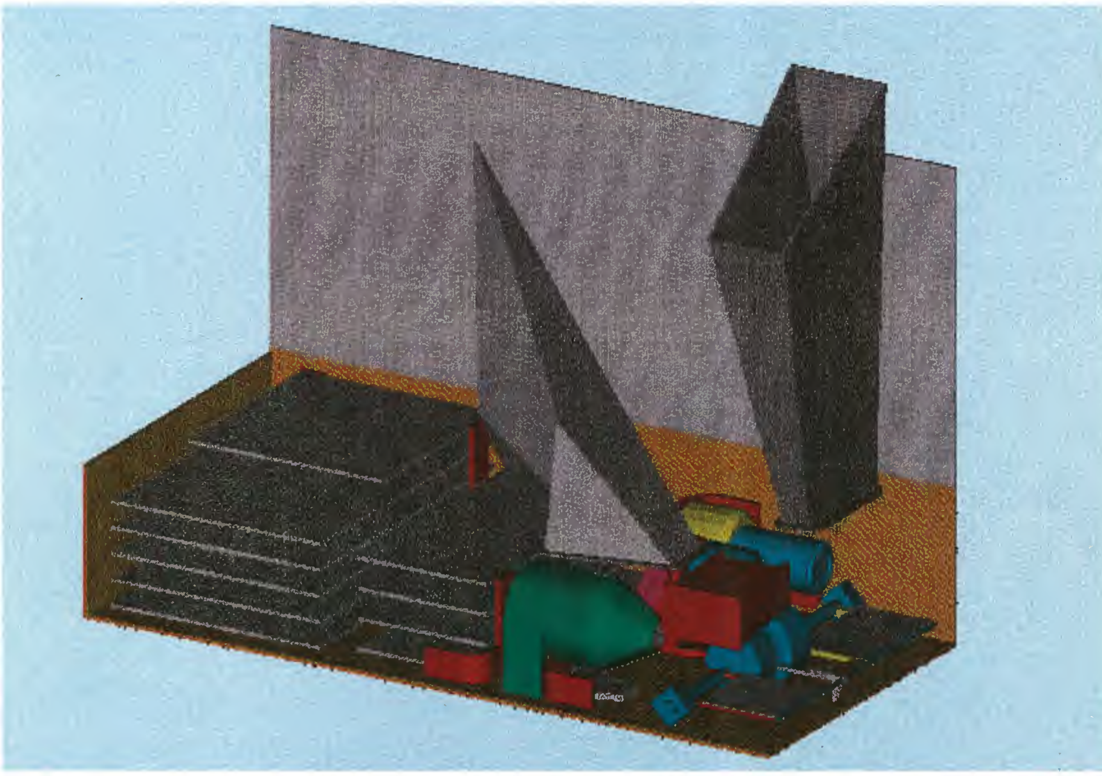

Figure 6.19. Multi-spectral imager general configuration.

The instrument electronics perform all data acquisition, formatting and distribution functions, including control of the detectors and the mechanisms. Instrument data are transmitted to the platform via the 1553 bus.

The mechanical design is dictated by the viewing requirements of the three chains, as well as the support of all hardware elements. Mechanism life is estimated to be well in excess of the actual cycles encountered during the nominal mission duration, providing good margin. The instrument is housed in a single box accommodated on the Sun face of the satellite; a 3D-view is presented in Figure 6.20.

The overall instrument thermal design is based on a purely passive concept. The thermo-electric coolers for the SWIR and TIR channels are integrated in the focal-plane assemblies. The TIR optics are de-coupled from the rest of the instrument to obtain a stable thermal environment. The instrument power is dissipated via a radiator on the Sun face and the box walls.

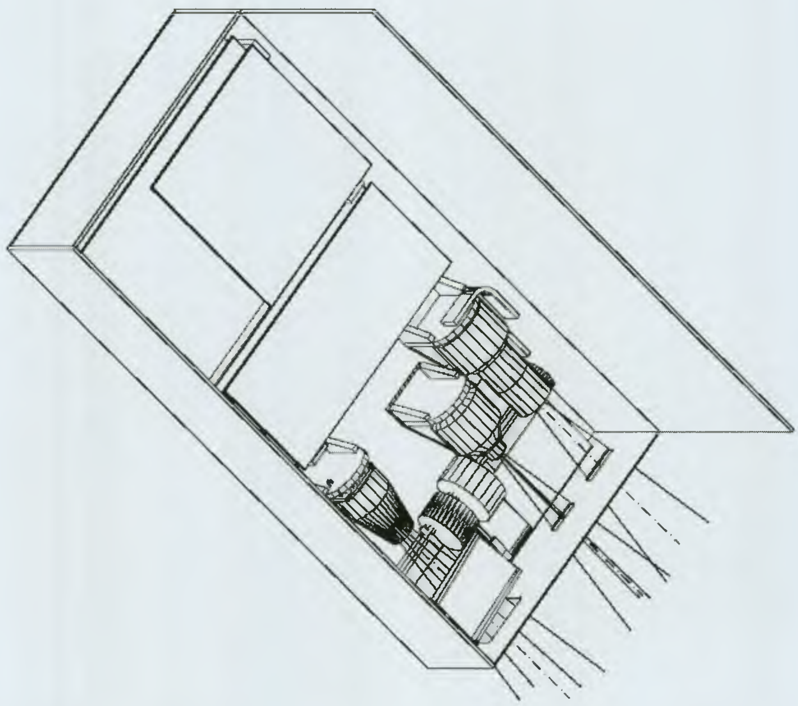

Figure 6.20. *Multi-spectral imager mechanical configuration; the dimensions are 253 mm (width), 528 mm (length) and 110 mm (height) without radiator.*

Instrument Performance

The radiometric performance has been extensively modelled on the basis of the detector characteristics and known error contributions. The results for the VNIR and the SWIR channels are listed in Table 6.13. All figures are given in terms of top of the atmosphere (TOA) reflectance. The requirement is a SNR of >200, equivalent to $NE\delta\rho = 5.10^{-3}$. The requirement on absolute accuracy, specified as <10%, is also met. The radiometric resolution includes all error sources that affect an image, like temporal and spatial noise, as well as short-term drifts.

Channel	**VIS**		**NIR**		**SWIR**	
Reflectance (max., min)	1	0.1	1	0.1	1	0.1
Radiometric resolution (10^{-3})	3.8	3.5	3.8	3.5	3.5	3.5

Table 6.13. *VNIR and SWIR radiometric resolution, in reflectance.*

The radiometric resolution of the TIR channels is given in Table 6.14. It is shown that the requirements, both for scene brightness temperatures of 300 K (0.25 K) and 200 K (0.8 K), are met.

Channel	TIR 1		TIR 2		TIR 3	
Scene brightness (K)	293	200	293	200	293	200
Radiometric resolution (K)	0.13	0.43	0.15	0.4	0.14	0.39

Table 6.14. *TIR radiometric resolution.*

Operations

The instrument acquires data continuously with short interruptions for calibration at regular intervals. These calibration sessions will be performed automatically on the basis of pre-programmed timelines.

Resource Budgets

The resource budgets are listed in Table 6.15. A margin of 20% has been applied to the mass estimate and 15% on power.

	Mass (kg)	Power (W)
Total	12.25	39
Margin	2.45	6
Total	**14.7**	**45**

Table 6.15. *Multi-spectral imager resource budget.*

The net data rate is 53 kbps for the 6-channel configuration, to which 7 kbps of housekeeping data have to be added.

Development Status

Although the instrument concept is new, the development risk appears moderate and is limited to the new elements like the bolometer arrays for the TIR channels. Although this device is in volume production, its application for the ERM imager is in fact new in that demanding radiometric performance is required. Therefore a study has been started to characterise this device, to accurately define its optimum operating conditions, in particular with respect to the temperature stability requirements, and to evaluate its performance. In addition, a development effort for specific devices has been launched by the Agency.

The bolometer detector array in its commercial version is equipped with a window, which is not suited for the in-field separation of the TIR channels. Whilst the development of such a window is not considered at all critical, its mating with the detector package will require some development effort. It should be noted that a similar device with a 10-channel window is being developed in the USA for another space mission, thereby demonstrating the basic feasibility of this approach.

The InGaAs line detector foreseen for the SWIR channel is flying currently on the French SPOT 4 mission. It has been shown that this detector is somewhat sensitive to radiation. Improved devices are in advanced development and should be available well in time for this mission.

All other elements of this instrument are considered of low development risk as they draw on a good heritage from other instruments. The chosen instrument concept presents a step forward towards the design of compact and simple imagers.

6.3.5 Broad-band Radiometer

Instrument Objectives and Operating Principle

The broad-band radiometer (BBR) is intended to provide estimates of the short-wave (SW, 0.2 to 4.0 μm) and long-wave (LW, 4 to 50 μm) flux components at the top of the atmosphere (TOA). The dynamic range is 0 to 450 $Wm^{-2}sr^{-1}$ in SW and 0 to 130 $Wm^{-2}sr^{-1}$ in LW. The radiance data have to be accurate to 1.5 $Wm^{-2}sr^{-1}$ with a resolution of 0.5 $Wm^{-2}sr^{-1}$. These figures apply to both channels and are to be understood as the rms error of the measured radiance with respect to the input radiance and the standard deviation of the measured radiance, respectively.

Calibrated measurements of the respective radiances will be performed in five pixels arranged in a cross-track swath and centred on nadir. The pixels will be scanned sequentially for all channels, including the required calibration data. Absolute instrument accuracy depends on the spectral content of the observed scenes. Such scene data will be provided by the multi-spectral imager during flight; a set of synthetic reference scenes has been defined for instrument performance assessment.

The width of the swath has been chosen to match the swath of the multi-spectral imager. The pixels have a size of 40 by 40 km^2 with some overlap so that the distance between pixel centres is 28.3 km, resulting in a swath of 113.2 km. The same overlap exists in the along-track direction. Due to the movement of the satellite, the line of pixels is not exactly perpendicular to the flight track, but slightly staggered. The pixel arrangement, as projected on the ground, is depicted in Figure 6.21.

Cross-calibration of the two measurement channels is essential, as they do not have the same spectral response in the short-wave range because of the filtering process. A cross-calibration parameter is therefore determined for each pixel by measuring the filtered response of both channels.

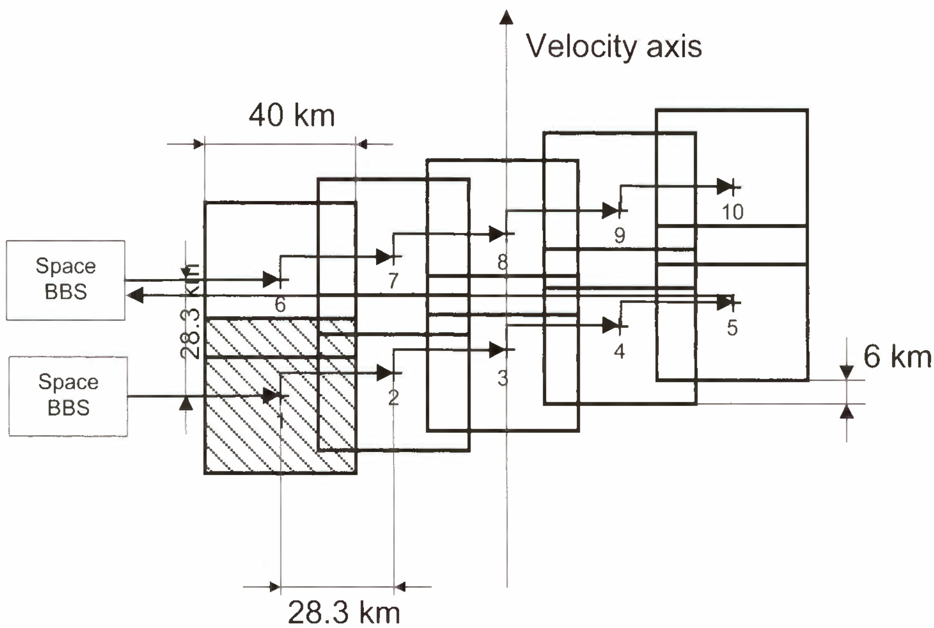

Figure 6.21. *BBR pixel and swath geometry.*

The measurement of the LW channel is performed by measuring the total spectrum and subtracting from it the output of the SW channel. Both channels share the pupil of the telescope, the spectral response of the short-wave channel being defined by a silica filter. The filtered and unfiltered scene sightings are performed by a wheel carrying silica filters and an open aperture for the total channel. This wheel rotates at a constant speed around the same axis as the telescope. The telescope oscillates over a range of -77.4 degrees and +41.4 degrees with respect to nadir for scene observation and also covers the internal calibration sources.

A pyroelectric detector has been selected because of its wide spectral response and high bandwidth. The necessary chopping function is performed by the closed spaces on the filter wheel.

Figures 6.22 and 6.23 show the arrangement of the telescope and the filter wheel.

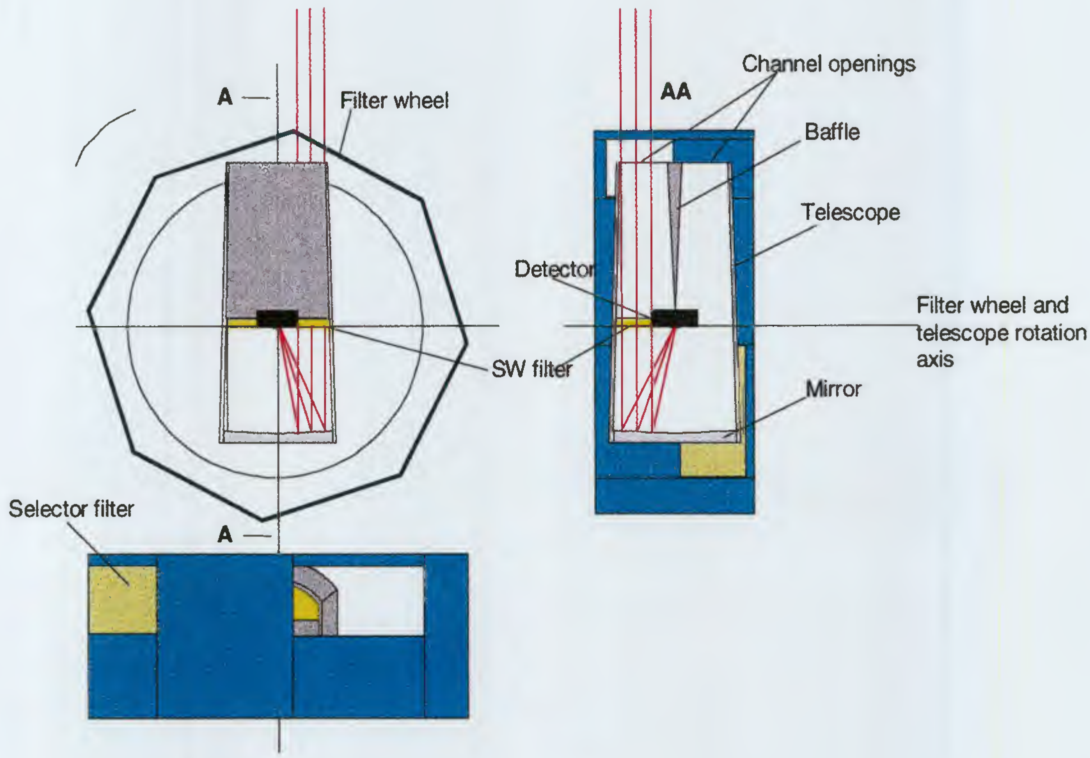

Figure 6.22. *BBR channel selection and telescope arrangement.*

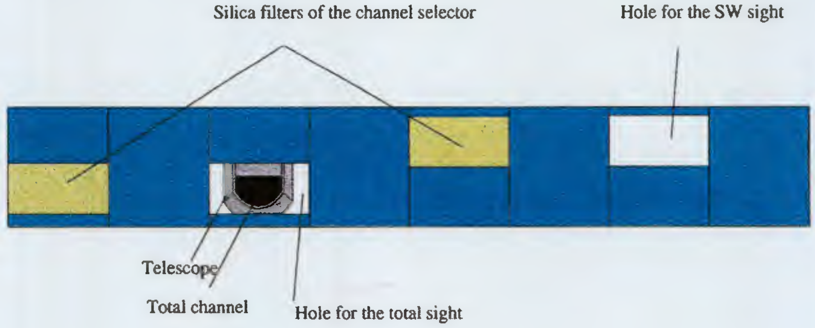

Figure 6.23. *Filter wheel, projected view.*

Instrument Architecture and Systems

The general configuration is shown in Figure 6.24.

The BBR consists of two modules, the optical head and the electronics unit. The optical head comprises the telescope with the detector, the filter wheel, the scanning mechanism, the blackbody simulator, the solar calibration device and the support structure. A cross-section of the optical head is shown in Figure 6.25.

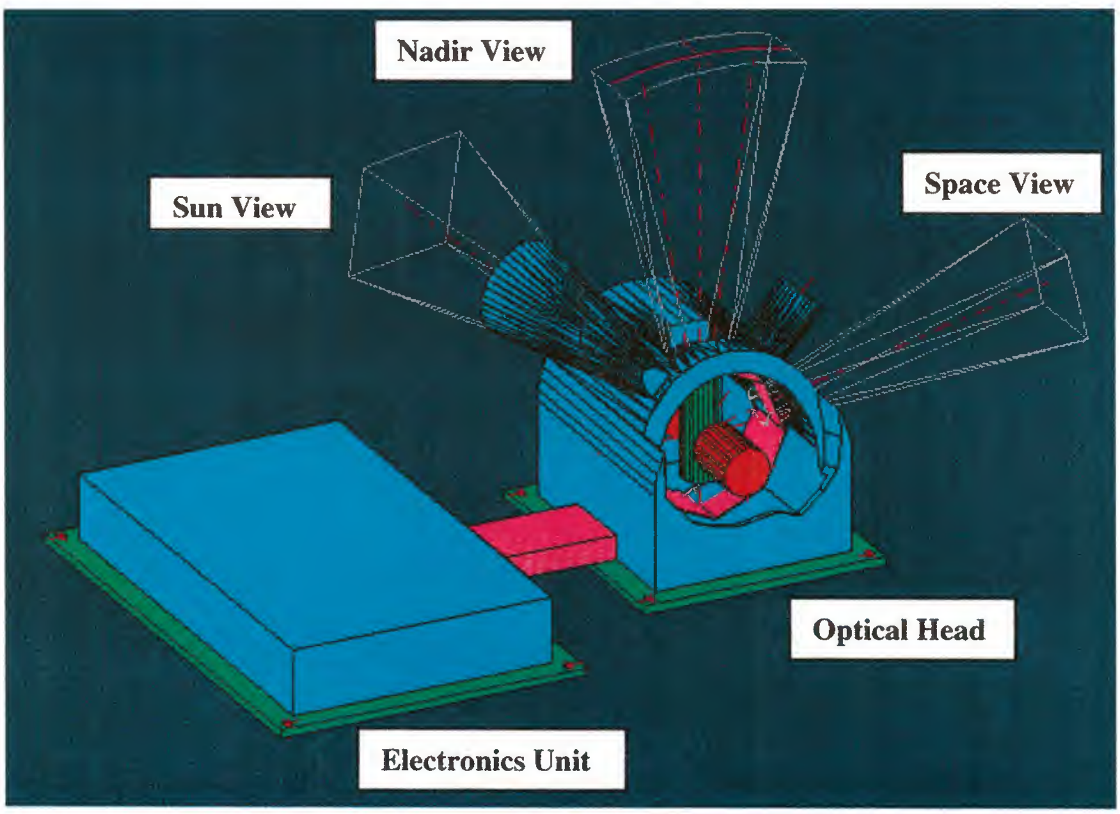

Figure 6.24. *BBR general configuration.*

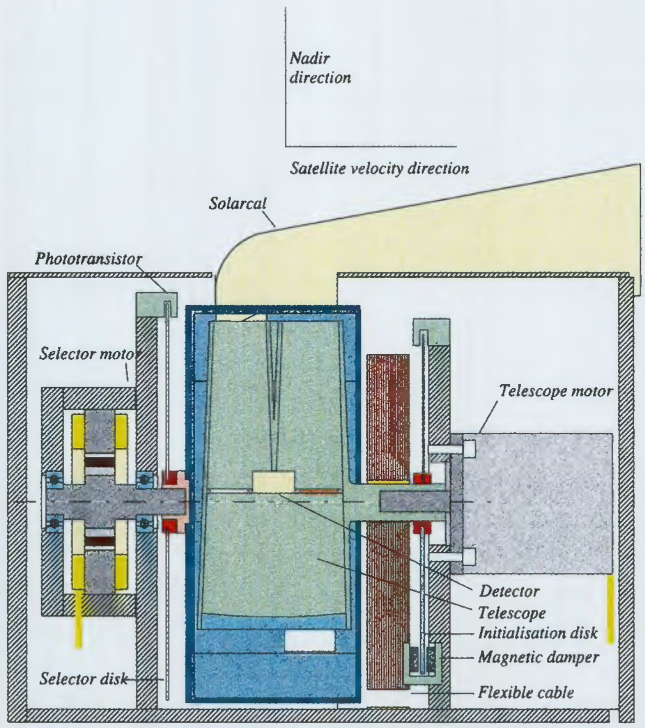

Figure 6.25. *BBR optical head, cross-section.*

The telescope consists of a single aluminium parabolic mirror of 30 mm diameter with an aluminium coating to ensure a good spectral response. The silica filter for the separation of the SW is located within the telescope; it carries a small wedge for the compensation of satellite motion and to improve channel registration. The pyroelectric detector, made of lithium tantalate, is located behind a field stop. The chosen geometry and material ensure good stability and signal-to-noise ratio. The detector is connected to the detection electronics via a flexible cable.

The scanning mechanism consists of two parts, the drive of the filter using a brushless motor and the telescope drive with flexible pivots actuated by a stepper motor. Both drives, operating at different speeds, are synchronised electronically by means of optical encoders.

The channel selector carrying the silica filters, in the shape of an octagon, revolves around the telescope at a constant speed. Aluminium has been chosen as manufacturing material in order to save mass and to minimise inertia. The selector is supported by a steel shaft running in two ball bearings lubricated by MoS_2.

Two instrument internal calibration devices form part of the design: a blackbody simulator (BBS) for the calibration of the system gain and a solar calibration device to determine slow drifts of the SW channel. Whilst the BBS is scanned at each cycle of the telescope, the solar calibration is only used eight times per year, by means of the viewing geometry of the device itself and the orbit. A view to deep space is provided to determine the detector offset. The viewing geometry of the calibration sources and the scene is shown in Figure 6.26.

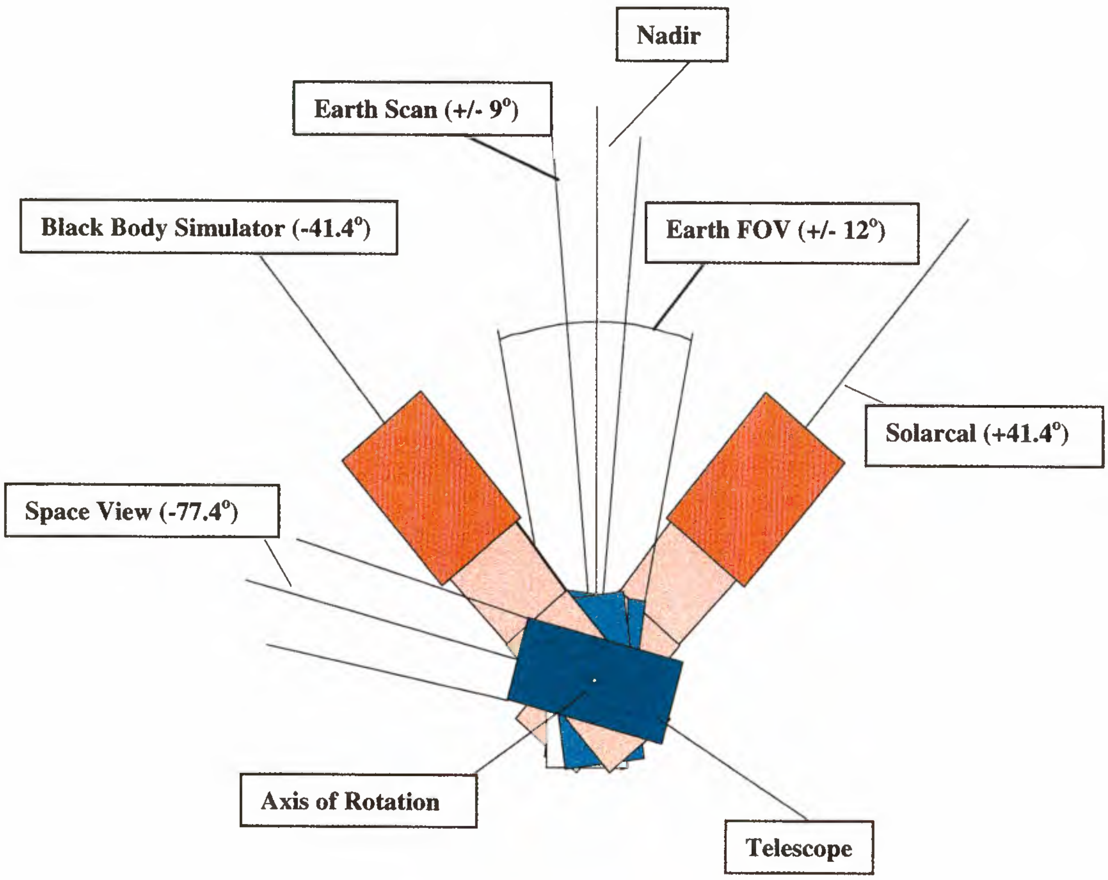

Figure 6.26. *BBR viewing geometry.*

The instrument electronics, housed in a separate module, comprise all analogue and digital signal processing, including the control of the two mechanism drive motors, the power supply and the data interface to the platform.

Instrument Performance

Analytical models have been developed, which simulate all instrument performance parameters, i.e. instrument geometry and radiometry. Because of the rather large pixel size, the geometry requirements are not very demanding. Consequently, they are readily met and actual performance is therefore not reported here.

The spectral contents of the observed scenes having a significant impact on the radiometric response, a set of 9 typical scenes has been specified with their spectral content. Transformation of the measured radiance, as filtered by the instrument, into unfiltered input radiance requires knowledge of the spectral response of the instrument and of the spectral profile of the scene. The latter information can be derived from the multi-spectral imager. Therefore performance has been estimated for three scene knowledge scenarios, i.e. no knowledge of the scene (case 1), perfect knowledge of the scene (case 2) and approximate knowledge of the scene, where a relative error of 5% in spectral content has been added (case 3). The results are listed in Table 6.16 for the SW channel profile.

Scene	Bare soil, clear sky, 15°	Bare soil, clear sky, 60°	Ocean, clear sky, 15°	Ocean, clear sky, 60°	Vegetation, clear sky, 15°	Vegetation, clear sky, 60°	Snow, clear sky, 60°	Cloud over ocean, 15°	Cloud over ocean, 60°
Scene ($W/m^2/sr$)	164.20	85.00	3.52	1.82	36.82	19.06	71.58	166.66	86.27
Error ($W/m^2/sr$) Case 1	2.38	1.28	0.20	0.15	0.50	0.31	0.57	1.98	1.08
Error ($W/m^2/sr$) Case 2	1.02	0.58	0.13	0.12	0.31	0.21	0.512	1.04	0.59
Error ($W/m^2/sr$) Case 3	1.03	0.59	0.13	0.12	0.31	0.31	0.51	1.04	0.59

Table 6.16. *SW absolute radiance error.*

It is seen that estimation of the scene spectral content (case 3) yields a result which is very close to the perfect knowledge, while ignoring this contribution would increase the error by a factor of more than two. The performance requirement of 1.5 $Wm^{-2}sr^{-1}$ is thus met by a reasonable margin for the worst case (bare soil, clear sky, 15^0) if case 3 is used as the baseline.

Instrument noise errors have been estimated at about 0.04 $Wm^{-2}sr^{-1}$, which comfortably meets the requirement of 0.5 $Wm^{-2}sr^{-1}$. In the LW channel, performance is almost independent of the scene SW spectrum. Absolute accuracy has been estimated at 0.46 $Wm^{-2}sr^{-1}$ and resolution at 0.04 $Wm^{-2}sr^{-1}$.

The instrument performance requirements are thus met by a good margin, reflecting the approach to calibration and the inherent simplicity of the instrument concept.

Operations

The BBR will be operated continuously during the mission. A set of operation modes has been defined covering all states from switch-off to signal acquisition, including calibration. The modes are stored internally and are executed upon platform commands, which are initiated in turn on the basis of pre-defined sequences up-linked from the ground. It should be noted that the nominal calibrations will not interrupt data acquisition as they are part of the scanning sequence.

Resource Budgets

The BBR resource budgets are shown in Table 6.17 with the same definition as for the other instruments regarding the margins. The data rate is 3 kbps, including overheads.

	Mass (kg)	**Power (W)**
Total	6	20
Margin	1.2	3
Total	**7.2**	**23**

Table 6.17. *BBR resource requirements.*

Development Status

The design of the BBR is based on the SCARAB instrument as flown on the Meteor and RESURS missions. Further refinements have been introduced in the course of the Envisat study and as a result of the development work on national and ESA programmes. A follow-on instrument is under study by CNES for the TROPIQUES mission.

Traditionally, some concern exists with respect to the use of mechanisms that are considered life-limiting items. However, the ERM design is not as demanding in terms of cycle life as SCARAB because of the lower number of revolutions and the shorter mission lifetime. Preliminary assessments have shown an expected service life in excess of ten years.

Limited redundancy has been foreseen in the design of the instrument. Only some parts of the mechanism are redundant in order to reduce complexity and cost. Subject to further analysis, the flexible cable could be made redundant, which appears readily feasible at this stage.

On the basis of its design heritage and the inherent simplicity of its design, the BBR can be considered a mature instrument.

6.4 ERM Satellite

6.4.1 Satellite Configuration

The chosen satellite configuration, as depicted in Figure 6.27, is the result of trade-offs between instrument accommodation and launch-vehicle payload volume. As for any other satellite, the configuration should be as compact as possible in order to make efficient use of the available volume, whilst at the same time satisfying the instrument accommodation requirements. It is for this reason that the classical concept of separating payload and platform functions into distinct modules has been abandoned in favour of a more volume-efficient solution. In the absence of a classical payload module, the structural design concepts for the active instruments, which by virtue of their mass and volume drive the configuration, have been adapted accordingly. The ATLID structure includes the load paths between the service module and the CPR, thereby minimising overall satellite mass and complexity.

It is the size of the CPR antenna and the viewing geometry that determine the accommodation of this instrument on top of the satellite, with ATLID forming the interface to the service module. The passive instruments, although smaller in size and less demanding, have to meet viewing requirements, both for nadir-looking and Sun/space calibration, which have to meet stringent constraints.

The design of the platform, housing all of the support functions, is derived from concepts well proven on other satellite projects. In principle, existing designs or even hardware should be reused to the maximum extent possible. However, it was found more convenient to adapt this concept, in that only the structural design concept and (where practical) subsystems are reused. Its overall configuration has been optimised to serve as an interface to the launch vehicle and offer sufficient volume and mounting area for subsystem accommodation.

The solar array, a rather classical two-wing configuration, is derived from an existing communication satellite project. Its accommodation is determined by the need for minimising viewing obstructions of the ATLID radiators and to a minor extent also those of the CPR. The orbit node crossing time of 1300 hrs allows an uncanted design to be used; the resulting small cosine loss in electrical power output is acceptable.

It should be noted that BBR and imager are accommodated on the platform in order to simplify the mechanical interfaces and satisfy the relevant field-of-view requirements.

The ERM launch configuration is shown in Figure 6.28. It can be seen that the available height in the cylindrical part of the fairing, as well the cross-section, are fully used. Launch vehicles with bigger fairings would offer some growth potential for the CPR antenna and thus instrument performance. ERM is compatible with Rockot with respect to mass and payload volume.

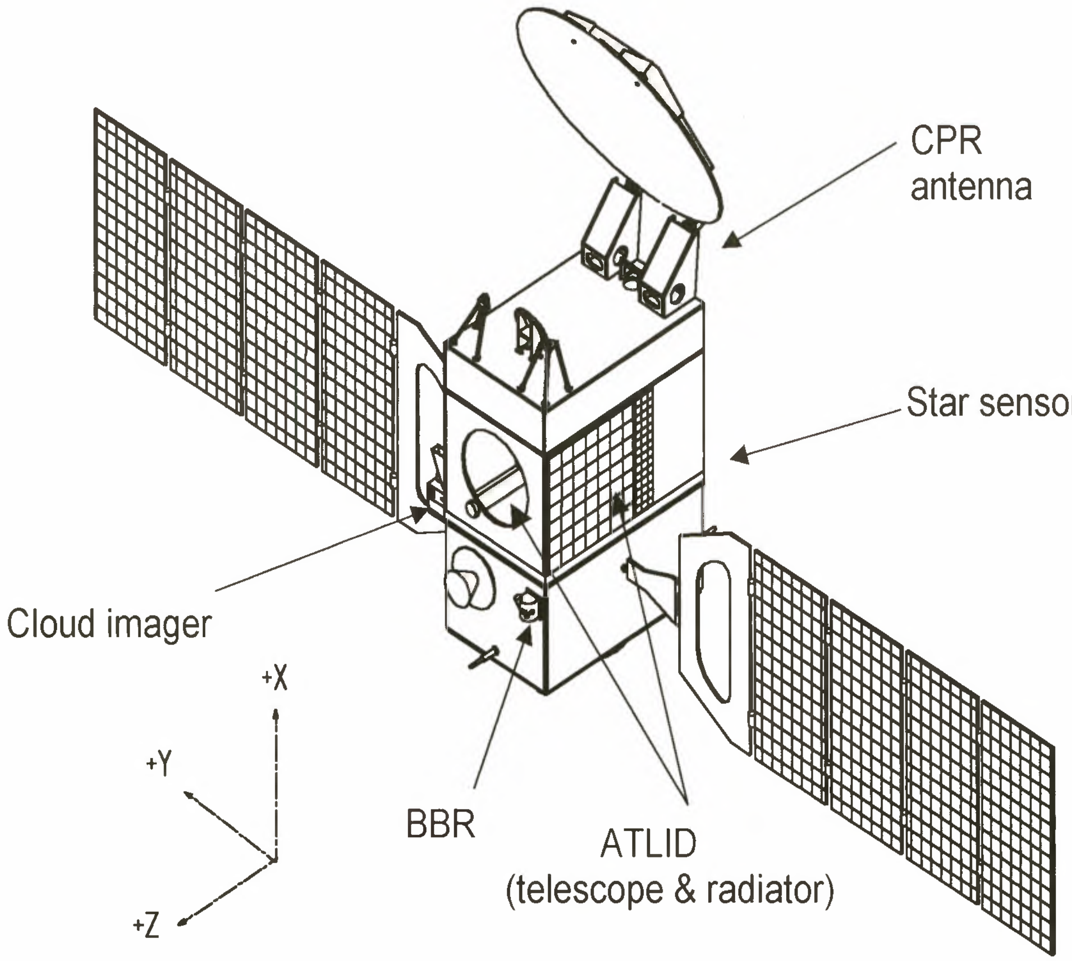

Figure 6.27. *ERM satellite configuration; the satellite axes are defined as flight (+X), Sun (+Y) and nadir (+Z).*

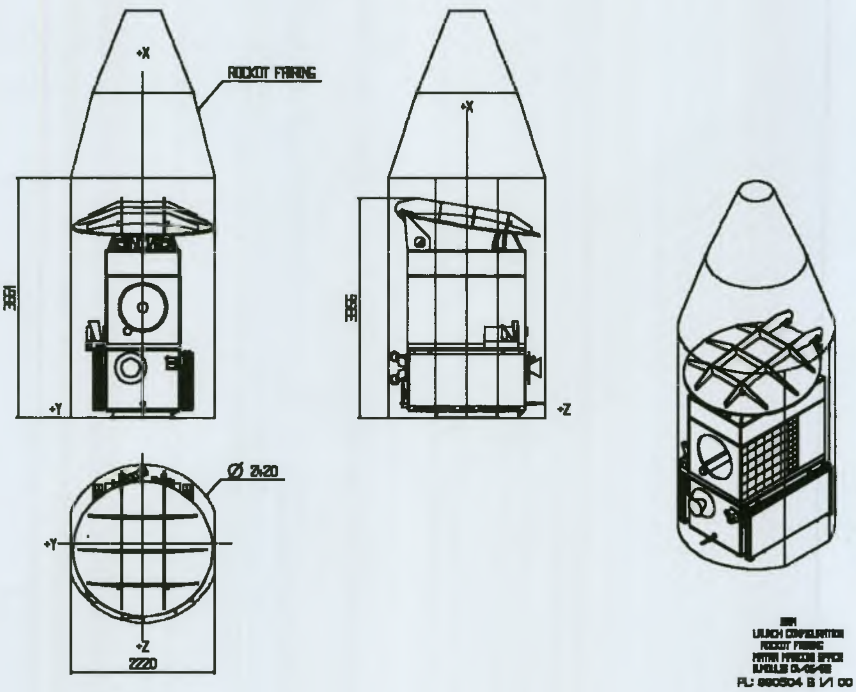

Figure 6.28. *ERM launch configuration.*

6.4.2 Satellite Architecture

The functional architecture of the ERM satellite is illustrated by the block diagram in Figure 6.29.

Data management is centralised in a single computer, which performs all instrument and platform processing functions. Low-rate instrument data are acquired via a MIL1553 bus from the CPR, the multi-spectral imager and the BBR, while the high-speed data generated by ATLID are acquired via a dedicated serial interface. Command and control data are transmitted via the MIL1553 bus as well. All attitude and orbit control processing functions are resident in the central computer, the data being transmitted via a mixture of digital and analogue lines. All science and housekeeping data are stored in a solid-state mass memory, housed in the same box as the computer and transmitted to ground via an X-band link. Housekeeping data are in addition down-linked via an S-band transponder. The power system consists of a two-wing solar-array, with a single NiH_2 battery.

The attitude and orbit control system uses reaction wheels and magnetorquers for the generation of the required control torques with inputs from star sensors, Sun sensors, gyros and magnetometers. A GPS receiver is used for navigation and the generation of precision timing signals. Orbit control is performed by a hydrazine propulsion system, which is not used for attitude-control purposes.

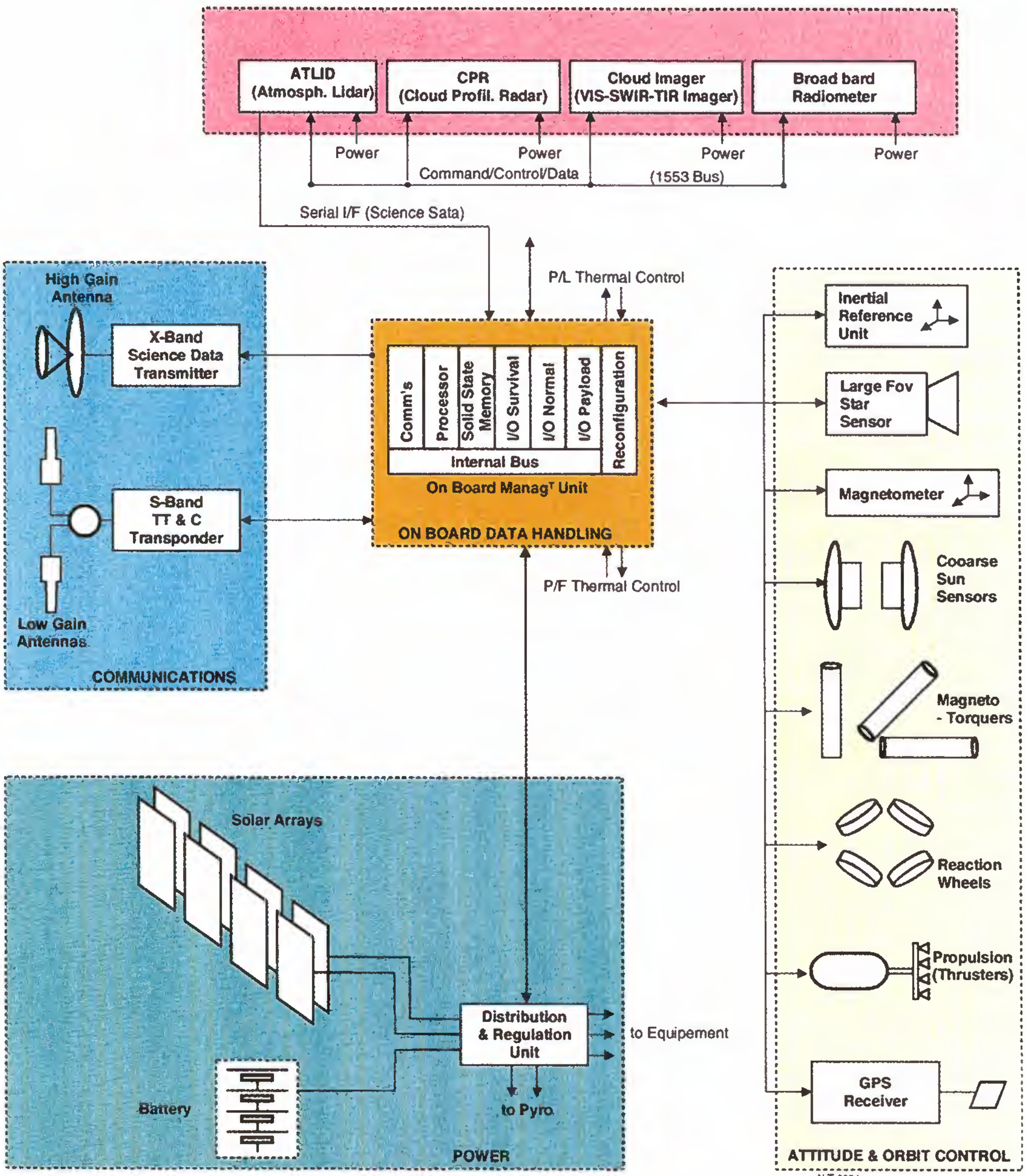

Figure 6.29. *ERM functional block diagram.*

6.4.3 Satellite Subsystems

Data Management

A centralised architecture has been selected, whereby all data acquisition, processing, storage and distribution functions are centralised in a single computer supported by the necessary input/output functions. This applies not only to the instrument data, but also to the attitude, power, communication and thermal-control subsystems. The relevant elements of the data management subsystem are redundant in order to eliminate single-point failures. A standard MIL1553 bus has been selected for data communication with the instruments, both for data acquisition, housekeeping and commanding. As the bandwidth of this bus concept is not adequate for the ATLID data rate (400 kbps), a dedicated serial line is necessary, the standard bus still being used for command and control functions. This data bus concept has been applied in many of the avionics units foreseen for ERM, thereby optimising the interfaces.

As the processor of the data management subsystem on which ERM is based has become obsolete, an ERC32 processor will be used instead, the performance of which should be more than adequate. Also the internal serial data bus structure will be replaced by the more powerful VME concept, which is in widespread commercial use.

Nominal data storage requirements call for a mass memory capacity of 25 Gbit to ensure full data coverage including the blind orbits. This capacity has to be increased by some 30% to allow for memory degradation in the course of the mission. Data formatting and encoding will performed to the CCSDS standard to ensure compatibility with the existing communications infrastructure.

The onboard software has a layered structure and is based on the VxWorks ERC32SC kernel. The application and general services layers are mission-specific and will be developed with C or ADA. All software will be stored in an EPROM and transferred to the RAM upon switch-on, which allows in-flight software updates to be readily implemented.

Attitude and Orbit Control Subsystem

The general architecture of the Attitude and Orbit Control Subsystem is shown in Figure 6.30.

Satellite attitude is estimated by a wide-field star sensor, supported by fibre-optic gyros for blind periods and to improve short-term stability. This function is performed during LEOP and SAFE mode by a magnetic field sensor and the tachometers of the reaction wheels in eclipse; the coarse Sun sensors will be used in sunlight. Satellite pointing is controlled by reaction wheels (0.2 Nm and 15 Nms) in a tetrahydral configuration. Momentum off-loading will be handled by a set of magnetorquers with a magnetic moment of 180 Am^2.

A GPS receiver will be used for satellite navigation to generate position, velocity and time inputs for the onboard orbit propagator. The precision time signal is also used in the data management subsystem.

Orbit control exploits a hydrazine propulsion system. The tank, reused from the XMM project (with a capacity of some 130 kg), is somewhat oversized for the ERM application, but allows extra propellant to be carried, if the mass margin at launch should allow this. A set of four 1 N thrusters, arranged in a circle around the velocity axis, two of which are redundant, is used for orbit control.

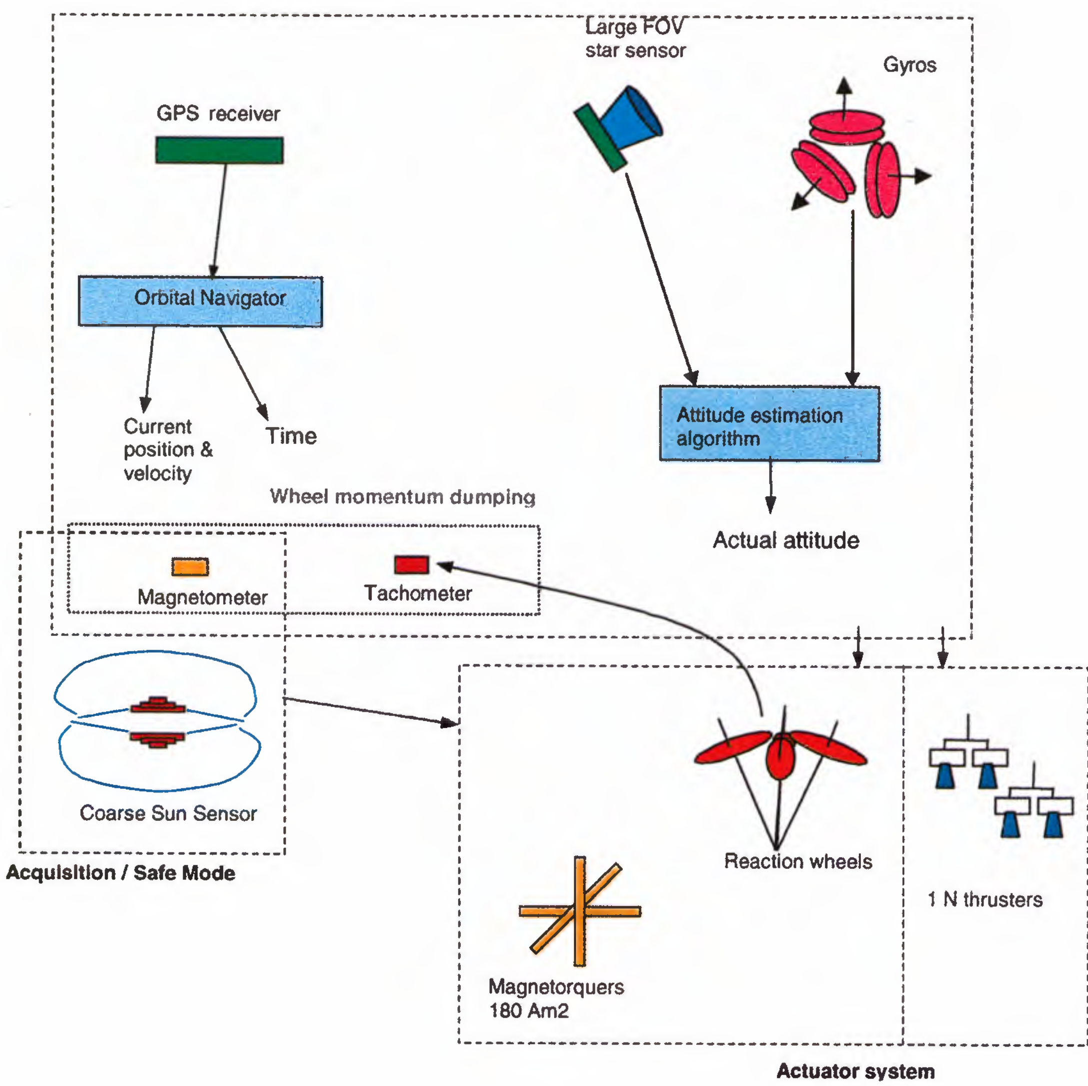

Figure 6.30. Attitude and orbit control subsystem architecture.

Electrical Power Subsystem

The design of the electrical power subsystem is driven by the requirement for supplying steady-state loads of some 870 W during eclipse and sunlight. In addition, the battery needs to be recharged, leading to a solar-array power level of about 1900 W. Whilst reuse of the Globalstar array has been baselined for the mechanical design, a change from Si to GaAs solar cells is necessary in order to satisfy the power requirements. An unregulated power-bus topology has been selected, with a single 24 cell 50 Ah NiH_2 battery. Bus regulation (and thus also battery management) will be performed by static switches on the solar-array sections commanded by the onboard computer (OBC).

Communication Subsystem

The communication subsystem consists of two parts, the X-band link for the transmission of stored science and housekeeping data, and the S-band transponder for the transmission of housekeeping data only, for telecommanding and also supporting ranging functions as back-up to the GPS-derived orbit determination.

The design of the X-band transmitter is driven by the data rate of 20 Mbps, which is necessary for the transmission of all data collected. This scenario assumes that only six passes per day can be used, with a total time of 40 minutes. A solid-state transmitter with an output power of 8 W is envisaged, in a cold redundant configuration with dedicated QPSK modulators. Data are Reed-Solomon (RS) encoded in order to improve the link budget. The design of the shaped gain antenna will be adapted from ongoing projects.

The S-band transponder is redundant for the up- and down-links, a 3dB hybrid providing the coupling to the two hemispherical antennas for omni-directional coverage.

Structure Subsystem

The satellite consists essentially of three separate modules (platform, ATLID, CPR), which need to be integrated and interfaced with the launch vehicle. These modules are to a large degree independent, but the stiffness of the assembly as a whole must be compatible with the launch-vehicle dynamic and static requirements. The ATLID and CPR structural design concepts having been described in the relevant sections already, only the design of the service module will be considered here.

A central cone structure has emerged as the most favourable design solution, as it avoids introducing running loads into the launch-vehicle interface and large concentrated loads into sandwich-panel structure elements. Aluminium sandwich panels are used for the accommodation of the various units; they also serve as the interface to the ATLID support structure. The structural concept is outlined in Figure 6.31, which also shows the accommodation of the single propellant tank.

A preliminary dynamic analysis has been performed for the ERM satellite in launch configuration, which has confirmed adequate margins for the natural frequency requirements. Also, design acceleration requirements have been derived from this analysis. A distortion analysis, as a basis for the alignment analysis, has yielded very low values.

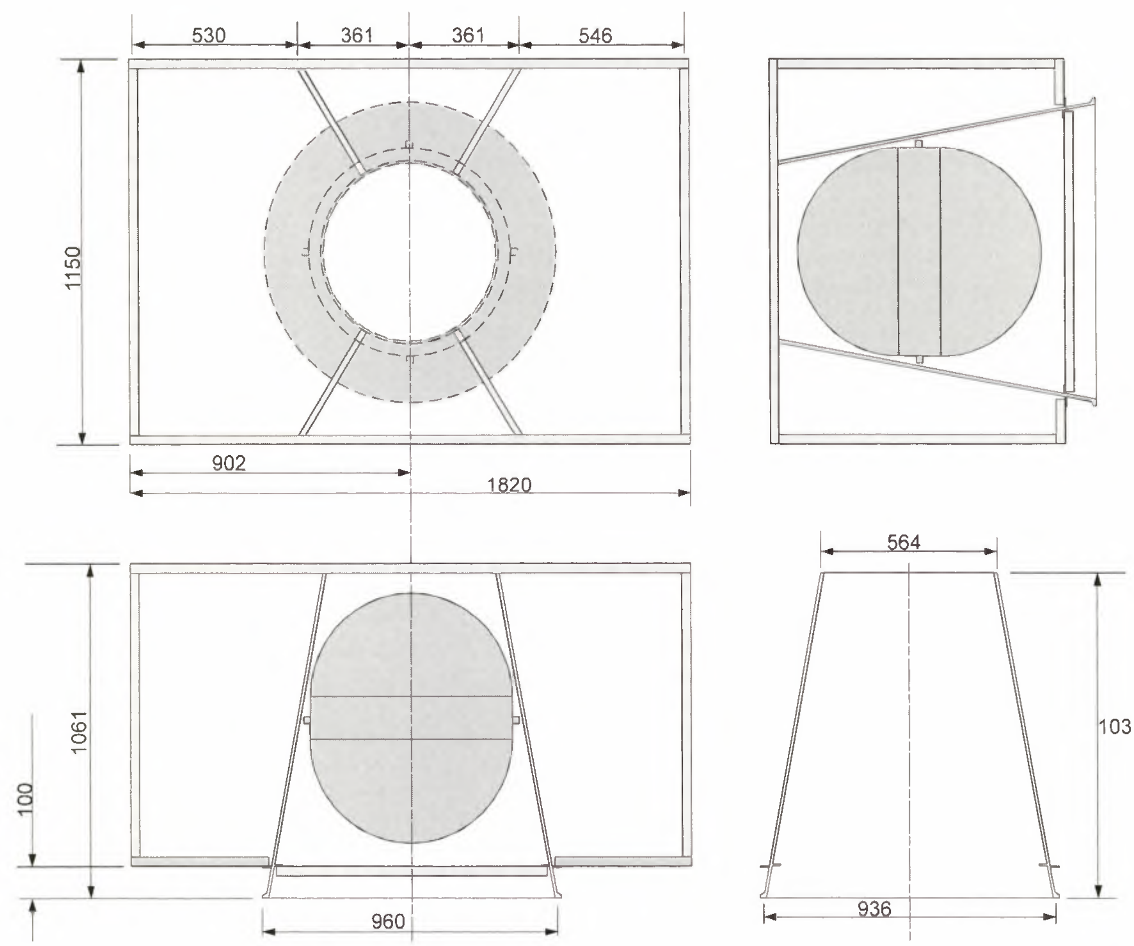

***Figure 6.31**. ERM platform structure concept.*

Thermal Control Subsystem

The instruments have their own independent thermal control, drawing heater power from the platform as necessary. Classical passive design methods are adequate for the platform in the light of the rather undemanding requirements. The design is based on the use of heaters, with external and internal radiators where necessary. A preliminary thermal analysis, using the ESATAN and ESARAD codes, has shown that all temperatures will be between 0 ^{0}C and 25 ^{0}C. Assuming an orbital variation of $\pm$ 5 ^{0}C, the overall temperature range will thus be between -5 ^{0}C and + 30 ^{0}C.

6.4.4 Budgets

In this Section both satellite performance and resource budgets will be covered. Most of the performance data have been derived from an interpretation of the observation requirements as set forth in Chapter 4. Engineering assumptions have been made where exact performance requirements were not available; their derivation will be explained in the text. In other cases engineering requirements emerged as a result of the selection of a particular design concept, the push-broom principle adopted for the multi-spectral imager being a notable example.

Geo-location, Pointing and Co-Registration

Whilst the data reported below are the result of the combination of several error contributions, only the end results will be given. All individual error contributions are again subject to variations due to their design and the operation in orbit. Typical examples are constant errors, harmonics resulting from the effects of the orbital period and noise. The resultant errors depend on the nature of the contributions, e.g. quadratic for independent random errors and summation for the harmonics.

The geo-location requirement has been set at 2 km rms and applies to the reconstitution of the nadir point. It includes the effects of satellite pointing, navigation, instrument alignment and timing.

Parameter	Requirement	Design
Geo-location	2000 m	599 m

The pointing requirement has been set at 2.5 mrad (2-sigma), which is equivalent to a pointing error of about 1000 m at nadir and applies to the lidar telescope's line-of-sight.

Parameter	Requirement	Design
Pointing	2.5 mrad	1.45 mrad

The instrument co-registration requirements have been derived from the observation requirements. Mission simulations have shown that for lidar-radar footprint separations of 500m, the retrieval algorithms already show some degradation. This value has been decreased to 400 m for the sake of a conservative design. The same value has been specified for the nadir pixel of the multi-spectral imager. The BBR contribution has been neglected, because of the much larger pixel size.

Parameter	Requirement	Design
Co-registration, Lidar – radar	400 m	340 m
Co-registration, lidar – imager	400 m	340 m

Delta-V and Propellant

The budget contributions for the orbital velocity correction and plane change after launch are listed in Table 6.18. So far no margins have been added; they will be taken up by the available volume of the propellant tank (130 kg) and the system mass margin.

	Delta-V (m/s)	**Propellant (kg)**
Inclination correction ($\pm$ 0.03 ^{0})	4	2
Initial altitude correction ($\pm$1% of nom. altitude)	2.3	1
Orbit maintenance	211	106
Total	**217**	**109**

***Table 6.18**: Delta-V and propellant budgets.*

Resource Budgets

The data in Table 6.19 are the 'current' estimates, i.e. the 'basic' estimates increased by the applicable margins (20% on mass, 15% on power) as shown in the relevant instrument and subsystem sections. An additional system margin of 10% has been added to the total satellite power, which is the basis for solar-array sizing. The system mass margin is given by the difference between the satellite total mass and the launch vehicle mass-to-orbit capability. This margin of 172 kg is equivalent to some 18%.

Whilst the difference between the 'basic' and 'current' mass figures is intended to cover instrument and subsystem design evolution in the course of the detailed design process, the system margin is held for changes to the system concept. A part of it may be used to increase the propellant supply to the maximum as given by the tank volume, providing more flexibility for orbit control and a potential extension of satellite lifetime.

No margins have been added to the data rate; the Reed-Solomon coding overhead will be included in the sizing of the data recorder and the communication links.

	Mass (kg)	Power (W)	Data (kbps)
Payload	384	558	493
Lidar	226	217	400
Radar	136	273	30
Multi-spectral imager	15	45	60
Broad-band radiometer	7	23	3
Platform	420	231	7
Structure, Thermal	121	23	
AOCS, RCS	78	68	
OBDH	36	74	
Communications	23	22	
Power, Harness	162	44	
Satellite dry mass	804		
Propellant	109		
Satellite total	**913**	**789**	**500**
Rockot mass-to-orbit	1085		
System margin	172	79	
Satellite bus power		**868**	

Table 6.19. *Satellite resource budgets.*

6.5 Launcher

The key criteria in the selection of the launcher have been the maturity expected in the 2005-2006 time frame, performance for a 1000 kg satellite to be placed in a 400 km Sun-synchronous orbit, fairing volume (2-2.5 m diameter is desired to accommodate the CPR antenna) and the cost. Several candidate launchers have been reviewed, which are listed in Table 6.20. Rockot, with its Breeze upper stage, has been selected as the reference launcher, with Athena-2 and PSLV as alternatives. The upgraded version of NASDA's J1 vehicle has also been considered in view of a co-operation scenario with ATMOS-B1. Several low-cost launch vehicles are under development now, like Kistler and Roton. Their use for ERM will be reviewed in the light of their early flight histories.

	Mass at 400 km SSO, kg	Fairing diameter, mm	Country	Cost approx. MUSD	Status
Rockot	1085	2420	Russia	12-14	Demo. flights in 1999
Athena-2	1200	**1980 (2700 mm planned)**	USA	25	**In service (recent failure)**
PSLV	1320	2900	India	25	In service
J-1 Upgraded	1300	2580	Japan	25	2003

Table 6.20. *ERM launch vehicle candidates.*

The typical Rockot launch profile is shown in Figure 6.32. After lift-off from Plesetsk and separation of the first stage, the fairing is jettisoned at around 120 km. The Breeze engine is started after separation of the second stage. Following a Hohmann transfer and simultaneous corrections of altitude and inclination at node crossing, the ERM satellite is delivered into its orbit less than 6000 s after take off.

The advertised Rockot performance regarding altitude, inclination and payload roll rate does not require propellant to be set aside for injection-error correction manoeuvres. In addition, a rather simple and energy efficient strategy for LEOP is feasible.

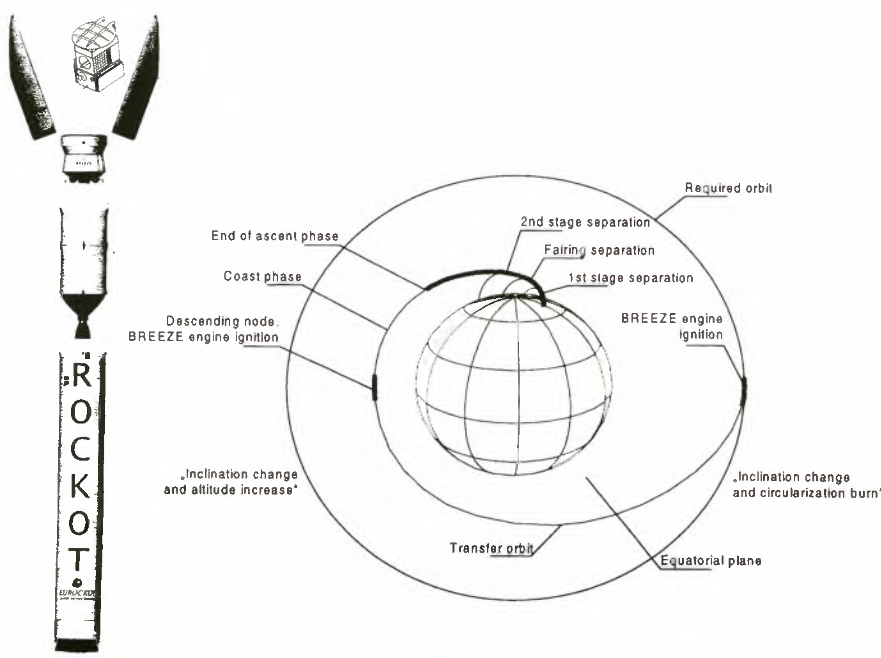

Figure 6.32. *The Rockot-ERM composite and the launch profile. Rockot is a three-stage, all liquid booster. The ERM satellite makes maximum use of the volume available under the fairing.*

6.6 Ground Segment

The ERM ground segment consists of three functional elements, as shown in Figure 6.33. The Command and Data Acquisition Element (CDAE), the Mission and Satellite Control Element (MSCE), and the Processing and Archiving Element (PAE).

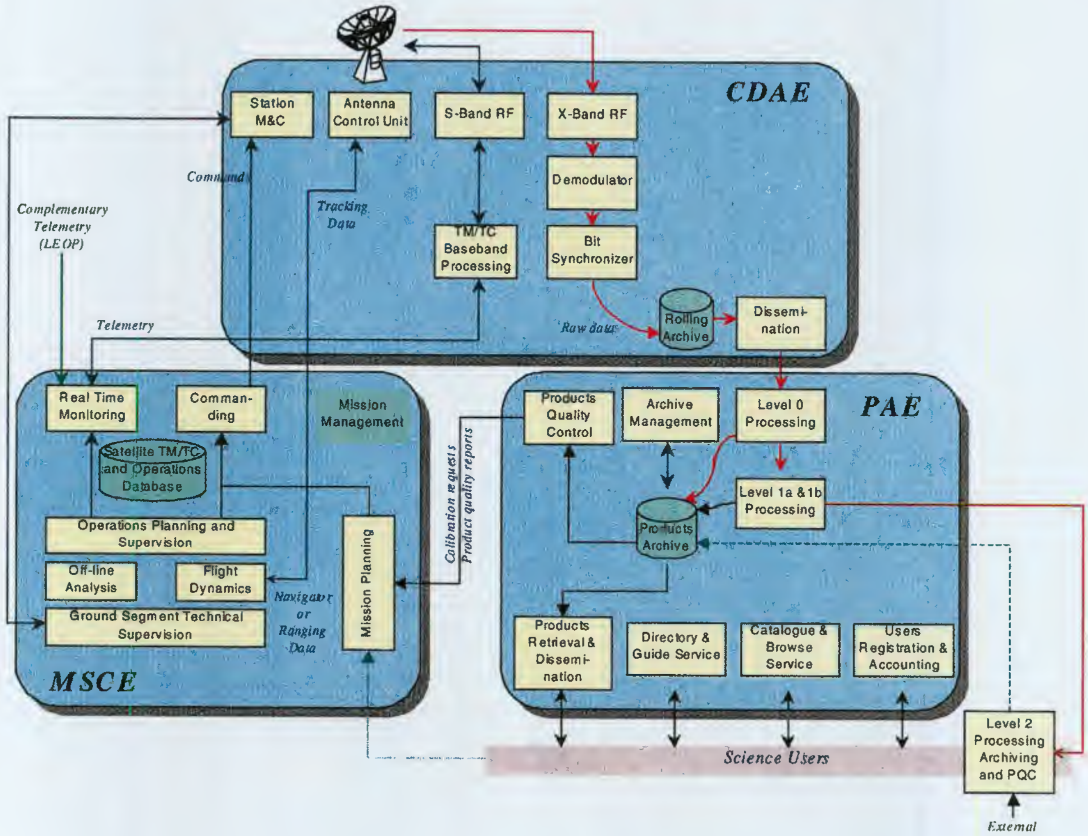

__Figure 6.33.__ Ground segment functional block diagram.

Command and Data Acquisition Element

The CDAE is in charge of direct interactions with the satellite. It will be implemented at the Kiruna Salmijaervi station. Two available S/X band antennas of 15 m and 13 m diameter will be available for telecommand transmission and for reception of housekeeping telemetry and science data.

The telecommand chain is able to handle 4 kbps, which is well above the 2 kbps required by ERM. The 67 dBW EIRP provides a link margin of more than 27 dB without tracking and more than 20 dB with tracking. The housekeeping data are received at 150 kbps, which is well within the capability of the station (more than 1 Mbps). The link margin is above 3 dB including ranging. The station provides facilities for accurate ranging, which may be used as backup to GPS-based position determination with a range accuracy of 0.007 m.

Science data will be received in X-band with PCM/QPSK modulation at 20 Mbps. The probability of frame loss is less than 10^{-6} with a link margin above 3 dB with R-S encoding. After down-conversion and demodulation, the raw data are stored in a rolling archive with capacity for one week's worth of data (40 Gbytes) to cater for outages in the data processing. The CDAE will be based to a large extent on the reuse of existing elements. The back-end will have to be upgraded to fully support CCSDS recommendations. Direct digital data ingestion technology will be used.

Mission and Satellite Control Element

The MSCE will be responsible for operations and satellite control. It will interface with the PAE for mission planning and product quality assessment and with the CDAE for telemetry and telecommand. The activities will be organised around existing mature functional blocks:

- Mission Control
- Flight Dynamics
- Performance Analysis and Reporting System

These blocks will be complemented with ERM-specific developments. The relative simplicity of the mission operations and the moderate complexity of the satellite will allow a high degree of automation and the sharing of resources between tasks with other ESA missions. Operations in the routine phase will be carried out during working hours from Monday to Friday.

Processing and Archiving Element

The PAE is in charge of data processing to Level 1, data archiving and dissemination, quality control, mission planning and user services, in addition to its own management and control.

The structure of the processing tasks is outlined in Figure 6.34, which also shows the intended high level of automation for processing and quality-control tasks. Figure 6.35 outlines the data processing and product quality-control tasks. The processing is only of moderate complexity and can be completed for all down-linked data within one orbital period, thus supporting the potential users with near-real-time data utilisation requirements. It is expected that the performance required for the ERM data processing, including 30% margin, can be met by a single work station.

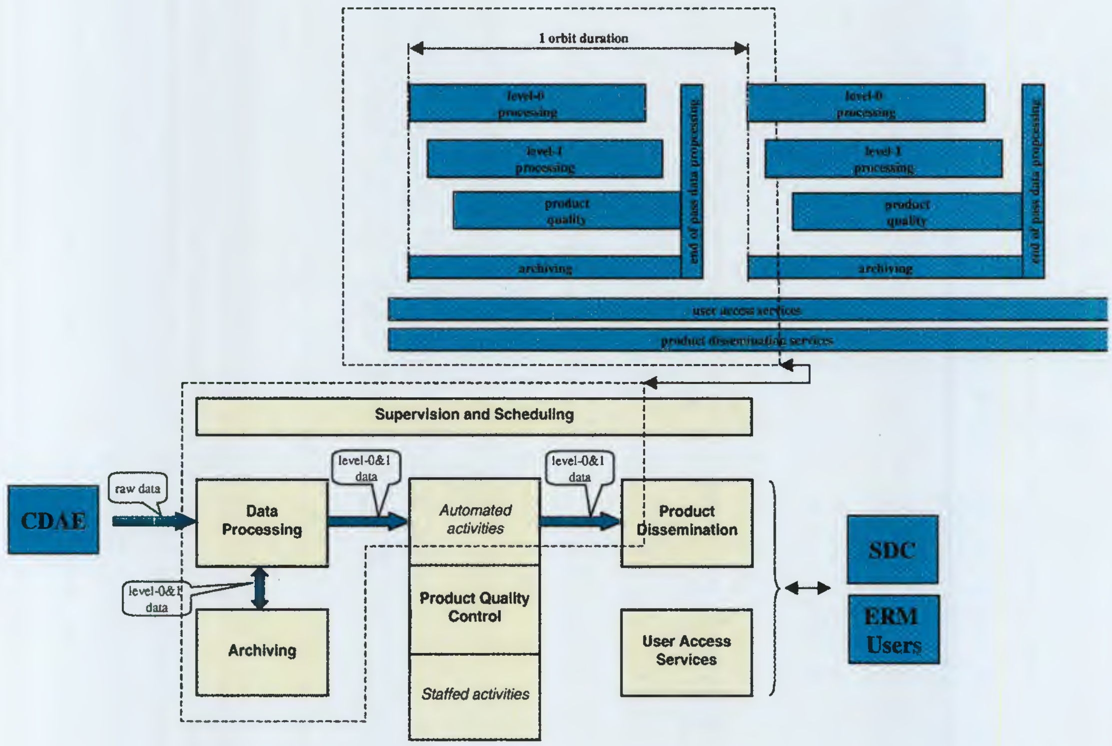

Figure 6.34. Data-processing and quality-control timeline.

It is proposed to allocate data-processing, quality-control, archiving and dissemination functions to the Kiruna station. This approach is similar to that for Envisat. As mentioned above, it ensures that the Level 1 products will be made available quickly to potential users who wish to use them in near-real-time, as mentioned in Chapters 4 and 5 and described in Chapter 7.

The archiving requirements are moderate compared with previous missions such as ERS and with Envisat. The archive size would be 13 Tbyte if all Level 0 and Level 1 data were archived for the two-year mission duration and there was no data compression. This is the proposed approach. The archive must be designed with sufficient flexibility to accommodate innovation and the evolution in user requests. Due to its moderate size an online archive can be implemented, although quasi-online and offline options are sufficient at this time to meet the user requirements. Given the interest in using ERM data for research in the field of applied meteorology, it is quite conceivable that a request will be received to connect the ERM archive to Eumetsat's UMARF. This is quite feasible.

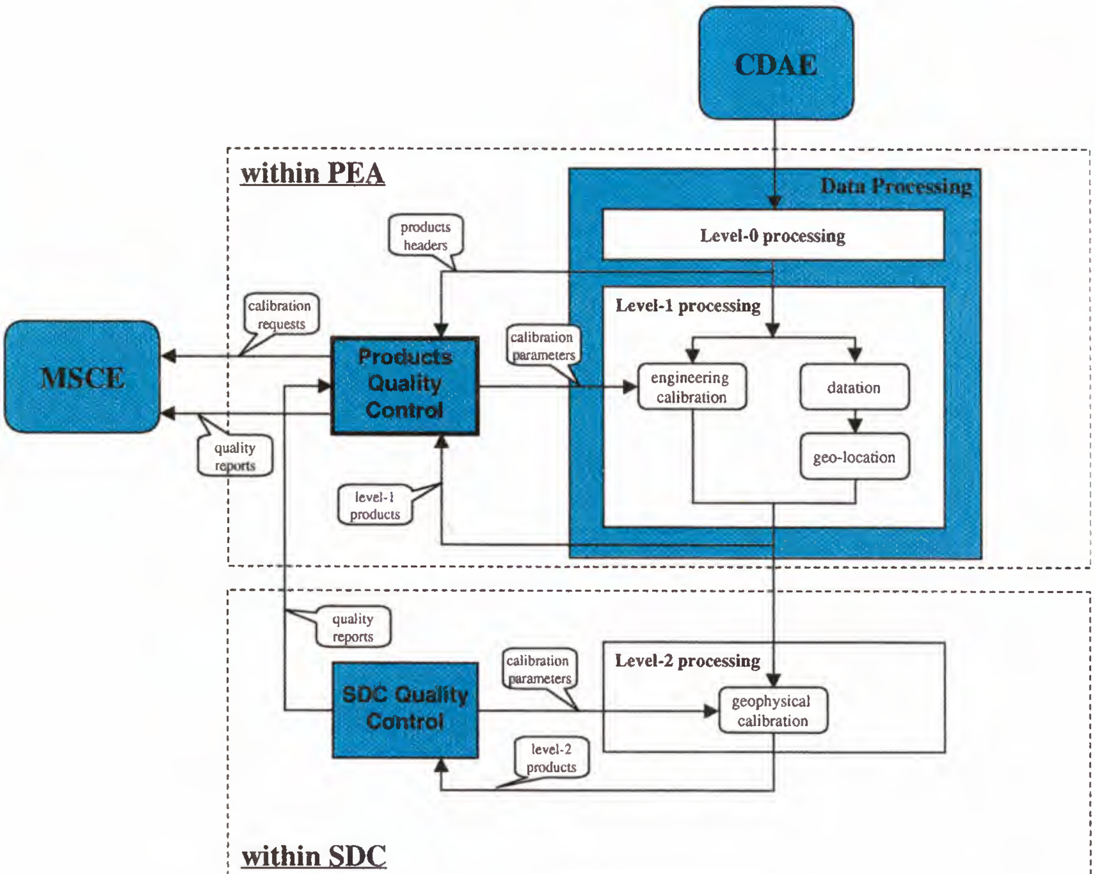

Figure 6.35. *Data-processing and quality-control tasks.*

The ERM data will be used also with data from other missions and from models, as discussed in Chapters 4, 5 and 7. The PAE will provide references to those other missions, mainly the operational geo-stationary and polar orbiting missions.

Communications

The communications between ground-segment elements for operations management will be carried out as usual with the enhancements allowed by technology development and reductions in costs. In general, data dissemination to the users does not have driving time-delivery requirements. It could be achieved via physical support media such as CD-ROM. However, it is expected that at the time of the mission such dissemination would be possible online via electronic links at very moderate cost. The archive and user services will be designed giving due consideration to the expected evolution of communications technologies and cost of services. It is also recalled that the processing tasks have been timed in such a way that data at Level 1 data can be made available in Kiruna within less than 3 hours of observation for the orbits visible from the station.

6.7 Conclusion

A system concept has been presented in the preceding sections that fully responds to the science requirements as defined in Chapters 2 to 5. This concept is technically feasible and economically affordable in the light of the constraints applicable to the Earth Explorer Core Missions.

The space segment, consisting of the platform and the instruments, is based on a sound combination of proven technologies and new design concepts. No design issues have been identified that would require the development of new technologies or extensive development efforts. The instruments, which have a good heritage of technology studies proving novel design concepts, are mature as far as their design definition is concerned. The remaining work, i.e. the detailed design and the manufacturing, does not appear to pose risks beyond the level of normal engineering work. For the platform, a design concept has been selected which is based on the reuse of existing principles and, where possible, even existing hardware, thereby minimising development risk and thus also cost. Good use has been made of new developments in the area of space engineering, such as advanced data-processing techniques, which have their roots in well-proven commercial applications, like the data management and attitude subsystems. Again, this is expected to reduce the overall development effort.

The successful drive for a small to medium-size system has allowed a launch vehicle to be selected which is at the lower end of the cost range. The Rockot heritage provides good prospects for successful operation. Whilst this vehicle has not seen a formal qualification for a civilian launch so far, the demonstration flights planned for the near future should provide sufficient confidence for its selection as the ERM baseline.

The ground-segment concept makes efficient use of the Agency's existing infrastructure in Kiruna, ESOC and ESRIN. Furthermore it will draw on the improvements planned for the Envisat mission. The inherent simplicity of the ERM concept allows the use of a highly automated system with low running costs. Improvements in data processing and transmission techniques which are to be expected in the foreseeable future, will be reviewed and implemented where proven to be cost-effective. Collocation of the CDAE and PDAE at Kiruna has been identified as a further means to simplify operations. This also provides near-real-time data delivery for the visible orbits.

Table 6.21 summarises the key data of the ERM system.

Payload	
Backscatter lidar	226 kg, 217 W, 400 kbps
Cloud profiling radar	136 kg, 273 W, 30 kbps
Multi-spectral imager	15 kg, 45 W, 60 kbps
Broad-band radiometer	7 kg, 23 W, 3 kbps
Satellite	
Mass, power, data rate	913 kg, 868 W, 500 kbps
Attitude & orbit control	3-axis stabilised, nadir-pointing, yaw steering, hydrazine propulsion
Data management	Centralised system, single processor
Communications	S-band 150 kbps, X-band 20 Mbps
Power	2-wing solar-array, single 50 Ah NiH_2 battery
Launch vehicle	Rockot, 172 kg mass-to-orbit margin
Orbit	1300 hrs, Sun-synchronous, 369 km
Ground segment	Reuse of Kiruna, ESOC, ESRIN infrastructure

Table 6.21. *ERM system parameter summary.*

7 Data Processing

This chapter discusses how the data from the complement of instruments defined in Chapter 6 will be used to satisfy the objectives of the mission described in Chapters 2 and 3.

7.1 Overview of Retrieval Algorithms for Single Instruments

7.1.1 Lidar

From Raw Data to Mission Observable

The flow diagram of ATLID on-ground data processing up to Level 1 is presented in Figure 7.1. The ATLID data-stream contains science as well as housekeeping data. The science data comprise:

- the atmospheric signal profile for each shot
- the internal calibration signal (mainly the energy of each outgoing pulse)
- the averaged signal value in the range from 100 km to 150 km altitude (mainly, background and dark current signal) and
- the noise signal from 100 km to 105 km, for the initialisation of boundary-detection algorithms.

The processing steps, as shown in the flow diagram, are necessary for converting the lidar raw data profile into a geo-localised attenuated backscatter profile. The data classification process sorts out the components as listed above. When the instrument flies over well-characterised surface targets at predefined geographical locations (mainly reflectivity-calibrated sites), the corresponding surface returns are used as external calibration data. It is currently assumed that such locations could be identified in deserts and in central Greenland, as proposed for the cloud-profiling radar. The calibration sites used by SPOT or Landsat could be used for ATLID calibration as well. After appropriate background and dark-current subtraction, the temporal signal will be normalised to the outgoing pulse energy and range-corrected (multiplied by the square of the range) to yield the normalised range-corrected signal. The geo-localisation process assigns the signal samples to the geographical co-ordinates, including altitude with respect to the mean geoid. The absolute calibration process determines the correct scaling factor to match the calibration site reflectivity corrected from atmospheric transmission to the inferred reflectivity from the integrated ground return.

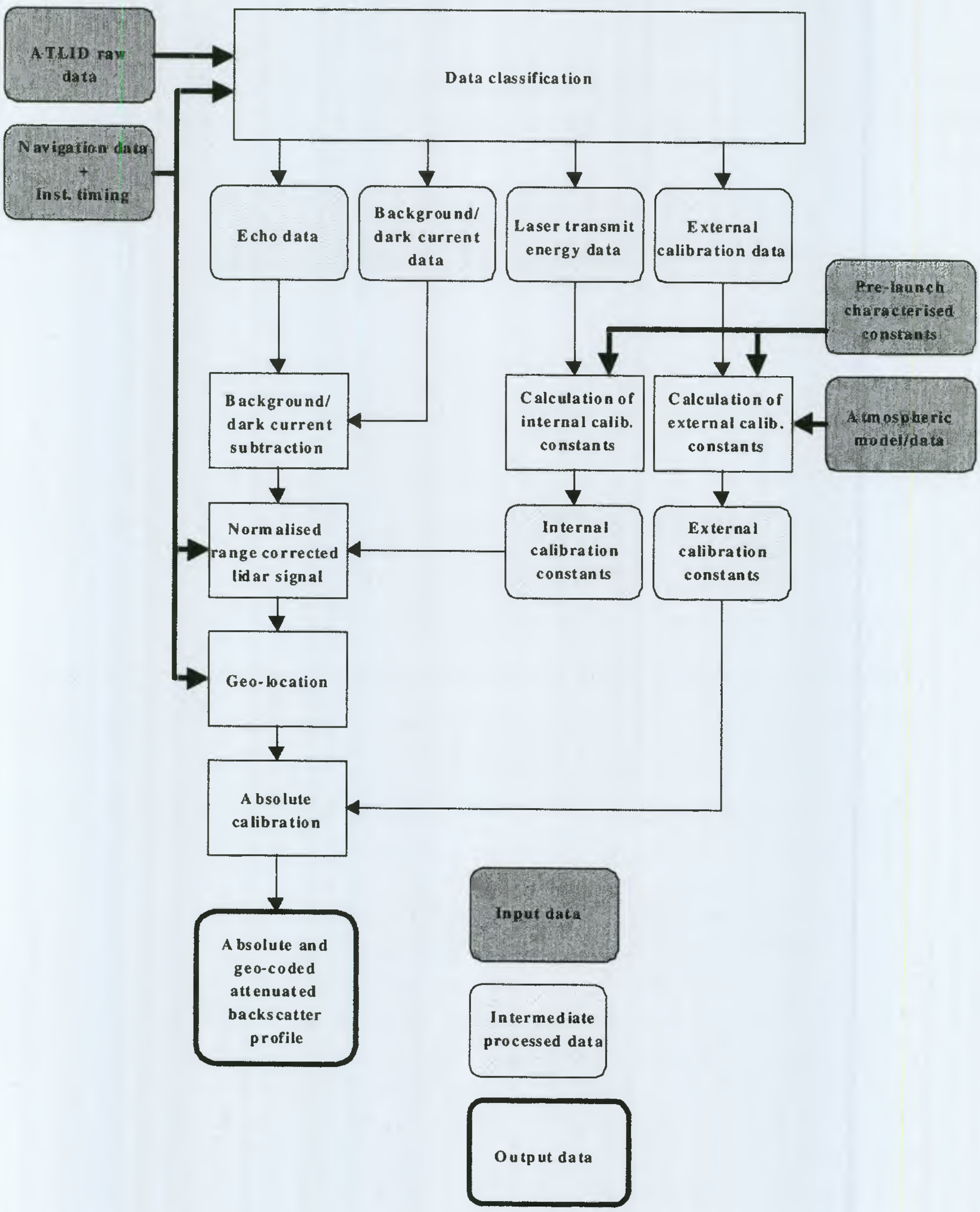

Figure 7.1. *Backscatter lidar data processing chain.*

Retrievals from a spaceborne lidar include, for the multiple cloud layers, the cloud coverage, cloud top/base height and optical thickness, as well as vertical profiles of the extinction and backscatter coefficients. For aerosols, the retrieved parameters are the aerosol layers, their optical thickness, the height of the planetary boundary layer (PBL) and the aerosol extinction and backscatter profiles.

The retrieval of cloud coverage is based on a threshold analysis of lidar profiles. The cloud top and base altitude retrieval is based on analysis of the profile of the intensity of the lidar signal. The determination of the cloud top uses the increase in the lidar signal due to the cloud backscatter. Vice-versa, the determination of the cloud base height for semi-transparent cirrus uses the decrease of the lidar signal The accuracy of the cloud top and cirrus base height retrievals is in the range of 100 m.

For dense water clouds, the cloud base height determination is impossible due to the limited lidar penetration depth (200-300 m). Moreover, the geometrical thickness of the optically thick cloud is affected by the stretching of the return signals due to the effect of multiple scattering.

For the retrieval of the vertical profiles of extinction, backscatter and optical thickness, a distinction has to be made between thin ice clouds and water clouds. Semi-transparent cirrus clouds at high altitudes are completely penetrated by the lidar, revealing vertical multi-layer structures. Low and mid-level dense water clouds show very strong returns from the cloud top and then a decrease of the signal with the penetration depth.

The accuracy of the lidar retrievals of cloud thickness, extinction and backscatter coefficients is a function of three main factors: the multiple scattering correction factor $Q(R)$, the calibration constant C and the backscatter to extinction ratio β/α.

The multiple scattering correction factor $Q(R)$ is calculated from the particle diffraction patterns near the forward direction and the internal transmission near the backward direction.

The calibration constant C is calculated from the calibration of the receiver, and the lidar ratio is estimated on the basis of typical measured data. The typical variation of the calibration constant is about 10%, the variation of the lidar ratio is in the range between 10% and 30%, and the variation of the multiple scattering correction factor is about 20%.

To invert the lidar equation to retrieve the cloud optical thickness and the extinction coefficient, several retrieval algorithms have been proposed. The approach is based on the integration of the profiles of the logarithm of the lidar signal, which is initially corrected for the R^2-range dependence. In the forward integration algorithms, the extinction profile is derived by the integration from the range nearest to the lidar, in the direction to greater ranges. In the backward integration algorithm, the return from the furthest range is inverted first.

Using the lidar signal alone, the backward integration algorithm cannot be implemented in space applications due to the unknown boundary value at the far-end. Therefore, the most reliable approach is the forward integration scheme with boundary value equal to the calibration constant C. However, together with the radar, a backward integration algorithm can be used. This is shown in Section 5.4.

To estimate the possible errors consistent with errors in the calibration constant C, multiple scattering factor $Q(R)$ and lidar ratio, the total error in the retrieved quantities has been calculated as the sum of the partial errors on the unknown constants.

It is, however, noted that the multiple scattering lidar signal is derived using the narrow-angle-scattering approach, which gives accurate results for thin cirrus with large ice crystals, and for water clouds for the first few optical penetration depths. At penetration depths larger than $\tau=4$, the photon random walk inside water clouds deviates considerably from the laser beam through large angular deflections. At these depths the approach is inaccurate.

7.1.2 Radar

From Raw Data to Mission Observable

The flow diagram for the CPR on-ground data processing up to product Level 1b is presented in Figure 7.2. The data-stream from the CPR contains science as well as housekeeping data. The science data comprise:

- radar echo profile
- internal calibration signals, including the transmitted-pulse replica
- noise signal (in absence of transmitted-pulse).

These signals are averaged on-board the satellite over a 1 km ground-track.

The processing steps, as shown in the flow diagram, are necessary for converting the raw instrument data into mission observables.

The data classification process sorts out the components as listed above. When the instrument overflies well-characterised target surfaces at predefined geographical locations (calibration or reference sites), the corresponding surface echoes are used as external calibration data. It is currently assumed that appropriate locations for external calibration purposes can be identified in Central Greenland. The reasons for this assumption are:

- The dry snow in Central Greenland undergoes very little or almost no morphological changes over the seasons due to the cold air temperature being well below the melting point.

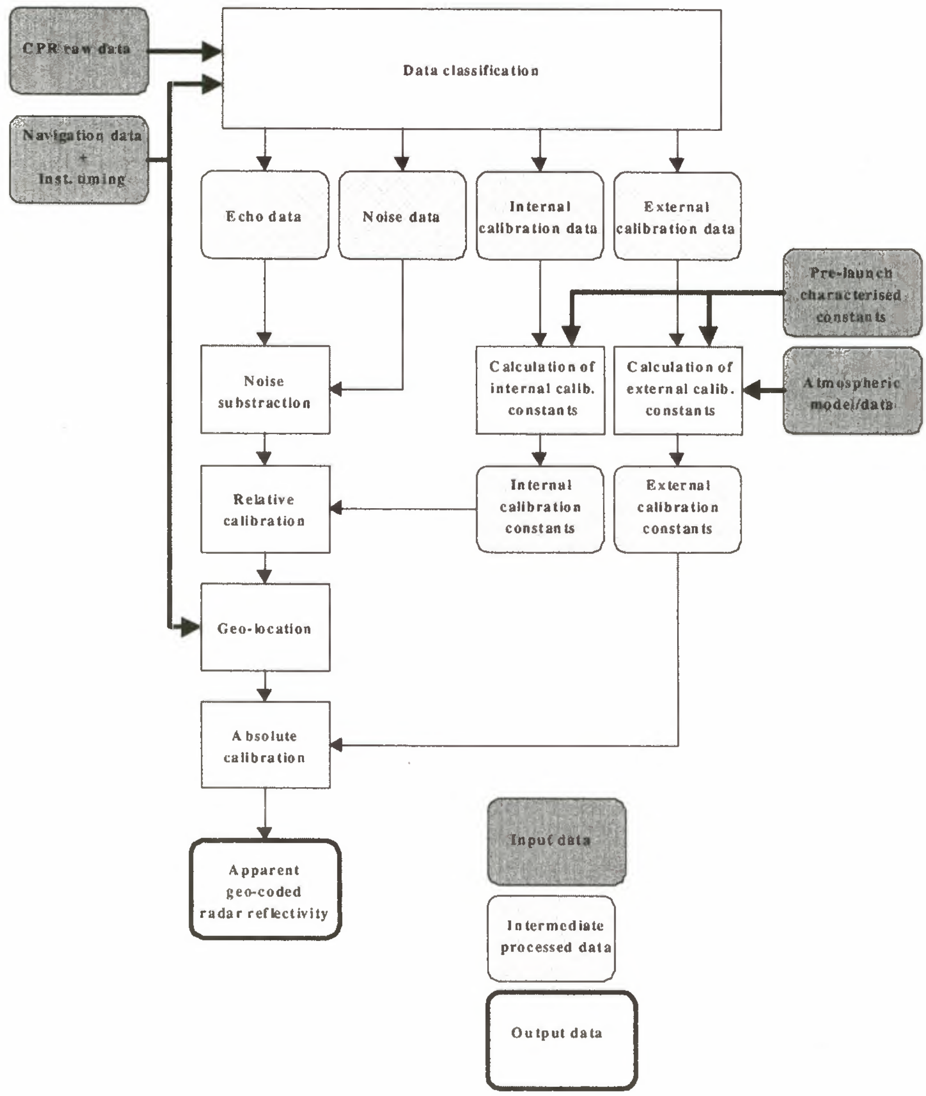

***Figure** 7.2. CPR data-processing chain*

- The topography of Central Greenland is almost flat (average slope less than 2°), and therefore represents a large, homogeneous radar target.

- Combined with the high altitude of the area, which lies above 3000 m, and the generally very dry atmosphere at high altitude, the total atmospheric attenuation is expected to be very low and predictable with low errors.

For radar echoes at the lower end of the measurement dynamic range, the instrument noise (background noise) level can be an order of magnitude higher than the signal itself. Hence, accurate noise subtraction is required for estimating the useful signal level.

The *relative calibration* determines the gain of the radar chain, within the internal calibration loops.

The *geo-location* processing assigns the signal samples to the geographical co-ordinates including altitude.

The *absolute calibration* determines the gain of the total radar chain, including the propagation effects between the radar and the calibration (reference) surface target.

Correction of Radar Reflectivity for Attenuation

If the values of radar reflectivity factor, Z, for ice clouds are to be interpreted quantitatively, then it is important to correct for attenuation. Table 6.11 of radar sensitivity in the absence of clouds shows that down to the freezing level (4 km in the tropics) the atmospheric attenuation is less than 0.5 dB or 10%. The use of a climatological profile for this correction will suffice.

The values of attenuation for ice clouds have been calculated from the ice particle size spectra referred to in Chapter 5. The results for the tropical data set (CEPEX) of 12 506 spectra and for the 14 701 spectra for the mid-latitude EUCREX data set are displayed in Figure 7.3. The ice density variation of the form 0.07 $D^{-1.1}$ has been used, where D is in mm and the density in g cm^{-3}. These computations show that even for the spectra with the highest ice water content and the highest reflectivity values, the two-way attenuation never exceeds 0.1 dB km^{-1} and can therefore be neglected.

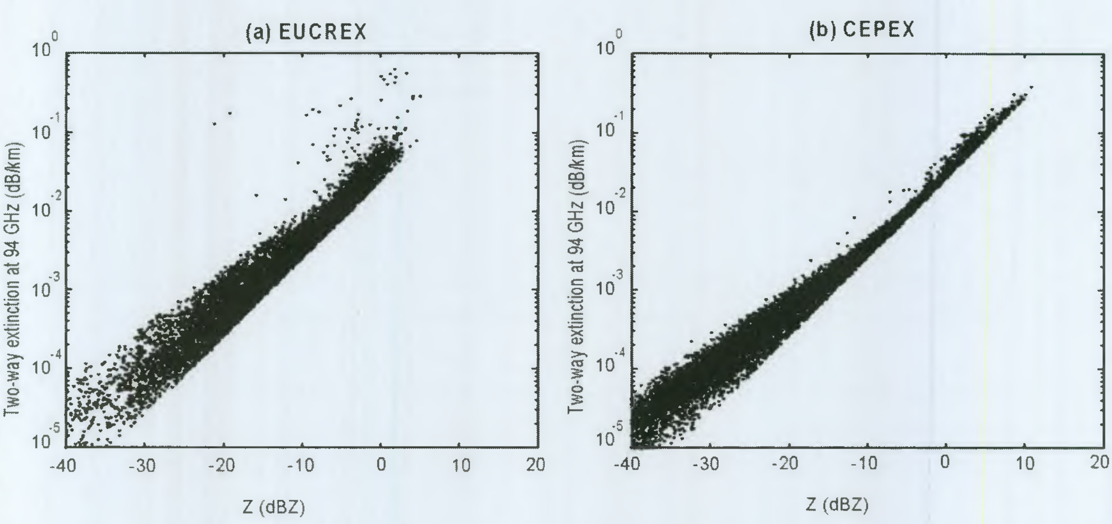

Figure 7.3. *Two-way specific attenuation (dB/km) in ice clouds for the EUCREX (mid-latitude) and CEPEX (Tropics) data sets.*

For liquid water clouds, it might be thought that the high attenuation by liquid water approaching 10 dB km^{-1} g^{-1} m^{-3} would pose a problem, but as it has been seen as soon as liquid water clouds become at all substantial, the presence of occasional drops larger than 100 µm increases the radar reflectivity by 20 or even 30 dB. Accordingly, even if there were appreciable attenuation, they would still be above the threshold for detection. The presence of these droplets, which dominate Z but have negligible liquid water content, means that the quantitative value of Z alone cannot be used to derive a value for liquid water content.

Inferred Value of Ice Water Content

The relationship between ice water content and radar reflectivity varies because of changes in the mean size of the ice particles as displayed in Figure 5.3. In Figure 7.4, the mean value of IWC and its standard deviation for each 2.5 dB step in reflectivity is displayed when the CEPEX tropical data set is classified in terms of temperature. The figure shows that there is a significant difference in the conversion of Z to IWC for different temperatures, and that the errors are reduced when the additional temperature information is used. This additional skill coming from using temperature, is a result of the well-known tendency for ice particle mean size to be a function of temperature; a tendency that is exploited in parameterisations of ice processes used in NWP and climate models.

From the data in Figure 5.3 it is estimated that if Z alone is available, then IWC can be estimated to a factor of 2 from Z, but Figure 7.2 shows that this is considerably improved if the temperature is known to 6 K. This can be derived from the height of the return in the tropics, where temperatures do not change much, and this is sufficient to define the temperature to 6 K, but in the more variable mid-latitudes the temperature from an NWP analysis should be used.

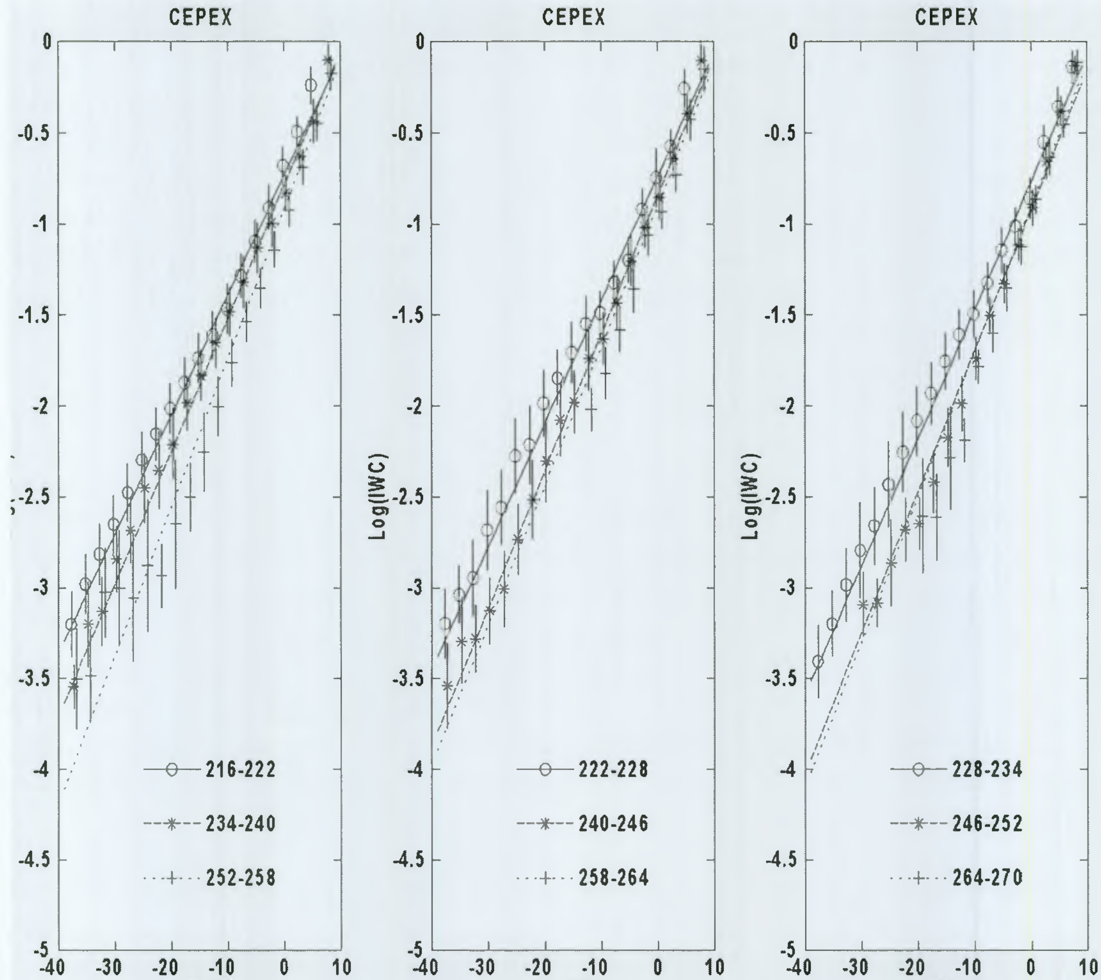

Figure 7.4. Ice Water Content (IWC) as a function of radar reflectivity (Z). Mean and standard deviation for each 2. 5 dBZ step in Z for nine different temperature ranges each of 6 K. For clarity, each panel has three curves for temperature ranges separated by 18 K; from one panel to the next the temperatures for the three curves increase by 6 K.

7.1.3 Multi-Spectral Imager

From Raw Data to Mission Observable

The data flow of the instrument from raw data to the geophysical parameters is shown in Figure 7.5.

As described in Section 5.5, the multi-spectral imager serves different tasks. The most important tasks are to contribute to the synergy algorithms (see Section 5.7) and to characterise cloud and aerosol fields.

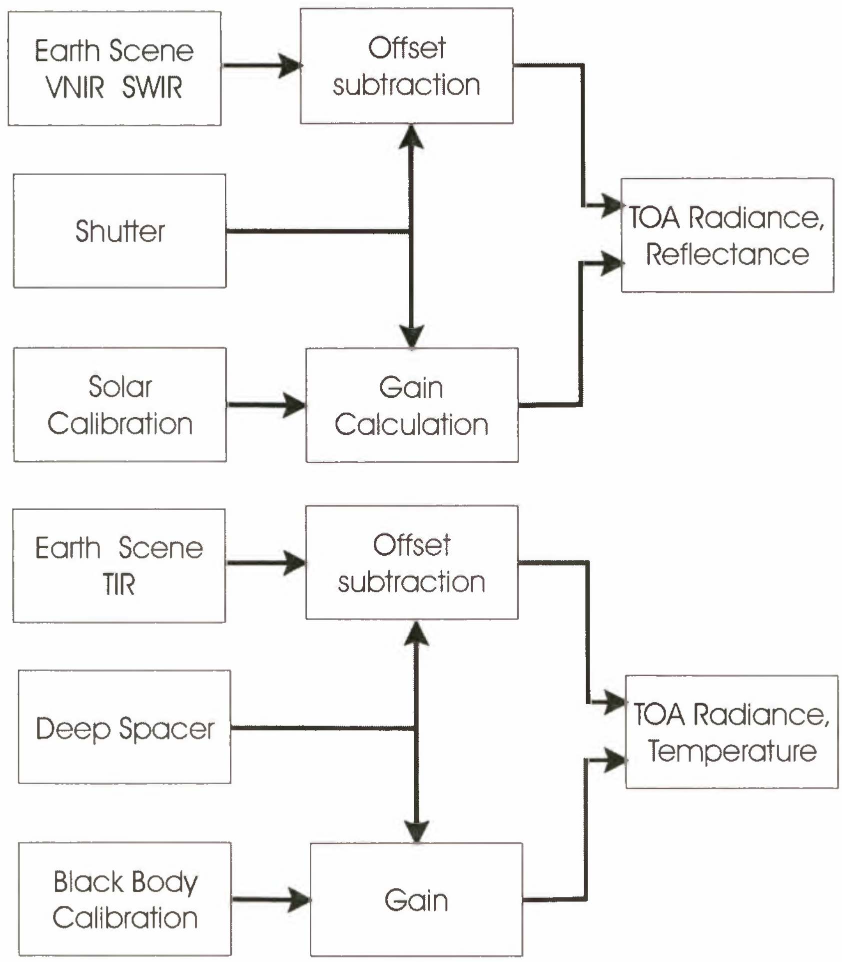

***Figure** 7.5. Multi-spectral imager data flow; visible and near-infrared channels above and thermal-infrared channels below.*

For the multi-spectral imager, the conventional data processing will be performed. This includes the provision of calibration routines for the different spectral channels. An online cloud and aerosol characterisation algorithm (cloud parameters and variability) will be run. The products of this algorithm will include cloud cover, apparent cloud top temperatures, phase information and information on the cloud variability (along- and across-track). Furthermore, a scene-identification algorithm will be used to improve the accuracy of the BBR-derived products.

There is considerable experience with the data processing of multi-spectral imager data. No critical problems are expected.

7.1.4 Broad Band Radiometer

From Raw Data to Mission Observable

The derivation of the LW and SW radiances from the Broad-Band Radiometer (BBR) data is shown in the two flow diagrams of Figures 7.6 and 7.7. The concept is very similar for both channels, except for the generation of the LW radiance. It consists of a combination of internal and external data sources, both in- and pre-flight. The BBR will, in addition to these calculations, perform an internal plausibility check, the result of which is inserted in the telemetry data.

Solar calibration is only used for the monitoring and correction of spectral drifts. As the Sun is a very stable and predictable source, these corrections need to be made only a posteriori.

The emergent short- (0.4 to 4.0 µm) and long-wave (4 to 50 µm) radiances computed from the other ERM instruments will be compared to those measured by the BBR.

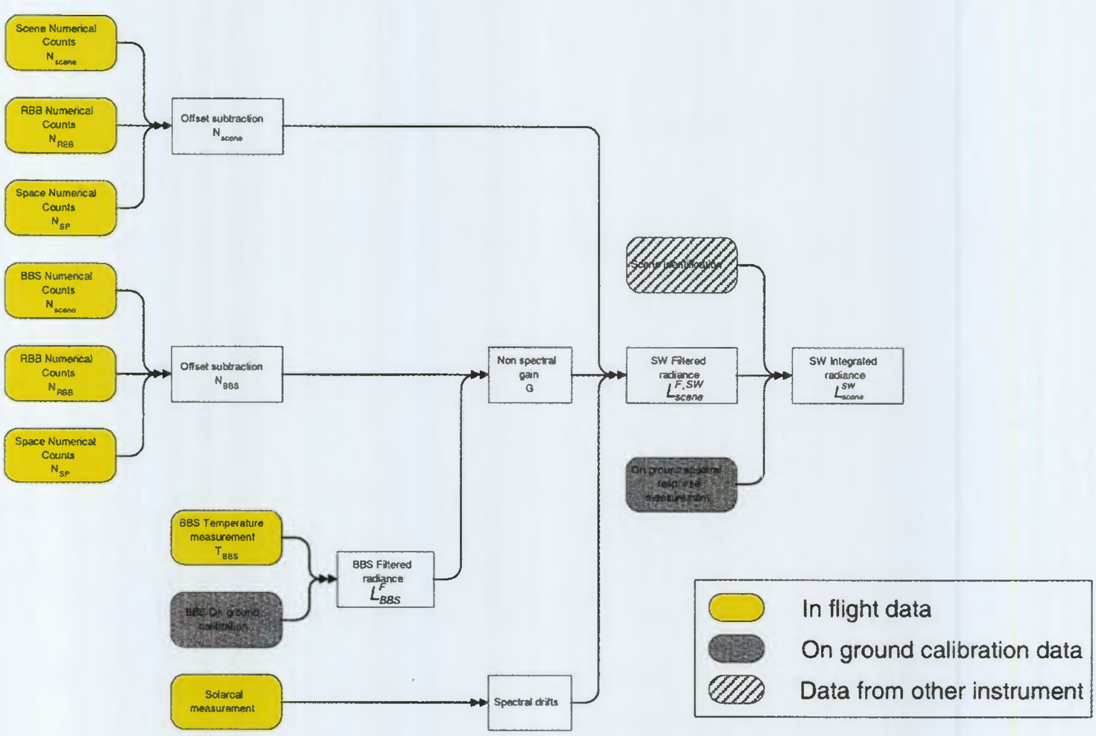

Figure 7.6. BBR SW integrated radiance computation.

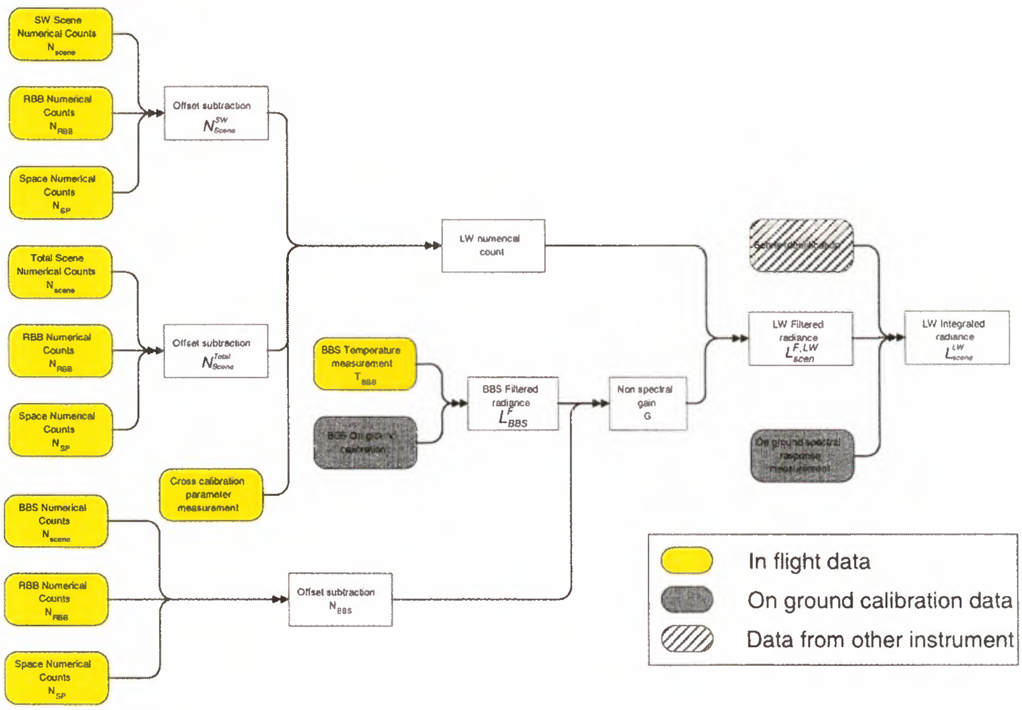

Figure 7.7. *BBR LW integrated radiance computation.*

To perform this exercise, it is necessary to know vertical and horizontal structure within the footprint of the BBR. The information required involves not only macro-physical properties such as cloud top(s) and base(s) and cloud overlap within the footprint of the BBR, but also micro-physical ones such as water content, effective radius or optical depth (obtained from the other ERM instruments).

In most cases, to compute the derived radiances, a simple plane parallel radiative-transfer scheme will not suffice. More complex schemes which also take into account the horizontal structure within the footprint of the BBR, are necessary. These more complex algorithms (e.g. 3-dimensional) are available.

Additional information regarding the surface and solar irradiation, not measured by ERM, is also required. In any case, even the observed TOA short- and long-wave radiances, without any further processing, will be of high scientific interest for numerical modellers.

7.2 Synergetic Retrieval Algorithms

The use of the combined radar and lidar backscatter to derive a profile of water content and cloud particle size was described in considerable detail in Section 5.4 with the aid of three figures. Essentially the ratio of the backscattered power for solid ice particles should vary as D^4 or with a more realistic ice density as D^2. The difficulty of correcting a lidar return for attenuation was highlighted in Section 7.1. Gate-by-gate corrections are notoriously unstable, but the new combined retrieval is stable because it uses the Z profile of the radar as a first guess for the estimate of the attenuation. The flow chart in Figure 7.8 summarises the synergetic retrieval algorithm described in Section 5.4.

The retrieval technique has to assume a particle size spectrum. In this case a normalised gamma function with an index of 5 and spherical particles is assumed. Tests show that the retrieval is not very sensitive to the precise value of the index chosen. Ice particle spectra are generally well-behaved and adequately described by a quasi-exponential spectrum. Figure 5.3 confirms this: the fact that the values of Z and IWC calculated from observed spectra are well-stratified and separated by their equi-volumetric mode diameter means that the exponential or gamma function is a sufficiently accurate description. Once the gamma function index is fixed, then two free parameters remain: the effective radius R_{eff} and the particle number density N_0.

By choosing the particle shape (in our case spheres), the backscatter/extinction ratio needed in the lidar equation is defined.

For every height range, there are two equations (the lidar and radar equation) with two unknowns, R_{eff} and N_0. These can be solved iteratively assuming a boundary value for the effective radius at the far end. The integrals are integrated backwards towards the beginning of the cloud.

One particularly important factor for the retrievals, using combined radar and lidar return, is that the two instruments view a common volume of cloud. In Chapter 5, Figure 5.7 demonstrates that the lidar signals from two lidar stations 4 km apart gave the same average profile, but that individual returns were virtually uncorrelated.

Figure 7.9 shows how the radar/lidar synergy degrades as a function of separation distance. The data are taken from the 12 506 CEPEX tropical ice particle spectra observed by aircraft. Each size spectrum is for a path of 1.94 km through the cloud and from each spectra the following variables were derived: ice water content (IWC), radar backscatter (Z), lidar backscatter (β).

From the ratio of Z/β, a particle size is calculated and then, using the particle size and the observed Z, a value of IWC is retrieved. Figure 7.9a compares the retrieved IWC when calculated from the radar Z alone (ordinate), with the 'true' IWC calculated directly from the spectra (abscissa). The 'true' data are sorted into 0.125 steps in $\log_{10}$(IWC) and the mean and standard deviation of the IWC retrieved from Z are calculated for each step in 'true' $\log_{10}$(IWC). The standard deviation confirms the factor of two errors in retrieved IWC from Z alone quoted in Chapter 5.

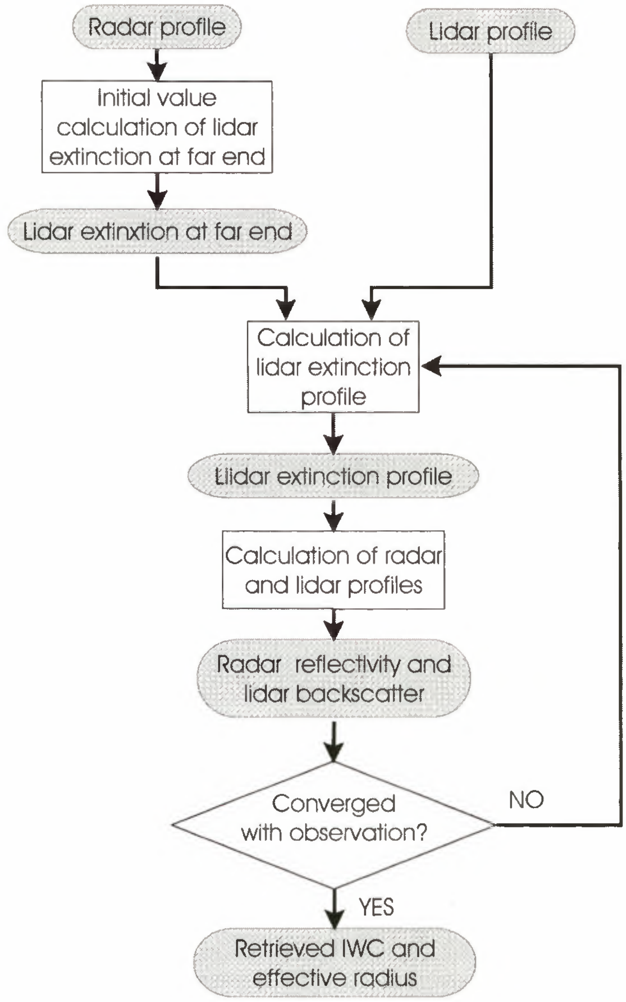

Figure 7.8. *Synergistic retrieval algorithm.*

Figure 7.9b shows the improvement when the IWC is calculated using the particle size (from Z/β) and the magnitude of Z. The error in the IWC retrieved from radar and lidar is now only 30-40% compared to the 'true' value calculated directly from the spectra.

The errors in Figure 7.9a and 7.9b should be contrasted with those in Figure 7.9c and 7.9d. In 7.9c and 7.9d the size of the particles is derived from the radar/lidar ratio, where the values of Z and β are calculated from adjacent spectra separated by 1.94 and 3.9 km, respectively. Even for a separation of 1.94 km, the errors are worse than those in Figure 7.9a, which shows the error when IWC is derived from Z alone using no lidar information. It is concluded that even a separation of 2 km means that the synergy between the two instruments is lost.

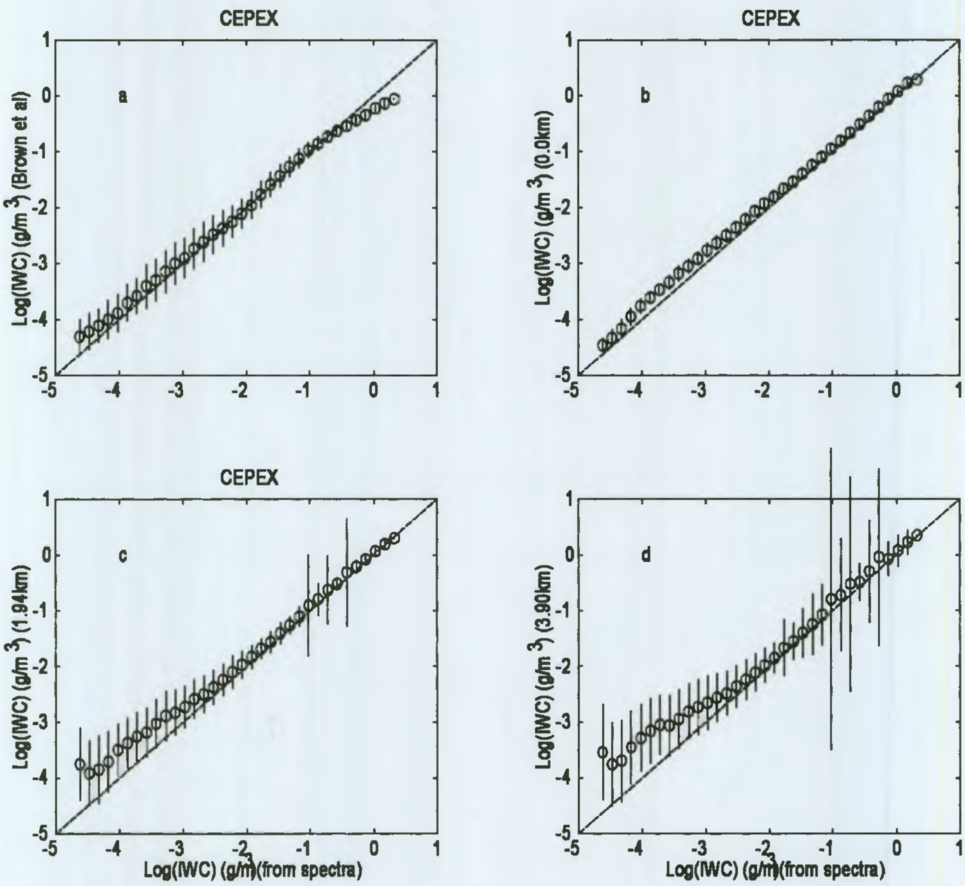

Figure 7.9. *Relationship between observed ice water content (IWC) and IWC derived from radar reflectivity (a); IWC derived from radar and lidar (b); IWC derived from radar and lidar but 1.94 km apart (c); and IWC derived from radar and lidar 3.9 km apart (d) (see text for further details).*

In conclusion, this clearly demonstrates that coincident observations of radar and lidar are required to derive microphysical products to meet the ERM objectives with the accuracies stated in Table 4.1.

7.3 Data Assimilation

Numerical Weather Prediction (NWP) models aim to provide a description of the atmosphere over periods of time ranging from a few hours to 10 days, starting from the best possible knowledge of its current state. The initial state of NWP models, called the *analysis*, is obtained by combining in an optimal way all possible sources of information on the atmosphere (observations of various types, climatology, atmospheric equilibrium, short-range forecasts) into a coherent picture. This complex process is achieved within a *data assimilation system,* which can only be maintained and developed by the main operational weather services such as ECMWF.

Global NWP models can explicitly describe atmospheric motions having horizontal scales larger than a few hundreds of kilometres. However, important physical processes take place in the atmosphere at much smaller scales (e.g. clouds, turbulence...). They need to be represented in NWP models because they contain significant amounts of energy, influencing the resolved scales.

This implicit description of physical processes, known as *parameterisation*, is a key issue in NWP model development. The reason is that they describe phenomena that are not properly sampled by conventional observations and, as a consequence, they are not yet sufficiently understood to be described accurately enough.

The description of clouds is a typical example. In early NWP models, clouds were described through empirical dependencies with relative humidity and others quantities (Slingo, 1987). This approach was initially chosen because of its simplicity, but also due to the lack of proper understanding on cloud formation and dissipation. This situation has recently evolved with the emergence of prognostic cloud schemes (e.g. Sundquist, 1994, Smith, 1990; Tiedtke, 1993) and the availability of new data sets coming from field experiments, satellite observations and cloud-resolving models.

7.3.1 Initialisation of Cloud Properties Using ERM

By definition, a prognostic cloud scheme includes prognostic variables additional to the classical ones evolved in NWP models (wind components, temperature, specific humidity, surface pressure). It poses a new problem of initialisation at the beginning of model forecasts.

In the ECMWF cloud scheme, the following quantities need initial values to run a model forecast: cloud fraction, cloud liquid water content and cloud ice water content. The lack of cloud observations in operational data-assimilation systems prevents a proper analysis of these quantities. Currently, these variables are initialised as the result of a 6-hour model forecast. Although this approach is better than an initialisation to zero, which generally leads to a degradation of the forecast quality in the short-range, as shown by Jakob (1995), there is an inconsistency between the non-cloudy regions of the atmosphere that have been modified by observations and cloudy areas that are kept to values from the previous short-range forecast.

The inclusion of cloud observations in the ECMWF data assimilation should lead to an improved initial state of the prognostic variables of the cloud scheme, which could in turn improve the quality of the forecasts. A new data assimilation system known as 4D-VAR (four-dimensional variational) has been implemented in November 1997 at ECMWF. This system, which is run operationally only at ECMWF, has proved to be better than its predecessors (3D-Var, Optimum Interpolation) in terms of quality of both analyses and forecasts (Rabier et al., 1997).

One of its main advantages is that the analysis is provided by an initial state leading to a model trajectory over a given window (between 6 hours and 24 hours) that best fits all the observations available during the integration period. Observations are weighted according to their accuracy and taken simultaneously during a minimisation process. The 4D-Var system is flexible enough to allow the assimilation of new types of observations. This can be possible when an *observation operator* and its linearised version exist. An observation operator provides the model counterpart of a given observation, which can be a simple spatial interpolation for conventional observations or a radiative-transfer model for satellite radiances.

Developments have started in this general area to include satellite-derived precipitation rates from the Tropical Rainfall Measuring Mission (TRMM) in the 4D-Var system (Mahfouf et al., 1998). The observation operator in such a case is the parameterisation of cumulus convection. The linearised version of both a radiative-transfer model and a cloud scheme are the observation operators that need to be developed for the assimilation of cloud properties and top-of-atmosphere (TOA) fluxes. Work in this direction has already started.

For the purpose of assimilation, it is necessary to have a near-real-time (3 to 6 hours) delivery of as much as possible of ERM data and products. These data would not be near-real-time for the whole globe due to the baseline of one ground station. However, the approximately 1/3 of the Earth covered in near-real-time is already of high interest.

7.3.2 Improving Physical Parameterisations Using ERM

Data from ERM can be used to improve the physical parameterisations, which will lead in turn to a better evolution of the atmosphere by the forecast model. Indeed, there still are large uncertainties in the description of the cloud and radiation processes in NWP models that are known to have a non-negligible influence on medium-range forecasts. Ice properties are not accurately described in the ECMWF model, either for the cloud scheme (where the microphysics is only accounted for through a terminal fall-speed velocity) or for the radiation scheme (where a constant effective radius is pre-scribed).

Quantitative information on the ice water path would help to reduce significantly the level of uncertainty related to the ice phase in the ECMWF model. Currently, the vertical structure of observed clouds is only known very crudely through three main layers derived from ISCCP satellite data. How clouds overlap in the vertical is of crucial importance for a number of physical processes such as radiative fluxes, evaporation of rainfall or ice sedimentation.

It has been shown in various sensitivity studies that uncertainties associated with the cloud overlap can influence TOA solar and thermal radiation and also the amount of precipitation reaching the surface (Morcrette and Jakob, 1999; Jakob and Klein, 1999).

The synergy between instruments measuring TOA radiances and instruments measuring cloud vertical profiles as proposed by ERM is necessary to make significant improvements in the description of cloud-radiation interactions. Indeed, the agreement of model radiative fluxes with observations should not compensate for an incorrect specification of the cloud cover or of the cloud water path. Although of obvious importance, the correct simulation of cloud occurrence is only a necessary but not sufficient condition for capturing the main hydrological and radiative effects of clouds in GCMs. A further requirement is the correct simulation of the amount of condensate present in the cloud.

For the purpose of improving the parameterisations, access to the archived ERM products will be necessary.

7.4 Validation Programme

A new and challenging mission like ERM requires a substantial validation programme. To combine simultaneous spaceborne measurements of different instruments, and in particular of lidar backscatter and radar reflectivity from clouds and aerosols, validation measurements from ground-based and airborne correlated experiments must be carried out.

Two levels of validation of the spaceborne measurements are needed. The first is to confirm that the instruments on-board the satellite are performing as specified. The second level is to validate the algorithms for retrieval of the geophysical variables such as optical depth, particle size and ice and water content and to confirm the accuracies that can be achieved. This second level can be further divided into two stages: before and after launch.

7.4.1 Validation of Retrieval Algorithms

The first stage should be carried out before the satellite is launched. It would involve a lidar and radar (which sample a common vertical profile of cloud) and *in-situ* microphysical measurements of the sample volume carried out by an aircraft. This would confirm the inferences made from the radar and lidar. Pilot studies have already been carried out in Europe such as CLARE'98 (ESA Contract No. 12957), CLARA (Russchenberg et. al, 1997) and CARL (ENV4970545) with ESA and/or EU support and the results have been quoted in this report. These studies have been restricted to Europe.

The radar and lidar can either be ground-based or airborne. For the airborne lidar and radar, at least two co-ordinated aircraft are needed, with the second aircraft providing the *in-situ* measurements of ice and liquid cloud particle shapes, sizes and concentrations. The crucial use of the lidar/radar backscatter ratio to retrieve particle size and accurate water content has been stressed in this report and does require further validation. The advantage of the multi-aircraft approach is that validation data are obtained along a line, which can be 50 km long. The use of a single aircraft and ground-based radar and lidar is more economical, but provides coincident validation only at the point where the aircraft flies over the ground-based instruments.

7.4.2 Validation of Satellite Data

This second stage, after launch, is more difficult than simple validation of the algorithms themselves. The difficulty arises from the ground velocity of the satellite (around 7 km s^{-1}) and the very narrow 'swath' (1 km or less) of the active instruments. The crucial validation is for the combined radar/lidar retrieval, which uses the backscatter ratio from the two instruments that must be sampling a common volume of cloud.

In the LITE experiment, validation was achieved by aircraft flying below the satellite track, but in this case only cloud top and base and their macro-physical characteristics were being validated and a separation of the aircraft and satellite footprint by tens of kilometres and/or several minutes could be tolerated. The demands of the radar/lidar retrieval mean that a much closer coincidence is needed.

One can envisage two approaches. A cheaper and more frequent ground-based validation site, and, secondly a more expensive but more flexible aircraft-based validation.

The difficulty of comparing a fixed radar/lidar on the ground with the satellite nadir-pointing radar and lidar is that the profiles from the two pairs of instruments must be within 1 km of each other. It could be arranged that the satellite over flies the ground site every three days or so with an orbit variation of about 10 km, but the precise orbit, to within 1 km, would only be known one day in advance. One can imagine portable equipment whose site could be adjusted by a few kilometres so that its position was precisely below the satellite. Such an arrangement is not very appealing. It places great restrictions on the orbit, and once the position of a single ground site is chosen orbit considerations restrict the possible choices for the positions of any other sites.

An aircraft with a lidar and radar on board that positions itself under the orbit to fly very accurately and samples the same profiles as viewed by the satellite radar and lidar would provide a more flexible validation. This approach will have to be adopted for *in-situ* measurements, though the length of correlative measurements will be relatively short due to the very big difference in the velocities of the aircraft and the satellite.

The same approach as used to validate the satellite inferences can also be used, to some extent, to evaluate the performance of the satellite's active instruments.

8 Mission Requirements and Performance

8.1 Mission Requirements

As shown in the introduction to this report (Chapter 2), all predictions of future global warming rely on numerical models of weather and climate. The major area of uncertainty in such models is the representation of clouds and aerosols. The aim of this mission is to provide global observations of the vertical profile of clouds and aerosols to validate and improve their parameterisation in numerical models and so give increased confidence in the ability of such models to predict future climate.

It is proposed to carry out the evaluation of atmospheric models by comparing the model data with the observations of vertical slices through the atmosphere. These 'snapshots' make it possible to assess the quality of the model performance in a unique way rather than relying on the traditional approach of using climatological mean values. Instead, individual vertical profiles of cloud and aerosols properties will be measured and compared with observed satellite radiance viewed at nadir, so that global data covering a larger variety of different scenarios (e.g. trade-wind cumulus, sub-tropical strato-cumulus, mid-latitude depressions, deep tropical convection, orographic and jet stream cirrus...) may then be compared with their representation in global circulation and climate models. From these evaluations, a new reliable cloud parameterisation scheme can be established.

In Chapter 4, an inventory is given of the parameters that must be known, such as the tops and bases of cloud layers, fractional cloud cover, cloud ice and liquid water content (IWC and LWC), cloud particle size and aerosol optical depth, together with the ideally required accuracies. The required accuracies (see Table 4.1) for all ERM instruments have been derived from the need to compute the instantaneous TOA flux to an accuracy of 10 W m^{-2}. This requirement will ensure that on a larger spatial scale, the determination of the mean TOA flux from the vertical profiles measured by ERM is better than 10 W m^{-2}. The values in Table 4.1 should be interpreted as guidelines for evaluating the mission performance. The observed 'snapshots' of the vertical profile will be used to evaluate model outputs.

8.2 Mission Performance

The space segment of ERM will comprise a satellite with four instruments. Each instrument has its own role in observing/deriving the radiatively relevant cloud and aerosol properties. In general, the lidar and radar provide profile information on backscatter profiles, while the multi-spectral imager and the broad-band radiometer provide observations of cloud and aerosol fields. The potential of the synergetic exploitation of the observations has been shown in Chapters 5 and 7. The performances as detailed in Chapter 6 will enable the retrieval of the geophysical parameters listed in Chapter 4. The achievable accuracies (together with those required, see Table 4.1) are shown in Table 8.1:

	Required		Achievable	
	Detectability*	**Accuracy**	**Detectability***	**Accuracy**
Fractional cloud cover	5%	5%	5%	5%
Cloud top/base ice liquid	n/a n/a	500 m 300 m	n/a n/a	100 m 300 m
Ice water content (IWC)	0.001 g m^{-3}	+40 / -30%	0.001 g m^{-3}	30%
Ice effective radius	n/a	+40 / -30%	n/a	30%
Liquid water content (and effective radius)+	Optical depth 1	+100% / -50%	Optical depth 1	+100% / -50%
Aerosol optical depth	0.04	10%	0.04	10%
Short-/long-wave radiances at TOA	n/a	1.5 W m^{-2} sr^{-1}	n/a	1.5 W m^{-2} sr^{-1}

* minimum threshold

\+ the detectability is for all liquid clouds with optical depth specified

Table 8.1. *Required and achievable mission specifications.*

A study of the proposed ERM specification has been conducted to evaluate quantitatively the consistency of the instrument requirements and the gain from the collocation of the four instruments on the same platform. This study simulated each instrument using detailed data sets generated by a Regional Climate Model (RCM) (Park et al., 1999). The data sets were prepared from the RCM at 50 km and 1 km resolution. The enhancement in the quality of the retrieved parameters from combining the different instruments is very high, as demonstrated in Chapters 5 and 7 and in Park et al. (1999).

The essential advantages of the proposed ERM mission were quantified using a number of case studies. The simulated meteorological fields covered a wide range of cloud structures. These fields were used to simulate the instrument signals from which the geophysical parameters were then retrieved using algorithms more primitive than those described in this document (Chapter 5). The retrieved geophysical parameters were then compared with the original fields. As a final comparison, the TOA flux before and after retrieval was also compared. Figure 8.1 shows a flow diagram of the method used and the comparisons performed.

These case studies provided insight into the accuracies achievable with such a system. Simulations were carried out for several cases including some during the CLARE'98 campaign (see Chapters 4 and 5). In the following figures the case of 14 October 1998 is shown as example. Figure 8.2 shows (left-hand panel) the synoptic situation (isobars at sea-level) and the cloud cover from the RCM (right-hand panel).

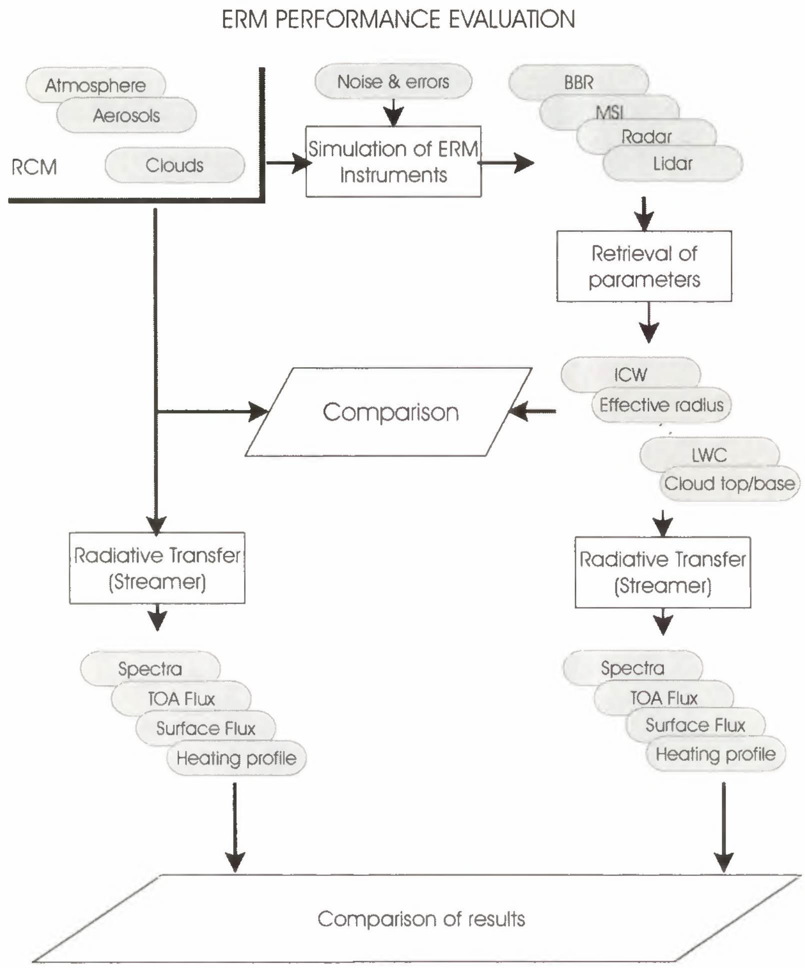

Figure 8.1. *Outline of the Mission Performance Evaluation Tool (Park et al., 1999).*

Figure 8.3 illustrates the resulting long- and short-wave TOA cloud forcing in a west-east direction (passing over Chilbolton where CLARE'98 took place) for radar only and radar with lidar in synergy. For averaged cases (i.e. average typically over 1000 km – synoptic scale) the errors in the net fluxes at the top and at the surface were of the order of 1 to 2 W m^{-2}. Under some specific conditions (e.g. cloud edges) errors of up to 40 W m^{-2} (e.g. in the middle of the figures for both long- and short-wave) can occur at a scale of 50 km while usually the errors stay in or below the 10 W m^{-2} level referred to in Section 8.1. For these studies, very preliminary synergetic retrieval algorithms have been applied. The results prove that the instrument requirements are consistent with the mean 10 W m^{-2} and that the synergetic use of the instruments (requiring collocation) is essential to achieve the objectives.

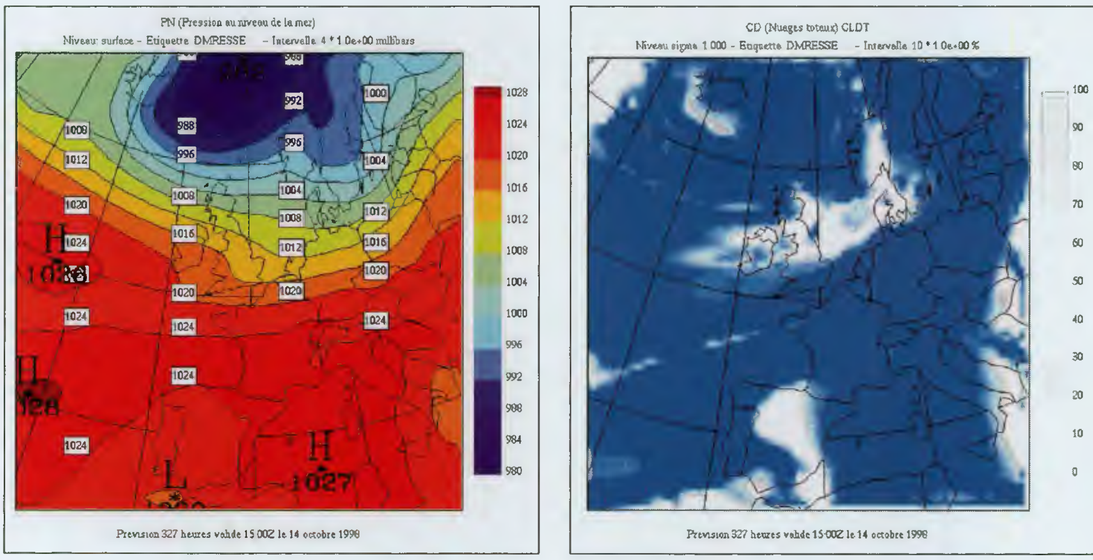

Figure 8.2. *The 14 October 1998 case study (Park et al., 1999). The left-hand panel shows surface pressure, the right-hand panel the modelled cloud cover (dark blue represents cloud cover of between 90 and 100% while white is between 0 and 10%).*

The study results of Park et al. (1999) give good confidence that the objectives of this mission can be achieved, since the ERM instrument complement allows:

- the radiative fluxes to be determined
- the measurement of the vertical cloud profiles of water and ice and their characteristics, including the detection of the presence of precipitation
- the detection and measurement of aerosol characteristics.

8.3 Conclusion

ERM will bridge the present gap between atmospheric models and observations of the vertical structure of clouds and aerosols, as has been demonstrated in this report. The mission has specifically been defined with the scientific objectives of determining worldwide the vertical profiles of aerosol and cloud field characteristics to provide basic input data for numerical modelling and studies of:

- the divergence of radiative energy
- aerosol-cloud-radiation interaction
- the vertical distribution of water and ice and their transports by clouds
- the vertical cloud field overlap and cloud-precipitation interactions.

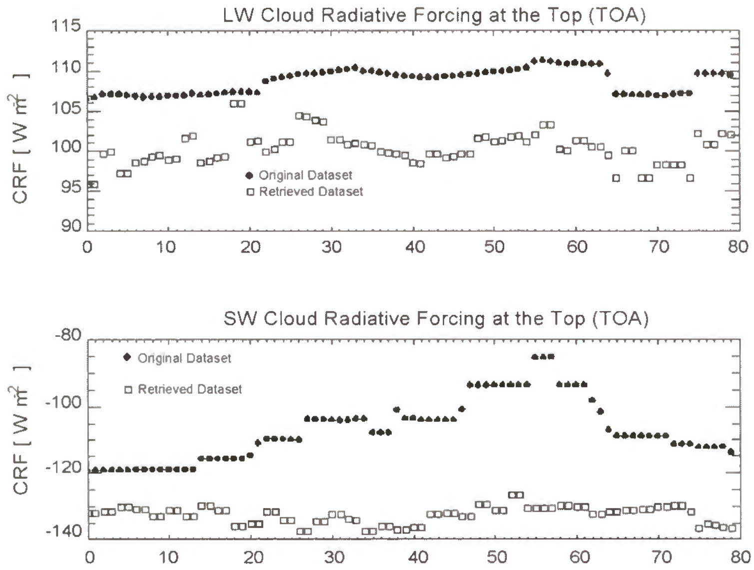

a)

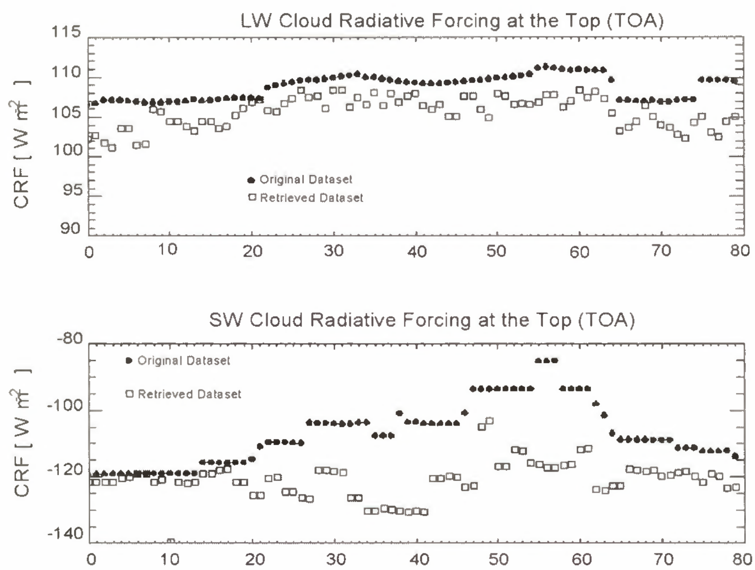

b)

Figure 8.3. *Long- and short-wave cloud radiative forcing at the top of the atmosphere computed for the simulated case of 14 October 1998 during the CLARE'98 campaign. The horizontal axis shows the number of the grid-pixel. Panel a) shows the results using only the radar, while panel b) shows the results when both radar and lidar are used (Park et al., 1999).*

With the present definition of ERM, as described in this report, these goals can be accomplished. The unique combination of a lidar, radar, multi-spectral imager and broad-band radiometer on a single platform will be a major milestone in Earth Observation Science. Innovative algorithms are under development to fully exploit the synergy between all instruments.

The accuracy of cloud and aerosols profiles to be given by ERM will be much higher than currently available products (e.g. ISCCP), particularly concerning the ice phase, which are major sources of uncertainty in cloud modelling. Moreover, the collocation of accurate nadir measurements of top-of-atmosphere radiances should lead to significant improvements in our understanding of aerosol-cloud-radiation interactions, which will in turn lead to improved parameterisation schemes in numerical models.

Numerical Weather Prediction (NWP) models will be essential tools for extrapolating the two-dimensional instantaneous structure of clouds to be measured by the ERM instruments to the full four-dimensional distribution of clouds to be used by the climate modelling community. By 2005, global NWP models will have horizontal resolutions about 20 km and vertical resolutions about 500 m in the troposphere, making most of the comparisons with ERM snapshots meaningful. From these comparisons, improved parameterisations of cloud and radiative processes will be included in forecast models to provide a better three-dimensional description of analysed cloud fields.

At the time of the ERM mission, cloud products given by data-assimilation systems should also be improved by direct use of observations related to clouds such as cloudy radiances from polar-orbiting and geostationary satellites or liquid water path and precipitation derived from microwave radiometers. Besides, it could also be possible to assimilate in the ECMWF 4D-Var system part of the ERM cloud profiles to be available in real-time since work has already been initiated in that direction.

The innovative nature of ERM is truly exploratory for both the physics and the technical aspects of this mission and will provide crucial data needed for the improvement of climate and weather forecasting models.

9 Programmatics

9.1 Introduction

Section 9.2 of this chapter presents the development approach proposed by the industrial team at the end of the Phase-A. Section 9.3 identifies the heritage and critical areas for the implementation concept. It will be shown that the risks are moderate and appropriate reduction measures have already commenced. Section 9.4 recalls the related missions, the possibilities for international co-operation and discusses the timeliness of the mission from the programmatic point of view. The contribution of the ERM to enhance the Earth observation capabilities and its application potential are outlined in Section 9.5.

9.2 Development Approach

The development schedule, shown in Figure 9.1, leads to a launch in mid-2005.

The model philosophy is defined considering the main issues identified in Chapter 6 and summarised in Section 9.3, and taking into account the financial and temporal development constraints. The approach is explained in detail in Figure 9.2.

The key features of this development approach are:

- parallel development of instruments and platform, allowed by design modularity
- no multiplication of instrument models, allowed by the pre-development activities
- manufacture of a single spacecraft model, preceded by mechanical validation and electrical / software / functional validation.

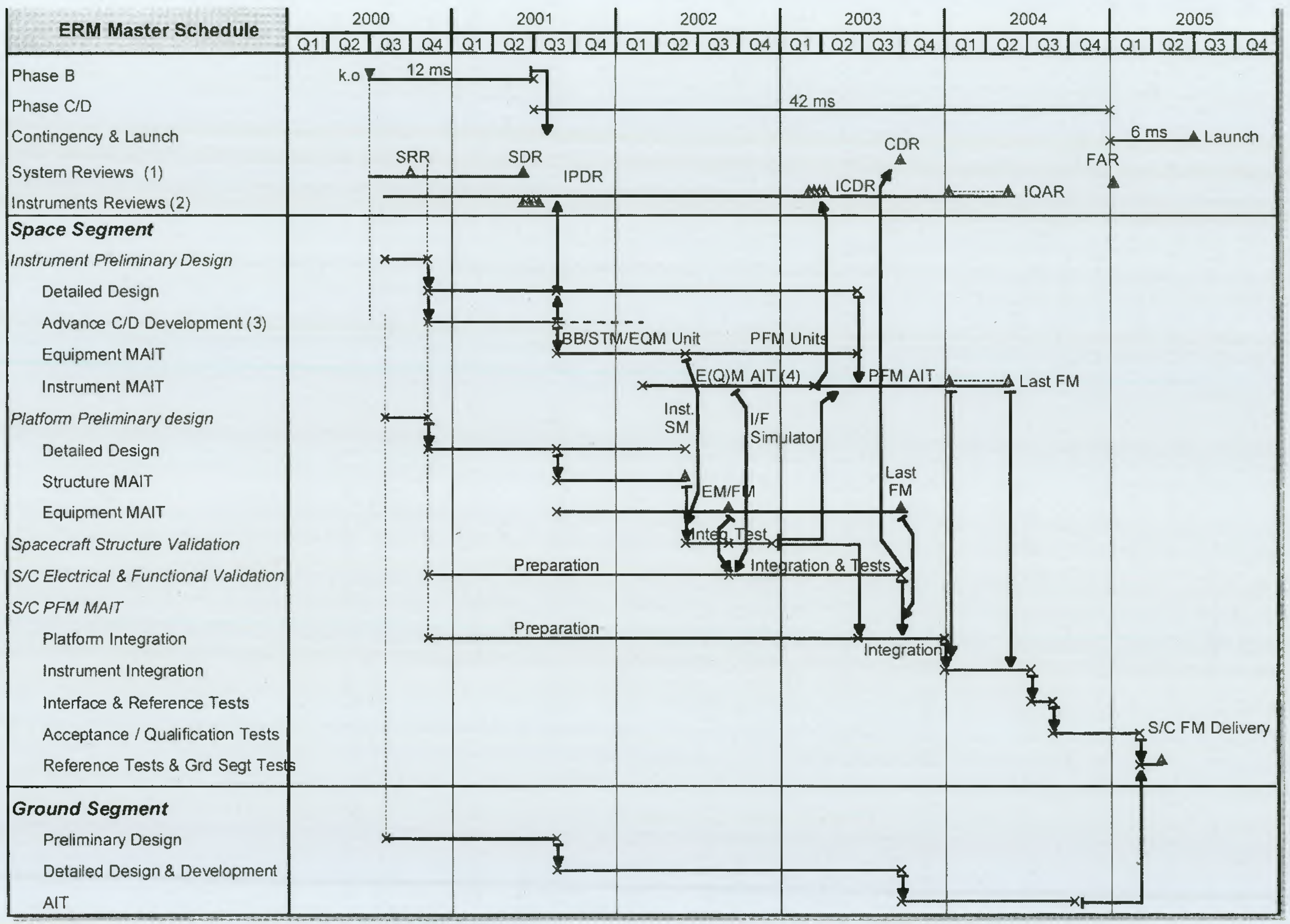

Figure 9.1. *The ERM development schedule assumes 5 years from start of Phase-B to launch. This is a tight, but feasible schedule, as the large heritage available allows a single-model development approach.*

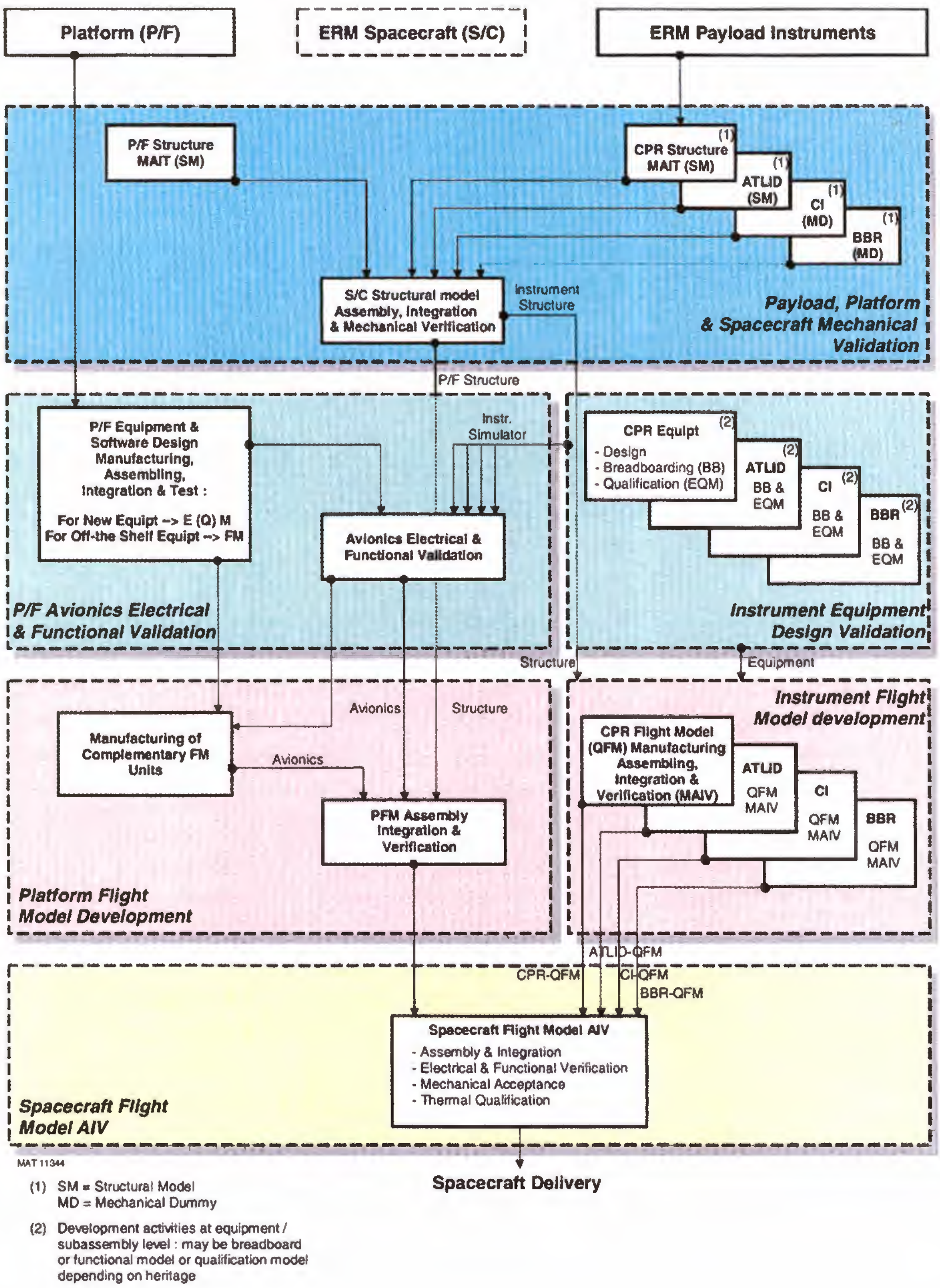

Figure 9.2. ERM development approach.

9.3 Heritage, Critical Areas and Risks

Tables 9.1, 9.2 and 9.3 summarise the ERM implementation and the heritage of the instruments and the platform.

	Implementation	**Heritage**
	Instruments	
ATLID		
Laser	Nd:Yag; 1.06 μm; 70 mJ pulse energy; 35 Hz repetition frequency..	Successfully breadboarded at ALS DIFESA under ESA contract (DPL-10 activities)
Telescope	MEYNEL type; SiC material	GLAS project; DTEL SiC demonstrator.
Laser head thermal control	Closed Fluid Loops	Implemented on STENTOR programme; results of ESA extensive R&D.
Detection chain	Detection Front Assembly using APD's	Manufactured and extensively tested in the frame of ESA GSTP 1 contract.
Electronics	Standard detection electronics	Conventional technologies
Structural concept	De-coupling of optical structure with respect to CPR supporting structure;	Conventional materials; reuse of GOMOS optical assembly mounting principle.
Calibration concept	In-orbit regular calibration; Dedicated detection chain	LITE experiment results.
Cloud Profiling Radar		
Antenna	Dual-offset Cassegrain reflector system	Processes reused from LOCSTAR antenna .
Deployment	Spring system	Reuse of AMOS reflector deployment
Diplexer	Quasi-optical diplexer, waveguide circulator as back-up	New because of 94 GHz frequency and high power; diplexer concept known from laboratory instruments
HPA	Extended Interaction Klystron (EIK) with an Electronic Power Conditioner (EPC)	Terrestrial EIK available, upgrade necessary for space applications
Receiver	LNA designed in InP based HEMT, technology, operated at < 240^0 K (passive cooling)	New component; required performance demonstrated in research laboratories
Electronics	Tailored to the instrument functional needs	New, however based on existing components / technologies
Thermal	Passive thermal control	Tailored, design and components will be standard
Structure	CFRP/Al sandwich and Al honeycomb	Tailored, design and processes are standard
Calibration	Permanent internal and infrequent external calibrations	Characterisation campaigns over reference sites required, e.g. central Greenland

Table 9.1. *Implementation and heritage for ATLID and the CPR.*

The 10-year pre-development effort for ATLID is reflected in Table 9.1. The deliberate choice for simplicity, which is not the enemy of performance, is clear for the CPR. The intention to re-use developments from non-space and non-Earth observation developments is to be noted.

The large heritage for the passive instruments is shown in Table 9.2. The innovation in the cloud imager is the use of microbolometers, which is a commercially well-established technology. Characterisation for their utilisation in the ERM was started during Phase-A.

Table 9.3 demonstrates a large heritage for all of the platform elements. This heritage exists not only at the level of reusing elements, but also for the design concepts and development approaches.

Although not shown in the tables, the reference launcher Rockot is based on proven elements for its three stages and the proposed launcher configuration as such will be demonstrated with two flights in 1999. The ground segment also has a large heritage.

Table 9.4 shows the critical areas and risk-reduction measures for ATLID and the CPR.

The critical areas for the active instruments are limited and most risk-reduction measures have already been started. Early breadboarding activities are proposed as from Phase-B. Their criticality is well within the scope of normal engineering activities.

Table 9.5 identifies the critical areas and risk-reduction measures for the passive instruments.

Table 9.5 shows the ongoing activities for the characterisation of microbolometers and recalls the lessons learned from problems encountered in the SPOT programme with the SWIR detectors. Breadboarding activities for the focal planes of the three spectral regions are proposed.

No critical areas are identified in the platform subsystems. A life time test of NiH_2 batteries is already foreseen in the frame of the Technology Research Development Programme. Concerning the launcher, alternatives to Rockot do exist, as presented in Section 6.5. No critical areas have been identified in the ground segment.

In summary, from the technical and programmatic point of view, the ERM is feasible and sufficiently mature to be implemented as one of the first two Earth Explorer Core Missions within the financial limitations of the programme.

	Implementation	Heritage
Multi-spectral Imager		
VNIR channel FPA and front-end electronics	Frame transfer CCD Si array with an in-field separation filter.	The same detector is used in current star sensors.
SWIR channel FPA and front-end electronics	InGaAs linear array.	Used for SPOT 4, alternative devices are identified.
TIR channel FPA + front-end electronics	2D microbolometer array with an in-field separation spectral filter.	The array exists for on-ground imaging applications, but is not yet used for space radiometry. The same type is planned for the IASI and PICASSO imagers. Several manufacturers have been identified in Europe and the USA.
Electronics	On board (instrument) processor, I/Fs and DC/DC section.	Tailored, but based on other standard designs and technologies.
Calibration unit VNIR/SWIR	Solar diffuser and dark signal calibration.	Similar to other units.
Calibration unit TIR	Blackbody and cold space view.	Similar to other units.
Thermal	Passive thermal control except, TEC control of SWIR and TIR FPA.	Tailored, design and components will be standard.
Structure	Aluminium panels.	Tailored, design and components will be standard.
Broad Band Radiometer		
Electronics	The electronics include 4 boards : – 2 for the DC/DC converter – 1 for the CPU – 1 for driving the Optical Head	Based on the electronics of the Sagem gyroscope Regys 3 S. Only the BBR board driving the optical head has to be developed. These electronics have been qualified for other space projects.
Optical Head	Includes 6 subsystems : – the telescope – the scanning mechanism – the channel selector – the Blackbody Simulator – the Solarcal – the mechanical structure	Space-qualified components. ScaRaB heritage will be exploited. The scanning mechanism and the channel selector will use ScaRaB-type ball bearings and space-qualified motors.

Table 9.2. *Implementation and heritage for the multi-spectral imager and the broad-band radiometer.*

	Implementation	Heritage
Multi-spectral Imager		
VNIR channel FPA and front-end electronics	Frame transfer CCD Si array with in-field separation filter.	The same detector is used in current star sensors.
SWIR channel FPA and front-end electronics	InGaAs linear array.	Used for SPOT 4, alternative devices are identified.
TIR channel FPA + front-end electronics	2D microbolometer array with in-field separation spectral filter.	The array exists for on-ground imaging applications, but is not yet used for space radiometry. The same type is planned for the IASI and PICASSO imagers. Several manufacturers have been identified in Europe and the USA.
Electronics	On board (instrument) processor, I/Fs and DC/DC section.	Tailored, but based on other standard designs and technologies.
Calibration unit VNIR/SWIR	Solar diffuser and dark signal calibration.	Similar to other units.
Calibration unit TIR	Blackbody and cold space view.	Similar to other units.
Thermal	Passive thermal control except, TEC control of SWIR and TIR FPA.	Tailored, design and components will be standard.
Structure	Aluminium panels.	Tailored, design and components will be standard.
Broad Band Radiometer		
Electronics	The electronic includes 4 boards : – 2 for the DC/DC converter – 1 for the CPU – 1 for driving the Optical Head	Based on the electronics of the Sagem gyroscope Regys 3 S. Only the BBR board driving the optical head has to be developed. These electronics have been qualified for other space projects.
Optical Head	Includes 6 sub-systems : – the telescope – the scanning mechanism – the channel selector – the Blackbody Simulator – the Solarcal – the mechanical structure	Space-qualified components. ScaRaB heritage will be exploited. The scanning mechanism and the channel selector will use ScaRaB-type ball bearings and space-qualified motors.

Table 9.3. *Implementation and heritage for the ERM platform.*

	Critical Areas	Risk Reduction Actions
ATLID		
Laser	Performance stability in flight environment	Complementary testing in Phase-B, de-rating of laser wrt. original design.
Optics	Design of the Fabry-Perot filter	Manufacturing and test of a dedicated EM model will be part of Phase-B.
Sensors	None	None, already validated on GSTP1.
Electronics	None	None
Thermal	Laser head fluid-loop qualification.	Dedicated evaporator qualification activity will be performed before FM manufacturing.
Structure	None	None
Calibration	Accuracy budget	On-ground end-to-end calibration will be performed before instrument delivery.
Cloud Profiling Radar		
Antenna	None	
Deployment	None	
Multiplexer	Inhomogeneity within the Faraday rotator because of different thermal loads inside the material.	ESA released an ITT to breadboard and test the Faraday rotator, high-power wave-guide circulator as back-up.
HPA	EIK cathode lifetime and EIK thermal control.	EIK design activity for space applications has been initiated by ESA, which promises even higher efficiency .
Receiver	Noise figure critical for instrument performance	Use of low-loss components is proposed to minimise the performance shortfall.
Electronics	None	
Thermal	None	
Structure	None	
Calibration	None	

Table 9.4. *ATLID and CPR critical areas and risk-reduction measures.*

	Critical areas	Risk reduction actions
Instrument		
Mutli-spectral Imager		
VNIR channel FPA + front-end electronics	Performance of the 'in field separation FPA' (detector + filter)	FPA breadboarding in Phase-B
SWIR channel FPA + front-end electronics	Detector behaviour in space (dark-current increase on SPOT devices)	Investigation of other manufacturers or other technologies (e.g. CMOS ROIC) as part of advance technological activities foreseen prior to Phase-B and FPA breadboarding in Phase-B
TIR channel FPA + front-end electronics	Behaviour of the OTS microbolometer design and their space qualification. Performance of the 'in field separation FPA'	On-going validation activities of theoretical assumptions on microbolometer array behaviour via the characterisation of an off-the-shelf device including radiation tolerance tests
Optics	None	
Electronics	None	
Calibration unit VNIR/SWIR	Assessment of diffuser lifetime (e.g. due to contamination).	Investigation of manufacturers of space qualified diffusers during Phase-B
Calibration unit TIR	None	
Thermal	None	
Structure	None	
Broad Band Radiometer		
	No critical areas concerning the system or the subsystems. No new technologies to be developed. No stringent requirements for the subsystems. The main difficulty arises from the accuracy of the on-ground calibration of the instrument.	Study the calibration at the beginning of the programme. Breadboards will be manufactured for the telescope, the mechanisms and the Solarcal. They will be used to validate the calibration set-up.

Table 9.5*. Multi-spectral imager and broad-band radiometer critical areas and risk-reduction measures*

9.4 Related Missions, International Co-operation Possibilities and Timeliness

The PICASSO-CENA and CLOUDSAT missions have been discussed in previous chapters. The ERM contribution relies on the higher sensitivity of its active instruments and on the synergetic exploitation especially of lidar and radar.

ERM-ATMOS B1

At this point, the Japanese ATMOS-B1 mission has to be mentioned for its large similarity with the ERM, as evidenced in the various meetings already held between the scientific advisory groups for both missions. ATMOS-B1 and the ERM are planned for the 2005-2006 horizon. Co-operation possibilities have been explored and look very promising. On the scientific side, the agreement on the objectives is very complete. From the programmatic point of view, the options for possible sharing of mission elements have been discussed. The partners are confident that the complementary interests could be harmonised and clear interfaces could be established. One possible scenario would be that NASDA contributes a dual-wavelength lidar and an FTIR (Fourier transform interferometer), the launcher and a ground station. This co-operation would significantly enhance the value of the proposed ERM by:

- increasing its scientific return
- broadening the scientific and operational user communities, and
- reducing the costs for both partner Agencies.

On the technical and programmatic side, the ERM is very timely. The 2005 launch date allows co-operation with ATMOS-B1. Furthermore, the low solar activity in the 2005-2006 period would allow a low orbit, thereby increasing instrument performance.

9.5 Enhancement of Capabilities and Applications Potential

The ERM would be the culmination and the start of the return of the investment made in a long development effort in Europe and Canada on lidar and radar technology which has yet to be flown in space. The compact instruments proposed have operational application potential. The technologies developed for the ERM have also large application potential. The science of the ERM will generate operational applications. The validation of the models with the ERM data will allow economically far-reaching decisions to be taken which will be based on more accurate predictions. In the immediate term, the ERM will have also operational utilisation potential, as demonstrated in on-going studies and by the interest of certain user groups in having some data delivered in near-real-time for assimilation into operational systems.

References

Ackerman S.A., C.C. Moeller, K.I. Strabala, H.E. Gerber, L.E. Gumley, W.P. Menzel, and S-C. Tsay, 1998: Retrieval of effective microphysical properties of clouds: A wave cloud case study, *Geophys. Res. Lett.*, **25**, No. 8, 1121-1124.

Brown, P.R.A., A.J. Illingworth, A.J. Heymsfield, G.M. McFarquhar, K.A. Browning, and M. Gosset, 1995: The Role of Spaceborne Millimetre-Wave Radar in the Global Monitoring of Ice Cloud, *J. Appl. Meteor.*, **34**, 2346-2366

Browning, K.A., 1993: The GEWEX Cloud System Study (GCSS). *Bull. Amer. Meteor. Soc.,* **74**, 387-399.

Cess, R.D., G.L. Potter, J.-P. Blanchet, G.J Boer, A.D. DelGenio, M. Deque, V. Dymnikov, V. Galin, W.L. Gates, S.J. Ghan, J.T. Kiehl, A.A. Lacis, H. Le Treut, Z.-X. Li, Z.-X. Liang, B.J. McAvaney, V.P. Meleshko, J.F.B. Mitchell, J.-J. Morcrette, D.A. Randall, L. Rikus, E. Roekner, J.-F. Royer, U. Schlese, D.A. Scheinin, A. Slingo, A.P. Sokolov, K.E. Taylor, W.M. Washington, R.T. Wetherald, I. Yagai, and M.-H. Zhang, 1990: Intercomparison and interpretation of climate feedback processes in 19 general circulation models. *J. Geophys. Res.*, **95**, 16601-16615

Cess, R.D., M.H. Zhang, W.J. Ingram, G.L. Potter, V. Alekseev, H.W. Barker, E. Cohen-Solal, R.A. Colman, D.A. Dazlich, A.D. Del Genio, M.R. Dix, V. Dymnikov, M. Esch, L.D. Fowler, J.R. Fraser, V. Galin, W.L. Gates, J.J. Jack, J.T. Kiehl, H. Le Treut, K. K.-W. Lo, B.J. McAvaney, V.P. Meleshko, J.-J. Morcrette, D.A. Randall, E. Roeckner, J.-F. Royer, M.E. Schlesinger, P.V. Sporyshev, B. Timbal, E.M. Volodin, K.E. Taylor, W. Wang, and R.T. Wetherald, 1996: Cloud feedback in atmospheric general circulation models: An update. *J. Geophys. Res.*, **101D**, 12791-12794.

Chahine, M., 1992: The hydrological cycle and its influence on climate, *Nature*, **359**, 373-380

Charlock, T., F.Rose, S.-K. Yang, T. Alberta, and G. Smith, 1992: An observational study of the interaction of clouds, radiation, and the general circulation, in Proceedings of *IRS'92: Current Problems in Atmospheric Radiation*, Tallinn, A. Deepak Publishing, 151-154

D'Almeida G.A., P. Köpke, and E.P. Shettle, 1991: *Atmospheric Aerosols.* A. Deepak Publishing, Hampton, Virginia, 561p

Derrien, M., B. Farki, L. Harang, H. LeGleau, A. Noyalet, D. Pochic and A. Sairouni, 1993: Automatic cloud detection applied to NOAA-11/AVHRR imagery, *Rem. Sens. Environ.*, **46**, 246-267

Durkee, P.A., F. Pfeil, E. Frost and R. Shema, 1991: Global analysis of aerosol particle characteristics, *Atmos. Environ.*, **25A**, 2457-2471.

Eloranta, E.W., R. E. Kuehn and R. E. Holz, 1998: Measurements of Backscatter Phase Function, Depolarisation and Particle Size in Cirrus Clouds made with the University of Wisconsin High Spectral Resolution Lidar, 4th International Symposium on Tropospheric Profiling, Snowmass, CO, Sept. 20-25.

ENV4970545: Investigation of clouds from ground-based and airborne radar and lidar, RTD Projects, European communities, 4th Framework Programme.

CLARE'98: CLARE – Cloud lidar and radar experiment, ESA, Contract No. 12957/98/NL/GD

European Space Agency, 1998: The Science and Research Elements of ESA's Living Planet Programme, *ESA SP-1227*, 105p

Flesia, C. and A. Starkov, 1998: Assessment of Multiple Scattering Effects for Spaceborne Back Scatter Lidar Signal processing, ESA/ESTEC Cnt. 11142/94/NL/CN.

Fowler, L.D., D.A. Randall and S.A. Rutledge, 1995: Liquid and ice cloud microphysics in the CSU general circulation model. Part I : Model description and simulated microphysical processes. *J. Climate*, **9**, 498-529

Fox N.I.and A.J. Illingworth, 1997: The potential of a spaceborne cloud radar for the detection of strato-cumulus clouds, *J.Appl. Meteorol*, 36, 676-687.

Fröhlich C., and J. Lean, 1998: The Sun´s Total Irradiance: Cycles, Trends, Related Climate Change Uncertainties since 1976. *Geophys. Res. Letters,* **25,** 4371-4380

Gates W.L., 1992: AMIP: The Atmospheric Model Intercomparison Project. *Bull. Am. Meteor. Soc.,* **73**, 1962-1970.

Gates, W.L., 1995: An Overview of AMIP sand Preliminary Results, in *Proceedings of the First International AMIP Scientific Conference*, (ed.: W.L. Gates), Monterey Cal., USA, 15-19 May 1995. World Climate Research Programme WCRP-92, WMO/TD-No. 732, 1-8.

Gates, W. L, J. S. Boyle, C. Covey, C. G. Dease, C. M. Doutriaux, R. S. Drach, M. Fiorino, P. J. Gleckler, J. J. Hnilo, S. M. Marlais, T. J. Phillips, G. L. Potter, B.D. Santer, K. R. Sperber, K. E. Taylor, and D. N. Williams, 1999: An Overview of the Results of the Atmospheric Model Intercomparison Project (AMIP I*), Bull. Amer. Meteor. Soc.*, **80**, 29-55

Greenwald, T.J., G.L.Stephens, S.A..Christopher, and T.A. Vonder Haar, 1995: Observations of the global characteristics and regional radiative effects of marine cloud liquid water, *J. Climate*, **8**, 2928-2946.

Gruber, A. and A.F. Krueger, 1984: The status of the NOAA outgoing long-wave radiation data set, *Bull. Amer. Meteor. Soc.*, **65**, 958-962

Harrison, E.F., P. Minnis, B.R. Barkstrom, V. Ramanathan, R.D. Cess, and G.G. Gibson, 1990: Seasonal variation of cloud radiative forcing derived from the Earth Radiation Budget Experiment. *J. Geophys. Res.,* **95**, 18687-18703.

Heise, E. and E. Roeckner, 1990: The performance of physically based cloud schemes in general circulation models. *Beitr. Phys. Atmos.*, **93**, 1-14

Husar, R.B., J.M. Prospero, and L.L. Stowe, 1997: Characterisation of tropospheric aerosols over the oceans with the NOAA advanced very high resolution radiometer optical thickness operational product, *J. Geophys. Res.*, **102 (D14)**, 16, 889-16, 909

Intergovernmental Panel on Climate Change (IPCC), 1995: *IPCC Second Assessment Report – Climate Change 1995*, UNEP/WMO

Intrieri J.M., G.L. Stephens, W.L. Eberhard, and T. Uttal, 1993: A method for determining cirrus cloud particle size using lidar and radar backscatter technique, *J. Appl. Meteor.*, **32**, 1074-1082.

Jakob, C., 1995: The impact of the new cloud scheme on ECMWF's Integrated Forecasting System (IFS). Proceedings of ECMWF/GEWEX Wokshop on Modelling, Validation and Assimilation of clouds, November 1994, ECMWF, Reading, United Kingdom, 277-294

Jakob, C. and S.A. Klein, 1999: The role of vertically varying cloud fraction in the parametrisation of microphysical processes in the ECMWF model. *Q. J. Roy. Meteor. Soc.,* **125**,941-965.

Joint Steering Committee (JSC), 1998: Annual Review of the World Climate Research Programme , Report WMO/TD-No. 929

King, M.D., Y.J. Kaufman, W.P. Menzel and D. Tanré, 1992: Remote sensing of cloud, aerosol, and water vapor properties from the moderate Resolution Imaging Spectrometer (MODIS), *IEEE Trans. Geosci. Remote Sensing*, **30**, No.1, 2-27.

Klett, J.D. 1981: Stable analytical inversion solution for processing lidar returns, *Appl. Opt.*, **20**, pp. 211-220.

Kriebel K.T., R.W. Saunders, and G.Gesell 1989: Optical properties of clouds derived from fully cloudy AVHRR pixels, *Beitr. Phys. Atmosph.*, **62**, 165-171

Van Lammeren, A., 1999: Analysis of ERM synergy by use of CLARA observation, *ESA Contract No. 12953/98/NL/GD*

Lhermitte, R.M., 1987: A 94-GHz Doppler radar for cloud observations. *J. Atmos. Oceanic Technol.*, **4**, 36-48.

Lin, B. and W. B. Rossow, 1996: Seasonal variation of liquid and ice water path in nonprecipitating clouds over oceans, *J. Climate*, **9**, 2890-2902.

Mace, G. M., C. Jakob, and K. P. Moran, 1998a: Validation of hydrometeor occurrence predicted by the ECMWF model using millimetre wave radar data. *Geophys. Res. Lett.*, **25**, 1645-1648.

Mace G G, K. Sassen, S. Kinne and T P Ackerman 1998b: An examination of cirrus cloud characteristics using data from millimetre wave radar and lidar: The 24 April SUCCESS case study, *Geophys Res. Lett.*, **25**, 1133-1136.

Mahfouf, J.-F., E. Gerard, V. Marecal, M. Miller and R. Saunders, 1998: User requirements for the assimilation of TRMM products in the ECMWF 4D-Var system. ECMWF Technical Memorandum No 264, 31p.

McCormick M.P., D.M. Winker, E.V. Browell, J.A. Coakley; C.S. Gardner, R.M. Hoff, G.S. Kent, S.H. Melfi, R.T. Menzies, C.M.R. Platt, D. A. Randall, and J.A. Reagan, 1993: Scientific investigations planned for the Lidar In-Space Technology Experiment (LITE), *Bull. Amer. Meteor. Soc.*, **74**, 2, 205.

Miller, M., M. Hortal, and C. Jakob, 1995: A major operational forecast model change, ECMWF Newsletter No 70, 2-5

Miller, S.D., G.L. Stephens, and A.C.M. Beljaars, 1999 : A validation survey of the ECMWF prognostic cloud scheme using LITE, *Geophys. Res. Lett.*, **26** , No. 10 , 1417

Minnis, P., and E.F. Harrison, 1984: Diurnal variability of regional cloud and clear-sky radiative parameters derived from GOES data. Part I: Analysis method, *J. Climate Appl. Meteor.*, **23**, 993-1011.

Morcrette, J.-J. and C. Jakob, 1999: The response of the ECMWF model to changes in cloud overlap assumption., *Mon. Wea. Rev.*(submitted)

Nakajima, T. and T. Nakajima, 1995: Wide area determination of cloud microphysical properties from NOAA AVHRR measurements for FIRE and ASTEX regions, *J. Atmos. Sci.*, **52**, 4043-4059.

Park, P., J.P. Blanchet, and S. Pal, 1999: Study on Synergetic Observations of Earth Radiation Mission Instruments, *ESA Contract 12068/96/NL/CN*

Peixoto, J. P., and A. H. Oort, 1992: *The Physics of Climate*, American Institute of Physics, N.Y.

Platt, C.M., 1997: A Parametrisation of the Visible Extinction Coefficient of Ice Clouds in terms of the Ice/Water Content. *J. Atmos. Sci.,* **54**, 2083-2098.

Platt C.M., S.A. Young, A.I. Carswell, S.R. Pal, M.P. McCormick, D.M. Winker. M. DelGuasta, L. Stefanutti, W.L. Eberhard, M. Hardesty, P.H. Flamant, R. Valentin, B. Forgan, G.G. Gimmestad, H. Jäger, S.S. Khmelevtsov, I. Kolev, B. Kaprieolev, Daren Lu, K. Sassen, V.S. Shamanaev, O. Uchino, Y. Mizuno, U. Wandinger, C. Weitkamp, A. Ansmann, and C. Wooldridge, 1994: The Experimental Cloud Lidar Pilot Study (ECLIPS) for Cloud Radiation research. *Bull. Am. Meteor. Soc.,* **75**, 1635-1654.

Potter, G., 1998: Systematic errors in cloud forcing and cloud amount from ANIP, in Workshop on *Cloud Processes and Cloud Feedbacks in Large Scale Models*, ECMWF, 9-13 November.

Rabier, F., J.-F. Mahfouf, M. Fisher, H. Jarvinen, A. Simmons, E. Andersson, F. Bouttier, P. Courtier, M. Hamrud, J. Haseler, A. Hollingsworth, L. Isaksen, E. Klinker, S. Saarinen, C. Temperton, J.-N. Thepaut, P. Unden, and D. Vasiljevic, 1997: Recent experimentation on 4D-Var and first results from a Simplified Kalman Filter, Technical Report 240, European Centre for Medium Range Weather Forecasts, Reading, U.K.

Raschke E., P. Flamant, Y. Fouquart, P. Hignett, H. Isaka, P.R. Jonas, H. Sundqvist, P. Wendling, 1998: Cloud-radiation studies during the European Cloud and Radiation Experi-ment (EUCREX), *Surv. Geophys.,* **19**, 89-138.

Ricard, J.-L., and J.-F. Royer, 1993: A statistical cloud scheme for use in an AGCM. *Ann. Geophys.*, **11**, 1095-1115

Rossow, W.B., and L.C. Garder, 1993: Cloud detection using satellite measurements of infrared and visible radiances for ISCCP, *J. Climate*, **6**, 2341-2369

Rossow, W.B., L.C. Garder, P.J. Lu and A.W. Walker, 1991: International Satellite Cloud Climatology Project (ISCCP): Documentation of cloud data. WMO/TD-No. 266, World Meteorological Organisation, 76 pp.

Rossow W.B., and R.A. Schiffer, 1999: Advances in Understanding Clouds from ISCCP. Submitted to *Bull. Am. Meteor. Soc.*

Russchenberg, H.W.J., V.K.C Venema, A.C.A.P. van Lammeren, A. Apituley, 1997: Radar-lidar observations of clouds during the CLARA-campaigns, in Proceedings of the *Workshop on Synergy of Active Instruments in the Earth Radiation Mission*, ESA EWP-1968 and GKSS98/E/10

Senior, C.A. and J.F.B. Mitchell, 1993:, Carbon dioxide and climate: the impact of cloud parameterisation, *J. Climate*, **6**, 393-418.

Slingo, J.M., 1987 : The developement and verification of cloud prediction scheme in the ECMWF model, *Quart. J. Roy. Meteor. Soc.*, **113**, 899-927

Slingo, A. and H.M. Schrecker, 1982: On the shortwave radiative properties of stratiform water clouds, *Quart. J. Roy.. Meteor. Soc.*, **108**, 407-426.

Slingo J.M., and A. Slingo, 1988: The response of a general circulation model to cloud long-wave radiative forcing. I: Introduction and initial experiments. *Quart. J. Roy. Meteor. Soc.,* **114,** 1027-1062.

Smith, R.N.B., 1990 : A scheme for predicting layer clouds and their water content in a general circulation model, *Quart. J. Roy.. Meteor. Soc.*, **116**, 435-460

Stephens G.L.S., S.C. Tsay, P.W. Stackhouse, and P.J. Flateau, 1990: The relevance of the microphysical and radiative properties of cirrus clouds to climate and climatic feedback, *J. Atmos. Sci.*, **47**, 1742-1753.

Stowe, L.L., R.M. Carey, and P.P. Pelegrino, 1992: Monitoring the Mt. Pinatubo aerosol layer with NOAA 11 AVHRR data, *Geophys. Res. Lett.,* **19**, 159-162.

Stowe, L.L., A.M. Ignatov, and R.R. Singh, 1997: Development, validation, and potential enhancements of the second-generation operational aerosol product at the National Environmental Satellite Data and Information Service of the National Oceanic and Atmospheric Administration. *J. Geophys. Res.,* **102**, 16.923-16.934.

Sundqvist H., 1994: Parameterisation of cloud microphysics for numerical atmospheric models. In *Report of Int. Workshop on Cloud-Radiation Interactions and their Parameterisation In Climate Models.* Camp Springs , Md, USA. WCRP-86

Sundqvist H., 1995: Modelling of cloud microphysics in GCMs, in ECMWF/GEWEX Workshop on Modelling, Validation and Assimilation of Clouds, 15 Oct.-1 Nov. 1994. European Centre for Medium Range Weather Forecasts, Reading, UK.

Tian, L. and J. Curry, 1989: Cloud overlap statistics, *J. Geophys. Res*, **94D**, 9925-9936

Tiedtke, M., 1993 : Representation of clouds in large-scale models. *Mon. Wea. Rev.*, **121**, 3040-3061.

Veefkind, P.J., G. de Leeuw, P. A. Durkee, P.B. Russell, P.V. Hobbs and J.M. Livingston, 1999: Aerosol optical depth retrieval using ATSR-2 and AVHRR data during TARFOX, *J. Geophys. Res*, **104**, No. D2, 2253-2260

Wang,W., M.P. Dudek, X. Liang, 1995: The greenhouse effect of trace gases. Chapter 9 in World Survey of Climatology, Vol. 16: *Future climates of the world: a modelling perspective,* (ed. A. Henderson-Sellers*),* Elsevier.

Watts, P.D. 1996: Along-track Scanning Radiometer (ATSR) estimation of cloud droplet size, optical depth and phase, Tech. Proc. of International Radiation Symposium, Wisconsin.

Weare, B.C. and AMIP Modelling Groups, 1996: Evaluation of the Vertical Structure of Zonally Averaged Cloudiness and Its Variability in the Atmospheric Model Intercomparison Project, *J. Climate,* **9**, 3419-3431

Webster, P. J. and G. L. Stephens, 1984: Cloud-radiation interaction and the climate problem. In *The Global Climate* (ed. J. T. Houghton), Cambridge University Press

Winker, D.M., R.M. Couch, and M.P: McCornick, (1996): An overview of LITE : NASA's lidar in-space technology experiment, Proc. IEEE, **84**, 164-180

World Meteorological Organisation (WMO), 1984: *Scientific Plan for the World Climate Research Programme*; WCRP Publ. Ser.2; WMO/TD-No.6; 95 p

Glossary

(A)ATSR	(Advanced) Along-Track Radiometer
ALEX	Airborne Lidar Experiment
AOCS	Attitude and Orbit Control System
AMIP	Atmospheric Model Intercomparison Project
APD	Avalanche Photo Diode
ARM	Atmospheric Radiation Measurement
ARMA	ATLID Reference Model of the Atmosphere
ATHENA	US launch vehicle
ATLID	Atmospheric Lidar
ATMOS	Japanese research satellite series
AVHRR	Advanced Very High Resolution Radiometer
BAHC	Biospheric Aspects in the Hydrological Cycle)
BB	Black Body
BBR	Broad-band Radiometer
BBS	Black Body Simulator
CCD	Charge Coupled Device
CCN	Cloud Concentration Nuclei
CCSDS	Co-ordinated Committee for the Standardisation of Data Systems
CDAE	Command and Data Acquisition Element
CERES	Clouds and the Earth's Radiant Energy System
CFRP	Carbon Fibre Reinforced Plastic
CLARE	Cloud Lidar and Radar Experiment
CLIVAR	Climate Variability
CLOUDSAT	Pathfinder Cloud Radar Mission
CNES	Centre National d'Etudes Spatiale
CPR	Cloud Profiling Radar
CRF	Cloud Radiative Forcing
DFEA	Detection and Front End Electronics
ECLIPS	Experimental Cloud Lidar Pilot Study
ECMWF	European Centre for Medium-range Weather Forecasting
EGSE	Electrical Ground Support Equipment
EIK	Extended Interaction Klystron
ENSO	El Niño Southern Oscillation
Envisat	Environmental satellite
EOL	End Of Life
EPC	Electric Power Controller
ERA	ECMWF Re-analysis
ERB	Earth Radiation Budget
ERBE	RB Experiment
ERBS	RB Satellite

ERM	Earth Radiation Mission
ERMAG	ERM Advisory Group
ERS	Earth Resources Satellite
EUCREX	European Cirrus Experiment
FOV	Field Of View
FPA	Focal Plane Assembly
FTIR	Fourier Transform Interferometer
GCM	General Circulation Model
GCSS	GEWEX Cloud System Studies
GEO	Geo-stationary Orbit
GERB	Geo-stationary ERB Experiment
GEWEX	Global Energy and Water Experiment
GOES	Geostationary Operational Environmental Satellite
GOME	Global Ozone Monitoring Experiment
GPS	Global Positioning System
GRP	GEWEX Radiation Panel
HPA	High Power Amplifier
ICSU	International Council of Scientific Unions
IFOV	Image Field of View
IGBP	International Geosphere Biosphere Programme
IPCC	Intergovernmental Panel on Climate Change
IR	Infrared
IRIS	IR Interferometer Spectrometer
ISCCP	International Satellite Cloud Climatology Project
ITCZ	Innertropical Convergence Zone
IWC	Ice Water Content
KESTREL	94 GHz Airborne Radar
Landsat	Land observation satellite
LEO	Low Earth Orbit
LEOP	Launch and Early Orbit Phase
LITE	Laser In-orbit Technology Experiment
LTDN	Local Time of the Descending Node
LW	Longwave
LWC	Liquid Water Content
MDS	Mission Demonstration Satellite
Metop	Operational Meterological Satellite
MGSE	Mechanical Ground Support Equipment
MMFG	Millimetre-wave Frequency Generator
MMIC	Microwave Monolithic Integrated Circuit
MIRACLE	94 GHz ground-based radar
MSCE	Mission and Satellite Control Centre
MSG	Meteosat Second Generation
NASA	National Aeronautics and Space Administration
NASDA	National Space Development Agency of Japan
NCEP	National Centre for Environmental Prediction

NEδρ	Noise Equivalent Delta Reflectance
NiH_2	Nickel Hydrogen
NIR	Near Infra-Red
NOAA	National Oceanic and Atmospheric Administration
NWP	Numerical Weather Forecasting
OBC	On-Board Computer
OBDH	On-Board Data Handling
OLR	Outgoing LW radiation
OSR	Optical Surface Reflector
PAE	Processing and Archiving Element
PBL	Planetary Boundary Layer
PCM	Pulse Code Modulation
PICASSO-CENA	Pathfinder Instruments for Cloud Aerosol Spaceborne Observations – Climatologie Etendue des Nuages et des Aerosols
POLDER	Polarisation and Directionality of Earth Reflectances
PRF	Pulse Repetition Frequency
PRI	Pulse Repetition Interval
PSLV	Polar Satellite Launch Vehicle, Indian launcher
QPSK	Quadrature Phase Shift Keying
RAAN	Right Angle of the Ascending Node
RCS	Reaction Control System
RFPU	Radio Frequency and Processing Unit
Rockot	Russian launch vehicle
RS	Reed-Solomon
ScaRaB	Scanner for Radiation Budget
SDC	Science Data Centre
SEVIRI	Scanning Enhanced VIS IR Imager
SiC	Silicon Carbide
SNR	Signal-to-Noise Ratio
SPOT	Satellite Probatoire de l'Observation de la Terre
SSM/I	Special Sensor Microwave / Imager
SW	Shortwave
SWIR	Short-Wave Infra-Red
TEC	Thermo-Electric Cooler
TIA	Trans-Impedance Amplifier
TIR	Thermal Infra-Red
TOA	Top of the Atmosphere
TRMM	Tropical Rainfall Measuring Mission
TT/C	Telemetry, Tracking and Commands
UNEP	United Nations Environmental Programme
USO	Ultra-Stable Oscillator
VAC	Vertical Atmospheric Column
VIS	Visible
WCRP	World Climate Research Programme

WMO	World Meteorological Organisation
XMM	X-ray Multi Mirror Mission

Acknowledgements

We are very grateful for the valuable contributions from A. Culoma, D. Donovan, J. Farrow, R. Hogan, C.-C. Lin, J.-F. Mahfouf, C. Mavrocordatos, R. Meynart, M. Miller, J.-J. Morcrette, M. Quante and A. Starkov.

Thanks are also extended to C.J. Readings, M.L. Reynolds and A. Tobias for their time and effort in reviewing the document, and to D. Wishart for preparing the document for publication.

European Space Agency
Agence spatiale européenne

Contact: ESA Publications Division
c/o ESTEC, PO Box 299, 2200 AG Noordwijk, The Netherlands
Tel. (31) 71 565 3400 - Fax (31) 71 565 5433